

Defects and Dopants in Zinc Oxide:

A study of the optoelectronic properties of thin films prepared by
spray pyrolysis

Robert Maller

Department of Materials

Imperial College London

May 2016

A thesis submitted in fulfilment of the requirements for the degree of Doctor of
Philosophy of Imperial College London

FORWARD

The work presented in this thesis describes the research undertaken towards my PhD in the Department of Materials of Imperial College London. The experimental component of this work was performed between the period of November 2012 and November 2015 by me alone with the exception of the following:

- Work function measurements, which were performed by Maurizio Morbidoni
- Solar cell measurements, which were performed by Jiaqi Zhang
- Transistor measurements, which were performed by Dr. Yoann Porte
- Pulsed Laser Deposition and Atomic Layer Deposition, which were performed by Dr. Yoann Porte and Claire Burgess respectively

All contributions from other sources have been appropriately referenced throughout.

Work presented in Chapter V of this thesis has also been published in the following academic journal:

'Probing the doping mechanisms and electrical properties of Al, Ga and In doped ZnO prepared by spray pyrolysis' Robert Maller, Yoann Porte, Husam N. Alshareef and Martyn A. McLachlan - Journal of Materials Chemistry C, 2016, 4, 5953 - 5961

The copyright of this thesis rests with the author and is made available under a Creative Commons Attribution Non-Commercial No Derivatives licence. Researchers are free to copy, distribute or transmit the thesis on the condition that they attribute it, that they do not use it for commercial purposes and that they do not alter, transform or build upon it. For any reuse or redistribution, researchers must make clear to others the licence terms of this work

ACKNOWLEDGEMENTS

I would first like to thank my supervisor, Dr. Martyn McLachlan for his constant support, encouragement and careful guidance of my research away from the many pitfalls and dead ends I endeavoured to find.

To everybody I have had the pleasure of encountering during my time at Imperial College, you have my warmest thanks. In particular Claire Burgess, Jorge Costa and Yoann Porte have been an ever-present of my time here and without them I could not have made it this far. Their patience with my persistent questioning into the darkest corners of materials science and, more importantly, their gentle distraction from it (usually in the form of coffee, guinea pigs and board games) makes them the best research companions I could have possibly hoped for.

To everybody else in the McLachlan group: Becky, Maurizio, Jiaqi, Tian, Bob, Jaspreet, Ahmed, Rob, Joe and John and every Masters student along the way – You’ve given this group the vibrant personality that it deserves and I hope you guys find a way to make it to Harry Potter World.

To Garrett, you made a foreign place feel like home, to Rob for late night snooker matches, to Dan for a number of interesting nights, and to Xuimei for her delightful questions about the English language.

To James, Joe and Troy for their own special understanding of my work, derived from many abstract metaphors - my favourite involving sharks and shopping trolleys.

To my family, for their love and support through the course of my education, for their diligence in reading this thesis, and for their reminders to use commas occasionally.

Finally to my partner, Ebbie, who has been by my side for all the adventures along the way. From murder mysteries to marathons, you brightened even the darkest moments of the past three years.

ABBREVIATIONS

4PP	four point probe
A	absorbance
AA CVD	aerosol assisted chemical vapour deposition
AC	alternating current
AFM	atomic force microscopy
ALD	atomic layer deposition
at%	atomic percentage
AZO	aluminium doped zinc oxide
B	magnetic field
c_1	elasticity constant
CBM	conduction band minimum
CG	carrier gas
CGP	carrier gas pressure
CVD	chemical vapour deposition
Cy	cycles
d	thickness
D	distance from hotplate
DC	direct current
EDX	energy dispersive spectroscopy
Eg	band gap
FEG	field emission gun
FIB	fast ion beam

FTO	fluorine doped tin oxide
GZO	gallium doped zinc oxide
HPC	hexagonal close pack
HT	hotplate temperature
ITO	indium tin oxide
IZO	indium doped zinc oxide
K	shape factor
k_B	Boltzmann constant
l	grain size
LED	light emitting diode
m_e^*	effective mass of electron
m_e	mass of an electron
n_r	refractive index
NS	nozzle size
PC	precursor concentration
PL	pause length
PS	precursor salt
PV	photovoltaic
q	elemental charge
R_e	electron penetration depth
r_H	Hall factor
R_H	Hall coefficient
R_{RMS}	roughness (root mean squared)

s	lattice site
s	mean speed
S	precursor solvent
SEM	scanning electron microscopy
SoP	speed of pass
SP	spray pyrolysis
St	substrate type
T	transmittance
Tc	texture coefficient
TCO	transparent conducting oxide
TEM	transmission electron microscopy
TFT	thin film transistor
UV-Vis	UV-Visible spectroscopy
VBM	valance band maximum
V_H	Hall voltage
XPS	X-ray photoemission spectroscopy
XRD	X-ray diffraction
Z	defect charge state
ZnO	zinc oxide
α_c	coulomb integral
α	absorption constant
β	resonance integral
Δ	divergence of strain

ϵ	dielectric constant
θ	Bragg angle
λ_m	mean free path of an electron
λ	wavelength
μ	charge mobility
ρ	resistivity
τ_m	mean free time between scattering

ABSTRACT

Interest in transparent conducting oxides (TCOs) has intensified over the past decade, driven by the requirement to find a suitable replacement to indium tin oxide (ITO). Of the many possible candidates identified, zinc oxide (ZnO) was selected owing to its favourable optical properties, abundance, low toxicity and chemical stability. This thesis is directed towards finding low cost routes to producing transparent conducting ZnO thin films that could be utilised in a range of current and emerging optoelectronic devices.

The spray pyrolysis technique is demonstrated as a highly appropriate low cost, large area deposition route to produce ZnO thin films. The necessity for, and the construction of, an automated rig for the deposition process is detailed. Excellent reproducibility is demonstrated compared with manual deposition.

The structural, electrical and optical properties of native and doped ZnO are examined with the overall aim to optimise performance for TCO applications. The novel, AC Hall effect technique is employed to study the factors controlling charge carrier concentration and charge mobility across the a wide doping range, including in previously unexplored regions such as in the undoped and low doping regimes. Investigations into the optimal crystal structure for the greatest charge carrier concentration and charge mobility are made and links between the degree of (002) texturing and charge mobility suggested. Further studies into the position of Al, Ga and In dopants in the crystalline lattice show that the ionic radius plays a key role in the solubility of the dopant in the lattice. Ingress and egress of the zinc vacancy (V_{Zn}), and emergence of the hybrid dopant substitution/zinc vacancy ($X_{Zn}V_{Zn}$ where X = Al, Ga, In) defects are suggested as likely candidate to explain observed electronic behaviour.

Finally, the effect of annealing ZnO films is studied, and the necessity for Zn-rich films for TCO applications determined. Annealing in oxygen poor environments is shown to greatly reduce resistivity of films, with V_{Zn} defects suggested to be the main contributor to this effect. The stability of electronic improvements following annealing is presented; no observable degradation in performance is seen subsequent to 180 days storage in ambient conditions.

CONTENTS

Forward.....	1
Acknowledgements.....	2
Abbreviations.....	3
Abstract.....	7
Contents	8
Table of Figures.....	12
Chapter I – Fundamentals.....	25
1.1 Introduction.....	25
1.2 Structural properties of ZnO	27
1.3 Band Theory of Semiconductors	28
1.3.1 Bloch Functions.....	28
1.3.2 The Tight Binding Approach.....	31
1.4 Electrical properties of ZnO.....	35
1.4.1 Intrinsic/unintentional impurity defects in ZnO	36
1.4.2 Extrinsic dopants in ZnO.....	45
1.4.3 Electron scattering mechanisms.....	49
1.5 Optical Properties of ZnO	57
1.5.1 Interactions between light and matter.....	57
1.6 Deposition Techniques	61
1.6.1 Vacuum based methods.....	61
1.6.2 Solution Based Methods	65
1.7 Chapter Conclusions.....	71
1.7.1 Crystalline and Electronic structure	71
1.7.2 Electrical properties.....	71
1.7.3 Optical Properties	72
1.7.4 Deposition routes.....	73
Chapter II – Experimental Methods.....	74

2.1	Introduction.....	74
2.2	Synthetic Methods.....	74
2.2.1	Spray Pyrolysis of ZnO.....	74
2.2.2	Substrate preparation.....	77
2.3	Physical and Structural Properties.....	78
2.3.1	Profilometry.....	78
2.3.2	X – Ray Diffraction.....	79
2.3.3	Scanning electron microscopy.....	82
2.3.4	Transmission Electron Microscopy.....	84
2.3.5	Energy Dispersive X-Ray Spectroscopy.....	87
2.4	Optical and Electrical Properties.....	88
2.4.1	Ultraviolet-Visible Spectroscopy.....	88
2.4.2	Four Point Probe.....	89
2.4.3	Hall Effect.....	90
2.5	Chapter conclusions.....	96
2.5.1	Synthetic methods.....	96
2.5.2	Physical and Structural properties.....	96
2.5.3	Optical and Electronic properties.....	96
Chapter III – Automated Spray Pyrolysis.....		97
3.1	Introduction.....	97
3.2	Hand Spraying and Associated problems.....	97
3.3	Fabrication of the Spray Rig.....	104
3.4	Comparison between hand and rig deposited films.....	107
3.5	Conclusions.....	110
Chapter IV – Growth and optimisation of ZnO by spray pyrolysis.....		111
4.1	Introduction.....	111
4.2	Parameter control.....	111
4.2.1	Preliminary studies.....	112
4.2.2	Thickness studies.....	117

4.2.3	Thickness dependence studies	118
4.2.4	Hotplate temperature.....	126
4.2.5	Nozzle height.....	128
4.2.6	Carrier gas pressure.....	128
4.2.7	Hotplate temperature, Nozzle height and Carrier gas pressure experiments.....	129
4.2.8	Precursor concentration	140
4.2.9	Precursor concentration experiments	142
4.2.10	Nozzle size.....	149
4.2.11	Nozzle size experiments.....	149
4.2.12	Carrier Gas	157
4.2.13	Carrier gas experiments	158
4.2.14	Growth on different surfaces.....	163
4.2.15	Different surface experiments	163
4.3	Conclusions.....	169
Chapter V – Doping and annealing Studies on ZnO prepared by spray pyrolysis		172
5.1	Introduction.....	172
5.2	Doping Studies	172
5.2.1	Preliminary results on trivalent dopants.....	175
5.2.2	Al doped ZnO.....	177
5.2.3	Aluminium at Low Doping Levels.....	189
5.3	Doping with Gallium and Indium	198
5.3.1	UV-Vis analysis of GZO and IZO	200
5.3.2	XRD analysis of GZO and IZO	202
5.3.3	SEM analysis of GZO and IZO	206
5.3.4	Doping mechanisms in GZO and IZO and a comparison with AZO	207
5.4	Annealing studies on Al, Ga and In doped ZnO	210
5.4.1	Annealing studies on AZO.....	211
5.4.2	Further Annealing studies on AZO	217

5.4.3	Stability of defects.....	221
5.4.4	Conclusions on group three doping studies.....	223
Chapter VI – Conclusions and Further Work.....		224
References.....		228
Appendix.....		245
Data from Chapter III.....		245
A. 1	Coding for Spray Rig (see section 3.3)	245
Data from Chapter IV		248
A.2	XRD patterns from section 4.2.7.2	248
A.3	XRD patterns from section 4.2.9.2	249
A.4	XRD patterns from section 4.2.11.2.....	251
Data from Chapter V.....		253
A.5	XRD data from section 5.2.1	253

TABLE OF FIGURES

Chapter I - Figures

Figure 1. 1 – Polyhedral model of wurtzite ZnO aligned along the c-axis. Red balls represent oxygen atoms and grey represent zinc. The unit cell is shown in the solid black box.....	27
Figure 1. 2 – reciprocal lattice of wurtzite ZnO, high symmetry points are labelled with Γ being the centre of the reciprocal lattice.	27
Figure 1. 3 – (a) shows a free electron a potential well between. (b) shows the periodicity of solutions between $\pm \pi/a$	30
Figure 1. 4 – a) the formation of a band of N molecular orbitals by successive addition of atoms to a chain. The width of the band increases by less upon each addition so that in an infinitely long chain the width is finite with infinite orbitals within. This effectively means an electron may reside at all energy levels with the band. b) the creation of s and p bands by successive orbital overlap.....	31
Figure 1. 5 – Energy band for $E(k) = \alpha_c + 2\beta\cos(ka)$. Adapted from reference [17].....	32
Figure 1. 6 – Visual representation of the s and p bands in sodium, magnesium and silicon extended lattices. Moving from left to right across the periodic table the atomic spacing of the lattice becomes smaller and the bands overlap more. When the bands are of similar enough energy they can hybridise, shown for the Si example. A material is classed as a metal when the Fermi energy (indicated by the shaded region) sits within a band. This explains why sodium and magnesium are metals whilst silicon is not.....	33
Figure 1. 7 – A simple sketch of the bonding in ZnO and the creation of the band gap ..	33
Figure 1. 8 – Band structure of bulk ZnO obtained from tight binding calculations. The band gap is shown in grey. This figure has been adapted from reference 8.	34
Figure 1. 9 – Positions of native point defects within the ZnO lattice, left shows zinc rich conditions and right shows oxygen rich conditions. The 0 eV position of the Fermi level represents the valance band maximum, the position at ~ 3.4 eV represents the conduction band minimum. Adapted from reference 10.	37
Figure 1. 10 – Charge states of native point defect in ZnO and how they vary across the with the Fermi energy. Adapted from reference 10.	38
Figure 1. 11 – A pictorial diagram of an oxygen vacancy. Red balls denote oxygen atoms, grey balls denote zinc atoms. The four nearest neighbour Zn atoms are displaced inwards by 12 % in the neutral V_o^x and outwards by 23 % in the $V_o^{\bullet\bullet}$	39

Figure 1. 12 – A schematic of a V_{Zn} . Red balls denote oxygen atoms, grey balls denote zinc atoms. The four nearest neighbour O atoms are displaced outwards by roughly 10 % in all three of the V_{0^x} , V_{0^y} , and V_{0^z} 40

Figure 1. 13 – A sodium interstitial site (Na_i') in sodium chloride. The lattice expands to support the small sodium ion - denoted in blue. Chlorine ions are denoted in green. [20].....41

Figure 1. 14 – Local geometries of the three stable interstitial sites. (a) and (b) show the split site whilst (c) shows the octahedral site. Once again oxygen is in red and zinc in grey. Reproduced from reference 11.....42

Figure 1. 15 – The local geometries of the octahedral site (a) shows the view through the wurtzite lattice looking down the 'b' axis, (b) shows the view through the 'c' axis. Reproduced from reference 11.....42

Figure 1. 16 – A pictorial diagram of a zinc antisite (Zn_o'') defect.....43

Figure 1. 17 – A schematic of a hydrogen interstitial(H_i^\bullet) defect. The yellow ball denotes a hydrogen ion.....44

Figure 1. 18 – The positions of hydrogen defects at increasing Fermi energies across the band gap. Positions were calculated in oxygen rich conditions at 0 K. Adapted from reference [29]......45

Figure 1. 19 – A (non-specific) group three metal substituting into the zinc lattice position. The dopant ion is depicted in orange. Lattice stressing will depend on the size and charge of the dopant.....46

Figure 1. 20 – The formation energies of aluminium extrinsic defects with increasing Fermi energy across the band gap. This was calculated in oxygen rich conditions at 0 K. Adapted from reference 16.....47

Figure 1. 21 – (a) charge trapping at a grain boundary; many low energy defect states mean charges can become trapped in a potential well. Mobile charges must have enough energy to avoid these for current to flow. (b) negatively charged potential barriers are formed from trapped carriers; the mobile charge must have enough energy to overcome the potential barrier for current to flow.....53

Figure 1. 22 - Electrons scattered by positive and negative ionised impurity centres. The maximum scattering angle from this type of scattering is 180° 55

Figure 1. 23 – The transmittance (T) and absorbance (A) spectrum of a typical Al doped ZnO film on a glass substrate. Wavelengths associated with Ultra-violet, visible and near infra-red are marked. Film shown has a thickness of ~ 300 nm and charge carrier concentration of $\sim 1 \times 10^{19} \text{ cm}^{-3}$57

Figure 1. 24 – (a) shows simplified band structure of an undoped semiconductor. (b) shows the band gap enlargement from a Burstein-Moss shift. (c) shows band gap narrowing (BG_n) from electron-electron and ionised impurity scattering.....59

Figure 1. 25 – A schematic of a spray deposition system with key components labelled.68

Figure 1. 26 – the size and temperature dependency on the nature of the droplets as they reach the substrate. A shows a constant droplet size with increasing temperature of the substrate (all temperatures are high enough to evaporate the solvent and vaporise the precipitate). B shows a constant substrate temperature with decreasing droplet size.68

Chapter I – Tables

Table 1. 1– Metal oxides frequently used as TCOs and typical dopants adapted from reference 1. Commonly used dopants are highlighted in bold.....25

Table 1. 2 – The pros and cons of common TCO material systems.....26

Chapter II – Figures

Figure 2. 1 – A photograph of a ZnO film on a glass substrate. Holes in the film were created using titania paste for profilometry measurements. The scale marker indicates 25 mm.	79
Figure 2. 2 – A diagram showing how X-rays are diffracted constructively. The crystalline planes are separated by a distance known as the d spacing - (d). When X-rays are reflected from lattice points of two planes they will constructively interfere when the path difference is equal to an integer value of the X-ray wavelength.....	80
Figure 2. 3 – Spatial resolution and depth of emissions following the irradiation from the electron beam. Irradiation is typically at 5 kV and R_e is the electron penetration depth.....	83
Figure 2. 4 – Stages of FIB cross sectioning using Helios Nanolab. (a) shows trenches milled into thin film surface. (b) shows the lamella welded to an OmniProbe after cutting out from the thin film. (c) shows the lamella positioned next to the TEM substrate holder. (d) shows the lamella welded to the sample holder. (e) shows the thinning process to achieve a sample which electrons can fully penetrate. (f) shows a fully thinned film ready for TEM imaging. Image f was reproduced courtesy of Ecaterina Ware,.....	86
Figure 2. 5 - Schematic diagram of the reflections from transparent film and related optical parameters used in the calculation of the optical constants. The terms r_1 , r_2 and r_3 represent the reflection portion or light at each interface and t_1 , t_2 and t_3 represent the transmitted portion. The figure was adapted figure 1 of reference 87.....	89
Figure 2. 6 – (a) shows the four metal probes on the head of the 4PP machine. (b) shows a schematic of the four probes in contact with the thin film, d is the film thickness, l and a are substrate dimensions l_p is the distance between the probes. Reproduced from reference 87.	90
Figure 2. 7 – Schematic showing the forces in effect across an n-type sample to produce the voltage drop known as the Hall Effect. Adapted from reference [92]	91
Figure 2. 8 –Electrode structure used for Hall effect measurements - Square structure with square and triangular contacts. Image adapted from Lakeshore 8407 User’s manual	93

Chapter II - Tables

Table 2. 1 – Target properties of TCOs.....	75
---	----

Chapter III - Figures

Figure 3. 1 – The ‘Iwata Eclipse HP-CS’ airbrush used for hand deposition. Labelled are the important components of the gun. The nozzle diameter is 0.35 mm, the precursor solution is gravity fed from a reservoir above the gun with plastic tubing connecting to a rubber bung inserted into the ‘solution inlet’. The carrier gas is supplied from a standard gas cylinder and connected to the ‘gas inlet’. Scale marker indicates 2 cm.	97
Figure 3. 2 – (a) shows a photograph of a ZnO film deposition on glass. (b) shows an SEM micrograph of the same film. Scale marker (a) indicates 20 mm, scale marker (b) indicates 200 nm.	98
Figure 3. 3 – An XRD pattern (a) and UV-Vis spectra (b) of ZnO prepared by spray pyrolysis. The XRD pattern matches that of wurtzite ZnO with a high preferential orientation towards the (002) reflection compared with the powder pattern. The large amorphous section seen between 20 – 40 ° is due to the glass substrate. Labelled are the four orientations seen in the films. The UV-Vis transmission spectra shows the fundamental absorption peak of ZnO at 360 nm and an excellent transparency between 450 and 900 nm displaying is potential for use in TCOs. Insert shows a Tauc plot of the UV-Vis data. The linear part of the plot was given a linear fit with the equation of the line shown, this gave a calculated direct bandgap of 3.25 eV.	99
Figure 3. 4 – The thickness of ten samples deposited under the same set conditions as measured by profilometry. Samples 1- 5 were measure on day one, 6-10 were measure on day two. Error bars show in-sample thickness inhomogeneity based upon standard deviations of the positions	100
Figure 3. 5 – XRD pattens of ten samples deposited by hand spraying nominally under the same conditions. The reflections are annotated with the appropriate planes of wurtzite ZnO.....	101
Figure 3. 6 – UV-Vis spectra of ten samples deposited by hand spraying nominally under the same conditions.....	102
Figure 3. 7 – Average thickness of hand sprayed films and their peak intensity (a) and transmittance minimum (from the ZnO fundamental absorption) (b). These graphs assume that there is a linear relationship between the peak height / minimum transmittance and thickness.	102

Figure 3. 8 – Annotated picture of the air gun used on the spray rig. The nozzle size is reduced from 0.35 mm - 0.2 mm. The precursor solution is delivered from the ‘solution bottle’, a small vacuum is created by the airflow so that when the trigger is pressed the carrier gas is released through the nozzle pulling solution to the nozzle where it is atomised.....	104
Figure 3. 9 – 3D sketch of the stage designed to carry the air gun over the hotplate. Left shows an aerial view of the stage, holes in the middle of the stage are for the nozzle and the linear actuator. Scale marker indicates 50 mm.	104
Figure 3. 10 – 3D sketch of the stage mounted on the rails with the belt attached and connected to the motor. The linear actuator is affixed to the stage. Electrical wiring connects the belt motor and linear actuator to a microcontroller.	105
Figure 3. 11 – 3D model of the spray rig setup with hotplate and encasement. The microcontroller is stored within the box on the front. The button and LED which act to start the program and display when the program is finished are shown on the microcontroller box.	106
Figure 3. 12 – Profilometry measurements of ten ZnO samples.	107
Figure 3. 13 – XRD patterns of ten rig films deposited under the same conditions. Labelled are the crystalline orientations of the ZnO films.....	108
Figure 3. 14 – UV-Vis transmittance spectra of ten rig deposited films deposited under the same conditions	109
Figure 3. 15 – Thickness measurements by profilometry and extracted from UV-Vis interference patterns of ten ZnO films deposited using the automated rig.....	110

Chapter III- Tables

Table 3. 1 – The spray parameters for initial deposition.....	98
Table 3. 2 – Spray parameters for rig vs. hand comparison.....	107

Chapter IV - Figures

Figure 4. 1 – the influence of thickness on electronic properties of IZO films. Left shows resistivity of as-deposited (AD), oxygen annealed (OA) and vacuum annealed (VA) films. Right shows Hall effect measurements of oxygen (OA) and vacuum (VA) annealed films.	117
Figure 4. 2 – The thickness of ZnO films deposited using increasing cycles, dotted line shows linear fitting. Points represent the average of measurements taken at three points on the sample shown in Figure 2. 1.	119
Figure 4. 3 – XRD patterns of ZnO films with increasing thickness. The different orientations are highlighted by vertical dashed lines.....	120
Figure 4. 4 – The texture coefficients of ZnO films with increasing thickness. An atomic representation of the lattice orientation is shown on the right.....	121
Figure 4. 5 – The crystallite size of ZnO films with increasing thickness.....	122
Figure 4. 6 – Optical transmittance of samples of different thicknesses. Insert shows Tauc analysis of optical data.....	123
Figure 4. 7 - Varying electronic band gap of ZnO with increasing thickness.....	123
Figure 4. 8 – Electrical properties of ZnO at increasing thickness measure using the Hall effect.	124
Figure 4. 9 – Thicknesses analysis from temperature, gas pressure and nozzle height optimisation experiments. Top, middle and bottom show pressures 1, 2 and 3 bar respectively, substrate temperature is found on the x-axis and which each chart showing nozzle height in different colours with 15, 18 and 21 cm indicated by cyan, blue and navy respectively. This notation will be used for all figures in this section unless otherwise stated.....	131
Figure 4. 10 – Texture coefficients of different crystal orientations (top to bottom - (100), (002), (101), (102), (110) and (103)) for ZnO films from temperature, nozzle size and height optimisation experiments. In this case pressures of 1,2 and 3 bars are displayed from left to right. A texture of 1 indicates zero texturing highlighted by dashed line.	133
Figure 4. 11 – The crystallite sizes derived from $d_{(101)}$ from temperature, gas pressure and nozzle height optimisation.	135
Figure 4. 12 – The average transmission from temperature, gas pressure and nozzle height optimisation experiments. The average transmission was taken to negate the influence of interference fringes and between 400 – 900 nm to avoid the fundamental absorption of ZnO found at ~360 nm.	136

Figure 4. 13 – AC Hall effect measurements temperature, gas pressure and nozzle height optimisation experiments. Carrier concentration, charge mobility and resistivity as shown (top to bottom), pressure of 1, 2 and 3 bar are displayed (left to right)	137
Figure 4. 14 – The crystallite size plotted against the charge mobility from temperature, gas pressure and nozzle height optimisation.	138
Figure 4. 15 – Figure of merit for TCO applications from temperature, gas pressure and nozzle height optimisation experiments.	140
Figure 4. 16 – Thickness trends in precursor concentration experiment. Zinc acetate concentration was set to 0.05, 0.1, 0.2 and 0.4 M and films were deposited for 1-10 spray cycles. Circled points indicate samples of comparable thickness used for further study.	142
Figure 4. 17 – XRD patterns of comparable thickness ZnO films from precursor concentration experiments.	143
Figure 4. 18 – Texture coefficient from precursor concentration experiment.	144
Figure 4. 19 – The crystallite size from precursor concentration experiment calculated using the Scherrer equation from the (002) peak.	145
Figure 4. 20 - Optical transmittance of samples with varying precursor concentration. Insert shows Tauc analysis of optical data.	146
Figure 4. 21 - Varying electronic band gap of ZnO with increasing precursor concentration.	146
Figure 4. 22 – AC Hall effect measures from precursor concentration experiment.	147
Figure 4. 23 – Thickness trends nozzle size experiment. Nozzle diameters of 0.2, 0.35 and 0.5 mm were used (black squares, red circles, green triangles respectively) and films were deposited for 1-4 spray cycles. Circles indicate films of comparable thickness used in further study.	150
Figure 4. 24 – XRD patterns of comparable thickness ZnO films from nozzle size experiment.	151
Figure 4. 25 – Texture coefficients from nozzle size experiment.	152
Figure 4. 26 – SEM micrographs of films from nozzle size experiment.	153
Figure 4. 27 - Optical transmittance of samples of different nozzle sizes. Insert shows Tauc analysis of optical data.	154
Figure 4. 28 - Varying electronic band gap of ZnO with increasing thickness. Trend line is purely to guide the eye.	155
Figure 4. 29 – AC Hall effect measures from nozzle size experiment.	156

Figure 4. 30 – XRD patterns of comparable thickness ZnO films from carrier gas experiment. XRD was performed upon films after Hall effect measurements, thus there are peaks present from the indium contacts labelled ‘In’ which should not be considered in analysis..... 159

Figure 4. 31 – Texture coefficients from carrier gas experiment..... 160

Figure 4. 32 - Optical transmittance of samples with varying carrier gas. Insert shows Tauc analysis of optical data..... 161

Figure 4. 33 – AC Hall effect measures from carrier gas experiment..... 162

Figure 4. 34 – XRD patterns of ZnO films grown upon different surfaces. The x-axis’ displaying the intensity are set to a logarithmic scale so that films can be compared.164

Figure 4. 35 – SEM micrographs of ZnO growth on various substrates. (a) shows 100 nm of ZnO grown on a soda-lime base. (b) shows 100 nm of ZnO grown on 10 nm of PLD deposited ZnO (glass substrate). (c) shows 100 nm of ZnO grown on 10 nm of ALD deposited ZnO (glass substrate). (d) shows 100 nm of ZnO grown on a transistor base with polycrystalline silicon on the left and gold on the right 165

Figure 4. 36 – Left shows TEM cross section of a ZnO film sprayed on to 10 nm of PLD grown ZnO. Right shows TEM cross section of a ZnO film sprayed on bare glass. The individual layers are labelled with the glass substrate at the bottom, above this the PLD grown ZnO then the sprayed ZnO, gold was sputtered on top to prevent charging from the electron microscope, platinum is deposited on the surface to protect the lamella from damage from the FIB. 166

Figure 4. 37 – Hall charge mobility and charge carrier concentration (left) and resistivity (right) of ZnO films grown on a bare glass surface and PLD grown ZnO surface. Trend lines are purely to guide the eye..... 167

Chapter IV – Tables

Table 4. 1 – Identified parameters to be controlled in the spray system..... 112

Table 4. 2 – Experimental parameters for thickness study 118

Table 4. 3 – Fixed parameters in hotplate temperature, nozzle height and gas pressure studies..... 129

Table 4. 4 – Experimental parameters for precursor concentration investigation 142

Table 4. 5 – Fixed parameters in nozzle size experiments..... 149

Table 4. 6 – Experimental parameters for carrier gas investigation 158

Table 4. 7 – Fixed parameters in surface experiments..... 163

Chapter V – Figures

Figure 5. 1 – Effects of Al doping on resistivity of ZnO, films range from 300-600 nm in thickness. Reproduced from figure 3 of reference 103.....	173
Figure 5. 2 – Effects of thickness and vacuum anneal on Al, Ga and In doped ZnO films. Reproduced from Figure 7 of reference [11].....	175
Figure 5. 3 – Sheet resistances of ZnO films doped with 2 atomic percent of Al, Bi, Ce, Ga, In and Y.....	176
Figure 5. 4 – The resistivities of aluminium doped ZnO films as measured by four point probe. Dopant concentration was varied from 0-2 at% in 0.5 at% intervals.....	180
Figure 5. 5 – a) displays the Hall charge mobility and charge carrier concentrations of aluminium doped ZnO. b) displays the resistivity of the same films as measured from the Hall effect. The samples used are the same as those measured by four point probe in Figure 5. 4.....	181
Figure 5. 6 – XRD patterns of ZnO films doped with 0-2 at% Al on glass substrates. The different orientations of the wurtzite structure are labelled.....	182
Figure 5. 7 – a) shows a TEM image of a ZnO film doped with 0.5 at% aluminium, the glass substrate and protective layers are also labelled. b) shows an EDX elemental spectra (orange dot area on a)), zinc, oxygen and aluminium are labelled. Peaks from silicon and platinum can also be seen along with copper which originates from the sample holder. Two other point scans (yellow dots on a)) were also taken showing similar spectra.....	184
Figure 5. 8 –a) shows a TEM image of a ZnO film doped with 2 at% aluminium, the glass substrate and protective layers are also labelled. b) shows an EDX elemental spectra - zinc, oxygen and aluminium are labelled. Peaks from platinum can also be seen along with copper which originates from the sample holder. The position of the three point scans are marked, with the sample shown in b) in orange and the position of two repeated measurements in yellow.....	185
Figure 5. 9 – A TEM image of ZnO doped with 2 at% Al. Individual crystallite regions are highlighted in white.....	186
Figure 5. 10 – EDX line scan of 2 at% Al doped ZnO. a) shows a dark field image of a cross section of the ZnO film. The different layers in the cross section are labelled and the damaged area where the line scan was performed (as well as three point scans) is highlighted in the white square. b) shows the elemental intensity of zinc, oxygen and aluminium across the line scan. c) shows the average elemental percent of Zn and Al across the scan.....	187

Figure 5. 11 – a) shows the Hall charge mobility and charge carrier concentration of aluminium doped into ZnO at 0-3 at% highlighting low level doping from 0-0.5 at%. Charge carrier concentration is displayed in red and hall charge mobility in blue. b) shows the resistivity of those same films.....	189
Figure 5. 12 – UV-Vis spectra of ZnO films doped 0 - 3 at% Al. Insert shows Tauc plots of films	191
Figure 5. 13 – XRD patterns of Al doped films. a) shows the full spectrum of each dopant level on an offset axis. b) shows a zoomed in view of the dominant (002) orientation.	192
Figure 5. 14 – Texture coefficients of ZnO doped with varying levels of aluminium extracted from Figure 5. 13.....	193
Figure 5. 15 – Crystallite size of ZnO samples doped with varying levels of aluminium.	194
Figure 5. 16 – SEM micrographs of films doped with a) 0 at%, b) 0.2 at% and c) 2 at%. Scale markers indicate 1 μm	195
Figure 5. 17 – Resistivity of ZnO films doped with 0-3 at% of gallium and indium.	198
Figure 5. 18 – Hall charge mobility and hall charge carrier concentration of ZnO samples doped with 0-3 at% gallium (a) and indium (b).	199
Figure 5. 19 – UV-Vis spectra of ZnO films doped with Al, Ga and In from 0-3 at%.....	201
Figure 5. 20 – Tauc analysis of ZnO films doped with Al, Ga and In from 0-3 at%.	202
Figure 5. 21 – XRD patterns of ZnO films doped with Al, Ga and In from 0-3 at%. Films were measured post analysis by Hall effect and *s represent metallic indium. a) shows the full pattern of undoped ZnO, b)-d) highlight the dominant (002) peak for AZO, GZO and IZO respectively.	203
Figure 5. 22 – Texture coefficients of (002), (101), (102) and (103) orientations for GZO and IZO films doped from 0-3 at%.....	204
Figure 5. 23 – (002) Texture coefficients of 0-3 at% AZO, GZO and IZO (top) compared with carrier charge mobility (bottom).....	204
Figure 5. 24 – Crystallite size of ZnO samples doped with varying levels of Ga (orange) and In (red).....	205
Figure 5. 25 – SEM micrographs of films doped with a) 0 at%, b) 0.2 at% AZO, c) 2 at% AZO, d) 0.2 at% GZO, e) 2 at% GZO, f) 0.2 at% IZO and g) 2 at% IZO. Scale markers indicate 1 μm	206
Figure 5. 26 – Electronic properties of AZO films as-deposited and following annealing in ambient and vacuum environments. a) shows the charge carrier concentration and carrier charge mobility), b) shows the resistivity.	212

Figure 5. 27 – Typical XRD patterns of as-deposited AZO and following anneal in air and in vacuum.	213
Figure 5. 28 – The peak position of the (002) reflection of ‘as deposited’ AZO, following annealing in air, and in vacuum $d_{(002)}$ spacing for each film is also displayed.	214
Figure 5. 29 – Charge carrier concentration, charge mobility and resistivity of 0-3 at% AZO as-deposited films and following subsequent two hours annealing treatments at 500 °C in Ar , O ₂ then a second anneal in Ar.	218
Figure 5. 30 – Trends in Hall effect measurements following annealing treatment experiment for of 0.5, 1 and 3 at% AZO.....	219
Figure 5. 31 – XRD measurements of the (002) position of as-deposited 2 at% AZO and following subsequent anneals in argon, oxygen then a second anneal in argon.	220
Figure 5. 32 – Stability of vacuum induced defects in ZnO and 2 at% AZO over 180 days	222

Chapter V – Tables

Table 5. 1- The minimum resistivity of ZnO doped with a series of dopants. Dopant % was optimised for each dopant. Reproduced from Table 1 of Reference 103.....	173
Table 5. 2 – Spray parameters of initial trivalent doping experiment.....	175
Table 5. 3 – Electronic properties of AZO films more than 300 nm cited in literature	178
Table 5. 4 – Electronic properties of films less than 300 nm cited in literature.....	178
Table 5. 5 – d spacings of different orientations taken from the 2 at% AZO XRD data.	186
Table 5. 6 – Electronic properties of AZO films cited in literature allowing post deposition annealing	210

Appendix

Figure A. 1 - Full XRD patterns from substrate temperature, stage height, gas pressure experiments.....	248
Figure A. 2 - Precursor concentration experiments: 0.05M	249
Figure A. 3 - Precursor concentration experiments: 0.1M	249
Figure A. 4 - Precursor concentration experiments: 0.2M	250
Figure A. 5- Precursor concentration experiments: 0.4M	250
Figure A. 6 - Nozzle size experiments: 0.2mm	251
Figure A. 7 - Nozzle size experiments: 0.35mm.....	251
Figure A. 8 - Nozzle size experiments: 0.5mm	252
Figure A. 9 - XRD patterns of ZnO doped with Al, Y, In, Ga, Ce and Bi. The (002) reflection is highlighted to show minimal peak shift.	253

CHAPTER I – FUNDAMENTALS

1.1 Introduction

Interest in transparent conducting oxides (TCOs) has intensified over the past decade, driven by the requirement to find a suitable replacement to indium tin oxide (ITO). Two stand-out applications in which the escalating cost of ITO is becoming increasingly problematic is in top contact layers for solar cells and transparent transistors. [1] There are also concerns over the leaching of indium and oxygen into the active layers of organic devices. [2] This is particularly pertinent for the relatively novel field of plastic electronics.

For a material to be used successfully as a TCO, it requires certain characteristics. These vary according to application but in general it should have: [3]

- High optical transparency (over 80 % between 400-700 nm).
- Low resistivity (in the region of $10^{-4} \Omega\cdot\text{cm}$)
- Low material costs and abundance of precursors
- Ease of processing (no harsh condition or expensive deposition environments)
- Low toxicity
- Long term chemical stability

Table 1. 1 shows the four oxide systems commonly used as TCOs along with typical dopants used to improve the optoelectronic properties.

Material	Dopant or Compound
In_2O_3	Sn , Ge, Mo, F, Ti, Zr, Hf, Nb, Ta, W, Te
SnO_2	Sb, F , As, Nb, Ta
CdO	In, Sn
ZnO	Al , Ga, B, In, Y, Sc, F, V, Si, Ge, Ti, Zr, Hf

Table 1. 1- Metal oxides frequently used as TCOs and typical dopants adapted from reference [1]. Commonly used dopants are highlighted in bold.

The state of the art for all four systems combines high transparencies (over 95 %) with resistivities under $10^{-4} \Omega\cdot\text{cm}$: F: SnO_2 (FTO) = $5 \times 10^{-5} \Omega\cdot\text{cm}$; [4] Sn: In_2O_3 (ITO) = $7.7 \times 10^{-5} \Omega\cdot\text{cm}$; [5] Al: ZnO (AZO) = $8.5 \times 10^{-5} \Omega\cdot\text{cm}$; [6] Sn: CdO = $1.4 \times 10^{-4} \Omega\cdot\text{cm}$. [7]

The pros and cons the four material systems are described in Table 1. 2.

Material	Pros	Cons
ITO	Ease of processing	Highest material cost High processing cost
	Established industrially	Can leach into active layers Can degrade at high temperature [8]
CdO	Material abundance	Highly toxic and carcinogenic [9]
	Chemically stable	High material costs
FTO	Low material costs	Processing can involve harsh chemical environments
	Compatible with solution processing [4]	Some toxicity associated with material and common dopants
AZO	Lowest material costs	Loses conductivity upon heating [10]
	Material abundance	
	Chemically stable Non-toxic	Difficult to achieve high conductivity by solution processing. [11]

Table 1. 2 - The pros and cons of common TCO material systems

An overview of these parameters suggests that doped ZnO is most suitable as a replacement to ITO. The challenge is to achieve higher conductivities using solution processing methods. This thesis will investigate a low cost solution processing technique with the aim of furthering the understanding of the underlying principles dictating the electronic properties of solution processed ZnO systems. The overall goal is to investigate the feasibility of producing highly conductive ZnO using solution processing techniques in ambient conditions as a potential replacement to the ITO.

In order to further explore the ZnO system a working knowledge of the fundamental theory governing the structural and electronic properties is required. The remainder of this first chapter will delve into the theory behind the optoelectronic properties of semiconductors. Following this the thin film deposition methods are discussed with the positives and negatives of each technique reviewed. A thorough literature review of the development of the deposition of ZnO by the chosen the chosen deposition method (spray pyrolysis) will be given in later chapters.

1.2 Structural properties of ZnO

ZnO can take three polymorphic crystalline structures: zinc blend, wurtzite and rocksalt. [12] The thermodynamically stable phase under ambient conditions is the wurtzite structure, which was determined by Bragg [13] and is shown in Figure 1. 1.

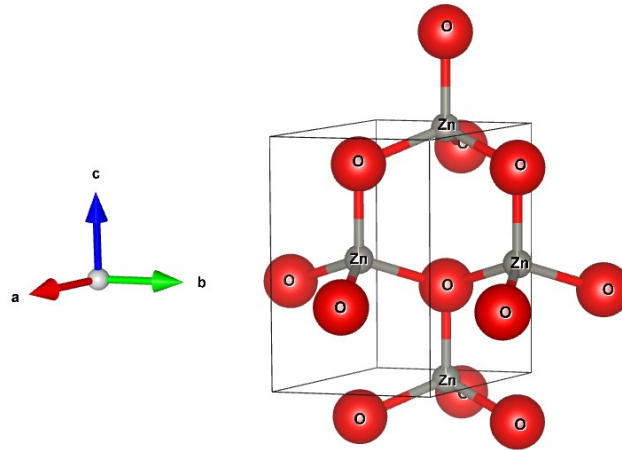


Figure 1. 1 – Polyhedral model of wurtzite ZnO aligned along the c-axis. Red balls represent oxygen atoms and grey represent zinc. The unit cell is shown in the solid black box.

The structure belongs to the $P6_3mc$ space group consisting of two interpenetrating hexagonal close packed (hcp) sub-lattices in which anions and cation are tetrahedrally bonded to four of their counterparts. The unit cell length: $a = b = 0.32489$ nm, $c = 0.52066$ nm, has been calculated for bulk ZnO (JCPDS 36-1451) however, these values can vary greatly in thin films and can be altered by doping and deposition conditions. [14] The reciprocal lattice, related the direct lattice by Fourier transform, is shown in Figure 1. 2.

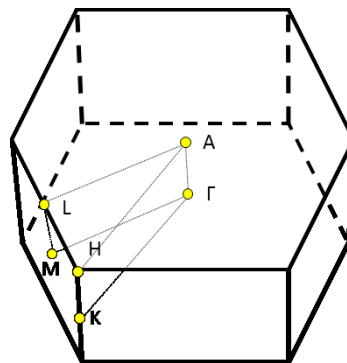


Figure 1. 2 – reciprocal lattice of wurtzite ZnO, high symmetry points are labelled with Γ being the centre of the reciprocal lattice.

The reciprocal lattice shares the same lattice spacing as the direct lattice. Transforming the lattice into reciprocal space allows, amongst other things, the calculation of the crystal structures from the Bragg spots obtained using X-ray diffraction. This will be explained in more detail in section 2.3.2. The reciprocal lattice is also useful when calculating the electronic structure of lattices as, discussed in the section 1.3, where the optoelectronic properties of ZnO are explained.

1.3 Band Theory of Semiconductors

The conductivity and the transparency of ZnO are underpinned by the electronic structures of the material. Thus, the optical and electronic properties of ZnO can be explained, predicted and enhanced by a detailed knowledge of band theory.

A full description of the quantised energy levels is given by the Schrodinger equation:

$$H\psi = E\psi ,$$

Equation 1. 1

where 'E' is the energy of the wavefunction (ψ) and 'H' is the Hamiltonian operator. However, the solution is a many body problem which requires the calculation of electron - electron, electron - nucleus and nucleus - nucleus interactions. This is impossible for multi-electron systems. Whilst an exact answer cannot be obtained it is possible to make some approximations to give quantitative solutions.

Work in this thesis will focus upon solids in crystallite lattices. As such, the tight binding approximation will provide a good model to describe the electronic band structures featured in this work. The following section summarises relevant background theory from reference [15], this begins with the origin of Bloch functions.

1.3.1 Bloch Functions

To start, an electron in a one dimensional potential well is incorporated into the Schrodinger equation (Equation 1. 2):

$$-\frac{\hbar^2}{2m_e} \frac{d^2\psi(x)}{dx^2} + V(x)\psi(x) = E\psi(x) ,$$

Equation 1. 2

where ' $V(x)$ ' is the potential, ' \hbar ' is the reduced Planck's constant and ' m_e ' is the electron mass. Focussing on a periodic lattice means that the potential of period ' a ' must satisfy:

$$V(x + Na) = V(x),$$

Equation 1. 3

where ' N ' is an integer. Taking this into reciprocal space by means of Fourier transform allows the creation of a periodic potential which includes only planes waves of wavenumbers ' h_n ' equal ' $n2\pi/a$ ', so the ' $V(x)$ ' component can be expressed as:

$$V(x) = \int_{-\infty}^{+\infty} V_n e^{ih_n x},$$

Equation 1. 4

Even if ' $V(x)$ ' is not periodic it can still have a continuous Fourier transform ' $V(q)$ ' so that:

$$V(x) = \int_{-\infty}^{+\infty} V(q) e^{iqx} dq.$$

Equation 1. 5

Taking a free electron with no periodic potential in a one dimensional box with a crystal length ' L ' (where L can tend to ∞), the wavenumbers (k), are found to be real with eigenvalues ($E(k)$) equal to ' $\hbar^2 k^2 / 2m$ ', so that the plane wave:

$$W_k(x) = \frac{1}{\sqrt{L}} e^{ikx},$$

Equation 1. 6

gives the potential shown in Figure 1. 3 - (a). A periodicity can be applied then by applying the Hamiltonian operator to the plane wave ' $W_k(x)$ ', so that the solutions to the Schrodinger equation ($\psi_k(x)$), are periodic between $\pm 'a'$, shown in Figure 1. 3 (b).

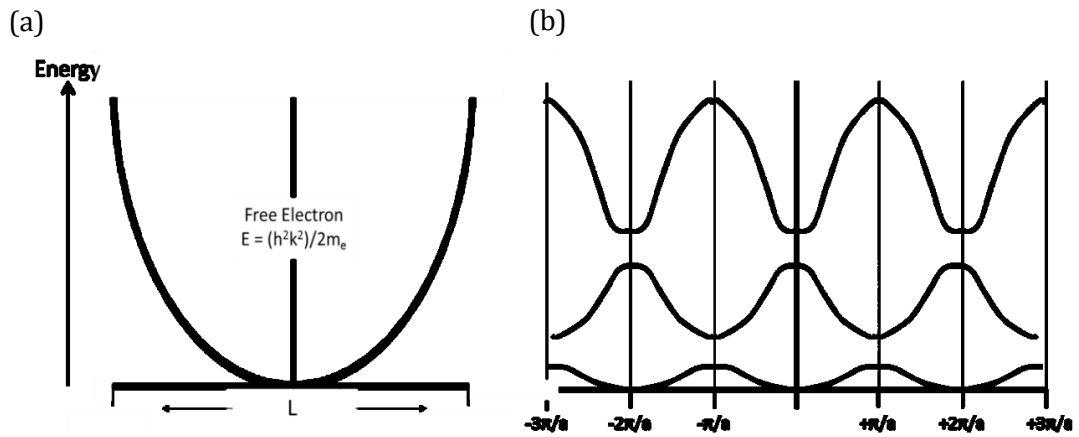


Figure 1. 3 - (a) shows a free electron a potential well between. (b) shows the periodicity of solutions between $\pm \pi/a$

The fundamental region of length ' $2\pi/a$ ' is known as the Brillouin zone. Any wavefunction can then be expressed as an appropriate linear combination of type:

$$\Psi_k(x) = \sum_n c_n(k) \frac{1}{\sqrt{L}} e^{i(k+h_n)x} .$$

Equation 1. 7

The wavefunctions of any crystalline lattice can be generically be described by:

$$\psi_k(x) = e^{ikx} u_k(x) ,$$

Equation 1. 8

where ' $u_k(x)$ ' is any function that is periodic and unchanging across all lattice positions.

This is known as the Bloch theorem.

1.3.2 The Tight Binding Approach

The tight binding approximation is complicit with Bloch theory by utilising Hückel Theory (a simplified form of molecular orbital theory). This uses the Coulomb Integral – the binding energy of isolated atomic orbitals - and the Resonance Integral – related to the strength of interaction between neighbouring atoms – to construct a hypothetical periodic one dimensional lattice.

The lattice starts with a sequence of 'N' atoms of equal energy. The interaction between the atomic orbitals removes the degeneracy, shown in Figure 1. 4, and the origin of bands can be described.

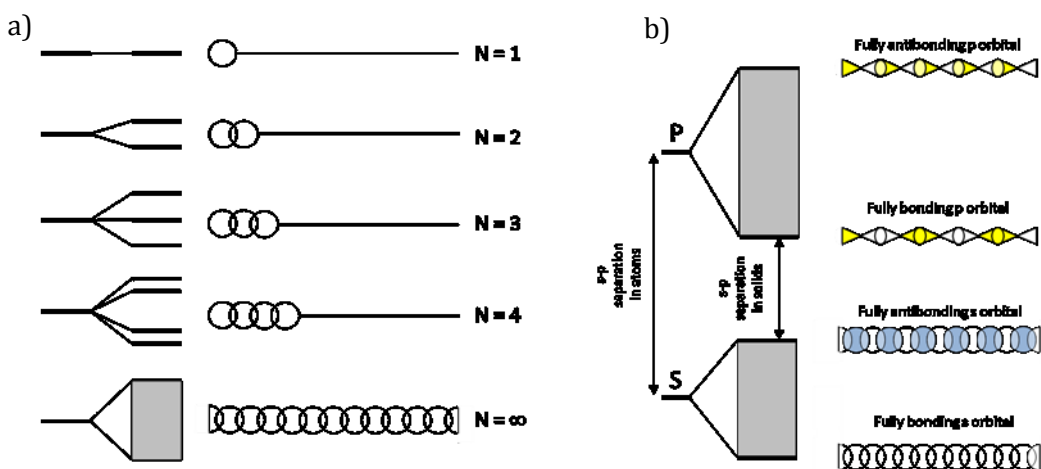


Figure 1. 4 - a) the formation of a band of N molecular orbitals by successive addition of atoms to a chain. The width of the band increases by less upon each addition so that in an infinitely long chain the width is finite with infinite orbitals within. This effectively means an electron may reside at all energy levels with the band. b) the creation of s and p bands by successive orbital overlap.

There are now infinite quantised energy levels given by the solutions to the Schrodinger equation between the top and bottom of the band. It is worth noting however that there are still energies between bands where no electrons can reside. These are known as band gaps.

To calculate the energy of individual orbitals within a band it is possible to take a general approach for all crystal lattices using a general standing wave function:

$$E(k) = \alpha + 2\beta\cos(ka),$$

Equation 1. 9

where ' α_c ' is the Coulomb integral – given by the energy of the band centre, ' β ' is the resonance integral – given by the width of the band (this takes negative values to simulate attractive atomic potentials). [16] Since ' k ' can be positive or negative the values of ' $\cos(ka)$ ' will lie between -1 and +1. This means that the energy limits of the band will mean ' k ' is found between ' $-\pi/a$ ' and ' $+\pi/a$ ', shown in Figure 1. 5.

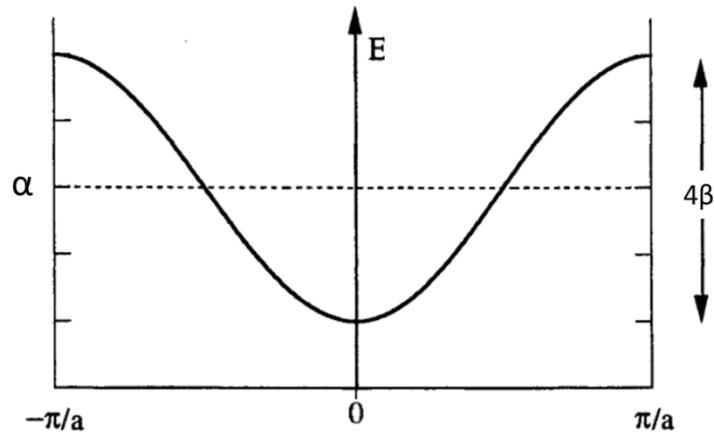


Figure 1. 5 - Energy band for $E(k) = \alpha_c + 2\beta\cos(ka)$. Adapted from reference [17]

The shape of the allowed band matches that of the Bloch function shown in Figure 1. 3 - a. The size of the bands (and thus the gaps) is dependent upon the amount orbital overlap. When the atoms are far apart, as is the case in Figure 1. 4, a gap between the s and p band can be seen. When atoms are positioned closer together, with more orbital interaction, the bands are split much wider. When the overlap between orbitals becomes too large the orbitals hybridise as shown in Figure 1. 6. The level of the Fermi energy in the band structure dictates whether a material will be metallic. [18]

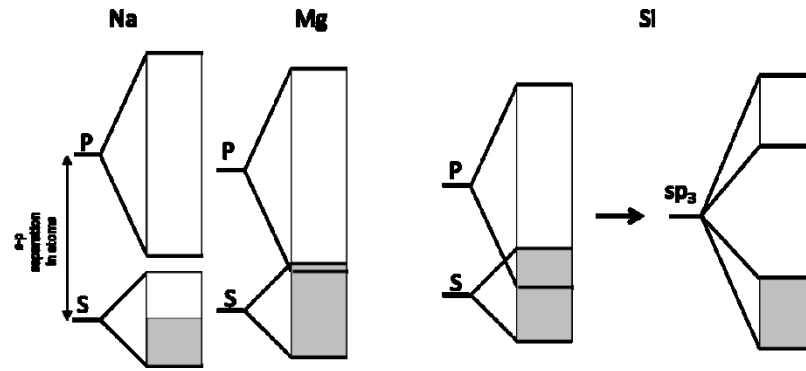


Figure 1. 6 – Visual representation of the s and p bands in sodium, magnesium and silicon extended lattices. Moving from left to right across the periodic table the atomic spacing of the lattice becomes smaller and the bands overlap more. When the bands are of similar enough energy they can hybridise, shown for the Si example. A material is classed as a metal when the Fermi energy (indicated by the shaded region) sits within a band. This explains why sodium and magnesium are metals whilst silicon is not.

1.3.2.1 Tight binding approach for ZnO

Figure 1. 6 shows single element lattices, ZnO however, is made up of two elements in a tetrahedrally bonded structure. The bonding between the zinc and the oxygen is derived from the overlap of the zinc 4s orbital and the oxygen 2p orbital. These form four sp_3 hybrid orbitals with the valence and conduction bands based on the energies of the atomic orbitals, shown in Figure 1. 7.

The hybridisation allows the electrons to exactly fill bonding orbital and they do not enter the antibonding orbitals. This gives results in a full valence band and empty conduction band. In the case of ZnO, this gap is relatively small and allows easy excitation from the valence band to the conduction band. As such, it displays semiconducting behaviour.

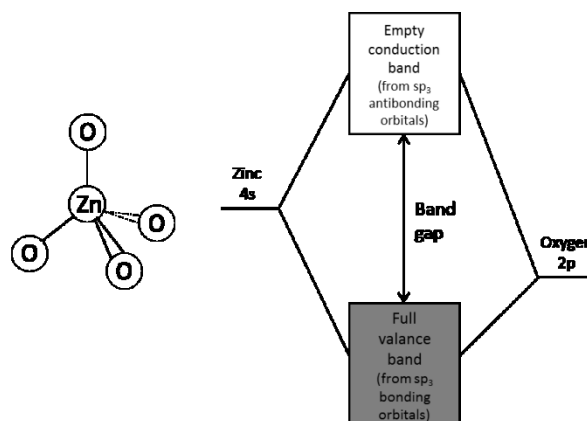


Figure 1. 7 – A simple sketch of the bonding in ZnO and the creation of the band gap

The dimensions and symmetry properties of wurtzite ZnO are shown in Figure 1. 2. Using the tight binding approximation a detailed description of the band structure can be obtained. This is achieved by calculating the wave functions across a series of high symmetry routes across its reciprocal lattice the band edges of ZnO can be shown. Figure 1. 8 gives a detailed description of the band structure of ZnO calculated using the tight binding approach. [19]

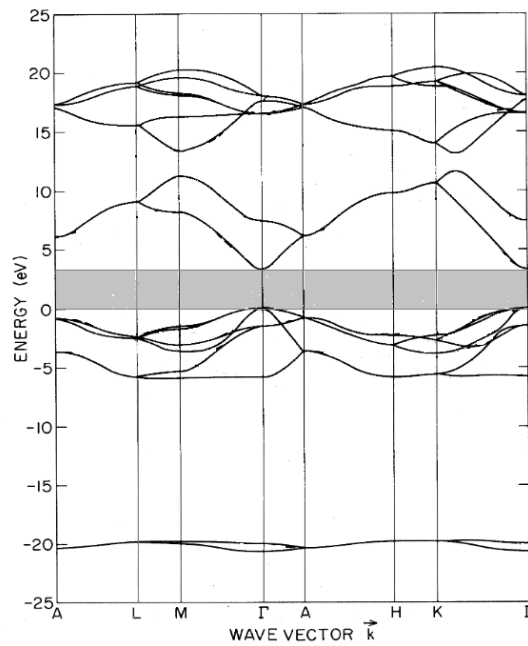


Figure 1. 8 – Band structure of bulk ZnO obtained from tight binding calculations. The band gap is shown in grey. This figure has been adapted from reference [19].

Electrons fill the states up to the zero energy position of Figure 1. 8 showing that ZnO has a direct band gap at the Γ position of roughly 3.4 eV. Stoichiometric ZnO is a wide bandgap semiconductor, however for use in TCO applications it is required to show near metallic conductivity.

1.4 Electrical properties of ZnO

The conductivity of a semiconducting material is dictated by the number of mobile charge carriers (electrons, holes or both), on the distributions of their thermal velocities and on the offset from the equilibrium distribution provoked by an applied electric field. [20]

Conductivity can be described simply by:

$$\sigma = nq \times \mu ,$$

Equation 1. 10

where 'n' is the number of mobile charge carriers, 'q' is the elementary charge and 'μ' describes the ease in which the mobile carriers can move within the system. For a perfect semiconductor crystal at zero Kelvin, the 'n' component would be zero – hence the material would have a conductivity of zero.

In real solids however, there will always be a number of thermally excited free electrons. The number of free carriers also gains a substantial contribution from charged crystal defects. These can either be intrinsic point defects or extrinsic impurity defects. When extrinsic defects are intentionally introduced to the system to improve properties they are known as dopants. The origins of native point defect and dopant defects are detailed in the following section.

The second component relates to the charge transport defined as the carrier charge mobility (μ). Charge carriers (electrons and holes) can be described as a superposition of Bloch waves travelling through a solid. For a perfect semiconductor crystal at zero kelvin these waves would travel undisturbed through the lattice - the interactions with the ions in the lattice is included in the Bloch solution. Once again the situation is more complicated in real solids, and the charge mobility of carriers is limited by scattering by a number of different mechanisms.

The many different scattering mechanisms and their relevance to ZnO are explained in section 1.4.3.

1.4.1 Intrinsic/unintentional impurity defects in ZnO

Point defects involve an anomalous situations occurring at a particular lattice site with respect to the rest of the crystal structure. Native point defects occur in all real crystal and can play an important role in the electrical properties of semiconductors by adding to (or taking away) charge carriers.

If a defect adds a local charge to a system it can become electronically active. Defects which add charge carriers in the form of mobile electrons to system are called n-type defects whereas defects, which add carriers in the form of holes are known as p-type defects.

An n-type defect occurs when a defect causes electrons to occupy an energy level within the band gap of the bulk material. Electrons in mid band gap states require less energy to excite them into the conduction band than bulk electrons in the valance band of a material. If a field is applied, free electrons become mobile within the conduction band and n-type conductivity is seen.

A p-type defect occurs when a defect state is positioned above the valance band, excitation of an electron into this state causes a positively charged vacant state within the valance band. This vacant state is also known as a hole. When an electron hops into the vacant state a positively charged site is created in its wake thus the charge can be seen as mobile. If a field is applied holes become mobile within the valance band and p-type conductivity is seen.

Impurity defects and native defects can be described using the Kroger-Vink notation which details species (M), the electric charge (q), and the lattice site (s) of the defect in the form: M_s^q . 'M' can be an atom, vacancy or electron. 'q' can be neutral given by an x, positive given by a '.', and negative given by a '''. If a charge is greater than one it is given by that number of marks. The site details which atom would usually be present at the lattice site in question, or given as an 'i' if the defect is in an interstitial site. [21] Possible defects in ZnO are given below, the charge on the defects are determined by the position within the band gap:

- Zn_{Zn}^x describes a zinc atom in a zinc site with a neutral charge while O_O^x describes an oxygen atom in an oxygen site, also with a neutral charge.
- $V_O^{..}$ describes a oxygen vacancy with a double positive charge, similarly $V_{Zn}^{''}$ describes a zinc vacancy with a double negative charge.

- O_i'' describes an oxygen atom in an interstitial site with a double negative charge, and $Zn_i^{••}$ describes a zinc atom in an interstitial site with a double positive charge.
- $Zn_O^{••}$ describes a zinc atom in an oxygen site with a double positive charge, and O_{Zn}'' describes an oxygen atom in a zinc site with a double negative charge.

The position of the native and impurity defects within the band/ band gap and the type of defects determines whether they are electronically active or not. A detailed description of how the position of a defect is determined is outside the scope of this work. However, as a simplified overview: defects with positions controlled by long range columbic interactions with ionic cores of atoms form ‘shallow defects’ near the band edges - these defects are generally good donors and acceptors; defects with positions controlled by the short range interactions with electrons form ‘deep defects’ further from band edges - these defects are generally poor donors and acceptors and even trap free carriers. [22]

A theoretical study by Janotti *et al*[23] describes the energy of native point defects of ZnO within its electronic structure. The positions of common defects obtained in this work provide the theoretical basis of the experimental defect analysis made later in this project.

A breakdown of the formation energies across the band gap from this work is shown Figure 1. 9.

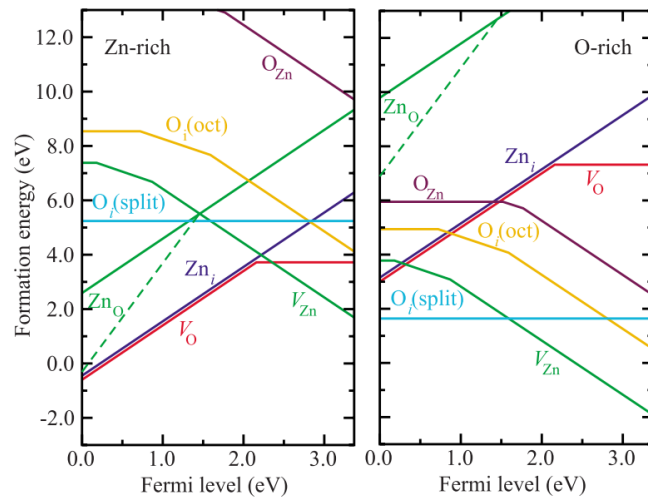


Figure 1. 9 – Positions of native point defects within the ZnO lattice, left shows zinc rich conditions and right shows oxygen rich conditions. The 0 eV position of the Fermi level represents the valance band maximum, the position at ~3.4 eV represents the conduction band minimum. Adapted from reference [23].

The formation energy of each defect depends both on its charge and its lattice environment. The charge state of the defect can change depending on its position within the band gap, shown in Figure 1. 10. When the charge state of the defect changes, the gradient its formation energy curve also changes, shown in Figure 1. 9. The lattice environment also plays a role; in zinc rich conditions oxygen vacancies become more favourable and vice versa. This manifests in the intercept values of the curves.

Each defect is explained in more detail in the following section along with its probability of formation and its effect on the electrical properties.

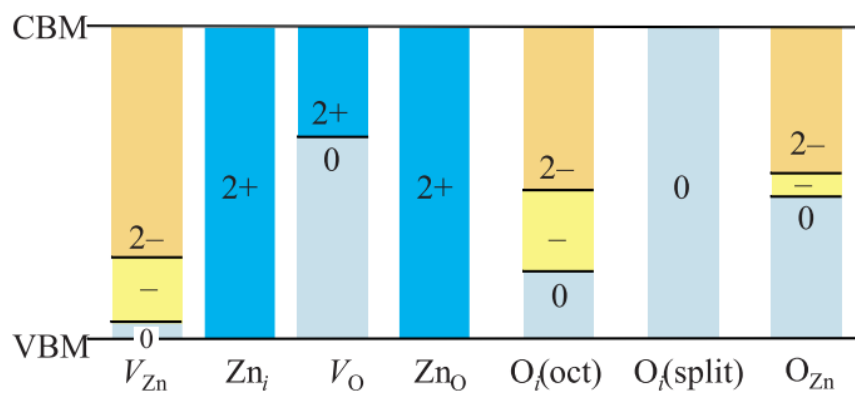


Figure 1. 10 – Charge states of native point defect in ZnO and how they vary across the with the Fermi energy. Adapted from reference [23].

1.4.1.1 Vacancies

Vacancies are possibly the simplest defect consistent of an atom removed from the bulk of a material and placed upon the surface. If the atoms are considered to be rigid in the structure, it requires energy (E_v) to remove an atom from the interior, however some energy (E_s) is reclaimed by placement of the atom on the surface. This gives the net formation energy of a vacancy to be $E_v - E_s$. As the positions of the atoms are completely rigid there is a further energy recovered by the relaxation of the lattice as the neighbouring atoms move towards the empty space. When a vacancy is created it has an associated charge depending on the number of electrons withdrawn or dangling bonds left. The charge can be present on the site or delocalised depending on the energetics of the system.

The Zn – O bond has substantial ionic character. In this case electrostatic neutrality should be satisfied. Across the entire ionic solid the electrostatic neutrality of the crystal is preserved if there are vacancies of the positive and negative species are in stoichiometric proportion. In a perfect ZnO crystal, it goes that for every zinc vacancy there must also be an oxygen vacancy. Vacancies of opposing charges which give electrostatic neutrality are known as Schottky defects. Schottky defects are compensating and not electronically active. In thin films this is not always the case, the kinetics of the system allow for vacancies and interstitials to exist independently as electronically active charged states.

1.4.1.1.1 Oxygen Vacancies in ZnO

V_o defects, shown in Figure 1. 11, have the lowest formation energy of donor defects as displayed in Figure 1. 9, and have such often been cited as a source of unintentional n-type conductivity. Following a series of ab-initio studies this is no longer considered to be likely. The neutral to doubly charged transition occurs at roughly 1 eV below the conduction band meaning that it is considered a ‘deep donor’. The size of the excitation energy makes it a low quantum yield route to creating free electrons carriers and thus, it cannot contribute greatly to the n-type conductivity. The formation energy at this position is also a significant barrier (3.72 eV), even in zinc rich conditions.

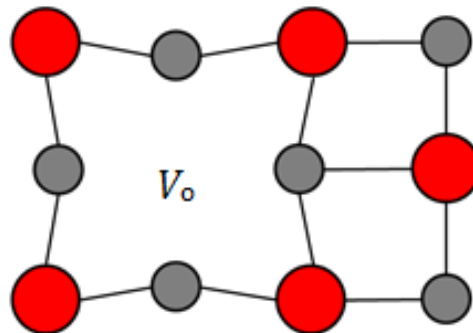


Figure 1. 11 – A pictorial diagram of an oxygen vacancy. Red balls denote oxygen atoms, grey balls denote zinc atoms. The four nearest neighbour Zn atoms are displaced inwards by 12 % in the neutral V_o^x and outwards by 23 % in the V_o^{2+}

This report uses the studies given by the van de Walle group. It is worth noting however, that there is still some ongoing debate amongst theoretical groups about the role that oxygen vacancies play in the conductivity of ZnO. In particular, the Zunger group [24][25] suggest that persistent photo-excitation provides the mechanism for oxygen vacancies to give native ZnO its n-type conductivity.

Oxygen vacancies have a calculated migration energy of 2.4 eV for $V_{O^{\times}}$ and 1.7 eV for $V_{O^{\bullet\bullet}}$. This effectively means that upon moderate annealing they can be significantly mobile within the lattice.

1.4.1.1.2 Zinc Vacancies in ZnO

In ZnO, a V_{Zn} defect, depicted in Figure 1. 12, introduces a partially occupied state in the band gap derived from the broken bonds of its nearest oxygen neighbours. These defects lie close to the valance band maximum and, because they are only half full, act as an acceptor state.

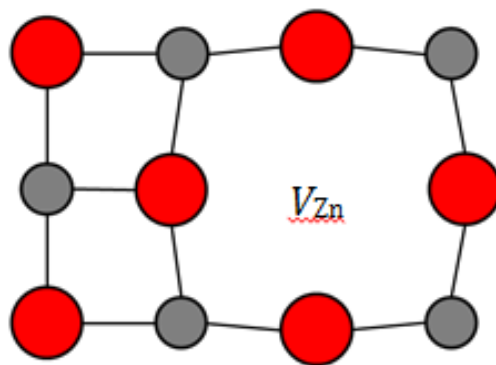


Figure 1. 12 – A schematic of a V_{Zn} . Red balls denote oxygen atoms, grey balls denote zinc atoms. The four nearest neighbour O atoms are displaced outwards by roughly 10 % in all three of the $V_{O^{\times}}$, $V_{O^{\bullet}}$, and $V_{O^{\bullet\bullet}}$

The formation energy of the V_{Zn} unsurprisingly decreases in oxygen rich conditions. It also decreases as the Fermi energy increases as is found in more n-type conditions. What this means is that in p-type conditions zinc vacancies have high formation energies and are unlikely to form. However, the formation energy is much lower in n-type conditions and so they are likely to form in moderate concentrations. These act as compensating negative centres.

V_{Zn} are found to be deep acceptors with transitions from 0 to 1- at 0.18 eV and 1- to 2- at 0.87 eV. Their migration mechanisms are similar to that of oxygen vacancies and have similar energetics.

In summary V_{Zn} are deep acceptors with high formation energies in p-type conditions so cannot add to p-type conductivity. They are likely however, to act as compensating centres in n-type conditions.

1.4.1.2 Interstitials

The second common point defect is a self-interstitial. This involves the placement of an atom of the native material from the surface to the interior of a crystal in the space between typical lattice sites. The inclusion of an atom to an interstitial site causes strain in the lattice surrounding the interstitial as atoms move to accommodate it. Interstitials are only possible in lattices which have the space available and are not seen in close pack structures.

For structures where one element is significantly bigger than the other, as illustrated in the simple case of sodium chloride, only sodium atoms with their smaller atomic radii can form interstitials. The formation energy of these defects is dictated by the ease of the inclusion into the lattice. An example is shown in Figure 1. 13.

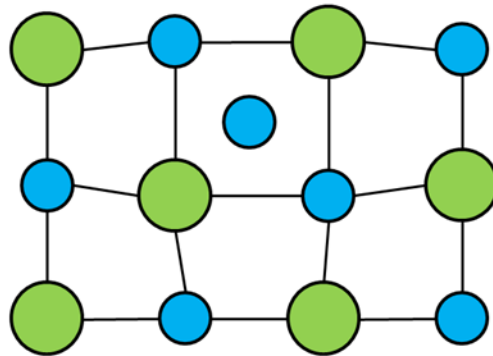


Figure 1. 13 - A sodium interstitial site (Na_i') in sodium chloride. The lattice expands to support the small sodium ion - denoted in blue. Chlorine ions are denoted in green. [20]

1.4.1.2.1 Oxygen interstitials in ZnO

The ZnO lattice is more complicated than that of the sodium chloride example shown above in that there are four possible interstitial sites in a wurtzite lattice. In terms of O_i defects, they can form in a tetrahedral site (with two zinc and two oxygen atoms at the points of the tetrahedron), in octahedral sites (with three zinc and three oxygen atoms at the points of the octagon) and in two split sites (in which the oxygen sits somewhere between the tetrahedral and octahedral sites). The tetrahedral site is found to be unstable and spontaneously relaxes into a split site. In the octahedral position the oxygen interstitial is isolated, however in the split positions it forms two weak oxygen-oxygen bonds. A three dimensional description of the structure of the three stable defects are shown in Figure 1. 14.

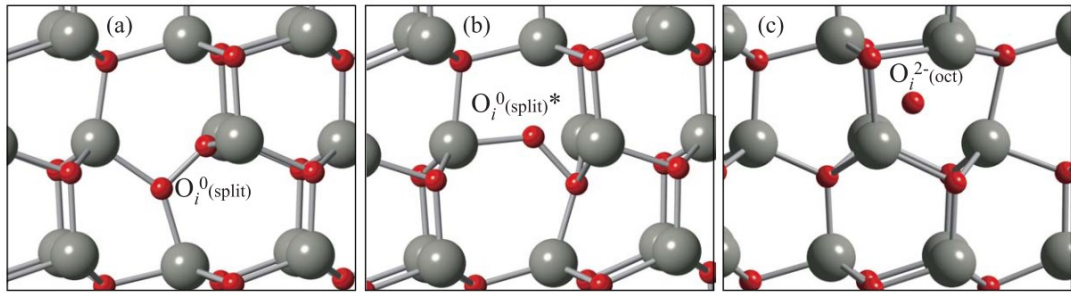


Figure 1. 14 – Local geometries of the three stable interstitial sites. (a) and (b) show the split site whilst (c) shows the octahedral site. Once again oxygen is in red and zinc in grey. Reproduced from reference[23].

The oxygen-oxygen bonds on the split site mean that the electronic states are filled and thus not electronically active. The octahedral site introduces an empty state into the lower section of the band gap meaning that it could accept two electrons. The states derive from oxygen p orbitals and are deep acceptors with the 0 to 1- transition at 0.72 eV above the valence band maximum and the 1- to 2- transition at 1.59 eV above.

The formation energies are high for all oxygen interstitial due to the size of the ion. They are not expected to be present in high concentrations.

1.4.1.2.2 Zinc interstitials in ZnO

Zn_i defects can be present only in octahedral sites as the tetrahedral site suffering severe geometric constraints. Zn_i in octahedral positions are donors with the 2+ state present at all Fermi energies in the band gap.

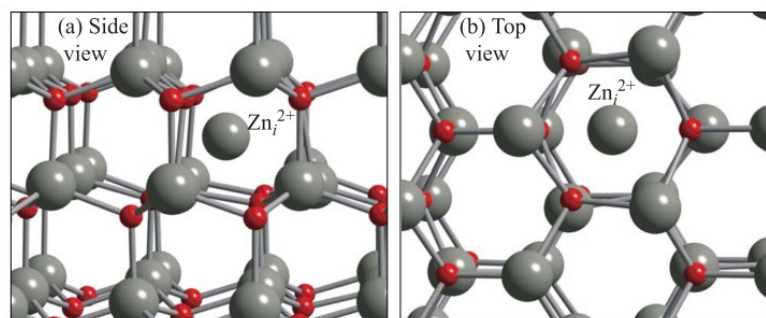


Figure 1. 15 – The local geometries of the octahedral site (a) shows the view through the wurtzite lattice looking down the ‘b’ axis, (b) shows the view through the ‘c’ axis. Red balls represent oxygen atoms and grey represent zinc. Reproduced from reference [23].

The zinc interstitial introduces a state with two electrons above the conduction band minimum. The electrons are demoted into the conduction band to add charge carriers. This mechanism means that they are effectively shallow donors.

Despite this zinc interstitials are not expected to be a source of n-type conductivity in ambient conditions because the formation energies are very high; at their lowest they are at roughly 6 eV in highly zinc rich conditions.

Zinc interstitials are the most mobile within the lattice and can migrate at modest temperatures. In fact the high charge mobility of zinc throughout the lattice can lead to crystal healing in some cases. [26]

1.4.1.3 Antisites

The last native defect to mention is an antisite. An antisite is characterised by an atom occupying the wrong kind of lattice site for example in NaCl if a Na atom was occupying a Cl site.

This defect usually exhibits the highest formation energy owed to the electrostatic and stoichiometric penalties, and can only form when the atomic radii of the atoms are of comparable size. When such defects do occur it usually involves the creation of fifty or one hundred antisites in a confined area generating a complex arrangement of atoms to counter the stresses of the system.[20]

1.4.1.3.1 Zinc and oxygen antisites in ZnO

Both zinc and oxygen antisites can nominally exist. They have significantly higher formation energies than all previously mentioned defects. The Zn_o (Figure 1. 16) is complex acting both as shallow donor with filled states within the conduction band similar to a Zn_i and a deep donor within the band gap similar to an V_o . The formation energy is even higher for O_{zn} which act as deep acceptors well within the band gap.

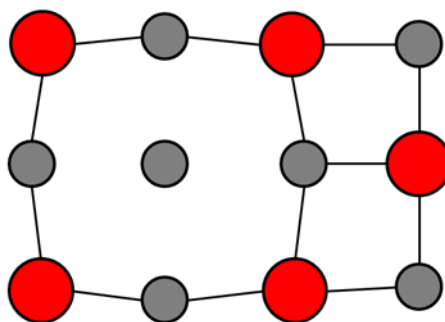


Figure 1. 16 - A pictorial diagram of a zinc antisite (Zn_o) defect. Red balls represent oxygen atoms and grey represent zinc

Whilst these defects are of academic interest, the high formation energies in all environments mean that they will not play a part in the electronic properties of ZnO in ambient conditions.

1.4.1.4 Hydrogen as an impurity defect in ZnO

Theory suggests that native defects appear not to be the cause of the latent n-type conductivity seen in ZnO. The present theory is that rather than the native point defects giving rise to the n-type conductivity it may actually be caused (or partially caused) by hydrogen impurity defects. [27][28]

Hydrogen has been suggested as a potential cause of n-type conductivity in ZnO due to its ubiquity in deposition environments and the properties it would display as a defect.

The hydrogen ion can be incorporated into interstitial sites forms a strong bond with an oxygen atom, and induce relatively large relaxations to the lattice shown in Figure 1. 17.

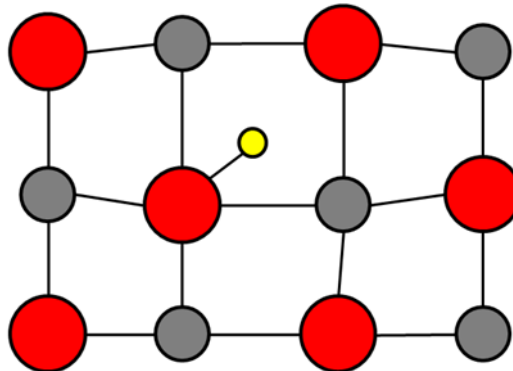


Figure 1. 17 - A schematic of a hydrogen interstitial(H_i^+) defect. Red balls represent oxygen atoms, grey represent zinc and the yellow ball denotes a hydrogen ion.

Hydrogen is present with a single positive charge at all Fermi energies in the band gap. It has a low energy of formation and is a shallow donor, thus could be present in high enough concentrations to provide the n-type conductivity seen in ZnO. A first principles calculation of the energy of H_i in ZnO at increasing Fermi energies is shown in Figure 1. 18.

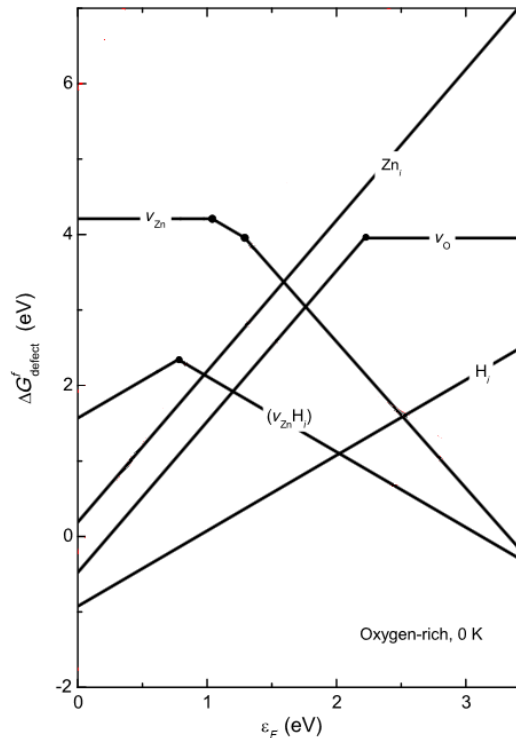


Figure 1. 18 – The positions of hydrogen defects at increasing Fermi energies across the band gap. Positions were calculated in oxygen rich conditions at 0 K. Adapted from reference [29].

Figure 1. 18 also highlights the possibility of extrinsic-intrinsic dopant complexes. In this case the positively charged hydrogen interstitial can complex with the zinc vacancy and change charge. In n-type conditions this complex defect forms an overall single negatively charged low formation energy defect, contributing to n-type compensation effects. This is particularly the case in oxygen rich conditions where the formation energy of the zinc vacancy is low.

Whilst hydrogen as the source of n-type conductivity gives a compelling case, it is unfortunately uniquely difficult to detect. As such this remains only a theory.

1.4.2 Extrinsic dopants in ZnO

Extrinsic doping of ZnO has been most well studied using the group three metals. In particular doping with aluminium, gallium and indium has received much academic interest. [30]–[34]

Group three dopants typically act as donor defects by substituting for zinc in the ZnO lattice shown in Figure 1. 19.

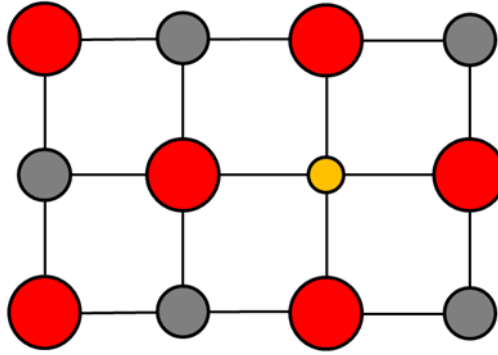


Figure 1. 19 – A (non-specific) group three metal substituting into the zinc lattice position. Red balls represent oxygen atoms, grey represent zinc and the dopant ion is depicted in orange. Lattice stressing will depend on the size and charge of the dopant.

The donor ions introduce partially filled states into the band gap of ZnO based on a single electron residing on the group three ion p orbital. These states reside just below the conduction band minimum; 59 meV for Al, 54.5 meV for Ga and 63.2 meV for In. [13] They are electronically active in the M_{Zn}^{\bullet} state at all Fermi energies. The differing ionic and covalent radii (zinc oxide has both an ionic and covalent nature to its bonding) of the dopant atoms compared with zinc cause different strains to the wurtzite lattice. The ionic radii are as follows: $Zn^{2+} = 0.60 \text{ \AA}$; $Al^{3+} = 0.39 \text{ \AA}$; $Ga^{3+} = 0.47 \text{ \AA}$; $In^{3+} = 0.62 \text{ \AA}$ and the covalent radii: Zn = 1.20 \AA ; Al = 1.24 \AA ; Ga = 1.23 \AA ; In = 1.42 \AA . [35] The closer match of the Ga ion to the Zn in terms of both ionic and covalent radii suggest that they will be most efficient donor materials. This has been suggested in literature, [32] [36] however, significant work has been dedicated to the study of both Al and In doped ZnO, where experimental results regarding the most effective remain the subject of academic discussion.

It is possible for dopant defects to form in other electronically active positions such as in interstitial positions or on the oxygen site, however, the formation energy of these positions is much higher. [29] This is demonstrated for AZO in Figure 1. 20.

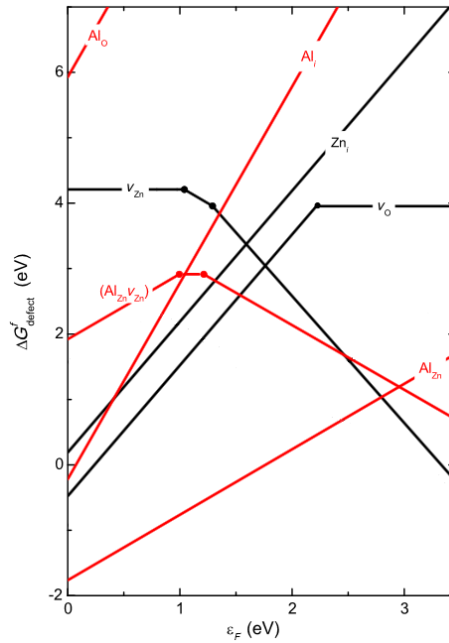


Figure 1. 20 – The formation energies of aluminium extrinsic defects with increasing Fermi energy across the band gap. This was calculated in oxygen rich conditions at 0 K. Adapted from reference [29].

Figure 1. 20 displays the high formation energies of Al_i and Al_o particularly in n-type conditions. It also shows a low formation energy defect complex: $(Al_{Zn}V_{Zn})$. In oxygen rich conditions $(Al_{Zn}V_{Zn}')$ is shown to have a lower formation energy than Al_{Zn}^{\bullet} providing a compensation mechanism n-type conductivity. As with the hydrogen-zinc vacancy complex, this is less prevalent in zinc rich conditions.

As well as group three metals, ZnO has also been doped with Si, Y, Sc, F, V, Ge, Ti, Zr and Hf with varying degrees of success. [37]–[45]

For all dopants, the aim is to incorporate the new ion into the ZnO lattice. There are competing mechanisms with this process which included the segregation of the dopant into secondary phases, or the production of new dopant-zinc-oxygen complexes. In group three doped ZnO, the formation of insulating M_2O_3 secondary phases is often cited as a reason for diminished conductivity. [34] The chance of the lattice incorporating the dopant into the system is often dependent on the ionic/covalent radii of the material closely matching that of either zinc or oxygen. If the size difference is too great, the strain from a dopant ion occupying a lattice site will dramatically increase its formation energy and reduce its chance of successful doping.

The addition of dopants can increase the carrier concentration of ZnO as high as $1.5 \times 10^{21} \text{cm}^{-3}$; this is usually achieved substituting Zn^{2+} with M^{3+} ions to add free charge carriers to the system. [46] For such high carrier concentrations the electronic states introduced from defects can form an impurity band. When this overlaps the conduction band, the material is referred to as a degenerate semiconductor. Degenerate semiconductors can have conductivities matching those of metals. Most TCOs are degenerate semiconductors. This conductivity however, is also reliant on charge mobility as seen in Equation 1.10.

Mechanisms which limit the charge mobility and their likely prevalence in ZnO are described in the next section.

1.4.3 Electron scattering mechanisms

This section describes how the conductivity is limited by the scattering of charge carriers. Much of the theory is based upon that detailed in reference [20] and [47]. The conductivity of a material is given by Equation 1. 10 and repeated here for convenience:

$$\sigma = nq \times \mu.$$

Equation 1. 10

The previous section detailed the 'nq' component relating to the charge carriers. The second component 'μ' is the carrier charge mobility briefly described in section 1.3.1 as the superposition of Bloch waves. If different types of charge carriers contribute to the electrical conductivity, they may have different mobilities. This is taken into account in Equation 1.11:

$$\sigma = (qn\mu_n + qp\mu_p),$$

Equation 1. 11

where n and μ_n are the carrier concentration and charge mobility of electrons, and p and μ_p are the carrier concentration and charge mobility of holes. The conductivity of ZnO is dominated by the movement of electrons, thus this report will now focus in detail on factors affecting electron charge mobility.

The electron charge mobility 'μ_n' is calculated by the ratio of drift speed (how quickly the electron can travel through the system) in m/s to applied field V/m and is given in units of m²/Vs. The drift speed is derived from the average effective mass of an electron across the Fermi surface (m_e^*), and how much the speed is limited by scattering mechanisms. This is measured using the term 'τ_m', which is the mean free time between scattering events, given by:

$$\mu_n = \frac{e\tau_m}{m^*} = \frac{e\lambda_m}{m_e c s}.$$

Equation 1. 12

It can also be described by the 'mean free path' for an electron (λ_m). This is the mean free time in a specific electron distribution, where 's_m' is the mean speed of its thermal and zero point motion given by:

$$\lambda_m = s_m \tau_m.$$

Equation 1. 13

How the electron charge mobility behaves as a function of temperature depends on:

- If the electron gas is in a degenerate environment,
- The relationship between the energy and the wave-vector for the lowest conduction band,
- Which process dominates scattering. These processes are likely to include scattering by:
 - Lattice scattering vibrations,
 - Neutral and ionised defects,
 - Dislocations and grain boundaries.

When two or more scattering processes have comparable rates, it would most accurate to calculate the total charge mobility by determining the quality as function of electron energy, then performing averaging operations with respect to electron speed as described in Equation 1. 14. In practice however, reasonable precision can be obtained if the mean free path of each scattering process is calculated independently and then averaged, as described in Equation 1. 15:

$$\tau = \left[\left(\frac{1}{\tau_{ma}} \right) + \left(\frac{1}{\tau_{mb}} \right) + \left(\frac{1}{\tau_{mc}} \right) + \dots \right]^{-1}$$

Equation 1. 14

$$\lambda = \left[\left(\frac{1}{\lambda_{ma}} \right) + \left(\frac{1}{\lambda_{mb}} \right) + \left(\frac{1}{\lambda_{mc}} \right) + \dots \right]^{-1} .$$

Equation 1. 15

This second, less precise, procedure allows the total electron charge mobility to be calculated from the contributions from the relevant scattering mechanisms with all other neglected described by Equation 1. 16:

$$\mu_n = \left[\left(\frac{1}{\mu_a} \right) + \left(\frac{1}{\mu_b} \right) + \left(\frac{1}{\mu_c} \right) + \dots \right]^{-1} .$$

Equation 1. 16

This is known as Matthiessen's rule. The origin of each scattering mechanism will be explained below.

In Hall measurements, which are used to determine the charge mobility of ZnO films in this report, both magnetic and electric fields are used. This means the Hall charge mobility ' μ_{hall} ' differs from the drift charge mobility ' μ_d ' slightly, this can be expressed in terms of relaxation time (τ_{hall}) in a weak field by:

$$\mu_{hall} = \frac{\langle \tau_{hall}^2 \rangle}{\langle \tau_{hall} \rangle^2} \mu_d = r_h \mu_d ,$$

Equation 1. 17

where the ' r_h ' is the Hall scattering factor, usually simplified to just Hall factor. For non-degenerate semiconductors this difference can be significant, as calculated using Equation 1.18:

$$\langle \tau^2 \rangle = \frac{\int_0^\infty x^2 e^{-x} dx}{\int_0^\infty x e^{-x} dx} ,$$

Equation 1. 18

where ' x ' is a dimensionless variable equal to ' $E/(k_B T)$ '. In high fields and for degenerate semiconductors however, the Hall factor approaches unity. This is true for ZnO so the drift charge mobility and Hall charge mobility can be considered to be equal.

1.4.3.1 Lattice Scattering

In a largely defect free semiconducting crystal where the bonding is primarily of the covalent type, the dominant scattering mechanism is by acoustic phonons. Acoustic phonons from lattice vibrations produce a series of local compressions and extensions to the lattice, these create local modulations in the positions of the conduction and valance bands (ϵ_c and ϵ_v respectively). The extent to which the CBM may change is given by the deformation potential constant:

$$\epsilon_1 = -V \left(\frac{\delta \epsilon_c}{\delta V} \right)$$

Equation 1. 19

When ' ϵ_1 ' is non-zero, phonons with the appropriate wave vector will create peaks and troughs in the conduction band. These can result in the scattering of an electron.

A model for calculating the acoustic scattering influence with respect to temperature was proposed in reference [48] as:

$$\mu_H^{ac} = r_H \frac{\hbar^4 c_1 q \sqrt{8\pi}}{3\epsilon_1^2} (m^*)^{-5} (k_B T)^{-3},$$

Equation 1. 20

where c_1 is the elasticity constant (for ZnO this is ~ 200 GPa [49]) and k_B is the Boltzmann's constant, a Hall factor of 1.18 is often used for this scattering mechanism. [13]

In a lattice with an ionic component to bonding optical photon scattering can add to acoustic scattering. In this circumstance, the displacement of atoms (in phase) induces a dipole electric moment which, in turn, induces an electronic field. This field can strongly scatter electrons; this scattering effect increases as a material becomes more polar. A model for calculating optical scattering with respect to temperature given in reference [50] as:

$$\mu_H^{opt} = r_H \phi \frac{q}{2\zeta\omega_0 m^*} \times e^{\left(\left(\frac{\hbar\omega_0}{k_B T}\right) - 1\right)},$$

Equation 1. 21

where ' ζ ' is a dimensionless constant for electron phonon coupling (for ZnO this is ≈ 1 [51]), ' $\hbar\omega_0$ ' is the energy of the optical phonon. The temperature dependant Hall factor ($r_H \phi$) is roughly equal to unity.

Together the two components can be grouped as lattice scattering effects. The charge mobility for this type of scattering in ZnO can be expressed in terms of the deformation potential by:

$$\mu_L = \frac{e\pi^2 \hbar^4 c_1}{(2m_e^*)^2 \Delta_c^2 N_L} \times \frac{\epsilon^{-\frac{1}{2}}}{k_B T},$$

Equation 1. 22

where ' Δ ' is the divergence of strain and ' N_L ' is the number of atoms in the lattice. In a degenerate system (for ZnO this applies roughly when $n < 3.8 \times 10^{18} \text{ cm}^{-3}$ [52]) the value ϵ becomes a constant so that the charge mobility can be greatly simplified to:

$$\mu_L \approx \frac{1}{T}.$$

Equation 1. 23

The scattering from phonons increases as elevated temperatures cause more vibrations, thus the charge mobility is reduced. In the low temperature range this type of scattering is low however, as temperature increases, the lattice scattering component becomes more significant.

1.4.3.2 Grain Boundary Scattering

Polycrystalline films are made up of many individual crystalline regimes known as grains. The meeting point between neighbouring grains is less stoichiometric than the bulk and lattice defect induced charge trapping states are prevalent. These states compensate some of the charge carriers from intrinsic and extrinsic dopants and in doing so create a potential barrier across the depletion region. This impedes carrier charge mobility between grains as shown in Figure 1. 21. The influence of grain boundary scattering becomes important when the width of the depletion layer becomes comparable with the grain size of the crystallites.

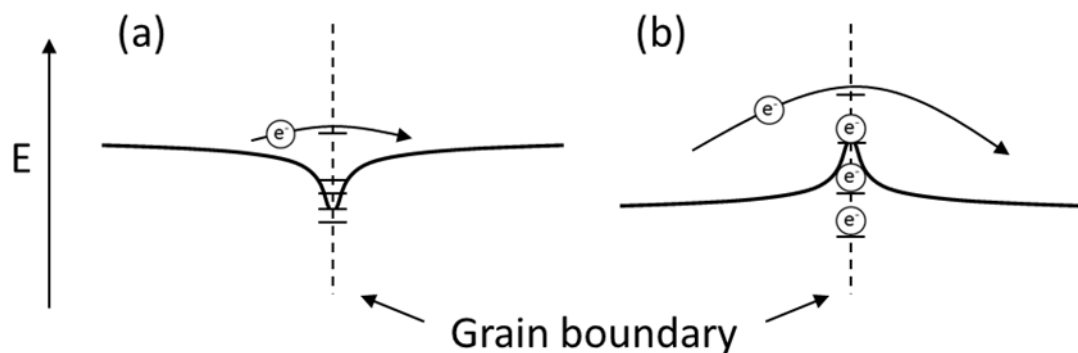


Figure 1. 21 - (a) charge trapping at a grain boundary; many low energy defect states mean charges can become trapped in a potential well. Mobile charges must have enough energy to avoid these for current to flow. (b) negatively charged potential barriers are formed from trapped carriers; the mobile charge must have enough energy to overcome the potential barrier for current to flow

In ZnO, grain boundaries often contain an amount of oxygen chemisorbed to the crystallites. These can capture electrons from the conduction band to make the grain boundary negatively charged. [53] The potential barriers thus strongly scatter the electrons in the conduction band.

The grain boundary charge mobility term (μ_g) for a non-degenerate system can be modelled by:

$$\mu_g = \sqrt{\frac{l^2 e^2}{2\pi m^* kT}} \times e^{\left(\frac{-V_B}{kT}\right)},$$

Equation 1. 24

where 'l' is the grain size and 'V_B' is the grain boundary potential (barrier height). V_B is found by:

$$V_B = \frac{e^2 N_D w^2}{2\epsilon\epsilon_0},$$

Equation 1. 25

where 'N_D' is the donor density and 'w' is the depletion width. In a degenerate system Fermi-Dirac statistics should be applied so that:

$$\mu_g = BT \times e^{\left(\frac{-V_A}{kT}\right)},$$

Equation 1. 26

where 'B' is a constant. 'V_A' is an activation energy related to V_B by:

$$V_A = V_B - (E_F - E_c),$$

Equation 1. 27

where 'E_F - E_c' is the gap between the Fermi energy and the conduction band in the neutral region. In degenerate TCO systems a Burstein Moss shift (see section 1.5.1) means that V_A is smaller than V_B. Thus, it follows that μ_g should be higher in degenerate films.

In TCO films with large crystallites sizes and high carrier concentration, the mean free path of an electron becomes a few nm. This is much smaller than the grain size and means that grain boundary scattering is unlikely to be a dominant scattering mechanism. [47] As the carrier concentration drops, however, grain boundary scattering becomes more important.

1.4.3.3 Ionised Impurity Scattering

In a more defective semiconductor, ionised impurity scattering has a large contribution to the electron charge mobility. When point and external dopants are charged, the ionic field they produce act as a scattering centres.

Mathematically this type of scattering is near identical to Rutherford scattering of an alpha-particle by an atomic nuclei, it must however be scaled by the dielectric constant of the medium.

A schematic of ionised impurity scattering is shown in Figure 1. 22.

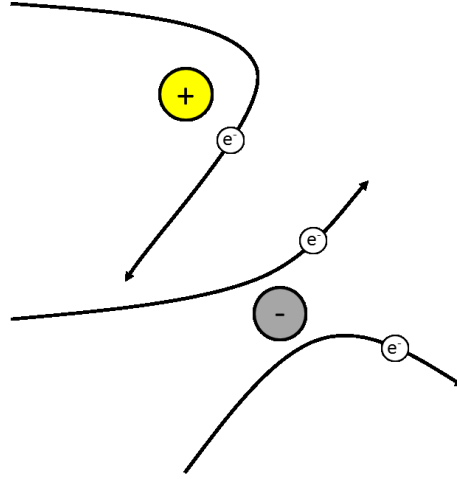


Figure 1. 22 - Electrons scattered by positive and negative ionised impurity centres. The maximum scattering angle from this type of scattering is 180 °.

The temperature dependent ionised impurity scattering component μ_{Tii} can be calculated using the formula described in reference [52] for non-degenerate conditions:

$$\mu_{Tii} = \frac{128\sqrt{2\pi}(\epsilon\epsilon_0)^2(k_B T)^{\frac{3}{2}}}{\sqrt{m^*}Z^2q^3N_i} \times \frac{1}{F_{ii}(\xi)}$$

Equation 1. 28

where ' ϵ ' is the dielectric constant, ' ϵ_0 ' is the vacuum permittivity, ' Z ' is the defect charge state, ' N_i ' is the number of ionised scattering centres and $F_{ii}(\xi)$ is given by:

$$F_{ii}(\xi) = \ln(1 + \xi) - \frac{\xi}{1+\xi}$$

Equation 1. 29

where ' ξ ' is also temperature dependent given by:

$$\xi = \frac{96\pi^2\epsilon\epsilon_0m^*}{N_i} \times \left(\frac{kT}{\hbar q}\right)^2$$

Equation 1. 30

In a degenerate system only the electrons near to the Fermi energy take part in conduction, thus charge mobility is temperature independent. The charge mobility can then be given by: [47]

$$\mu_{ii} = \sqrt{\frac{2}{m^*}} \times \frac{\sqrt{\epsilon} E_F^{\frac{3}{2}}}{\pi e^3 N_i Z^2} \times \frac{1}{\ln\left(1 + \frac{\epsilon E_F}{\sqrt[3]{N_i Z e^2}}\right)^2},$$

Equation 1. 31

where 'Ze' is the ion charge.

Ionised impurity scattering becomes influential as defects become more prevalent. It is the dominant mechanism when grain boundary and lattice scattering are low. This is often the case in TCOs at low temperatures.

At room temperature ionised impurity scattering appears to dominate even under the theoretical charge carrier concentration required. Degeneracy and non-parabolicity of the conduction band have been cited as possible reasons for this deviation from the predicted result. [1]

1.5 Optical Properties of ZnO

As well as being able to conduct electrical charge, TCOs are required to have high optical transmittance of visible light (400 – 800 nm). The optical properties are intrinsically linked with electronic band structure of a material. Figure 1. 23 shows a typical UV-Vis spectrum of an AZO film displaying the transmittance and absorbance over optically significant wavelengths.

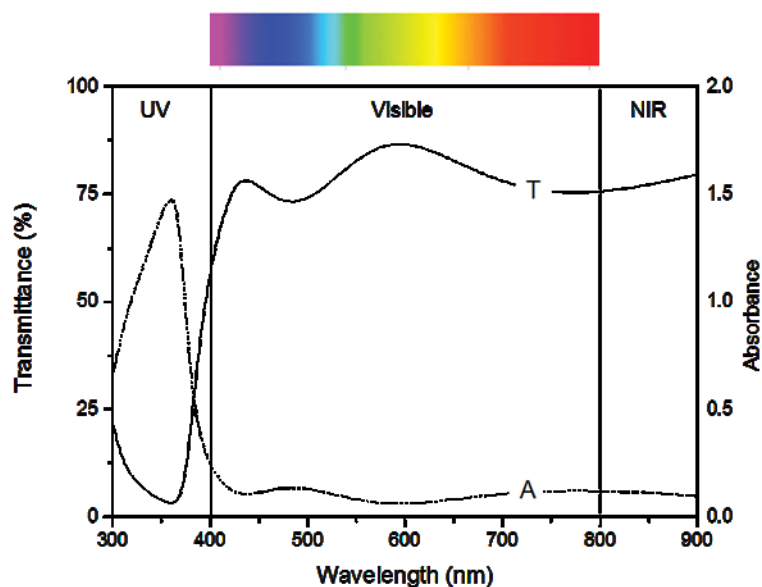


Figure 1. 23 – The transmittance (T) and absorbance (A) spectrum of a typical Al doped ZnO film on a glass substrate. Wavelengths associated with Ultra-violet, visible and near infra-red are marked. Film shown has a thickness of ~ 300 nm and charge carrier concentration of $\sim 1 \times 10^{19} \text{ cm}^{-3}$

1.5.1 Interactions between light and matter

When electromagnetic radiation interacts with a material it can, on a simple level, be reflected, propagated or transmitted. As light is incident on the surface of a material it induces small oscillations of polarisation in atoms (or electrons for metals); these in turn produce small secondary waves in all directions. The accumulation of the backward proportion of these waves is known as specular reflection and the forward parts are known as refraction. Refraction does not affect the intensity of light as it propagates through the material. Reflection and refraction can occur at both the front and back surface of a material. The oscillation patterns seen in Figure 1. 23 are caused by the interference of incoming light with light reflection from the interface between the film and substrate.

If the frequency of the propagated light resonates with electronic transitions in the material, then it can be absorbed. In simple models of absorption an assumption can be made that only one electron is promoted to a higher energy level and all others are unaffected. A probable transition is that from the highest occupied molecular orbital to the lowest available unfilled orbital. Many other transitions can also be observed, however, not all transitions are symmetry allowed. Symmetry forbidden transitions are possible but these usually require the assistance of symmetry altering phonon, and as such, have a lower quantum yield. The excited state is short lived (10^{-15} s) and during this time the atoms do not move.

In an undoped single crystal this wavelength (λ) corresponds to E_g by:

$$\lambda = \frac{hc}{E_g}$$

Equation 1. 32

The dominant absorption in ZnO usually occurs at ~ 365 nm, although this varies with deposition conditions. The absorbance maxima in Figure 1. 23 is found at 360 nm which would equate to a band gap of 3.44 eV. This is a large band gap for a semiconductor meaning that ZnO absorbs in the UV region and transmits light in the visible region. This explains why its optical properties are conducive for application in TCOs.

Upon doping the optical band gap of a semiconductor can be altered. As the free carriers fill states within the band gap and conduction band the Fermi level rises. This means phonons require a greater energy to excite electrons from the valance band into unoccupied states found above the Fermi level. This enlargement of the optically measured band gap is known as a Burstein-Moss shift which was discovered independently by Burstein and Moss in 1954. [54], [55]

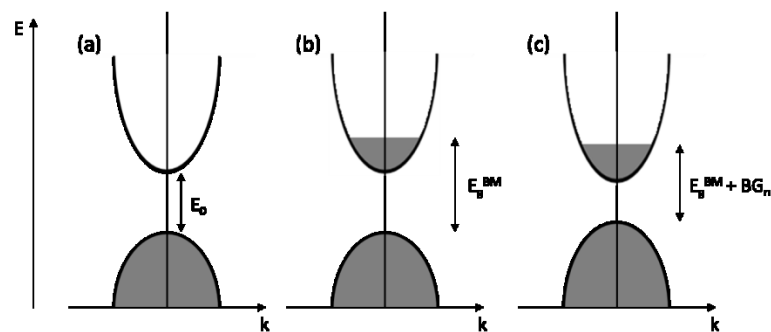


Figure 1. 24 – (a) shows simplified band structure of an undoped semiconductor. (b) shows the band gap enlargement from a Burstein-Moss shift. (c) shows band gap narrowing (BG_n) from electron-electron and ionised impurity scattering.

The increase in the measured band gap from a Burstein-Moss shift can be calculated using Equation 1. 33: [56]

$$\Delta E_g^{BM} = \frac{\hbar^2}{2m_{p+n}^*} (3\pi^2 n)^{\frac{2}{3}},$$

Equation 1. 33

where 'm_{p+n}^{*}' is the combined effective masses of holes and electrons.

In many doped TCOs this effect is partially compensated by a downwards shift in conduction band and upwards shift in the valence band caused by electron-electron and ionised impurity scattering brought about by the increase in charge carriers and charged defect states induced by impurity doping.

An excited electron can lose its energy as heat or, sometimes as light. The spontaneous emission of light following absorption is known as luminescence. This does not always relate to the energy of absorbed light as the de-excitement of electrons can follow different mechanisms.

There are two important luminescent mechanisms associated with ZnO. One is at short wavelengths near the absorbance edge, this has a short decay time (~0.7 ns) and has an excitonic nature. The second is present at longer wavelengths (in the green spectral range) and has a broad nature. [57] There is much scientific debate regarding the cause of the green luminescence with studies linking the luminescence with intrinsic defect states including: zinc vacancies, [23], [58] oxygen vacancies, [59] zinc interstitials, [60] and even oxygen antisites. [61]

This work will not focus on the luminescence of ZnO experimentally however, it is worth noting that the photoluminescence technique can be used to attempt to divulge the nature of point defects in ZnO.

Another propagation phenomenon occurs if the light directly collides with an atom, resulting in scattering. The total number of photons remains unchanged but the direction is changed. Scattering can be elastic if no energy is lost in this collision or inelastic if the scattered light loses a proportion of its energy to an atom in the collision.

The scattering properties of ZnO nanoparticles are often used in solar cell stacks as a method of harvesting incident solar radiation.[62]

The propagation of light through a transparent medium is described by the refractive index (n_r). This is defined as the ratio of the velocity of light in free space to that in the material (c_m) by:

$$n_r = \frac{c}{c_m} .$$

Equation 1. 34

The absorption proportion is quantified by the absorption coefficient (α). This is the fraction of the power absorbed by the unit length of the material. If the light is propagating in the 'z' direction and the intensity (power per unit area) at a position 'y' is 'I(y)' then the decrease in intensity is dependent on increasing thickness (δz) given by:

$$\delta I = -\alpha \delta(z) \times I(y) .$$

Equation 1. 35

This can be integrated to give Beer's law:

$$I(y) = I_0 e^{-\alpha z} ,$$

Equation 1. 36

where 'I₀' is the absorbance of a material at thickness equal to zero. Section 2.4.1 will discuss how these properties can be used to calculate the thickness from a UV-Vis transmittance spectrum.

Finally, light can also pass through a material unchanged; this is known as transmission. High transmission of light is important for a TCO, with values of over 80 % required for functioning TCOs.

1.6 Deposition Techniques

The defect and structural features in ZnO, and thus the film properties, are highly dependent on the method of deposition and specific parameters of that method. For TCO applications, the deposition route must produce films of appropriate conductivity and transparency however, there are some commercial consideration to take into account for a technique to be industrially viable. The method should be:

- Scalable – meaning that it must be compatible with roll to roll processing or other large area deposition practices;
- Low cost – reducing the materials costs is only better value if the manufacturing costs do not rise to match it;
- Adaptable - to allow facile inclusion of different dopants;
- Safe – limiting the use of toxic precursors and high pressure environments.

Deposition methods generally fall in to two categories: vacuum based techniques where films are grown from components in the vapour phase; and solution based methods in which films are deposited from solution, usually involving a chemical reaction at (or near) the substrate. The next section will give an overview of common deposition methods.

1.6.1 Vacuum based methods

Vacuum based methods usually provide excellent control over deposition conditions, producing highly crystalline thin films. The films are usually smooth and homogeneous but can often be greatly defective. The use of a vacuum chamber to deposit films has an inherent cost and often the precursors and targets increases this further. This makes vacuum techniques relatively expensive. The deposition rate can also be slow compared with solution processing routes. Common vacuum techniques are detailed below.

1.6.1.1 Chemical Vapour Deposition

Chemical vapour deposition (CVD) is perhaps the most widely used vapour deposition route in industry. In this method, a precursor gas (for ZnO this is often diethylzinc) is directed toward a heated substrate using an inert carrier gas. At the substrate this gas reacts with an oxygen containing gas to form a solid which is deposited as a film.

Dopants can be incorporated into the bulk film by the addition of the appropriate partial pressure of a dopant gas reagent. Doped ZnO films deposited by CVD typically have resistivities in the range of $1 \times 10^{-3} \Omega \cdot \text{cm}$. [63] High quality ZnO films can be grown at a rate of 0.5-4 nm/s, [64] this is relatively fast and is one of the reasons it is an attractive industrial technique.

One drawback is the requirement for volatile precursors. The incompatibility of precursors limits some attractive synthetic routes. Another drawback, caused by the fast growth, is that films grown by CVD are often found to be fairly rough (root mean squared (R_{RMS}) \sim 70-80 nm [65]). This limits its application as some devices require smooth interfaces between films. In applications such as TCOs as top contacts in PV devices however, the increased roughness can lead to increased scattering. This facilitates light trapping in the device leading to increased absorption by the active layer.[66]

Films grown by CVD tend to have small randomly orientated crystallites at low thicknesses. This can limit conductivity, particularly when electron transport is grain boundary limited. For ZnO, CVD is more appropriate for applications when transport is required to be parallel to the substrate. When high mobilities are required through the layer then the benefits from the common high c-axis preferential orientation are lost.

1.6.1.1.1 Aerosol assisted chemical vapour deposition (AA CVD)

One method of gaining access to non-volatile precursor materials is to use Aerosol assisted chemical vapour deposition (AA CVD). In this technique precursors need not be volatile at the set temperature, merely soluble in an appropriate solvent. Once dissolved, the solution is vaporised and carried to a surface by an inert carrier gas. Further advantages are a lower processing cost, higher deposition rate and better control of stoichiometry. [67] This method falls between solution processing and physical deposition techniques in terms of attributes. When carried outside of a vacuum chamber, is analogous to the spray pyrolysis technique discussed in section 1.6.2.3.

1.6.1.2 Atomic Layer deposition

Atomic layer deposition (ALD) is another vapour phase deposition technique. It differs from CVD in that growth is limited to one monomolecular layer at a time. This is achieved by cycling alternative precursor vapours. Precursor 1 can only grow upon certain surfaces and cannot proceed past one layer due to the specific nature of surface that it creates. Precursor 2 in turn can only grow upon the surface created by precursor 1 and not on top of the surface that it creates or upon the bare substrate. As such, the film is built up layer by layer flushing the reaction chamber with inert gas between each reagent. For the growth of ZnO, diethyl zinc and water vapour are usually used as the two gaseous precursors. [68] Doping can be achieved, as in CVD, by the addition of dopant precursor gases (Al doping is often achieved using trimethyl aluminium).

This technique allows for careful control of the film thickness, gives excellent conformality, and ultra-smooth films. Doped ZnO films have been deposited with resistivities of $7 \times 10^{-4} \Omega \cdot \text{cm}$ [69] It also has the advantage of low temperature processing with conditions usually between 100-200 °C. There are reports of room temperature deposition although this does reduce the conductivity.[70] This means that it is possible to grow high quality oxide films on top of organic layers, highly advantageous for hybrid devices.

However, this careful growth comes at the cost of deposition speed. ALD typically has a growth rate of 0.03-0.1 nm/s (100-300 nm/h) which is significantly slower than other techniques.

1.6.1.3 Magnetron Sputtering

Sputtering is the process of ejecting particles from a target of the chosen material by means of bombardment by high energy particles. In vacuum conditions positive ions from an inert gas are attracted to the surface of a target connected as a cathode. The chamber surface plays the role of the anode. For deposition of ZnO films, a metallic zinc target would be used.

If the bombardment is energetic enough, a Zn ion would be ejected and directed towards a substrate. This is then oxidised to deposit as a thin film on the substrate. Dopants are added either by the addition of the dopant to the target composition or by the injection of dopant gas into the chamber.

The simple sputtering technique has a limited growth rate and poor process repeatability. It is usually adapted for academic and industrial use by magnetic confinement of the bombarding ions (plasma) in front of the target. This adjustment increases the deposition rate to 1-2 nm/s and improves the quality and reproducibility of the process. This is known as magnetron sputtering.

The low oxygen levels in the chamber lead to highly defective films with low resistivities - undoped Zn films typically in the range of $3 \times 10^{-3} \Omega \cdot \text{cm}$ and doped ZnO in the range of $2 \times 10^{-4} \Omega \cdot \text{cm}$ [71]. This has drawbacks when using magnetron sputtering to deposit semiconducting films, which require a post deposition anneal. However, this is an ideal vacuum technique for TCO applications and, as such, is regularly used in industry for this purpose.

1.6.1.4 Pulsed Laser Deposition

Pulsed laser deposition (PLD) again uses a target of the desired material. In this technique a high powered laser is used to evaporate material (metallic zinc for ZnO films) from the target. The material is also melted, excited and ionised in the process. This forms an energetic and directional plume which interacts with the gases introduced to the chamber and condenses on a substrate. PLD typically has a growth rate of 0.16 nm/s.

The oxygen partial pressure in the chamber is used to control the properties when depositing thin films of ZnO. This is a low temperature technique with the possibility of deposition at room temperature. Like ALD, PLD allows for growth upon organic films. [72] As with magnetron sputtering dopants are introduced by addition to the target or by inclusion of dopant reactive gases in the chamber.

PLD has been used to grow films with resistivities in the range of $1 \times 10^{-4} \Omega \cdot \text{cm}$ [6], [73] however, the slower growth rate and high associated costs mean that magnetron sputtering is preferred for industrial application. The ability to carefully control deposition conditions means that PLD is an excellent tool for academic study of a deposition process.

1.6.2 Solution Based Methods

When solution processing, it is usually more difficult to control the deposition conditions and the films deposited are typically less crystalline, more rough and less homogeneous. There are many advantages to solution processing: the deposition rate are considerably faster; processing films in non-vacuum conditions dramatically reduces the cost; and the precursors used are typically lower cost, more stable and less hazardous. It is also typically easier to include dopant ions and vary their concentration within the films.

A common tool in solution processing is the creation of a sol-gel. In this method precursor particles are suspended in a solution prior to processing. This solution is the sol-gel which is processed into a homogeneous layer before thermal annealing to a dense solid phase. ZnO is usually processed from a zinc acetate precursor salt. The formation of the sol-gel involves the hydrolysing and subsequent condensation of the precursor to form $(\text{Zn-O-Zn})_n$ networks before the final decomposition into ZnO. The creation of the sol-gel mitigates the restricting decomposition temperature of zinc acetate (237 °C) and increases compatibility with organic bottom layers. Doping is achieved by simply adding the appropriate concentration of dopant salt into the precursor solution. Aluminium chloride is typically used to produce AZO films.

1.6.2.1 Spin Coating and Dip coating

Spin coating is perhaps the most widely used solution processing method. Here a sol-gel is pipetted liberally in the centre of an appropriate substrate. The substrate is then rotated at high speed (typically 2000-5000 rpm) using centrifugal forces to spread the solution across the substrate at a uniform thickness. The substrate is then transferred to a hotplate where the solvent is evaporated and the remaining salt undergoes thermal decomposition into the desired film. Film thickness is increased by multiple iterations of this process.

Sol-gel spin coating has limited scalability as it is not easily compatible with roll to roll processing. However, it provides a facile route to quickly test processing conditions and study the physical properties of sol-gel derived films. For TCO applications spin coated doped ZnO films typically show resistivities in the range of 1-50 $\Omega\cdot\text{cm}$ after an initial anneal in air although, this can be reduced to the order of $1 \times 10^{-2} \Omega\cdot\text{cm}$ by annealing in oxygen-poor conditions to induce defect states.[74]

The dip coating method involves simply dipping the substrate into the sol-gel before thermal annealing as in the spin coating method. This is more scalable than the spin coating method and simpler to carry out. However, homogeneous films are more difficult to achieve. Similar resistivities are found for dip coating doped ZnO as for spin coating with a minimum resistivity in the order of $2 \times 10^{-2} \Omega \cdot \text{cm}$. [75]

1.6.2.2 Electrochemical Deposition

Electrochemical deposition is a low temperature, scalable technique viable for large area thin film growth. It finds much industrial use in areas such as corrosion resistant coatings. In this technique metal precursors are dissolved in solution and a potential is applied using a conducting substrate cathode. The current is generated via the reduction of precursors which produce OH^- ions in the vicinity of the substrate. The associated pH change causes the precipitation of the desired material on the substrate.

This technique was first carried out to deposit ZnO in 1996 [76] using zinc chloride salts. Further work shows careful controlling of thickness, grain size and growth rate as well at the production of nanostructures.[77] It is found to produce highly crystalline films without the need for post deposition annealing; this is an advantage over many solution processing techniques

The major drawback is that the substrate is required to be conducting; this puts large limitations on the number of applications in which electrochemical deposition may be used and excludes all those associated with TCOs. Furthermore, the conducting substrate means that the electrical properties of the deposited material are difficult to measure.

1.6.2.3 Spray Pyrolysis

Spray pyrolysis (SP) is a scalable technique, compatible with roll to roll processing and also with complex substrate geometries. It can produce crystalline, continuous films at low thicknesses (<20 nm) all of which give it an advantage over other popular solution processing methods such as spin coating and dip coating. [17]

Deposition is achieved using a solution of a precursor salt, dissolved in a suitable solvent. This is atomised by means of passing it through a nozzle, carried by an inert gas. The resulting aerosol is directed towards a heated substrate where it thermally decomposes to give a thin film of the desired material. It was first devised in 1966 for the deposition of cadmium sulphide films used in solar cell applications. [78] Since then, it has been used for the deposition of many oxide films including for ZnO [79], SnO₂ [80], In₂O₃ [81], (ITO) [82] as well as many others.

Doped ZnO films have been prepared by SP films with resistivities in the range of $1.4 \times 10^{-3} \Omega \cdot \text{cm}$ [83] although films of this low resistivity are usually subjected to post deposition annealing treatments.

There are three main drawbacks when using SP for the deposition of ZnO for TCO applications. Firstly ZnO is very sensitive to changes in the deposition conditions. In SP there are a large number of parameters to control therefore the process requires a lot of optimisation in order to achieve the most desirable films. This can also be seen as an advantage as it means the film's properties are highly tuneable. Secondly, it is a moderately high temperature route (often > 300 °C); this is limited by the decomposition temperature of the precursors and the necessity for rapid evaporation of the solvent. This usually restricts the growth on organic substrates. Thirdly, the resistivity of ZnO is highly dependent upon intrinsic defects and lower conductivities are seen in as-deposited films. As such, post deposition annealing is often required to produce films with conductivities comparable to vacuum based methods.

Whilst the precise setup of spray systems in the literature varies from one paper to the next they all share key components. A schematic of a generic spray system is shown in Figure 1. 25.

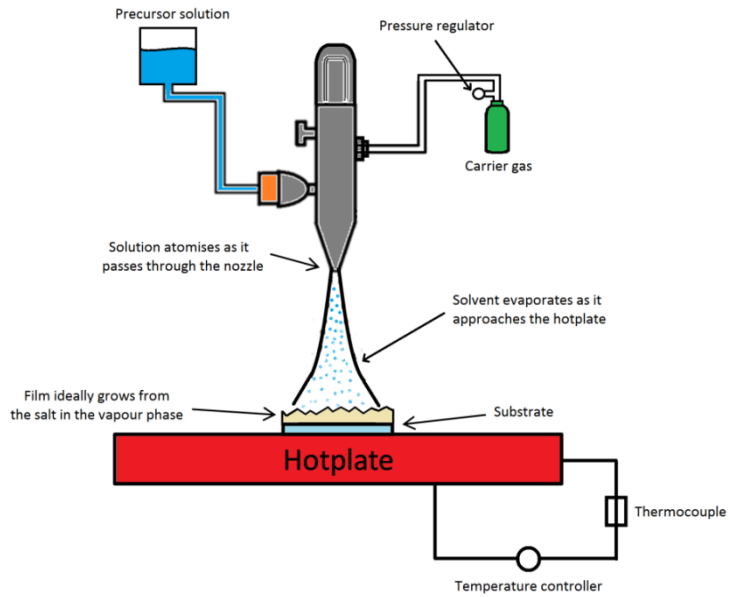


Figure 1. 25 – A schematic of a spray deposition system with key components labelled.

1.6.2.4 Plume dynamics

The properties of the film are highly dependent on the state of the solvent mist (plume) as it arrives at the substrate. There are four possible pathways for the droplets to take in the spray system after they are expelled from the nozzle, displayed in Figure 1. 26. [84], [85]

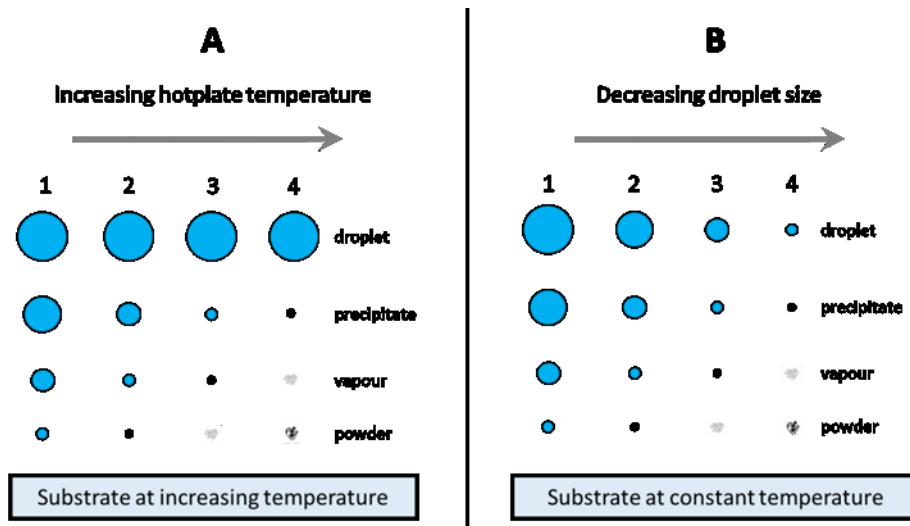


Figure 1. 26 – the size and temperature dependency on the nature of the droplets as they reach the substrate. A shows a constant droplet size with increasing temperature of the substrate (all temperatures are high enough to evaporate the solvent and vaporise the precipitate). B shows a constant substrate temperature with decreasing droplet size.

In both scenarios (A and B in Figure 1. 26), droplets 1-4 reach the substrate in the same format: droplet, precipitate, vapour and powder respectively. The final droplet state is controlled both by the initial droplet size and by the substrate temperature. Variations in each can push the droplets towards the different states. The deposition pathways to arrive in states 1 to 4 are described below.

1.6.2.4.1 Deposition pathway one

The droplet is large enough at the specific temperature that the solvent does not fully evaporate before it reaches the substrate. It impacts on the substrate, entirely vaporises and a dry precipitate is left on the surface. The evaporation process locally reduces the temperature at the substrate which causes adverse effects to the reaction kinetics. The precipitate can decompose on the substrate to form the film however this process has a weak sticking probability which means that the precipitate is more likely to be carried away from the surface by the inert gas. At very low temperatures/very large droplets the vaporisation of the droplet may not be instantaneous leading to a coffee ring effect, a large amount of substrate cooling and very poor quality films.

1.6.2.4.2 Deposition pathway two

The droplet size/substrate temperature conditions lead to the solvent fully evaporating and an amorphous salt precipitate forming just above the substrate. The precipitate impacts on the substrate whereupon decomposition occurs. Some particles vaporise and condense onto gaps the growing film, where a surface reaction occurs. This process has a medium sticking probability

1.6.2.4.3 Deposition pathway three

The processing conditions lead to the solvent evaporating mid-flight and the precipitate vaporising as it approaches the substrate. The vapour undergoes a heterogeneous chemical reaction at the surface. This is comparable to classic CVD. The reactant diffuses to and adsorbs onto the surface. It can then undergo a chemical reaction at the surface incorporating the desired product into the film lattice. Finally, the by-products desorb and diffuse away from the surface. This pathway has high sticking potential and leads to high quality films. This is the desired outcome of the spray procedure.

1.6.2.4.4 Deposition pathway four (P4)

When the temperature is too high or the droplet is too small, a vaporised precipitate state is reached significantly above the surface of the substrate. The thermal decomposition of the salt occurs in the gaseous state with the crystalline product forming as a powder before it reaches the substrate. The powder impacts on the film but is not incorporated into the lattice. The powder can however remain on the surface and act as a barrier to further deposition.

It is important to note that at higher temperature the impact of thermophoresis will increase. This force acts upon particles travelling through a thermal gradient pushing away from the hot surface to the cooler surroundings. The dynamics of this process are complicated and outside the scope of this work, however, simply put: at higher temperatures, small particles are more likely to be carried away from the surface limited 'pathway 3' like deposition.

The plume dynamics and which pathway the droplets are likely to follow are dictated by the deposition conditions. These are investigated in Chapter IV.

1.6.2.5 Conclusions and chosen technique

Reviewing the current deposition pathways to produce ZnO for TCO applications it is clear that vacuum routes, in particular magnetron sputtering, offer excellent optoelectronic properties. However the associated cost means that achieving comparative properties using solution processing methods would be preferable. Spray pyrolysis is an attractive solution processing option for TCO applications. This is particularly true in research, where the high throughput and adaptability of the technique allows for the study of many deposition conditions and a large range of dopants, and many dopant concentrations. It offers greater scalability to sol-gel routes and is easily adaptable to roll-to-roll processing. It is for this reason that spray pyrolysis was chosen as the deposition route to ZnO films in this work. The exact experimental procedures are given in Chapter II.

1.7 Chapter Conclusions

This section provides an overview of important notes to take from the fundamentals section looking forward to using ZnO as a TCO.

1.7.1 Crystalline and Electronic structure

- ZnO is present in ambient conditions in the wurtzite crystal structure.
- ZnO is a semiconductor with a large direct band gap.
- A perfect single crystal would display high transparency but very low conductivity.

1.7.2 Electrical properties

- Conductivity is based upon the number of free charge carriers and the charge mobility of these carriers.
- Defect states can increase the charge carrier density.
- Scattering mechanisms can reduce the carrier charge mobility.

1.7.2.1 Defects

- ZnO has a series of native point defects which may add charge carriers.
- Oxygen vacancies are the lowest formation energy donor defect, however they are deep within the band gap. They are therefore not a likely source of n-type conductivity.
- Zinc interstitials are shallow donors but in n-type conditions their formation energy is too high.
- Zinc antisites are both shallow and deep donors but have exceptionally high formation energies.
- Native defects may not provide the mechanism for n-type conductivity as such, hydrogen defects have been suggested as a possible source.

1.7.2.2 Dopants

- With purely intrinsic defects, the resistivity of ZnO is still too high for TCO applications.
- ZnO can be doped with trivalent ion (Al, Ga, In) to substantially improve its conductivity.

1.7.2.3 Carrier Scattering

- Charge carriers charge mobility is limited by scattering mechanisms.
- Lattice scattering is small at low temperatures but at room temperature it may become significant. This includes both optical and acoustic modes.
- Grain boundary scattering is significant when carrier concentrations are low. In degenerate conditions it is diminished.
- Ionised impurity scattering increases as the defect level increases and is independent of temperature in degenerate films.
- At room temperature, undoped ZnO films are likely to be influenced both by lattice scattering and grain boundary scattering.
- At room temperature, doped ZnO films are likely to be influenced both by lattice scattering and ionised impurity scattering.

1.7.3 Optical Properties

- Light interacts with thin films by reflection, refraction, absorption, emission and scattering.
- TCOs aim to limit interactions so that transmission is high.
- Reflection of light occurs from interfaces, and can be used to measure thickness in ZnO.
- ZnO absorbs strongly in the UV region as electrons are excited across its band gap. The wavelength of maximum absorption can be used to measure the size of the band gap.
- Doping in ZnO can cause band gap enlargement from a Burstein-Moss shift and band gap narrowing from electron scattering mechanisms.
- Luminescence in ZnO occurs in two areas – from excitonic electrons associated with the dominant absorption and a green emission associated with defect states.
- Scattering processes can occur to limit transmittance. This scattering can be useful in solar cell stacks.
- Light which isn't reflected or propagated is transmitted. High transmission of over 80 % is required for ZnO to perform in TCO applications.

1.7.4 Deposition routes

- Vacuum techniques offer high quality films with good optoelectronic properties.
- Magnetron sputtering is the most attractive for TCO films.
- However, vacuum techniques are high cost.
- Solution processing techniques offer a low cost alternative.
- Spray pyrolysis is the most attractive solution processing route to ZnO for TCO application and hence was chosen as the deposition technique used in this thesis.

CHAPTER II – EXPERIMENTAL METHODS

2.1 Introduction

This chapter is divided in to two sections.

The first section will describe the experimental routes to obtain the ZnO films used in this report. It will focus on practical aspects of the chosen technique before detailing the basic synthetic methods used to deposit ZnO in the experimental section of this thesis.

The second section will focus on the characterisation techniques used to analyse the deposited films. This analysis will be split into three parts - analytical techniques which probe the physical and structural properties, those which study the optoelectronic properties and those which probe the composition of the films.

2.2 Synthetic Methods

2.2.1 Spray Pyrolysis of ZnO

The spray conditions were optimised for the preparation of ZnO by varying parameters to achieve the most desirable properties for application as a TCO – these are highlighted in the Introduction section and described in Table 2. 1. This study also highlighted deposition conditions that give physical properties which may be desirable for other applications.

Property	Target value
High optical transparency	Over 80 % between 400-700 nm
Low resistivity	In the region of $10^{-4} \Omega \cdot \text{cm}$
Low material costs and abundance of precursors	Significantly lower than Indium – $\text{In}(\text{NO}_3)_3$ is $\sim \text{£}7/\text{g}$ (Sigma Aldrich)
Ease of processing	Limit harsh chemical condition or expensive deposition environments
Low toxicity	Not carcinogenic/toxic/damaging to fetuses/damaging to wildlife etc.
Long term chemical stability	Lifecycle of > 10 years un-encapsulated

Table 2. 1 – Target properties of TCOs

SP was originally carried out using a commercially available ‘Iwata Eclipse HP-CS’ airbrush. During optimisation, there was a change from handheld spraying to an automated process using a ‘SataJet 20B’ spray gun. The details of this switch and the building of the machine are described in Chapter III.

With the optimised spray rig operational, work was then focused on the doping of ZnO with a number of trivalent ions. Doping with Al^{3+} , Ga^{3+} , In^{3+} , Bi^{3+} , Ce^{3+} and Y^{3+} was attempted from the following metal salts: $\text{AlCl}_3 \cdot 6\text{H}_2\text{O}$, $\text{Ga}(\text{NO}_3)_3 \cdot x\text{H}_2\text{O}$, $\text{In}(\text{NO}_3)_3 \cdot x\text{H}_2\text{O}$, BiCl_3 , $\text{CeCl}_3 \cdot 7\text{H}_2\text{O}$ and $\text{YCl}_3 \cdot 6\text{H}_2\text{O}$.

Studies of post annealing treatments in different atmospheres was investigated, vacuum annealing was performed using a Lenton 5208 tube furnace, and anneals in nitrogen, oxygen and argon were performed using a Carbolite MTF 12/48/250 tube furnace with a constant flow of the appropriate gases.

Both guns (Iwata and SataJet) were operated using a trigger to release a plume of atomised precursor solution. The trigger controlled a needle which, when in the 'off' position, blocks the nozzle so that no solution was released. It also controls the carrier gas inlet. When the trigger was pressed, the needle was removed and the carrier gas released. This forced the solution through the nozzle at elevated pressure, atomising the solution and carrying it towards a substrate. The precursor solution was gravity (Iwata) or suction (SataJet) fed into the gun. The carrier gas was supplied via a cylinder controlled by a regulator. Decomposition of the precursor occurred at the heated substrate, the temperature of which was controlled by the hotplate and measured with an IR heat gun. To help improve the homogeneity of the films the plume is passed multiple times over the substrate so that all areas are evenly covered. These passes were initially performed by manually sweeping the gun, but were later automated as described in Chapter III.

It was found that after periods of prolonged spraying that the substrate temperature decreased. This may be due to evaporation of solvent on the surface. The carrier gas also may have a cooling effect; this phenomenon occurs even at temperatures in which the solvent is expected to have evaporated before it reached substrate. At low temperatures both are likely to play a part. A drop in temperature would affect the conditions for subsequent droplets and is likely to have an adverse effect on film growth. Pauses in the spray process were introduced to allow the substrate to return to the set temperature and limit this effect. A secondary effect of the pause is that the samples received a longer period of heating. This effectively acted as a mid-deposition anneal. The length of pause was set to the time taken for the substrate to return to temperature; this differed depending on the hotplate temperature but was in the range of 20-40 seconds.

The pause in spraying added another parameter to the process – how many passes over the hotplate should be taken before a pause. This is related to the speed of each pass. Together these were optimised with the length of pause to ensure the substrate remained at a stable temperature. An odd number of passes was chosen so that different sides were cooled first on the beginning of the set of passes, this improved the thickness homogeneity of the films. Two sets of passes were therefore required to return the gun to the starting position. Two sets of passes (and associated pauses) will hereon in be referred to as a cycle.

Once the films were deposited they were, when required, annealed in a Carbolite MTF 12/48/250 tube furnace pre-heated to the temperature needed.

2.2.2 Substrate preparation

The thin films were deposited upon three types of substrate the preparation of which is detailed below.

Unless otherwise stated, films were deposited on 1 x 1 cm squares of soda-lime glass. This was either cut to size using a diamond pen from VWR microscope slides or, when the exact shape was important (such as for Hall effect measurements), substrates were bought 'to size' from UQG Optics Ltd.

When films required a post deposition anneal at temperatures above 550 °C (the softening point of soda-lime glass), and when the additives in soda-lime interfered with compositional measurements, quartz (fused silica) glass was used.

For work function measurements where a conductive substrate was needed, glass substrates coated with a patterned layer of indium tin oxide (ITO, PsiOtec Ltd., 12 x 12 x 1 mm, 12 x 8 mm active area, 12 - 16 Ωsq^{-1}) were used.

All substrates were cleaned by ultrasonication in water followed by acetone for 5 minutes each. The final ultrasonic cleaning was carried out in the solvent base of the precursor solution. In most cases this was methanol. They were then blow dried using N_2 gas.

2.3 Physical and Structural Properties

Films deposited in this work were analysed by a number of structural characterisation techniques. Discussed in this section are techniques to measure the crystal structure - X-Ray diffraction (XRD); the topography and microstructure - scanning electron microscopy (SEM), transmission electron microscopy (TEM) and atomic force microscopy (AFM); and the film thickness - profilometry.

2.3.1 Profilometry

The thickness of the deposited films had a significant influence on their structural, optical and electrical properties. It was important to obtain an accurate measurement of the film thickness. It is possible to calculate the thickness using a number of methods. Optical measurements have many benefits as they are usually non-destructive, however, they are also limited by the necessity to know a number of optical constants; possess a chemically pure sample; and it places a restriction on how thin the film can be.

A more reliable, although more demanding, method is to use profilometry. Unless otherwise stated, thickness measurements in this study were performed using this method on a 'Veeco Dektak 150' profilometer. This apparatus uses a diamond tipped stylus with radius 5 μm . This was lowered onto the surface with a force of 3 mg. The tip was drawn in a straight line across the surface of the film tracking any changes in height over a specified distance. To measure the thickness of the films, a step was created from the surface of the film to the substrate below. This was attempted by scoring this film with a blade, however, it was difficult to know if the substrate had been reached. Furthermore, the oxide films were difficult to scratch due to their hardness. The creation of a step was also attempted by etching the film with acid, however, this often did not create a well-defined step, rather resulting in a slope from the substrate to the surface. This method also did not give consistent results.

Eventually, it was found that a step could be created by the addition of titania paste to a substrate prior to deposition. The film was grown on the decorated substrate and, following deposition, the paste was removed using commercially available cotton buds. This created a sharp step to the bare glass below. A picture showing the steps created by the titania paste are shown in Figure 2. 1.

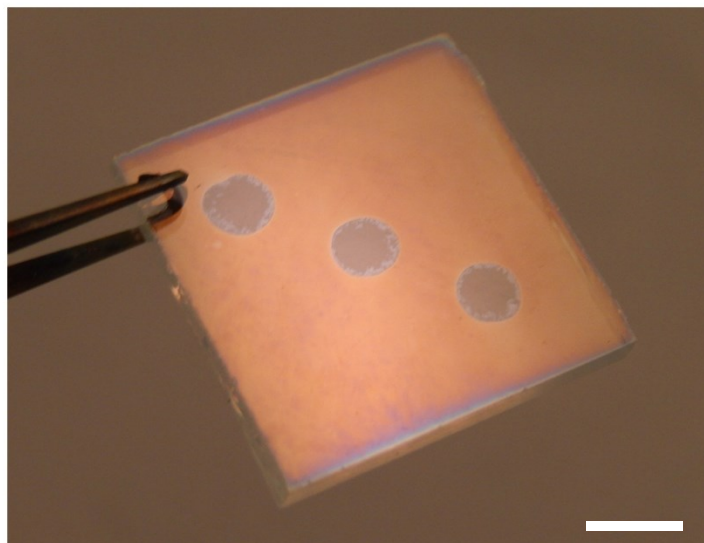


Figure 2. 1 - A photograph of a ZnO film on a glass substrate. Holes in the film were created using titania paste for profilometry measurements. The scale marker indicates 25 mm.

Profilometer measurements in the three positions gave a good idea of both the thickness of the film and the homogeneity of the thickness across the sample. At least two measurements were made at each hole in the film, giving a minimum of 6 readings for each sample. The average of these positions was taken as the thickness for the film. If the sample showed a large amount of in-sample inhomogeneity then it was discarded and a repeat film was deposited.

Substrates with titania derived steps were deposited on in parallel with another bare substrate. The two deposition positions were shown to produce films of equal thickness, thus, a method for measuring the thickness was obtained.

2.3.2 X - Ray Diffraction

XRD provides a non-destructive method of probing a material's crystalline structure and gives access to a large variety of information about a film's structural properties. For this study, polycrystalline thin films were analysed for compositional information; for the number of crystalline phases present; the size and shape of the crystalline lattice; the orientation of the crystals; the size of the crystallites; and the degree of crystallinity.

To perform XRD analysis, a sample is irradiated with monochromated X-rays. These X-rays are elastically scattered by atoms in the material and a diffraction pattern is formed. The intensity and angle of the diffracted beam is measured. The technique is underpinned by Bragg's Law which is given in Equation 2. 1:

$$n\lambda = 2d_{hkl}\sin \theta_{hkl},$$

Equation 2. 1

where 'n' is an integer, 'λ' is the wavelength of the incident radiation, 'd_{hkl}' is the separation between lattice planes. Sine 'θ_{hkl}' is the scattering angle at which the intensity maximum is observed. The 'hkl' noted in Equation 2. 1 are known as the Miller indices, these describe the reciprocal lattice parameters of a crystal structure (Figure 1. 2) and are related by Fourier transform to its Bravais lattice.

The distance between two planes in a Bravais lattice is defined as the 'd spacing', this is in a similar order to the wavelength of an X-ray. This d spacing acts as a grating so that, when a crystalline sample is irradiated with X-rays, the incident radiation can be diffracted. Most of the diffracted signal cancels through destructive interference, however, at some incident angles the interference is constructive leading to maxima in the beam intensity. This is related to the size of the d spacing as shown in Figure 2. 2.

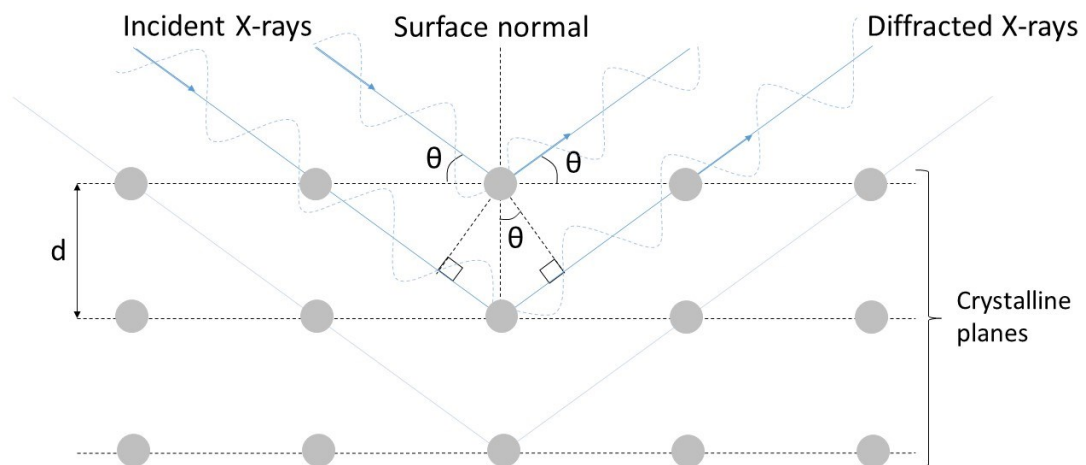


Figure 2. 2 - A diagram showing how X-rays are diffracted constructively. The crystalline planes are separated by a distance known as the d spacing - (d). When X-rays are reflected from lattice points of two planes they will constructively interfere when the path difference is equal to an integer value of the X-ray wavelength

The instrument used to perform XRD analysis is known as a diffractometer. This directs an X-Ray beam at a material from angles between roughly 2-45 ° and collects the diffracted beam intensity at each angle (expressed in terms of 2θ). Each different hkl plane in a crystal structure satisfies Bragg's law at a specific value of θ. Different structures will generate unique diffraction patterns, these are indexed and the diffraction patterns of all common crystalline materials are stored in a database which is constantly built upon with new findings. XRD analysis can thus give information on the composition and structure properties of materials.

In this study, XRD patterns were obtained using two instruments: a Bruker D2 Phaser and a Panalytical X'Pert Pro. Both instruments were equipped with a Cu X-ray source. X-rays are produced by directing an accelerated beam of electrons at the metal. This leads to the ionisation of 1s electrons and the demotion of an outer electron to fill this core hole. Either a 2p - 1s transition (generating K_{α1} (1.5405 Å) and K_{α2} (1.5444 Å) radiation), or a 3p - 1s transition will occur (generating K_β radiation). K_β radiation is subsequently removed using a Ni filter. The Bruker D2 Phaser generated X-rays using a tension of 30 kV and a current of 10 mA. The Panalytical X'Pert Pro generated X-rays using a tension of 40 kV and a current of 40 mA. All samples were acquired using a step-size of 0.033 ° 2θ, the time-per-step was varied depending on function but was usually set 0.5 s. Data was acquired using a step-size of 0.033 ° 2θ. Samples were mounted on a holder levelled using a hand-press, and subsequently spun during the measurement at a speed of 60 rpm.

As well as structural information, Scherrer analysis was used to estimate the crystallite size in thin films. The Scherrer equation, shown in Equation 2. 2, gives an estimate of crystallite size by measuring the diffraction peak broadening. This is found to increase as the grain size decreases. [86]

$$d = \frac{K\lambda}{(\beta_{meas} - \beta_{ins}) \cos \theta}$$

Equation 2. 2

'd' is the crystallite size in angstroms, 'K' is a shape factor (perfectly crystalline films would have a shape factor of unity, where the shape is not known 0.9 is often used), [87] 'λ' represents the X-ray wavelength, 'β_{meas}' is the full width at half the maximum height (FWHM) of a sample peak, 'β_{ins}' is the measured instrumental broadening (0.08 ° 2θ) and 'θ' is the Bragg angle of the peak.

Instrumental broadening of the peak can be taken by measuring the broadening seen in a single crystal. In a perfect system this would tend to zero so the width of a peak derived from a single crystal should be solely due to instrumental broadening.

The Scherrer equation provides only an approximation of crystallite size, this approximation becomes a poor one in the case of three main conditions:

1. If the crystallites are too large (over 100 nm);
2. If there are other factors such as lattice strain which lead to peak broadening as the Scherrer equation does not include this possibility so will under predict crystallite size in highly strained samples;
3. When using 0.9 as a shaping factor it is assuming the crystallite to be spherical, if this is far from the true shape then the approximation will be inaccurate. [88]

Some of the deposited films exhibit a preferential crystallite orientation. Quantitative information concerning the preferential crystallite orientation can be obtained from the texture coefficient 'T_{c(hkl)}' defined as:

$$Tc_{hkl} = \frac{I_{(hkl)} / I_{x(hkl)}}{(1/n_d) \sum I_{(hkl)} / I_{x(hkl)'}}$$

Equation 2. 3

where 'n_d' is the total number of diffraction peaks, 'I_(hkl)' and 'I_{x(hkl)}' are the integrated intensity of a textured film and a randomly orientated film respectively. Values increasingly > 1 indicate an increasingly preferential orientation. [89]

2.3.3 Scanning electron microscopy

Scanning electron microscopy is topographical imaging technique capable of nanometre resolution. This makes it ideal for the study of thin film surface morphology such as homogeneity, coverage, detection of pinholes, roughness and grain size.

In terms of operation SEM is analogous with reflected light microscopy, however, the radiation scattered from the surface is given by a stream of electrons rather than visible light. The wavelength of light is in the order of 300 nm whilst the wavelength of electrons is in the order of 0.05 nm. The smaller wavelength of an electron beam allows for vastly improved magnification so that nanoscale resolution can be achieved. [90] The typical grain size of ZnO was found to be between 10-100 nm, imaging using SEM thus provided excellent resolution for studying surface properties of thin films in this report.

Micrographs in this report were obtained using a field emission gun (FEG); this enhancement produces an electron beam which is more coherent, brighter and with a smaller diameter than a traditional filament. The image produced by a FEG-SEM has less electrostatic distortion and better spatial resolution.

The electron stream is produced in the FEGSEM system and directed toward a sample surface. There are various interactions which occur at the surface, these give different information about the nature of the specimen. An overview of these interactions and the emission they produce and the sample depth at which they occur are shown in Figure 2. 3.

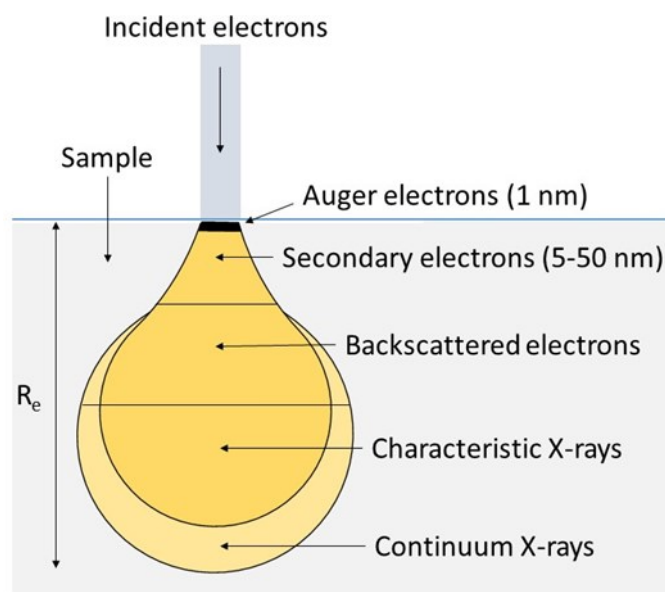


Figure 2. 3 – Spatial resolution and depth of emissions following the irradiation from the electron beam. Irradiation is typically at 5 kV and R_e is the electron penetration depth typically up to 500 nm at 5 keV.

Inelastic collisions occur between the electrons from the sample beam and those from the sample to produce ‘secondary electrons’. In simple terms, the sample absorbs high energy electrons and ionises. The sample emits lower energy ‘secondary’ electrons which can be collected to produce a 3D image of the surface and in doing so loses the excess charge. These electrons can penetrate 5-50 nm meaning that data from these electrons refers to the top 50 nm of the sample. Inner shell ionisations lead to Auger and X-ray emissions which have distinct quanta of energy. X-rays can penetrate further and can be used to obtain composition information of the sample; energy-dispersive spectroscopy is one such technique which will be described later in this section.

Elastic collisions occur between electrons from sample beam and the nuclei of atomic in the sample. The sample electron is emitted with the same energy in a process analogous with Rutherford scattering discussed in section 1.4.3.3. These are referred to as backscattered electrons. Whilst both topographic and compositional information can be gained from these emissions, such analysis was not carried out in this work and thus this report will not expand on backscattering SEM. [90]

This report shows data collected with a LEO 1525 FEG-SEM using secondary electrons to construct an image. An accelerating voltage of 5 kV was used for all images with gun and chamber vacuums of $\sim 10^{-10}$ and $\sim 10^{-5}$ Torr respectively. A working distance of 10 mm was used for SEM images in this work. When non-conductive samples were imaged, a charge can build up on the surface to repel other incident electrons and affect the image quality. For this reason, non-conducting samples were coated with thin layers of gold or chromium to dissipate this charge.

2.3.4 Transmission Electron Microscopy

Transmission electron microscopy is a powerful technique capable of producing high resolution imaging ($< 1\text{nm}$) and electron diffraction patterns of nano-scale regions within a film.

Similarly to SEM the technique, it utilises emission data from an electron beam accelerated towards a sample through a condenser lens to reduce the beam diameter. TEM differs in that the measured sample is $< 100\text{ nm}$ thick so that high energy electrons can penetrate through the entire sample. Information relating to the sample is then collected from transmitted electrons by a screen on the other side of the sample. The scattering of the electrons (or lack of) produces an image based on the size of the atoms and lattice orientation of the sample material.

Two independent parallel electron beams are directed at the sample where a part of each beam is diffracted (scattered by 2θ). The objective lens directs the beam towards the object aperture which acts to filter the beam so that either only diffracted or only undiffracted electrons may pass through. A selected area diffraction (SAD) aperture can be introduced to great reduce the diameter of the diffracted beam, so that only electrons from a selected area of the sample are seen. The beam then passes through an intermediate lens the strength of which may be varied depending on application and a final projector lens of set strength to magnify the image onto a fluorescent screen.

To produce a high resolution image of the sample, an object aperture is inserted. In a bright field image only undiffracted electrons are allowed to pass, in a dark field image only diffracted electrons are allowed to pass. Bright field images are used predominantly in this work, however, dark field images were used when performing EDX analysis on samples (section 2.3.5). For this analysis, the SAD aperture is removed and the electron beam passes through two further lenses to magnify the image and project it onto the screen.

The projected beam at the end of the column will produce a greyscale image. Heavier atoms will scatter the beam more than light atoms, thus, significant regional contrast can be expected between sections of different composition. This is also true of sections of different thicknesses in the film. In polycrystalline films, regions of different crystalline orientation will also give different levels of scattering; this was used to highlight the grain structure of ZnO films.

To obtain an electron diffraction image the SAD aperture is again inserted and the object aperture removed (to allow both scattered and un-scattered electrons to pass). Whilst electron diffraction patterns were obtained on select samples, crystallographic analysis was solely performed using XRD.

Cross sectional samples of ZnO films were collected using the Japanese Electron Optics limited (JOEL) 2000FX and 2100F TEMs. The samples were milled from the surface of thin films using a focused ion beam (FIB) the process for which is detailed in the following section.

2.3.4.1 Focused ion beam cross sectioning for transmission electron microscopy

TEM was used to analyse cross sectional images of ZnO films. To capture these images lamellas of ~ 100 nm thick were cut out from thin films using a Helios Nanolab SEM-FIB operated in 'slice and view' mode.

The operation of the system is as follows:

- The films were first protected from damage from the ion beam by depositing a layer of platinum (~250 nm) on the site of interest;
- Two trenches are milled on either side of the protected area using a gallium ion source at 21 nA;

- The cross section is then cleaned using a lower current (6.5 nA) to give a uniform thickness. The milled trenches and cleaned cross section are shown in Figure 2. 4 - a;
- An OmniProbe (a needle precisely controlled using the equipment software) is then inserted and welded to the protecting layer on the cross section using platinum;
- A lamella is then milled out of the bulk material leaving the cross section attached only to the OmniProbe;
- The OmniProbe is lifted out shown as Figure 2. 4 - b and carried to TEM sample holder shown in Figure 2. 4- c;
- The lamella is brought into contact with the sample holder and welded in place using platinum;
- The connection to the OmniProbe is then milled away leaving the sample attached to the sample holder Figure 2. 4 - d;
- The lamella is then thinned using sequentially smaller currents to produce a sample thin enough for TEM analysis Figure 2. 4- e and f;

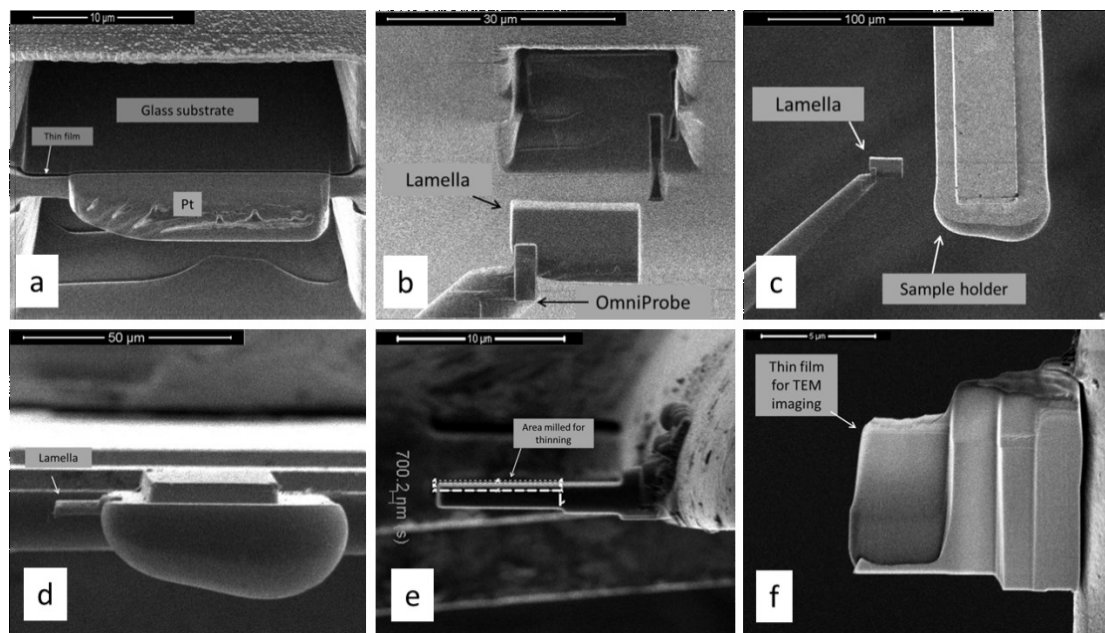


Figure 2. 4 – Stages of FIB cross sectioning using Helios Nanolab. (a) shows trenches milled into thin film surface. (b) shows the lamella welded to an OmniProbe after cutting out from the thin film. (c) shows the lamella positioned next to the TEM substrate holder. (d) shows the lamella welded to the sample holder. (e) shows the thinning process to achieve a sample which electrons can fully penetrate. (f) shows a fully thinned film ready for TEM imaging. Image f was reproduced courtesy of Ecaterina Ware,

2.3.5 Energy Dispersive X-Ray Spectroscopy

In EDX an electron beam is accelerated towards a sample and data is collected from the energy of emitted X-rays (Figure 2. 3). It is often coupled to SEM and TEM systems so that the electron beam can be focused on selected regions. The EDX analysis carried out in the work was coupled to JOEL FX 2000 and F2100 electron microscopes.

When electron beam interacts with the sample, a characteristic X-Ray signal can be collected. The X-ray signal is created as the high energy electrons are absorbed by atoms on the surface and inducing a negative charge. To remove this charge, a core electron is emitted so that the absorbed electron can drop into this space. By measuring the energy of the X-Rays the energy of an inner shell of the sample atom can be calculated. The core energy levels of different elements are known so that the emissions can be matched with a database and a quantitative measurement of the film composition can be obtained. [91]

X-rays are highly penetrating and a signal can typically be collected from up to 2 μm within the material. The advantage of this is that the analysis is not limited to the surface (as is the case with X-Ray photoelectron spectroscopy), however, it means that care must be taken in substrate choice when measuring films of $< 2 \mu\text{m}$ thick. Here the X-ray penetration depth would be greater than the film thickness, thus, it was important to measure Al content on quartz substrates as soda-lime glass contains Al as an additive. It also meant that measuring the oxygen:zinc ratio was not possible using this method.

2.4 Optical and Electrical Properties

Films deposited in this work were also analysed to gain insight into their optical and electrical properties. Discussed in this section are techniques to measure the optical transmittance and optical band gap (UV-Vis spectroscopy) and electrical properties such as the resistivity (Four point probe, Hall effect), charge carrier concentration and hall charge mobility (Hall effect).

2.4.1 Ultraviolet-Visible Spectroscopy

Ultraviolet-visible spectroscopy is an optical technique capable of measuring the transmittance, absorbance and reflectance of thin films. This is achieved by directing a monochromated light source towards a film deposited on a transparent substrate. The wavelength of the light is varied and the percentage of the beam that is transmitted, absorbed or reflected compared to a background reading is measured. In this work transmittance spectroscopy was used exclusively on a Bentham 605 single beam system, using BenWin+ software.

The transmittance of ultraviolet, visible and near infra-red light was measured, scanning wavelengths between 300 and 900 nm and using a step size of 1 nm. An air background was used so that optical transmittance includes a reduction based upon the substrate; this is typical for TCO applications where a substrate will always be present in a device. A spot size of 2 mm was used and the data was processed using BenWin+ software.

The optical bandgap was often extracted from UV-Vis data. This is found using the Tauc model where the absorbance coefficient is a parabolic function of the incident energy the band gap (E_g), given by:

$$\alpha = \frac{A\sqrt{h\nu - E_g}}{h\nu},$$

Equation 2. 4

where 'A' is a function of the refractive index and 'hν' is the photon energy. If $(\alpha h\nu)^2$ is plotted as a function of the energy of the light source the band gap can be extracted from the x-intercept of an extrapolation of the linear section of the curve. This is true for crystalline direct bandgap semiconductors. For indirect bandgap or amorphous semiconductors the term $\sqrt{\alpha h\nu}$ is used.

Another useful feature of UV-Vis, are the interference patterns seen in transmittance spectra (see Figure 1. 23). These patterns are caused by reflections from the different interfaces: air – film; film – substrate; and substrate – air. This is shown in Figure 2. 5. The reflective light interacts constructively and destructively to form the peaks and troughs and can be used to measure the thickness of a transparent film. [92]

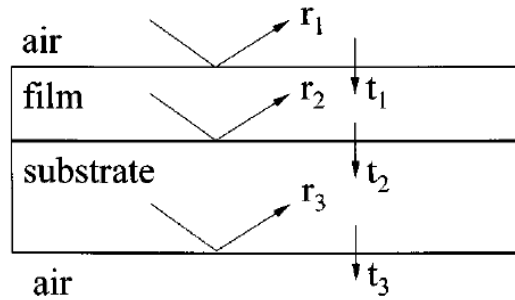


Figure 2. 5 - Schematic diagram of the reflections from transparent film and related optical parameters used in the calculation of the optical constants. The terms r_1 , r_2 and r_3 represent the reflection portion or light at each interface and t_1 , t_2 and t_3 represent the transmitted portion. The figure was adapted figure 1 of reference [92] .

With knowledge of the refractive index of the transparent film the thickness (d) can be extracted from Equation 2. 5:

$$d = \frac{\lambda_1 \times \lambda_2}{2[n(\lambda_1)\lambda_2 - n(\lambda_2)\lambda_1]}$$

Equation 2. 5

where ' λ_1 ' is the wavelength at one peak and ' λ_2 ' is the wavelength an adjacent peak. ' $n(\lambda_1)$ ' and ' $n(\lambda_2)$ ' are the refractive index at these two wavelengths. This method requires the films to be above a certain thickness to give the required patterns and is only accurate for films where the absorbance at the desired wavelengths is small.

2.4.2 Four Point Probe

The four point probe (4PP) technique is a basic method of determining sheet resistivity of thin films. In the 4PP technique, four liner metallic probes are put in contact with a film. The arrangement of the 4PP machine is shown in Figure 2. 6.

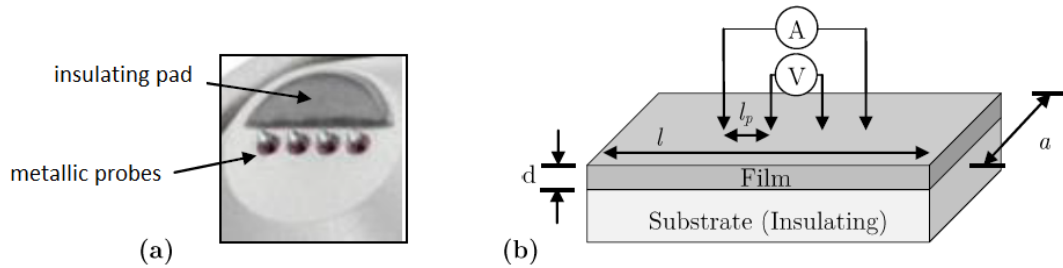


Figure 2. 6 - (a) shows the four metal probes on the head of the 4PP machine. (b) shows a schematic of the four probes in contact with the thin film, d is the film thickness, l and a are substrate dimensions l_p is the distance between the probes. Reproduced from reference [93].

A high current is passed between the two outer contacts and the voltage is measured between the two inner contacts. Spring loaded tungsten carbide probes were used in this work. These probes had a diameter of 0.3 mm and spacing (l_p) of 0.6 mm. The film thickness and substrate dimensions must be greatly in excess of l_p for reliable results. The voltage was measured at 6 different currents over two orders of magnitude. A linear increase in voltage confirmed the validity of the measurements. The sheet resistances was calculated using the $V=IR$ relationship. This was divided by the thickness to give the resistivities quoted in 4PP measurements.

2.4.3 Hall Effect

The Hall Effect is a significantly more powerful technique for determining the electronic transport properties of thin films. Named after its discoverer Dr Edwin Hall, it was used to measure the resistivity of films deposited in the work and dissect the charge carrier concentration ' nq ' and charge mobility components ' μ ' (see Equation 1. 10). Detailed theory behind the Hall Effect is given in the Lakeshore 8407 User's manual with important aspects to this work highlighted here.

The Hall Effect is a phenomenon which occurs when a magnetic field is set perpendicular to an electric current. This causes deviation of some carriers from the current line, as shown in Figure 2. 7.

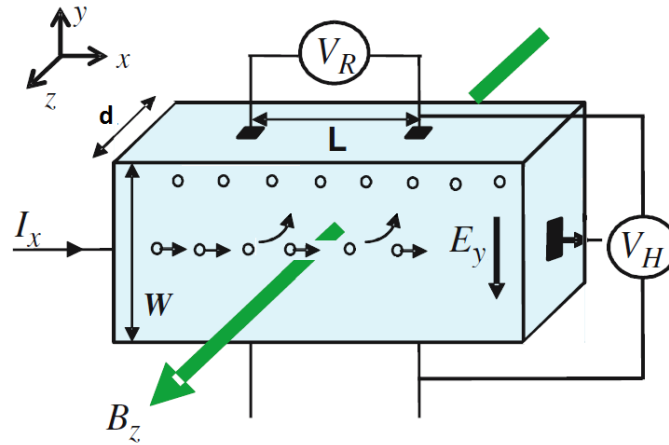


Figure 2. 7 – Schematic showing the forces in effect across an n-type sample to produce the voltage drop known as the Hall Effect. Adapted from reference [94]

The current is the total charge ‘I’ per second flow along a sample of width ‘W’ and thickness ‘d’ is related to the velocity ‘v_x’ by:

$$I = nqv_x Wd.$$

Equation 2. 6

If a static direct current (DC) magnetic field is present in the ‘z’ direction (B_z) then the force on the charges is given by:

$$F_L = ZvB,$$

Equation 2. 7

Where ‘Z’ is the size of the charge, ‘v’ is the velocity of the charge and ‘B’ is the magnetic field. This is known as the Lorentz force (F_L) deviating the charges along the curved lines seen in Figure 2. 7.

Since no current can flow out of the surface of sample, a charge builds up to create an electric field in the ‘y’ direction (E_y) to create a potential difference across the top and bottom surfaces of the film. This voltage, perpendicular both to the magnetic field and to the electric current, is known as the Hall voltage (V_H).

The repulsive effect of the surface charge means that a steady state is reached. When the Hall voltage is equal to the Lorentz force the following can be said:

$$V_H = E_y W = \frac{IB_z}{ane}.$$

Equation 2. 8

For convenience the term ' $-1/nq$ ' is given defined as the Hall coefficient R_H so that, for an n-type semiconductor:

$$V_H = -\frac{R_H I B_z}{d}.$$

Equation 2. 9

The magnetic field, the current, the Hall voltage and the thickness can all be measured; as such the Hall Effect can be used to extract the charge carrier concentration. With a known charge carrier concentration all it takes is the relatively simple task of measuring resistivity (ρ) and the charge mobility can be extracted from:

$$\mu = -\frac{|R_H|}{\rho}.$$

Equation 2. 10

There is a slight adjustment made to R_H when inelastic carrier scattering mechanisms are possible, in this case a constant known as the Hall factor (r_H) (previously mentioned in Equation 1. 17) is added so that;

$$R_H = -\frac{r_H}{nq}.$$

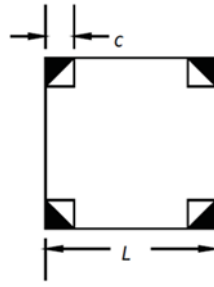
Equation 2. 11

In the ZnO films measured in this work r_H was set to one.

2.4.3.1 Resistivity

The resistivity obtained by the Hall Effect measurements for this work, used the method devised by van der Pauw in 1958. [95] It is based on the concept that samples may be an arbitrary shape as long as the contacts from instrument to film are as small as possible, on the periphery of the film, and that the film is of uniform thickness without pinholes. Four contacts are required to make measurements of charge carrier concentration and resistivity.

Whilst it is possible to perform measurement on arbitrary shapes it is convenient to use symmetric configurations. The substrate structures used in this work is shown in Figure 2. 8.



Square structure

Figure 2. 8 -Electrode structure used for Hall effect measurements - Square structure with square and triangular contacts. Image adapted from Lakeshore 8407 User's manual

When 'c/L' is 1/6 the correction factor is +2 % (square contacts) and + <1 % for triangular contacts. The correction factor for the Hall voltage is ~ +15 V.

Square structures were used for the ease of processing. Metallic indium contacts were attached to the corners of samples. Indium was chosen over, for instance sputtered gold, due to the close work function match with ZnO (Sputtered Au: 4.7 eV, metallic In: 4.1 eV, measured ZnO by spray pyrolysis: 4.18 eV). This limited the contact resistance in the measurements. In this work correction factors were accounted for by the Lakeshore measurement software.

The resistivity is calculated from the square structure by:

$$\rho = \frac{\pi d}{\ln 2} \times \frac{(R_A + R_B)}{2} \times f,$$

Equation 2. 12

where 'R_A' and 'R_B' are the resistances measured between two adjacent contacts and 'f' is the correction factor. *f* is equal to one when a perfectly symmetrical sample is used.

2.4.3.2 Eliminating Errors – AC field Hall Effect measurements

In an ideal measurement, the Hall voltage would be equal to zero when no field is applied, however, this is not always the case. Voltages measured at zero field can be due to two main reasons – a thermal gradient in the sample giving a thermoelectric voltage 'V_{TE}' and asymmetry between contacts giving a misalignment voltage 'V_o'. [96], [97]

The thermoelectric voltage is independent from the current. This means if the voltage is measured before and after a current reversal then the difference between the two voltages will give the thermoelectric voltage. Using this method, the V_{TE} term can be calculated and corrected for.

Similarly, the misalignment voltage is independent of the magnetic field, by measuring the voltage in two different magnetic fields, V_o can also be calculated and corrected for. However, the misalignment voltage becomes high at low mobilities; this noise restricts Hall Effect measurement in a fixed magnetic field to films with mobilities of $> 0.1 \text{ cm}^2/\text{V.s}$.

Using an AC magnet gives the field a sinusoidal shape with a time dependency. The signal is now split into an AC and DC components given by:

$$V_{measured} = R_H I B \cos(\omega t) - \beta B \omega \sin(\omega t) + V_o + V_{TE}$$

Equation 2. 13

where 't' is time and ' ω ' is the frequency. The DC V_o and V_{TE} erroneous components can be eliminated by passing the signal through a capacitor. However, another source of error is now added due to inductive pickup from the wires in the changing magnetic field, this is equal to ' $-\beta B \omega \sin(\omega t)$ '. Fortunately this signal is 90 degrees out of phases with the Hall voltage, thus, by using a lock-in amplifier, these signals can be separated and the Hall voltage can be isolated as:

$$V_{measured} = V_H = \frac{R_H I B_z \cos(\omega t)}{d},$$

Equation 2. 14

Small errors in the phase can be removed following this measurement using a current reversal.

Using the AC Hall effect measurement system it is possible to accurately measure films with mobilities down to $10^{-4} \text{ cm}^2/\text{V.s}$. These adjustments were applied for measurements in this report.

AC field Hall measurements were performed using a Lakeshore 8400 system with AC current between 10 nA and 50 mA, and with a sinusoidal magnetic field of 1.19 T.

Whilst the AC field method allows the measurement of mobilities that are practically impossible in a DC field there are some drawbacks:

1. The frequency of the measurement is limited, typically 0.1 Hz or less, resulting in a relatively slow measurement;
2. AC field methods cannot be used to determine if a sample has parallel conduction;
3. The method is not as common as DC, and consequently, it may be difficult to compare results from other systems;
4. There is less foundation for interpreting results of very low charge mobility Hall measurements.

2.4.3.3 High Resistance Mode

Measurements were conducted with a high resistance attachment to increase the top of the resistance range from 10 M Ω to approximately 200 G Ω . This allowed the measurement of undoped ZnO films which typically displayed resistivities of 200 M Ω /sq.

In high resistance measurement the input impedance of the voltmeter begins to load the sample and weaken the voltage. Current leakage becomes a more significant source of uncertainty. Technical enhancements were attached to the measurement system to minimise these effects

2.5 Chapter conclusions

This section gives a summary of the experiment methods discussed and their function in work to follow. It also summarizes the analytical tools discussed and the information that can be retrieved from them.

2.5.1 Synthetic methods

- Films were deposited by the spray pyrolysis technique.
- In early work this was done by hand but the process was quickly automated.
- Film properties largely depend on the plume dynamics as it reaches the substrate.
- Plume dynamics are controlled by many parameters.
- The control of these parameters and resulting properties are the focus of chapter four.
- Films were doped to improve the electronic properties. The resulting properties is the focus of Chapter V.

2.5.2 Physical and Structural properties

- Profilometry was used to measure film thickness.
- XRD was used to measure crystalline phases present, crystallite size and lattice spacing.
- SEM was used to display topographic features.
- TEM was used to display cross sectional grain structure, porosity, thickness and some crystallite properties.
- EDX was used for compositional analysis.

2.5.3 Optical and Electronic properties

- UV-Vis was used to measure optical transmittance and optical band gap.
- 4PP was used to measure resistivity.
- Hall Effect measurements were used to measure resistivity, charge carrier concentrations and mobilities of deposited films.
- The Hall Effect system used an AC field with a high resistivity attachment to measure films of low charge mobility and high resistance.

CHAPTER III – AUTOMATED SPRAY PYROLYSIS

3.1 Introduction

This chapter focuses on the automation of the spray deposition process. It first shows initial depositions of ZnO and general properties before focussing on the problems with hand spraying. Following this, the chapter will describe the making of the automated spray rig. The optimisation and use of the rig for experimental deposition will be discussed in subsequent chapters.

3.2 Hand Spraying and Associated problems

Preliminary depositions were carried out using the hand-held commercially available airbrush shown in Figure 3. 1. The gun was held over a hotplate with the temperature set between 300 and 500 °C. Films were deposited in the manner described in section 1.6.2.3. The deposition process was loosely based upon the experimental conditions of Bashir *et al.* [98] To alleviate potential decreases in the set temperature from solvent evaporation on the surface, a pause between sweeps was implemented.

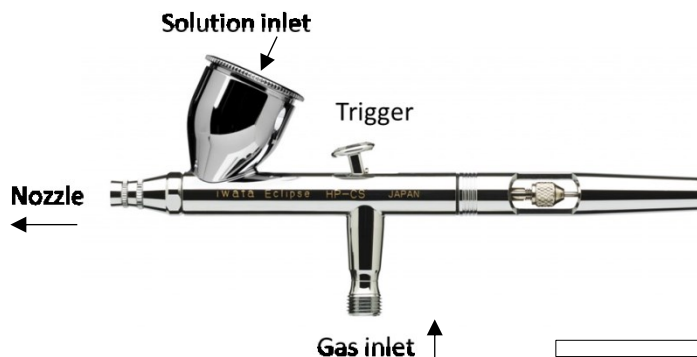


Figure 3. 1 – The ‘Iwata Eclipse HP-CS’ airbrush used for hand deposition. Labelled are the important components of the gun. The nozzle diameter is 0.35 mm, the precursor solution is gravity fed from a reservoir above the gun with plastic tubing connecting to a rubber bung inserted into the ‘solution inlet’. The carrier gas is supplied from a standard gas cylinder and connected to the ‘gas inlet’. Scale marker indicates 2 cm.

When the trigger (shown in Figure 3. 1) is pressed down the carrier gas is released to the nozzle. Sliding the trigger horizontally controls a needle. When fully forward, the needle blocks the nozzle and neither the carrier gas nor solution can pass through. As it is slid backwards more solution can pass through. When the trigger is both pressed and slid backwards, the solution is forced through the nozzle by the carrier gas producing an aerosol of precursor solution. The size of the plume could be varied by the position of the trigger on a sliding scale.

Figure 3. 2 shows a photograph and SEM micrographs of a ZnO film deposited by hand using the conditions shown in Table 3. 1.

Hotplate temp (°C)	Gun height (cm)	Carrier gas	Carrier gas pressure (bar)	Precursor solvent	Precursor concentration (M)	Pause length (s)	Passes per cycle	Speed of pass (s/p)	Cycle s
400	18	N ₂	1	MeOH	0.2	30	10	1	3

Table 3. 1 – The spray parameters for initial deposition

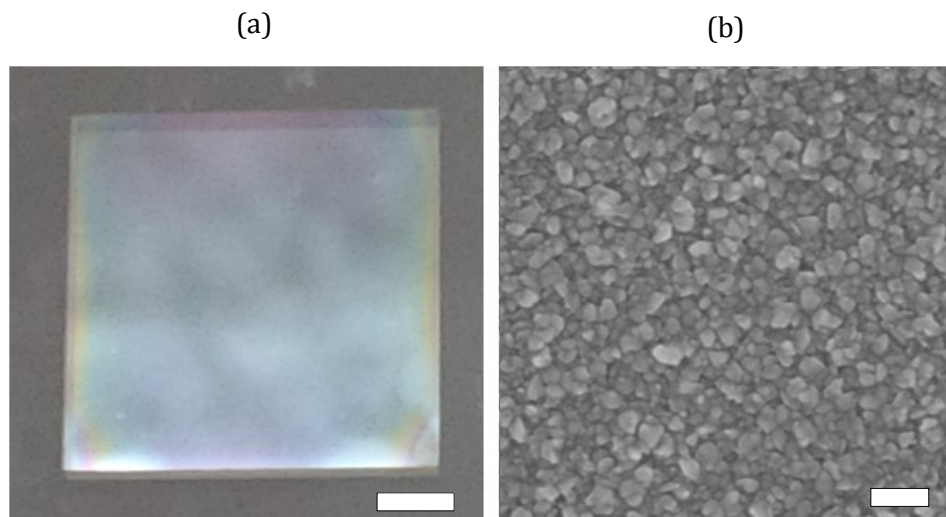


Figure 3. 2 – (a) shows a photograph of a ZnO film deposition on glass. (b) shows an SEM micrograph of the same film. Scale marker (a) indicates 20 mm, scale marker (b) indicates 200 nm.

The photograph in Figure 3. 2 (a) shows that the sprayed ZnO films are, to the eye, transparent and continuous. There are relatively few visible defects however the discolouring towards the edges of the film suggests that the film is thinner in these places. Some variation in colour is also seen across the surface of the films, this suggests some inhomogeneity in thickness is present.

The SEM micrograph (Figure 3. 2 (b)) shows a continuous, pinhole-free film comprised of many grains. These grains are in the region of 100 nm, however, they vary greatly in size with the smallest as low as 10 nm and the largest up to 175 nm.

Figure 3. 3 shows a typical XRD pattern and UV-Vis spectra of the ZnO film in Figure 3. 2. The data confirms the presence of ZnO. The XRD reflections match those of wurtzite ZnO whilst the UV-Vis shows the fundamental absorption at 360 nm associated with ZnO.

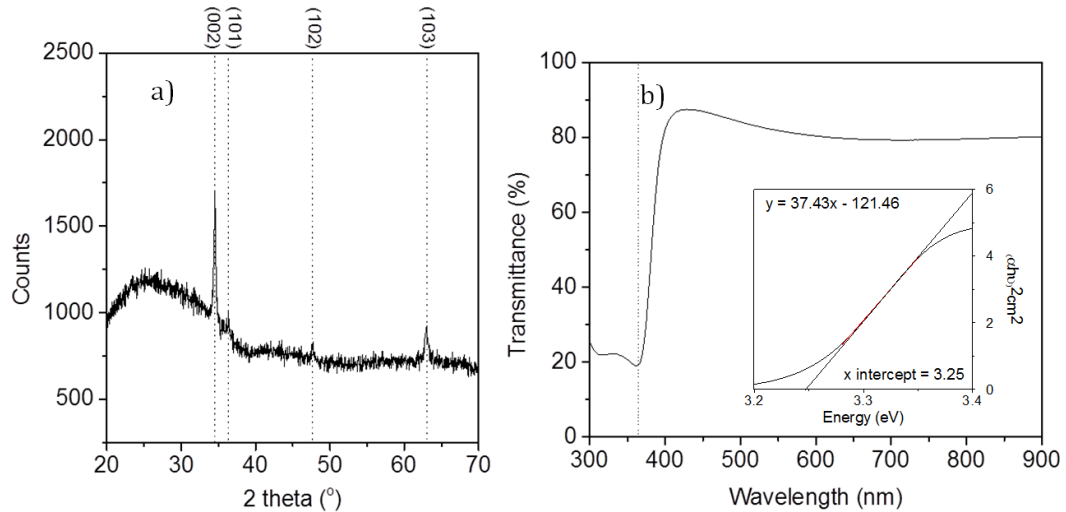


Figure 3. 3 – An XRD pattern (a) and UV-Vis spectra (b) of ZnO prepared by spray pyrolysis. The XRD pattern matches that of wurtzite ZnO with a high preferential orientation towards the (002) reflection compared with the powder pattern. The large amorphous section seen between 20 – 40 ° is due to the glass substrate. Labelled are the four orientations seen in the films. The UV-Vis transmission spectra shows the fundamental absorption peak of ZnO at 360 nm and an excellent transparency between 450 and 900 nm displaying its potential for use in TCOs. Insert shows a Tauc plot of the UV-Vis data. The linear part of the plot was given a linear fit with the equation of the line shown, this gave a calculated direct bandgap of 3.25 eV.

The XRD pattern shows that the structure is highly orientated towards the (002). There is some evidence of this seen in the SEM micrograph shown in Figure 3. 2 – (b) with the shape of the grains bearing a resemblance to the hexagonal structure which characterises the (002) direction. The structural shapes of each orientation are shown in Figure 4. 4.

Whilst hand spraying could produce continuous, crystalline ZnO films, the small variations in the height, speed and position at which the air gun was passed over the hotplate meant that inhomogeneous thicknesses were seen in single films and between samples.

To better show and quantify this phenomenon, ten ZnO films were deposited by hand and their thickness, optical transmittance, and XRD patterns were recorded. The films were deposited over two days to study day-to-day variations, samples 1-5 deposited on the first day and sample 6-10 deposited on the second day.

The thicknesses of the ten samples were measured by profilometry with the results shown in Figure 3. 4.

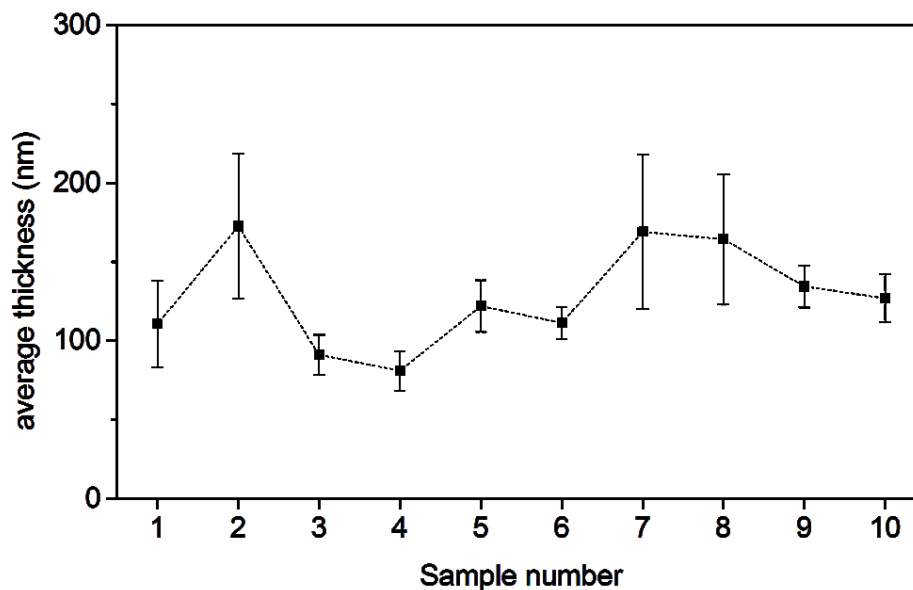


Figure 3. 4 – The thickness of ten samples deposited under the same set conditions as measured by profilometry. Samples 1- 5 were measure on day one, 6-10 were measure on day two. Error bars show in-sample thickness inhomogeneity based upon standard deviations of the positions

Figure 3. 4 shows the thickness ranging from 81 to 172 nm, with an average of 128 nm and a standard deviation of 30.4 nm. This represents an error of $\pm 24 \%$. There is no obvious thickness variation from day one to day two, however, this test is by no means exhaustive and further investigation would be needed to clarify this. By examining the measurements across the three positions on the samples (section 2.3.1), the in-sample thickness inhomogeneity could be measured. Samples 2, 7 and 8 show large differences in measured thickness across the sample suggesting that sample thickness inhomogeneity can be a problem when spraying by hand. The average percentage variation in the three measurements is $\pm 17 \%$.

The samples were studied using XRD and UV-Vis analysis to investigate the variation in the structural and optical properties brought about by hand spraying. XRD patterns of the ten samples are shown in Figure 3. 5 and UV-Vis spectra in Figure 3. 6.

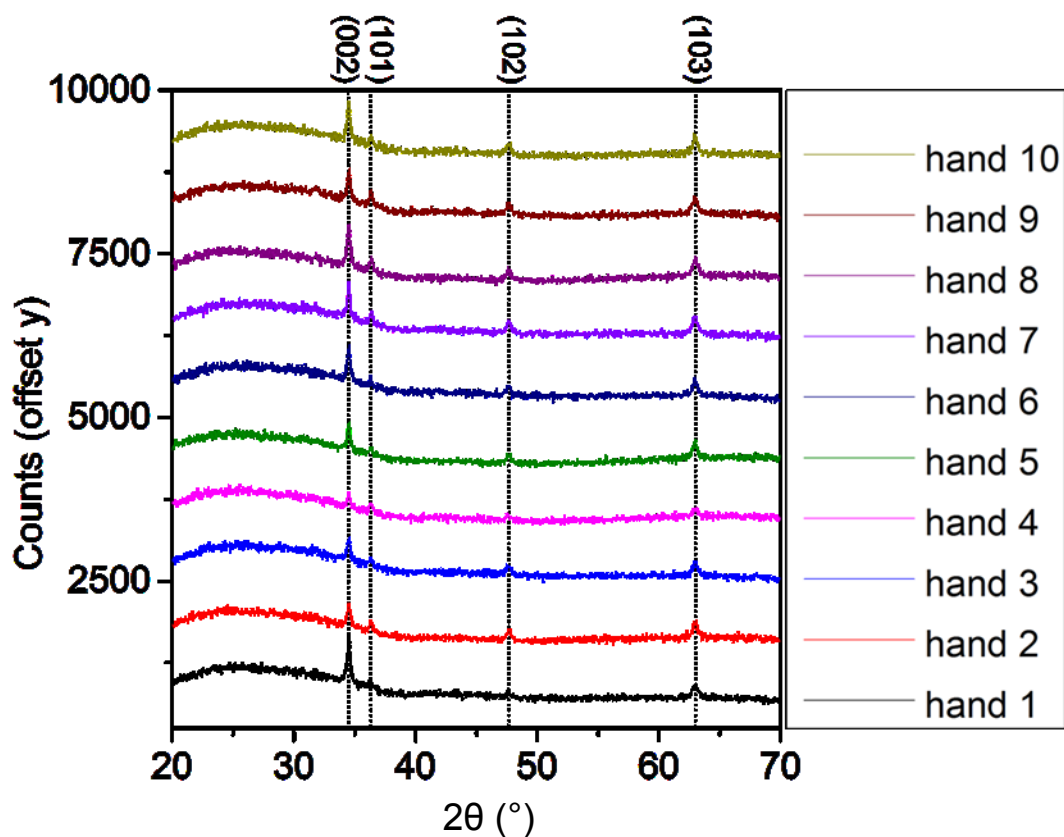


Figure 3. 5 - XRD patterns of ten samples deposited by hand spraying nominally under the same conditions. The reflections are annotated with the appropriate planes of wurtzite ZnO.

The films all show one phase with similar preferential growth in the (002) orientation. The intensities of the peaks are seen to fluctuate, this is expected with varying film thickness and there is a good correlation between thickness and peak intensity. It is not a perfect fit however (Figure 3. 7 - (a)), suggesting that variations in spraying by hand may cause some changes to the crystallinity of films outside of that expected from variation in thickness.

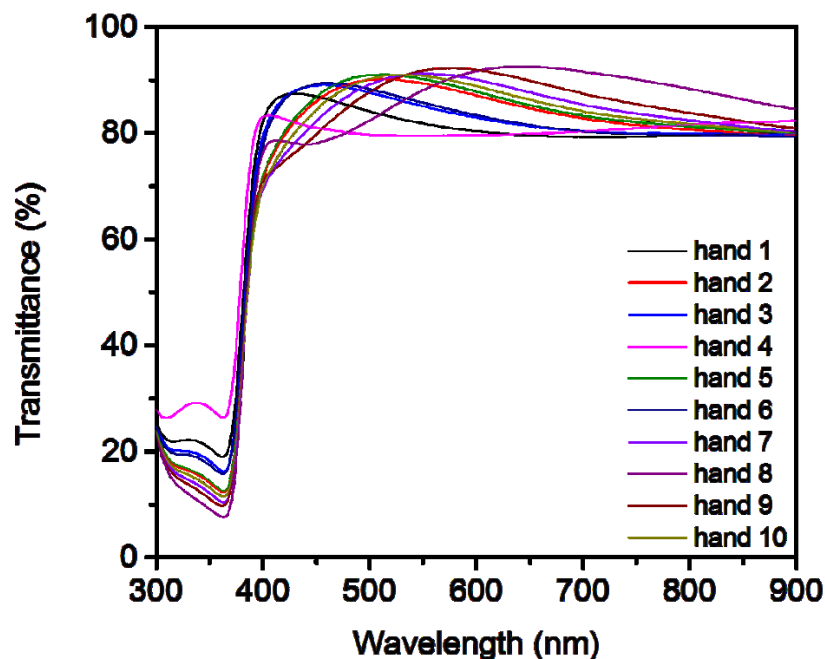


Figure 3. 6 – UV-Vis spectra of ten samples deposited by hand spraying nominally under the same conditions.

The UV-Vis spectra in Figure 3. 6 show a similar thickness dependent trend to the XRD (Figure 3. 7 - (b)). The thickness of the film varies the intensity of the fundamental absorbance from the ZnO film shown. The deviation from linear fit shows that conditional variation from hand spraying may also produce films of differing optical properties outside of that expected from variation in thickness.

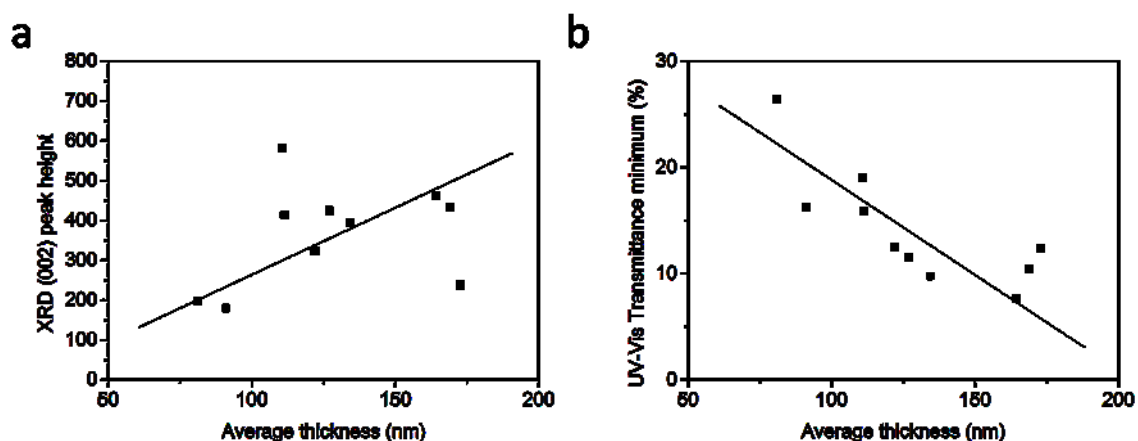


Figure 3. 7 – Average thickness of hand sprayed films and their peak intensity (a) and transmittance minimum (from the ZnO fundamental absorption) (b). These graphs assume that there is a linear relationship between the peak height / minimum transmittance and thickness.

The poor repeatability was proposed to be due to difficulties in maintaining a constant height and speed of sweep, especially between samples deposited on different days. Moreover, there was often inhomogeneity in single films when the plume was not well directed over the sample.

The data from Figure 3. 7 highlights the problems with inconsistent thicknesses. When investigating the optical and structural properties of the films associated with different conditions trends may be missed, or wrongly interpreted, because of thickness variation between samples. This factor is not often given enough significance in many academic reports into sprayed ZnO and may undermine some conclusions made.

The process could be significantly improved by automating the process where an entirely constant height, speed of pass and direction of plume can be maintained and the improved consistency of results may reveal trends missed in reports involving hand sprayed samples. The next section will detail the fabrication of the automated spray rig.

3.3 Fabrication of the Spray Rig

The aim of automating the process was to pass a spray gun over a hotplate at a consistent rate, maintaining a consistent height, and delivering a regular plume of solvent aerosol directly over the sample.

The original airgun was not ideal for the task; the design of the trigger mechanism (Figure 3. 1) allowed for variation in the amount of solution released to the nozzle. This was one possible cause of inconsistencies in the deposited films. A new gun was chosen which had a smaller nozzle size and a more appropriate trigger mechanism. The gun chosen was the SataJet 20B shown in Figure 3. 8.

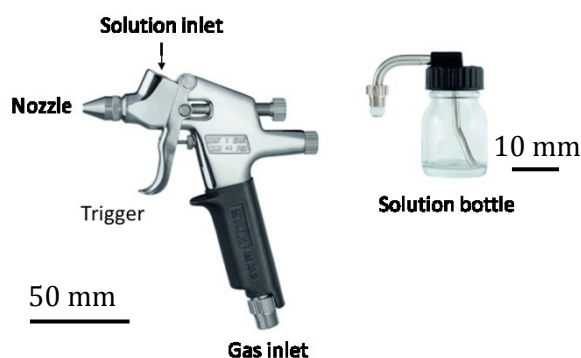


Figure 3. 8 – Annotated picture of the air gun used on the spray rig. The nozzle size is reduced from 0.35 mm - 0.2 mm. The precursor solution is delivered from the ‘solution bottle’, a small vacuum is created by the airflow so that when the trigger is pressed the carrier gas is released through the nozzle pulling solution to the nozzle where it is atomised.

The challenge was to design a mechanism to move the spray gun over the sample. A stage was modelled on SketchUp (Figure 3. 9) and 3D printed to carry the gun. This mounting upon a set of rails.

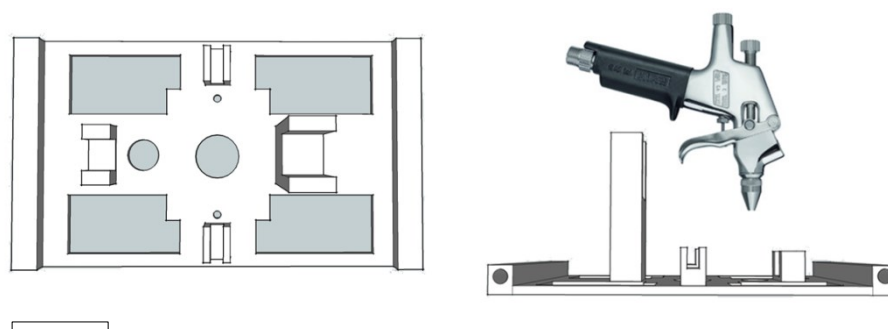


Figure 3. 9 – 3D sketch of the stage designed to carry the air gun over the hotplate. Left shows an aerial view of the stage, holes in the middle of the stage are for the nozzle and the linear actuator. Scale marker indicates 50 mm.

The stage was pulled over the hotplate using a tracked belt powered by a stepper motor. The trigger was controlled using a linear actuator which drives a metal thread upwards to press the trigger and downwards to release it. It is affixed to the stage by two screws and positioned under the stage directly below the trigger mechanism. The rails are fixed to a purpose built metal structure, and the distance from the hotplate to the sample can be controlled by adjusting the height of this fixture. The attachments of the motors and rails are shown in Figure 3. 10.

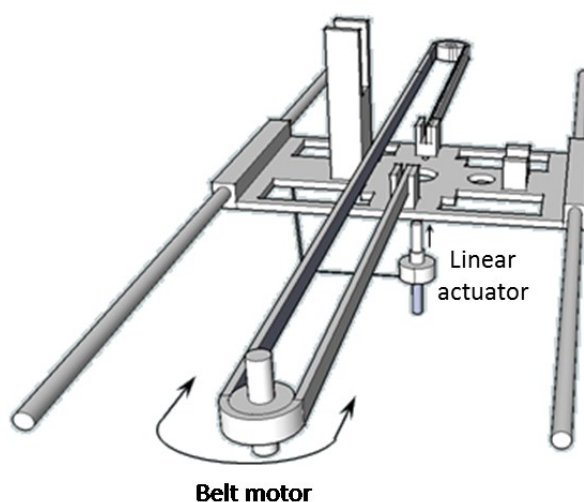


Figure 3. 10 – 3D sketch of the stage mounted on the rails with the belt attached and connected to the motor. The linear actuator is affixed to the stage. Electrical wiring connects the belt motor and linear actuator to a microcontroller.

The stepper motor and linear actuator are controlled using an Arduino microcontroller. A program was developed in C++ to pass the stage over a hotplate a set number of times at a set speed using the belt stepper motor. Simultaneously the linear actuator determines whether the trigger is enabled or disabled. The Arduino also powers a button to start the program and an LED light to show the position of the program, turning off when the machine is in motion and turning on again once it is complete. A separate button powers a cleaning program and an emergency stop program.

The coding for the microcontroller is shown in the Appendix (section A.1).

One of major failings of the hand spraying was the tendency to not direct the plume immediately over the sample. This led to one side of the sample being thicker than the other. There were also problems with samples occasionally displaced by the force of the plume. To solve these problems a metal plate was created to sit upon the hot plate, it was designed with two sample sized inlets cut into it so that the surface of the sample sat flush with the metal plate. This setup also helped to reduce 'edge effects' caused by variation in surface temperature around the edge of the substrate.

The stage was pulled across the rails over the plate. A solution containing blue ink was used to map the travel of the plume. In this way the plate could be positioned correctly so that the ink trail ran exactly over the sample cuts.

By optimising the position in this way, it became apparent that the air flow from the fume hood in which the spray deposition was performed was having a significant effect on the plume. The extractor fan pulled the plume towards the back of the fume hood giving it an inhomogeneous shape. Panels of polymethyl methacrylate (PMMA) were used to create an enclosure around the hotplate to solve this problem. A 3D model of the full spray rig is shown in Figure 3. 11.

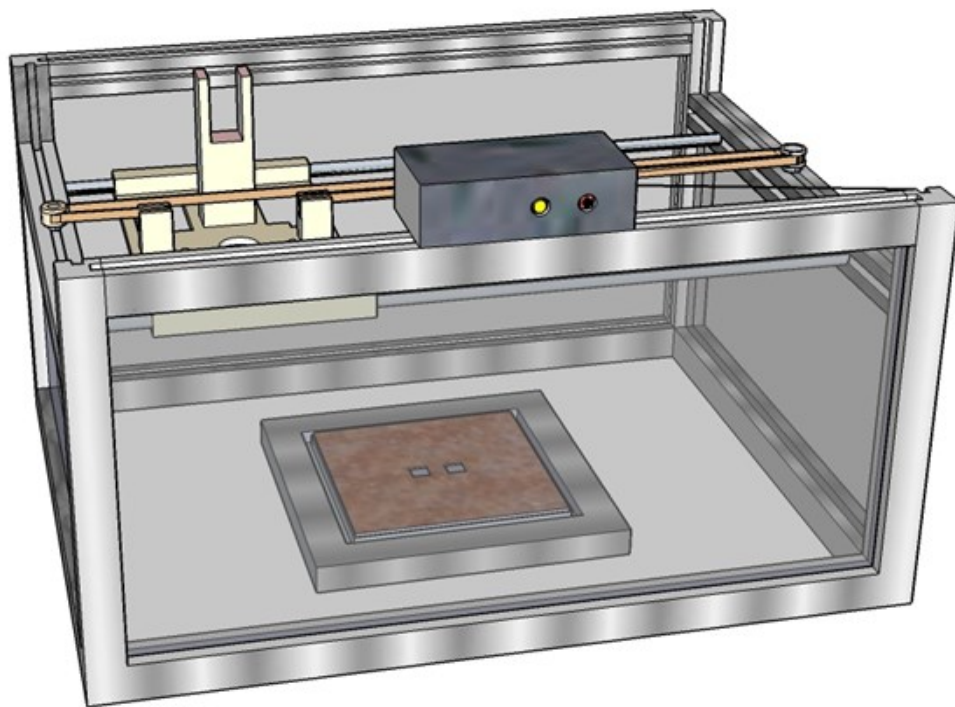


Figure 3. 11 - 3D schematic of the spray rig setup with hotplate and encasement. The microcontroller is stored within the box on the front. The button and LED which act to start the program and display when the program is finished are shown on the microcontroller box.

3.4 Comparison between hand and rig deposited films

Using comparable settings ten samples of ZnO were deposited using the rig. The results were compared with those deposited by hand spraying. There was one unavoidable change in the conditions; the motor had a top speed of 4.5 s/pass whilst, in the hand spray setup, the speed was set to 1 s/pass. In an attempt to counter this, the number of passes in a cycle was dropped from ten to three so that even thickness for each sample was achieved. As seen in Figure 3. 12 comparable thicknesses were not achieved. A larger plume was created by the new gun, thus, the samples were found to be considerably thicker. The spray setup is shown in Table 3. 2.

Hotplate temp (°C)	Gun height (cm)	Carrier gas	Carrier gas pressure (bar)	Precursor solvent	Precursor concentration (M)	Pause length (s)	Passes per cycle	Speed of pass (s/p)	Cycles
400	18	N ₂	1	MeOH	0.2	30	3	7	3

Table 3. 2 – Spray parameters for rig vs. hand comparison

The ten samples were once again deposited on two separate days. The thicknesses were measured by profilometry. These measurements, alongside the hand sprayed samples for comparison, are shown in Figure 3. 12.

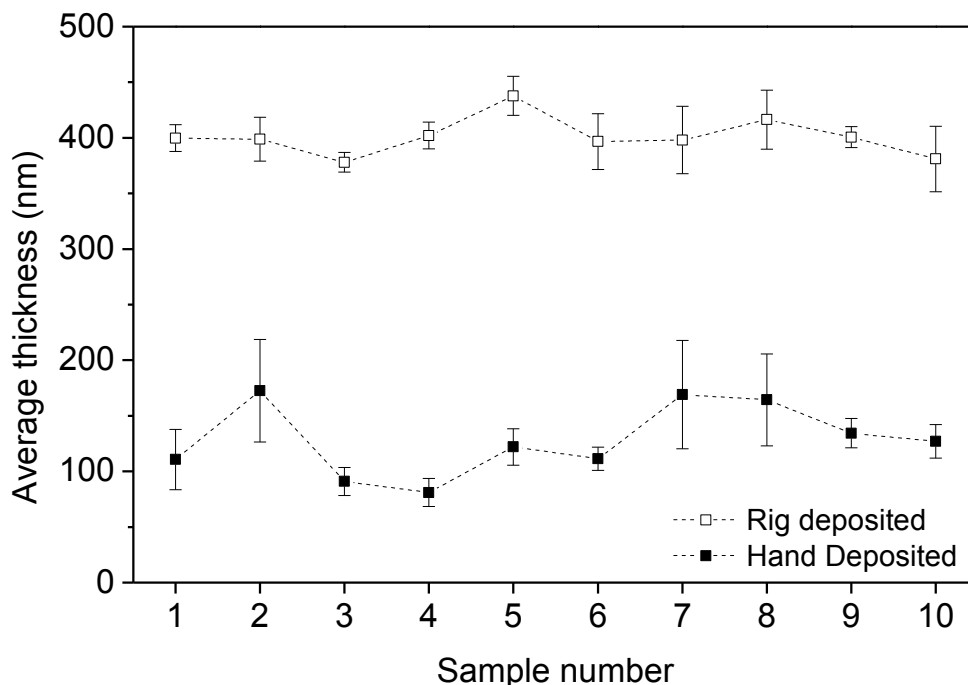


Figure 3. 12 – Profilometry measurements of ten ZnO samples.

There is a clear difference between the samples in that the rig deposited samples are 2-3 times thicker. It is also clear that the rig deposited samples are more consistent in thickness. The rig deposited samples ranging from 378 to 437 nm with an average of 401 nm and a standard deviation of 16 nm. This represents an error of $\pm 4\%$, a great improvement on the 25% error observed for hand sprayed films. The film thickness also has less in-sample variation. The average percentage variation in the three measurements is 5% for the rig deposited compared with 17% seen in hand deposited films.

The XRD patterns of the films deposited are shown in Figure 3. 13.

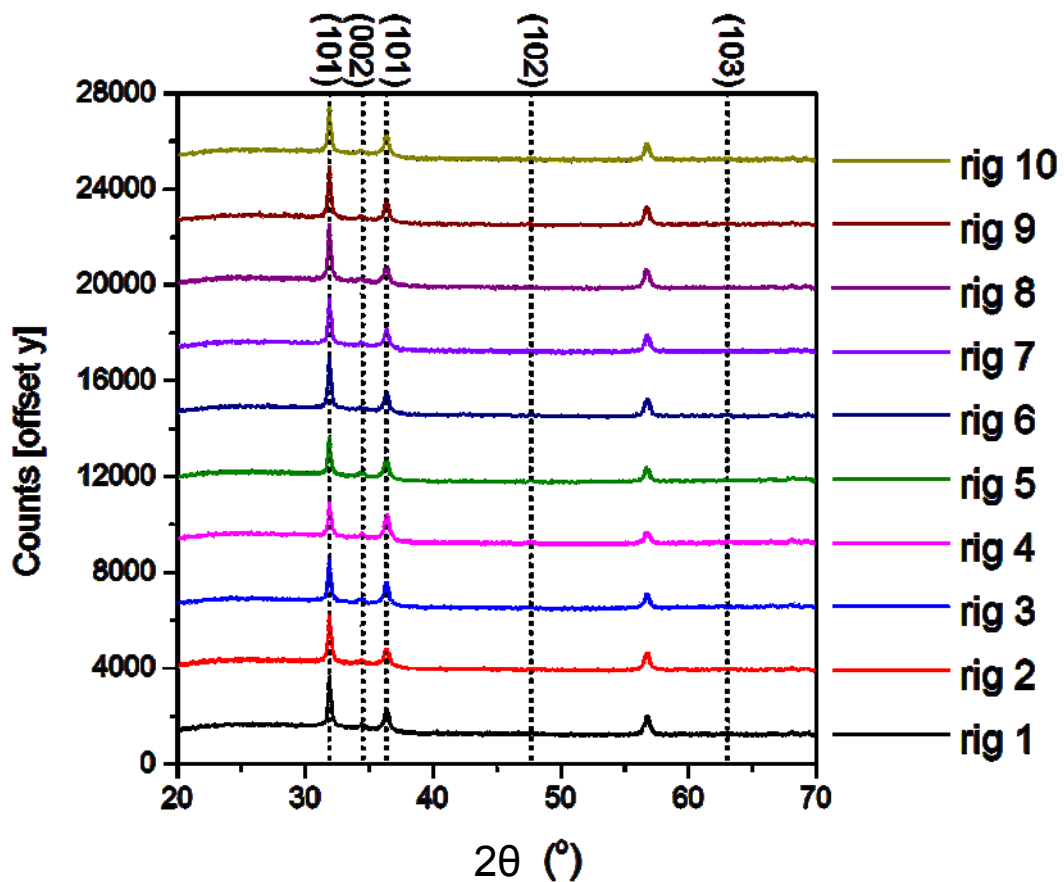


Figure 3. 13 – XRD patterns of ten rig films deposited under the same conditions. Labelled are the crystalline orientations of the ZnO films.

The rig deposited XRD patterns show films of highly comparable intensities and orientations. There is a change of preferential orientation from the (002) in the hand sprayed samples to the (101) in the rig sprayed. Reasons for this change are believed to be linked to the difference in velocity, droplet size and plume size – the three main differences between the rig and hand routines.

The UV-Vis spectra of the films deposited using the rig are shown in Figure 3. 14.

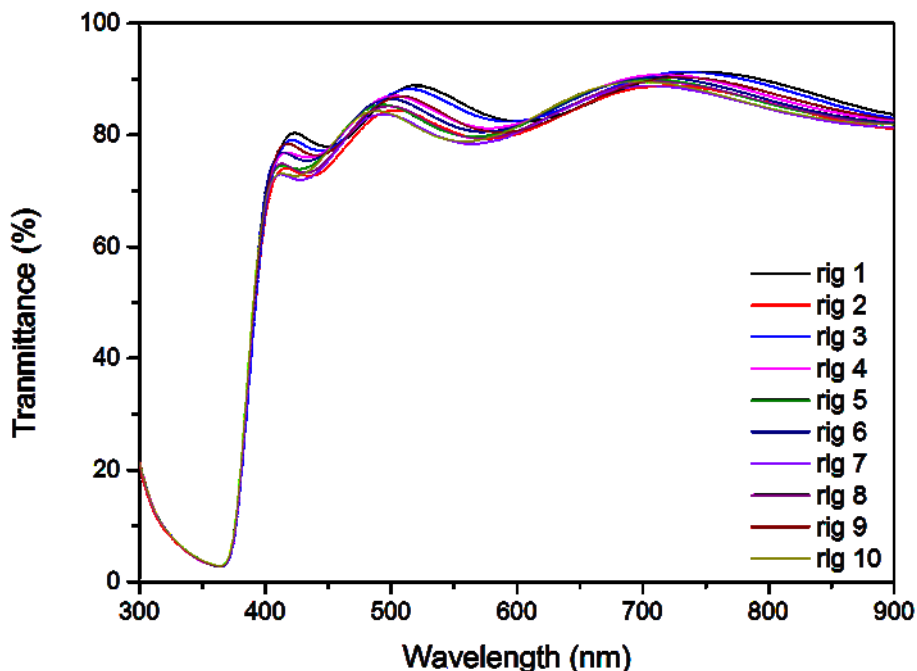


Figure 3. 14 - UV-Vis transmittance spectra of ten rig deposited films deposited under the same conditions

The optical transparency of the ZnO rig deposited films is comparable with those deposited by hand despite having up to three times the thickness. The rig films are much more alike, confirming the lower range in thicknesses observed in profilometry measurements. The distinct interference patterns show the films to have an excellent film/air interface and the consistency of pitch of amplitude of these patterns highlights the uniformity of the films. The difference in the fundamental absorption between samples is near zero. A comparison between Figure 3. 6 and Figure 3. 14 highlights the advantage of the automated system. It is possible to extract the thickness from the fringes, as described in section 2.4.1. Figure 3. 15 shows the thicknesses of the ten films extracted from the UV-Vis alongside the profilometry measurements.

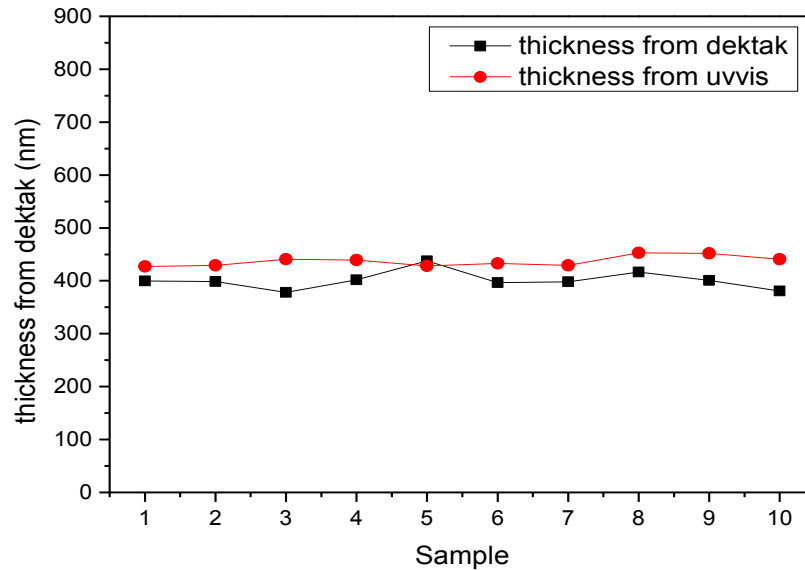


Figure 3. 15 – Thickness measurements by profilometry and extracted from UV-Vis interference patterns of ten ZnO films deposited using the automated rig.

The UV-Vis thickness measurements agree well with those made using the profilometer although they are consistently 20 nm thicker. The agreement of the two techniques backs up the reliability of both measurements with the UV-Vis extracted thicknesses once again showing little variation.

3.5 Conclusions

This chapter has shown the problems with hand spraying and how these problems were solved by the automation of the process. It also described the methods involved with designing and making the spray rig.

To summarise:

- Hand sprayed samples showed large thickness variation between samples
- Hand sprayed samples showed large in-sample thickness inhomogeneity
- The XRD and UV-Vis suggested some minor optical and structural differences between hand sprayed samples
- The automated rig produced films of greater uniformity in all three areas

With a repeatable method of depositing films of comparable thickness, structural and optical properties it was now possible to optimise the system for the deposition of oxide films for various applications. The details of this optimisation will be discussed in the Chapter IV.

CHAPTER IV – GROWTH AND OPTIMISATION BY SPRAY PYROLYSIS

4.1 Introduction

In this chapter the spray pyrolysis technique is investigated in detail for the depositions of ZnO films. This work follows the design and fabrication of an automated spray rig, conducted to improve the repeatability of the process. Initial work looks at optimising the spray conditions of the automated rig. Specifically this is for the deposition of transparent and conductive films.

In parallel to the optimisation, Chapter IV investigates the electronic properties of undoped ZnO deposited by spray pyrolysis. There is much in the literature [99]–[106] discussing the optimisation doped ZnO for use as a TCO. When investigating links between structural and electrical properties however, studies are often complicated by the addition of external defects. Using AC Hall measurements to probe the less conductive, undoped films has enabled detailed investigation into the effect of crystalline structures on the electronic properties of native ZnO.

A key feature of spray pyrolysis as a technique, is the large number of parameters which can be controlled. Varying each on can have a profound effect on the properties of the deposited films. This can be seen as a disadvantage, as all these parameters require optimising. It does however, allow the careful tuning of parameters to produce bespoke films for a range of application.

Much of the experimental work also focuses on the optimisation of the system and the tuning deposition parameters towards achieving the lowest possible resistivity. This provides a backdrop for the work discussed in Chapter V where external dopants are added to the system. Ensuring the deposition conditions are optimised for the native oxide is essential before the effects dopants may have on the system can be considered.

4.2 Parameter control

Section 1.6.2.4 discussed the various pathways for droplets of solvents containing precursor salt to be deposited on the substrate. These pathways are determined by the plume dynamics and the deposition conditions. A large proportion of the experimental using the spray pyrolysis technique was directed towards optimising the large number of parameters involved. The parameters involved in the deposition process of this study are listed in Table 4. 1.

Parameter	Possibilities
Precursor salt (PS)	Acetates, chlorides, nitrates
Precursor solvent (S)	Water, methanol, ethanol
Precursor concentration (PC)	0.01 – 0.5 M
Carrier gas type (CG)	Compressed air, nitrogen, argon, oxygen
Carrier gas pressure (CGP)	Up to 3 bar
Hotplate temperature (HT)	200 – 500 °C
Distance from nozzle to substrate (D)	10 – 20 cm
Substrate type (St)	Float glass, quartz, silicon
Number of total cycles (Cy)	Dependent on required thickness
Speed of passes (SoP)	4 – 10 s/pass
Nozzle size (NS)	0.5, 0.35, 0.2 mm

Table 4. 1 – Identified parameters to be controlled in the spray system

These parameters needed to be understood and regulated in order to control the physical properties of the film. Another parameter controlled for individual experiments was the pause length (PL) - set as the time it takes for substrate temperature to return to the set point. The variables listed in Table 4. 1 were studied in order to optimise the system and discover the most desirable films primarily for TCO applications.

4.2.1 Preliminary studies

Whilst some parameters were studied in detail in this work, there were some parameters already well defined by the literature which this work did not progress significantly. Some simple studies are outlined and the parameter choices are explained. Following this, the importance of film thickness is demonstrated.

4.2.1.1 Precursor Salt

The choice of precursor salt was important to which 'pathway' the sprayed droplets would follow. This is because the temperature of decomposition and of vaporisation differs from salt to salt.

A variety of zinc precursors salts have been used in the deposition of ZnO by spray pyrolysis. The most commonly studied have been: zinc acetate ($\text{Zn}(\text{OCH}_2\text{CH}_3)_2 \cdot 2\text{H}_2\text{O}$); [107] zinc chloride (ZnCl_2); [108] and zinc nitrate ($\text{Zn}(\text{NO}_3)_2 \cdot 6\text{H}_2\text{O}$); [109] although other precursors such as zinc pentanedionate ($(\text{C}_5\text{H}_7\text{O}_2)_2\text{Zn} \cdot \text{H}_2\text{O}$) have also been examined. [110]

These precursors are often chosen due to their low cost, low toxicity and range of decomposition/vaporisation temperatures. The salts were often used in their hydrated forms for increased stability in air and in solution.

Romero *et al* studied structural difference when depositing from the acetate and chloride salts. [111] Here, the crystalline orientation is shown to be temperature dependent changing from a (100) orientation at 300 °C to (002) at 400 °C when using the acetate salt. The chloride however, remains heavily (002) textured at all temperatures from 300-500 °C. It is also shown that a 50:50 mixture of zinc acetate and zinc chloride also produces a highly (002) textured film. Crystallite size is seen to be greater in the zinc chloride films (~40 nm) than in zinc acetate (~15 nm).

Bacaksiz *et al* studied zinc acetate, zinc chloride and zinc nitrate in a larger study. [112] All films were deposited at 550 °C and again showed the zinc chloride films to be highly textured in the (002) direction, zinc nitrate showed moderate texturing whilst zinc acetate showed a random orientation. Morphological studies showed that films deposited from zinc chloride formed discrete hexagonal columns, zinc acetate formed nano-pyramids and plate-like structures whilst the zinc nitrate films were rough, non-granular with large surface defects. Resistivities were found to be in the range of $10^3 \Omega \cdot \text{cm}$ for the acetate and nitrate derived films but in the range of $10^4 \Omega \cdot \text{cm}$ for the chloride. Charge carrier concentrations were found to be in the range of $1 \times 10^{14} \text{ cm}^{-3}$ for the acetate and nitrate samples and $9 \times 10^{13} \text{ cm}^{-3}$ for chloride whilst charge mobility was found to be 5, 8.5 and $10.4 \text{ cm}^2/\text{V} \cdot \text{s}$ for the nitrate, acetate and chloride samples respectively. The film thickness was not stated in this case.

Krunk *et al* highlighted the potential problem in using zinc chloride in that chloride ions may contaminate the ZnO films. This is suggested to be due to a higher decomposition temperature led to lower observed optical transparency. [113], [114]

Subsequently, Arca *et al* studied the same three precursors. [115] In this study, films grown from the nitrate and chloride were shown to become microscopically damaged by acidic by-products of the pyrolytic decomposition producing HNO₃ and HCl respectively whilst the acetate produces volatile organic components and CO₂ neither of which causes film damage.

Recently, Kenanakis *et al* studied zinc acetate and zinc nitrate precursors to deposit ~40 nm films using ultrasonic spray pyrolysis. [116] These films were shown to be smooth ($R_{\text{RMS}} \sim 4$ nm) with grain sizes of ~ 20 nm. The Zn films are seen to be significantly less homogeneous but offer a faster growth rate.

4.2.1.1.1 Precursor salt choice for this work

Films grown from zinc acetate produce the highly textured, homogeneous, ZnO films with no drawbacks such as contamination or acid etching. Preliminary studies were carried out upon ZnO films prepared from zinc acetate, nitrate and chloride showing visibly higher film qualities in the acetate than those prepared from the nitrate and chloride derivatives. Most zinc nitrate and zinc chloride gave films of immeasurably poor quality. For this reason zinc acetate dihydrate was used as the precursor to all films shown in this work.

4.2.1.2 Precursor Solvent

The solvent plays a large role on which pathway the droplet will undergo, the boiling point of the solvent will dictate how quickly it evaporate. The surface tension of the different solvents also plays a role because it affects droplet size.

Many different solvents have been used in precursor solutions. In early work deionised water was predominantly used as the solvent [109], [113] however, even before this time, it was found that using alcohols (either entirely or mixed with H₂O) improved the performance of film.

Guillemoles *et al* compared using water, methanol and a 50:50 water:alcohol mix as the solvent (alcohol = methanol, ethanol or isopropanol (IPA)). [117] Using alcohols changed the orientation from a random orientation to a highly (002) textured film. It also improved the transmittance (~50 - 80 %) and lowered the resistivity (~18 - 0.4 Ω .cm). Mixing with water or using purely alcohol had similar effect although subtle changes could be seen using methanol, ethanol and (IPA) in the water mix.

Santiago *et al* later studied using methanol, ethanol and IPA - water mixes (7:3) in more detail whilst investigating F-doped ZnO films. [118] This work found that methanol gave lower resistivity films than ethanol and IPA. It was suggested that the lower boiling point methanol produced higher quality films by favouring a 'CVD growth process. This work also highlighted the advantages of aging the solution with lowest resistivities seen in nine day old methanol solutions. The inclusion of the F dopant, however, may play a role in this finding.

Most work in the last decade has used either methanol or a methanol:water mix. The exact ratio of the mix is usually dependent on the exact setup of the system used. It is also well documented that most zinc precursor salts have a higher solubility in methanol than ethanol and IPA.

It is also interesting to note that the surface tensions of the solvents will affect droplet size. Water has a surface tension of 71.40 mNm⁻¹ at 20 °C with methanol and ethanol having very similar surface tensions of 22.60 and 22.10 mNm⁻¹ at 20 °C respectively. [119] Due to the lower surface tension, alcohols are expected to produce smaller droplets.

The pH of the precursor solution has also been shown to impact the quality of films. Caillaud *et al* showed the importance of pH on the chemical state of precursor salts in 1993. [120] The ideal pH for film deposition is outlined to be 3.1 < x > 4.7. Above pH 4.7 basic salts, adsorption compounds and precipitates slow the growth rate and decrease film quality; below 3.1 and Zn²⁺ ions form instead of the acetate hindering growth. Additionally, the carboxyl CH₃-COO⁻ group from has been suggested to attach to the polar (101) surfaces, this inhibits film growth in these directions and thus, increases growth in the (002) direction. [121] Following this work, an amount of acetic acid was added in almost all reports of sprayed ZnO. The concentration of acetic acid to solvent has since been optimised.

Maldonado *et al* studied 3 at% IZO films, deposited from a pH 3.2 solution and a pH 3.8 solution. [122] Crystalline structures are seen to be highly (002) textured in films deposited from pH 3.2 solution at substrate temperatures from 400-500 °C (25 °C steps), however, in the pH 3.8 solutions the texturing only becomes apparent in the 500 °C sample. Hall effect measurements showed an order of magnitude lower resistivity in the pH 3.2 samples at 475 and 500 °C compared with lower temperature samples, this was driven by an increase in charge carrier concentration. At these temperatures the pH 3.2 samples have roughly equal resistivity to the pH 3.8 samples. At lower temperatures the pH 3.8 samples showed lower resistivity than the more acidic samples. The morphology of the pH 3.8 deposited films are shown to be granular whilst at pH 3.2 films are smooth.

Recently, Alejandre *et al* studied the impact of the concentration of acetic acid (0 – 20 vol%) added to a IZO precursor solution and its effect on roughness, grain size, crystalline structure and resistivity. [123] The average roughness decreased upon addition of acetic acid from a R_{RMS} of 8 nm at 0 vol% to ~5 nm at 2.5 vol% above this value it rises again reaching 8 nm at vol%. Grain size is seen to decrease on the addition of acetic acid from 30 - 25 nm at 2.5 vol% before increasing to 40 nm at 10 vol%. The resistivity drops by a factor of three from 0 until 5 vol%, after which an increase is seen and, at 20 vol%, is higher than the non-acidified sample.

4.2.1.2.1 Precursor solvent choice

The literature suggested that alcohols act as good solvents in spray pyrolysis. Of these, methanol possesses the highest volatility with a boiling point of 65 °C and also offers the highest solubility to zinc acetate. Preliminary studies show that mixing methanol 50:50 with water gave immeasurably poor quality films. For this reason pure methanol was used as the solvent in work shown here. 2.5 vol% acetic acid was also added to maintain the pH of the solution to $\text{pH } 4 \pm 0.5$ and promote growth in the (002) direction.

4.2.2 Thickness studies

The thickness of ZnO films has a significant impact on the structural, morphological and optoelectronic properties. This parameter is often overlooked in studies as highlighted in literature review of individual parameters – particularly in studies upon precursor concentration as detailed in the section 4.2.8.

Major *et al* described the influence of thickness on the crystal structure of pure ZnO and IZO and investigated its influence of thickness on the electric properties for IZO. [124] Films were grown from zinc acetate at 400 °C. XRD analysis showed films of 90 nm displayed a random orientation whilst 800 nm films displayed a texturing towards the (002) orientation although other orientations were present. 950 nm IZO films showed even greater (002) texturing. The electrical properties were measured for IZO films following both vacuum annealing and oxygen annealing (Figure 4. 1). A strong thickness dependence particularly from 50-400 nm, it is suggested that this is due to the random orientation of low thickness films causing more oxygen trap states adsorbed to grain boundaries.

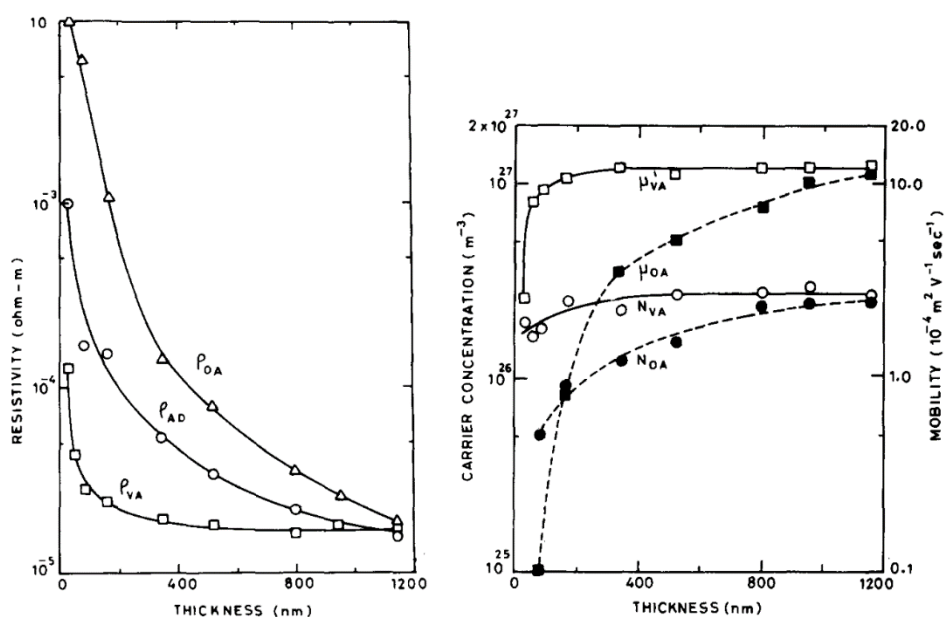


Figure 4. 1 – the influence of thickness on electronic properties of IZO films. Left shows resistivity of as-deposited (AD), oxygen annealed (OA) and vacuum annealed (VA) films. Right shows Hall effect measurements of oxygen (OA) and vacuum (VA) annealed films.

The electronic component of these results was confirmed by Olvera *et al.* This is investigation the morphology and optical properties are also studied for AZO, GZO and IZO films (thicknesses - 200, 1000 and 2400 nm). [11] Grain size is shown to dramatically increase with thickness from SEM analysis. The optical properties are similar for all films, however, thicker films displayed slightly lower transparency. The structural properties show little difference, however, the doping of the films is suggested to promote a (002) texturing. [125] Films lower than 200 nm were not investigated. Further studies have also discussed this thickness effect, however, few study thicknesses lower than 200 nm. [126]

Reports studying the electronic properties of undoped ZnO have been limited by the high resistivity of as-deposited films. Moreover thicknesses studied in literature are often inappropriate for many devices where component layers are often between 30 – 200 nm thick.

4.2.3 Thickness dependence studies

The thickness of ZnO samples was varied by increasing the number of cycles. Other parameters were fixed as shown in Table 4. 2.

CG	HT (°C)	D	CGP (bar)	St	PC (M)	PL (s)	SoP (s/p)	Cy	NS (mm)
N ₂	400	18	2	Soda lime	0.2	25	5	1-7	0.2

Table 4. 2 – Experimental parameters for thickness study

The following section details thickness measurements and studies their effect on the structural and electronic properties.

4.2.3.1 Thickness calculations

The thickness of films deposited using 1, 2, 3, 5 and 7 cycles is shown in Figure 4. 2.

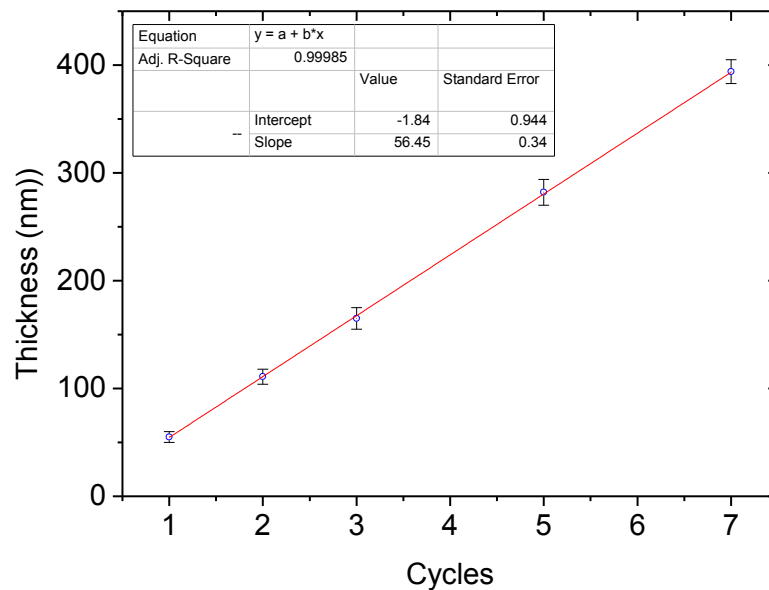


Figure 4. 2 - The thickness of ZnO films deposited using increasing cycles, dotted line shows linear fitting. Points represent the average of measurements taken at three points on the sample shown in Figure 2. 1.

The linear fit shows that the deposition rate remains constant with increasing cycles. At the present parameters the deposition rate is 55 ± 1 nm per cycle.

4.2.3.2 Structural analysis

The structural properties of deposited films were investigated by XRD, shown in Figure 4. 3. The thicker films show a greater intensity, however, the texturing of films also appears to change. The emergence of minor peaks is also seen in thicker films.

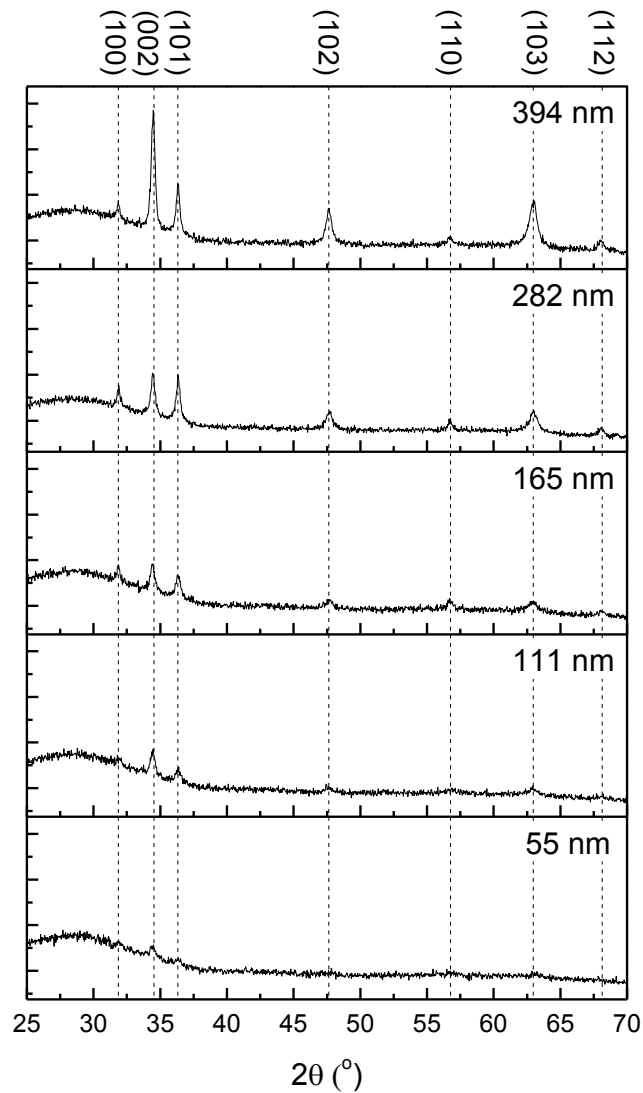


Figure 4. 3 – XRD patterns of ZnO films with increasing thickness. The different orientations are highlighted by vertical dashed lines

It is clear that the texturing of the film is dependent upon the thickness. This was quantified by calculating the texture coefficient shown in Figure 4. 4. The 55 nm film is included in the analysis, however, the XRD pattern is weak and brings the reliability of this data into question. Films at all thickness show texturing towards the (002), although, the dominant orientation becomes (103) in the 394 nm sample. This orientation becomes increasingly dominant as thickness increases. The (100) decreases in intensity as thickness increases until it is highly unfavoured in 394 nm films. The preferred orientation of a self-textured film is dependent of the surface free-energies of each orientation; this can change depending on growth conditions. The exact dynamics of surface energies are outside the scope of this work, however, this topic is discussed in more detail by Fujimura *et al.* [127]

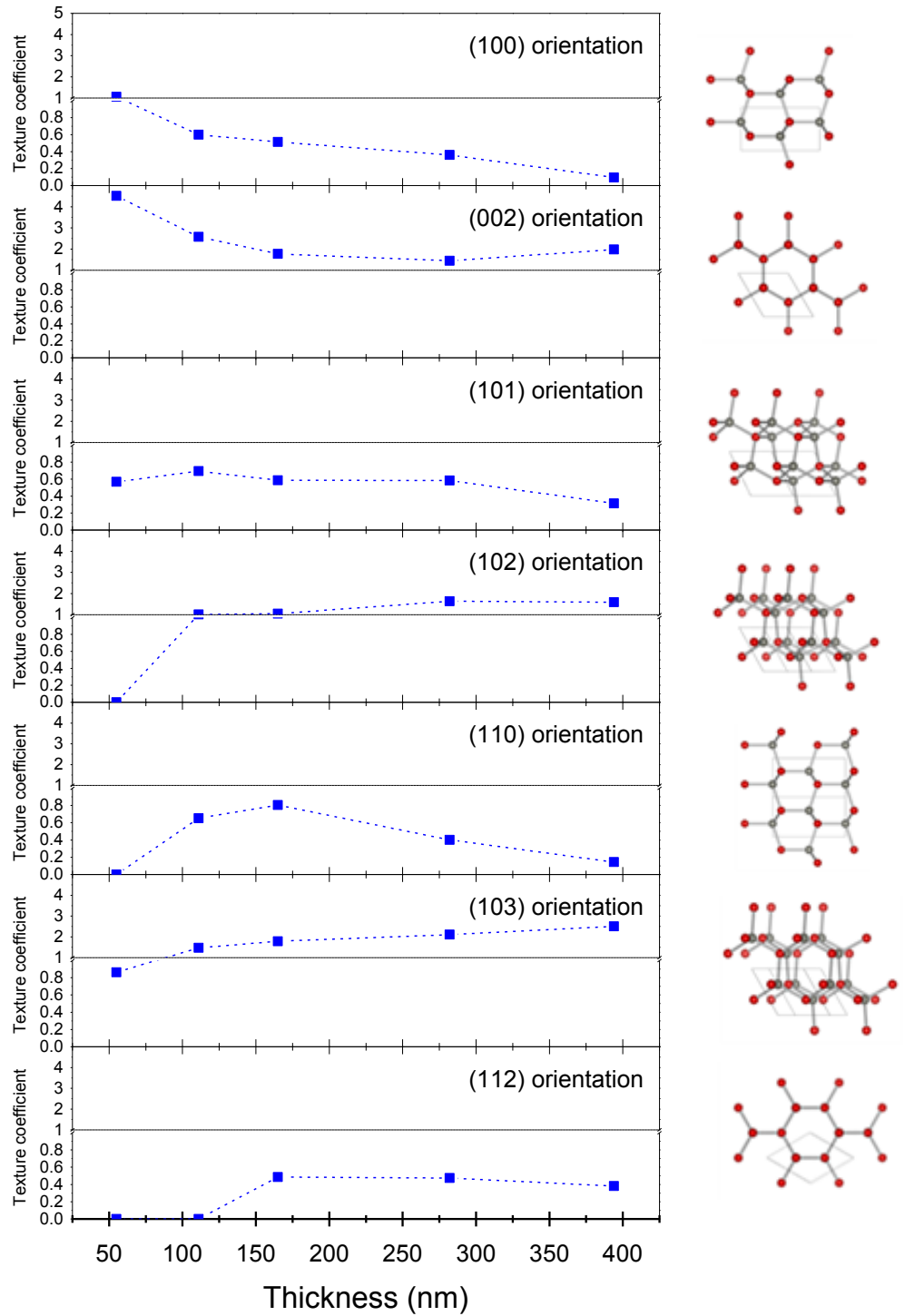


Figure 4. 4 – The texture coefficients of ZnO films with increasing thickness. An atomic representation of the lattice orientation is shown on the right.

Crystallite sizes were approximated using the Scherrer equation (Equation 2. 2), using the (002) peak present at a reliable intensities in all films (Figure 4. 5).

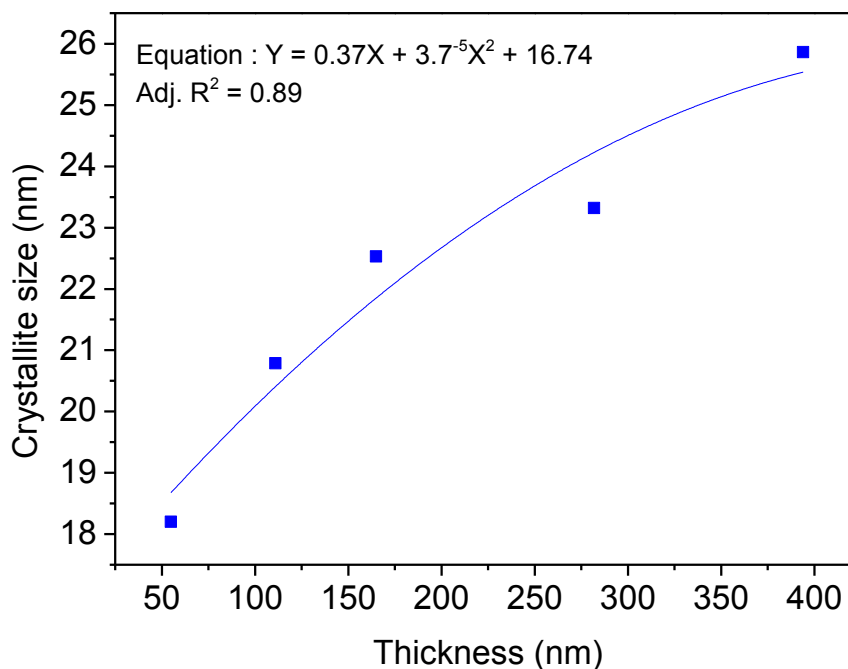


Figure 4. 5 - The crystallite size of ZnO films with increasing thickness.

An increase in the crystalline size from ~18 – 26 nm (44 %) is observed as the thickness is increased from 55 – 394 nm. The increase is sharpest between 50 – 150 nm, this it likely linked to diminishing thickness limitations to the crystallite size. The polynomial fit (Figure 4. 5) gives marginally better fitting than linear ($R^2:0.88$) suggesting the increase in crystallite will tail off at higher thicknesses, however, a more in depth experiment would be needed to study the exact nature of the relationship.

4.2.3.3 Optical analysis

The optical properties of deposited films were investigated by UV-Vis spectroscopy shown in Figure 4. 6. The thicker films show lower transmittance between 300 – 370 nm due to increased absorbance from the ZnO.

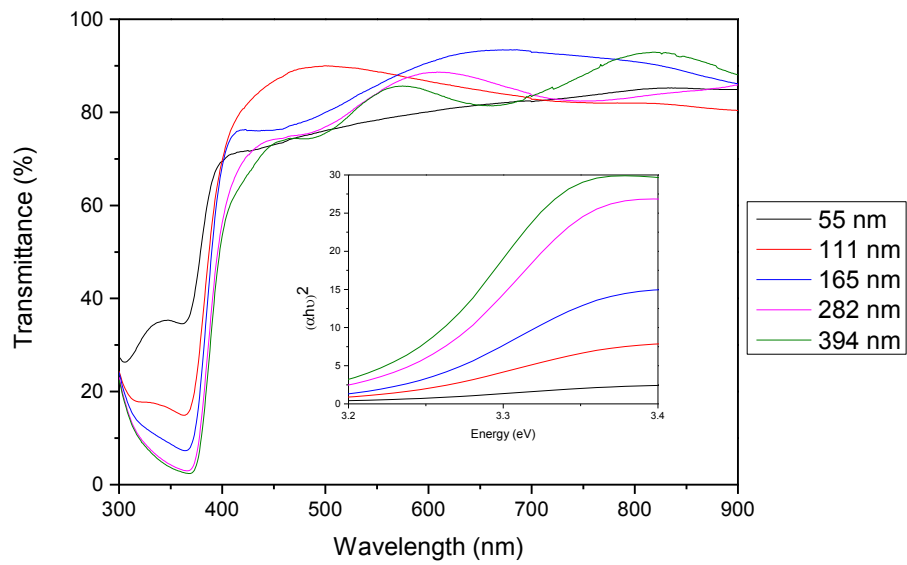


Figure 4. 6 – Optical transmittance of samples of different thicknesses. Insert shows Tauc analysis of optical data.

Tauc analysis (see section 2.4.1), shown in Figure 4. 6 – Insert, was used to investigate whether thickness had a significant effect on the band gap of the films. Results are displayed in Figure 4. 7.

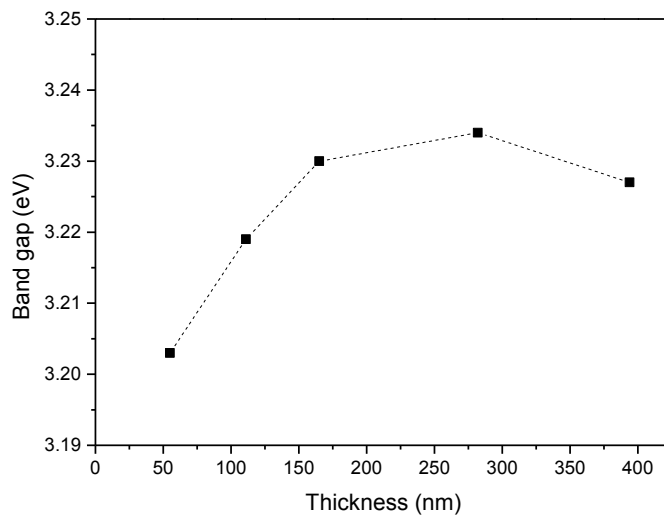


Figure 4. 7 - Varying electronic band gap of ZnO with increasing thickness

The data shows an increase in the electronic band gap of the ZnO of 0.03 eV between 55-200 nm. This may be linked with variation in the intrinsic defect levels within the films.

4.2.3.4 Electrical Measurements

The impact of thickness on the electrical properties was studied using the AC Hall effect technique. The results are displayed in Figure 4. 8.

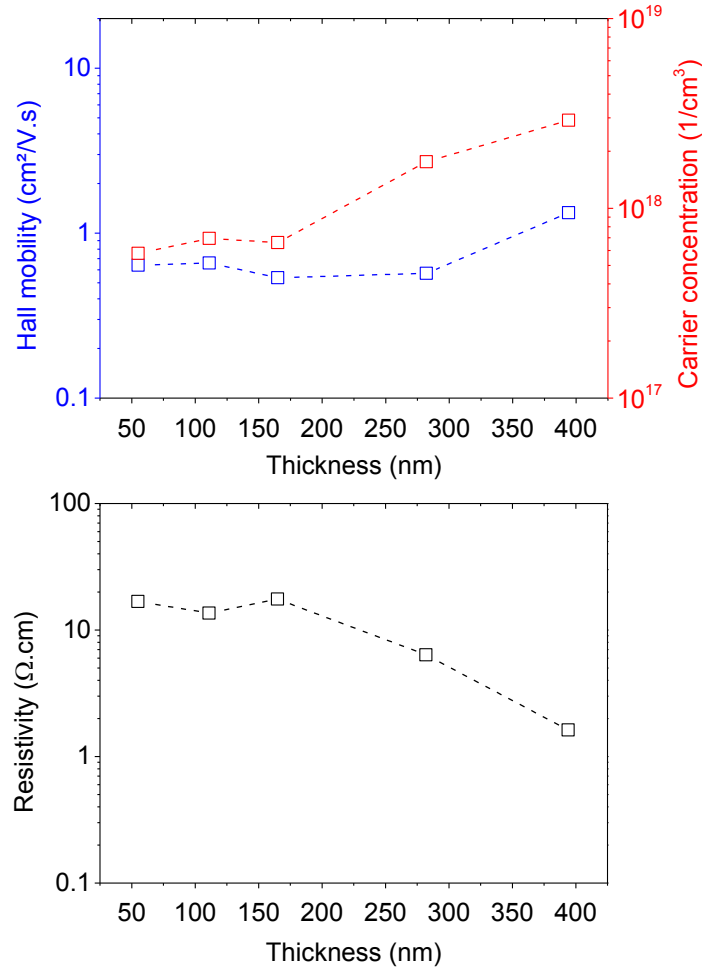


Figure 4. 8 - Electrical properties of ZnO at increasing thickness measure using the Hall effect.

The resistivity appears to remain stable between 50-160 nm whereupon it falls until 400 nm, the trend suggests this decrease will continue past 400 nm. This decrease is driven predominantly by an increase in charge carrier concentration although there is a small increase in charge mobility. This suggests that charge carrier concentration is greater in the bulk than on the surface. This is attributed to charge trapping states such as oxygen desorbed to the surface.

The slight increase to charge mobility is attributed to the increase in crystallite size. The charge mobility is believed to be limited by grain boundary scattering thus the small increase in grain size may give the small rise in charge mobility observed.

The increase in band gap does not coincide with increases in the charge carrier concentration, conversely the rise in band gap is seen when the charge carrier concentration is level and vice versa. It is possible that band gap narrowing effect dominates the Burstein-Moss effect in this system

4.2.3.5 Conclusion

It is clear to see that thickness has a profound effect on the structural and optoelectronic properties of ZnO. In the future experiments efforts will be made to examine films of comparable thicknesses.

4.2.4 Hotplate temperature

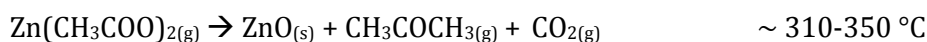
The hotplate temperature (and as such substrate temperature) has a great effect on the size of droplet as it reaches the substrate. This parameter has the largest influence on evaporation rate as it dictates the free-energy of particles involved in film growth. Temperature therefore plays a role in the direction and speed of crystal growth.

The decomposition route to ZnO from zinc acetate dihydrate, based upon TGA and DTG studies, is shown below. [107], [128]



Synthesis route 1

Or



Synthesis route 2

Or



Synthesis route 3

The exact decomposition pathway depends on the pH of the solution and the humidity of the deposition environment. In low humidity conditions Synthesis route 3 would be less likely. This is because there are less free H₂O molecules available for the first stage of the reaction. In acid conditions (pH < 4) Synthesis route 1 is less likely. This is because the equilibrium of the first stage would be pushed to the left, lessening the production of basic zinc acetate.

It's important to note that this analysis makes the assumption that TGA and DTG data is representative of reactions occurring in the aerosol deposition. In-situ studies into the thermodynamics and kinetics of the deposition from droplet would help divulge the strength of this assumption.

The effect of substrate temperature was the subject of early studies by Krunk *et al.* [113] In this investigation ZnO is deposited from 0.2 M zinc acetate from an H₂O:IPA solution at temperatures ranging from 200 – 425 °C. This work showed that the crystalline growth is highly dependent on this factor with a switch in preferential orientation from the (100) to (002) dominance occurring between 275 and 350 °C. Films in this report were 500 – 1000 nm thick.

Ma *et al* used ultrasonic SP to perform a similar investigation. Using 0.01 M zinc acetate in methanol as a precursor, a similar switch in orientation between 350 – 400 °C in 150 nm films was observed. [129] This shift in orientation has been observed in many reports; the exact temperature of the depends on the specific setup of each system. [79], [130], [131] In some reports, particularly when using H₂O as the precursor solvent, this point was not reached [132]–[134].

The onset of the (002) dominance has been linked to the lower surface energy of the orientation; [130] it is unlikely that this only factor since the onset temperature varies from report to report. It has been suggested that at higher growth temperatures the films are more porous allowing more random growth. [111] It is expected that the 'deposition pathway' the droplet follows also plays a significant role in this process.

The optical properties of Krunk's films were shown to improve with increasing temperature. A transmittance of < 30 % was observed in films grown at 200 °C whilst, up to > 90 % was observed in films grown at 425 °C. Good optical properties at lower growth temperatures have been realised (> 85 % at 300 °C), [135] however, the optical quality of has not been greatly improved upon the last 20 years. An optical transmittance of > 90% is suitable for most applications of TCOs so research has been mostly directed toward improving the material's conductivity.

Jauarez *et al* showed the effect of substrate temperature on the resistivity. In this report ~200 nm ZnO films were deposited at 325-500 °C. [40] A steady decrease in resistivity was seen between 325-425 °C, falling from 10⁵ Ω.cm to a minimum of ~10² Ω.cm. Above 425 °C the resistivity began to increase, reaching 10³ Ω.cm at 500 °C. The origin of this decrease is, however, not explained.

These results were confirmed by Tokumoto *et al* in films of ~400 nm thickness deposited at 300, 400 and 450 °C. A steady decrease in resistivity was observed - from 10¹² Ω.cm at 300 °C to 7 Ω.cm at 450 °C. This study did not continue to 500 °C and also did not explain the origin for the lower resistivity.

Studies by Zahedi *et al* saw the same decrease in resistivity - from immeasurably high at 200 and 300°C to $\sim 2 \Omega \cdot \text{cm}$ at 400, 450 and 500 °C. [130] Unlike previous reports, an increase was not seen at high temperatures, however, a large reduction in film thickness was seen between 400 – 500 °C which may have altered the films properties. An increase in crystallite size from 40-50 nm was also observed from 400 – 450 °C.

Vent *et al* showed that the optimum resistivity of 425-450 °C is equally true when films were doped. [136] In was used as a dopant; the optimum temperature of 450 °C was linked to the grain size and film thickness. A study using Hall effect measurement showed this decrease was driven by increase both in charge mobility and charge carrier concentration. The crystallite size was seen to increase from 25 – 32 nm between 400 - 450 °C in agreement with work by Zahedi *et al*. It was suggested that this increase was responsible for the observed increase in Hall charge mobility (from 10 to 15 $\text{cm}^2/\text{V}\cdot\text{s}$). After 450 °C the increase in resistivity is suggested to be driven by decreases in crystallite size (32-25 nm) and thickness (700-500 nm).

4.2.5 Nozzle height

The distance between substrate and nozzle affects the time it takes for the droplets to reach the substrate and thus the length of time the droplets are heated for and the temperature gradient the droplets experience between the nozzle and substrate. This parameter is heavily linked to the hotplate temperature and also the carrier gas pressure (described in the following section), thus, is often not studied specifically. Many articles, instead, mention an optimum value used in their work. One report by Ambia *et al* did, however, show how there is a near linear relationship between the nozzle height and film thickness. [137]. In ultrasonic SP, values typical values are in the range of 1-5 cm; [108],[123] whilst, in pneumatic SP values are typical values are greater, in the range of 20-30 cm. [115],[132],[138]

4.2.6 Carrier gas pressure

The carrier gas pressure is linked with two variables contributing opposing effects on the droplet evaporation pathway. At higher pressures of carrier gas the droplet size is decreased, [139] however the velocity at which the droplets travel increases. The droplet pathway is also linked with the nozzle height and substrate temperature. Typical values in pneumatic SP are quoted are 2- 3 bar. [135], [140]-[142]

4.2.7 Hotplate temperature, Nozzle height and Carrier gas pressure experiments

The three parameters (hotplate temperature, nozzle height and gas pressure) all have an influence on the mechanism the droplets undergo in the deposition process, therefore, the optimum substrate temperature at a pressure of 1 bar and nozzle height of 20 cm may not be optimum at two bar or 15 cm. The parameters were studied in parallel so all variations could be explored.

Hotplate temperatures of 300, 400 and 500 °C were investigated to optimise the spray system used in this work. The upper limit of 500 °C was chosen as, according to literature, films did not show improved properties past this value. 300 °C was chosen as the lower limit – below this temperature it is expected the zinc acetate will not fully decompose.

Distances from 15, 18 and 21 cm were studied, 15 and 21 cm acted as practical upper and lower limits of the automated spray rig.

Gas pressures of 1, 2 and 3 bar were investigated. The pressure was limited to 3 bar by the spray gun specifications and below 1 bar deposition rate was seen to be impractically low.

Films were deposited at all combinations of these three parameters so that 27 different conditions were investigated and the optimum parameters settings could be identified.

Other parameters were fixed, as described in Table 4. 3.

CG	St	PC (M)	PL (s)	SoP (s/p)	Cy	NS (mm)
N ₂	Soda lime	0.1	25	5	3-5	0.2

Table 4. 3 – Fixed parameters in hotplate temperature, nozzle height and gas pressure studies

Attempts were made to achieve films of comparable thickness. This was difficult to achieve exactly, however, by varying the number of cycles for each temperature (300 °C: 3 cycles; 400 °C: 4 cycles; 500 °C: 5 cycles) the thickness could be restricted to 175 nm ± 50 nm.

The hotplate set temperature was recorded with an IR gun during the deposition process. It was found the substrate temperature was lower than the hotplate temperature. The hotplate thermocouple also was slow to detect temperature change; using the IR gun it was found that the temperature was cooled by up to 20 °C from the start of the cycle to the end (when the temperature was restored). The substrate temperature was found to be 290, 380 and 460 °C for the 300, 400 and 500 °C set temperatures respectively.

The thickness, structural, optical and electronic properties of each film was studied. How conditions affect each parameter, and how they may be linked, is covered in the sections below.

4.2.7.1 Thickness measurements

The thicknesses of the ZnO samples are shown in Figure 4. 9. It was seen that samples deposited at $D = 15$ cm samples and $CGP = 3$ bar, were significantly lower in thickness than other samples. In these samples it is believed that the droplet velocity was too great and particles were carried away from the substrate without deposition. This is backed up by the slight increase in thickness seen in the 460 °C sample where the speed of vapourisation would be increased.

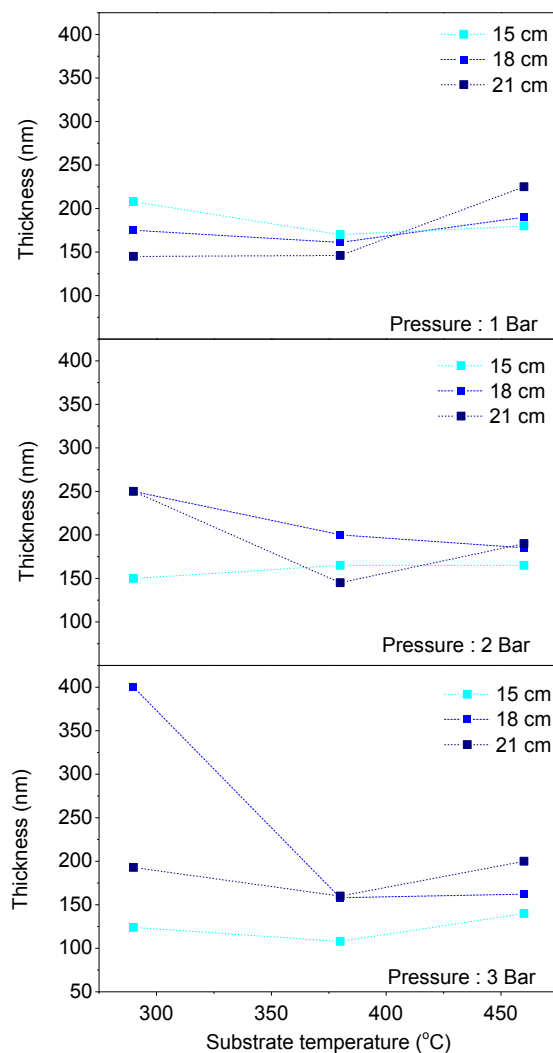


Figure 4. 9 - Thicknesses analysis from temperature, gas pressure and nozzle height optimisation experiments. Top, middle and bottom show pressures 1, 2 and 3 bar respectively, substrate temperature is found on the x-axis and which each chart showing nozzle height in different colours with 15, 18 and 21 cm indicated by cyan, blue and navy respectively. This notation will be used for all figures in this section unless otherwise stated.

The sample grown at “St: 290 °C | D: 18 cm | CGP: 3 bar” is anomalously thick, the cause of the error in this sample not known. There are some thermophoretic effects seen particularly in the films grown at 380 °C, 1 and 2 bar; with 18 cm often resulting in thicker films than the 21 cm. This is expected as the greater distance would likely result in smaller droplets more likely to be carried away by thermophoretic currents. Whilst the point will be including in analysis following this, any conclusions take the increased thickness into account. There is also some minor variation in the thicknesses of other samples which should be considered when analysing the results.

4.2.7.2 Structural analysis

Structural information on the films was obtained using XRD, the full dataset of the twenty seven diffraction patterns can be found in the Appendix (section A.2). The texture of the films could be quantified using the texture coefficient, as described in section 2.3.2 and shown in Figure 4. 10.

The substrate temperature has a great influence on the texturing of the films. Films grown at 290 °C show similar texturing even with different pressure and heights. The same is true for films grown at 380 and 460 °C although some subtle change to texturing is seen.

In samples deposited at 'St: 290 °C', films show texturing towards the (100) and (110) orientations; the (002) orientation is usually not present. Only small changes are seen in texturing as the nozzle height and carrier gas pressure are varied in films grown at this temperature. The presence of the (100) and (110) are believed to be linked to droplets undergoing pathways one and two. This is because their intensity diminishes at higher temperatures.

Films growth at 'St: 380 °C' are mostly randomly orientated, however, there is some texturing towards the (100) orientation. The (102) and (103) orientations do not feature. Given that these are low intensity orientations in a powder sample, it may be that the peaks were merely too small for analysis. The (002) peak shows significant variation in texturing. Both nozzle height and pressure have a significant influence on the texture of the deposited films. This emergence of the (002) orientation is believed to be linked to the deposition method; the lowest surface energy orientation growing as a result of droplets undergoing pathway three. Indeed, at this temperature (slightly lower than the literature optimum (~400 °C)), films grown from 'D: 15 cm' show the lowest (002) texture. This improves as the nozzle height increases. This is consistent with the theory; as droplets would have longer to vapourise in the 'D: 21 cm' samples, thus at the lower temperature, this would be expected to increase the (002) texture.

With six orientations considered, a film entirely showing one orientation would have a texture coefficient of six with all other values being zero. A texture coefficient of one indicates a randomly oriented film. Below one indicates an unfavoured orientation.

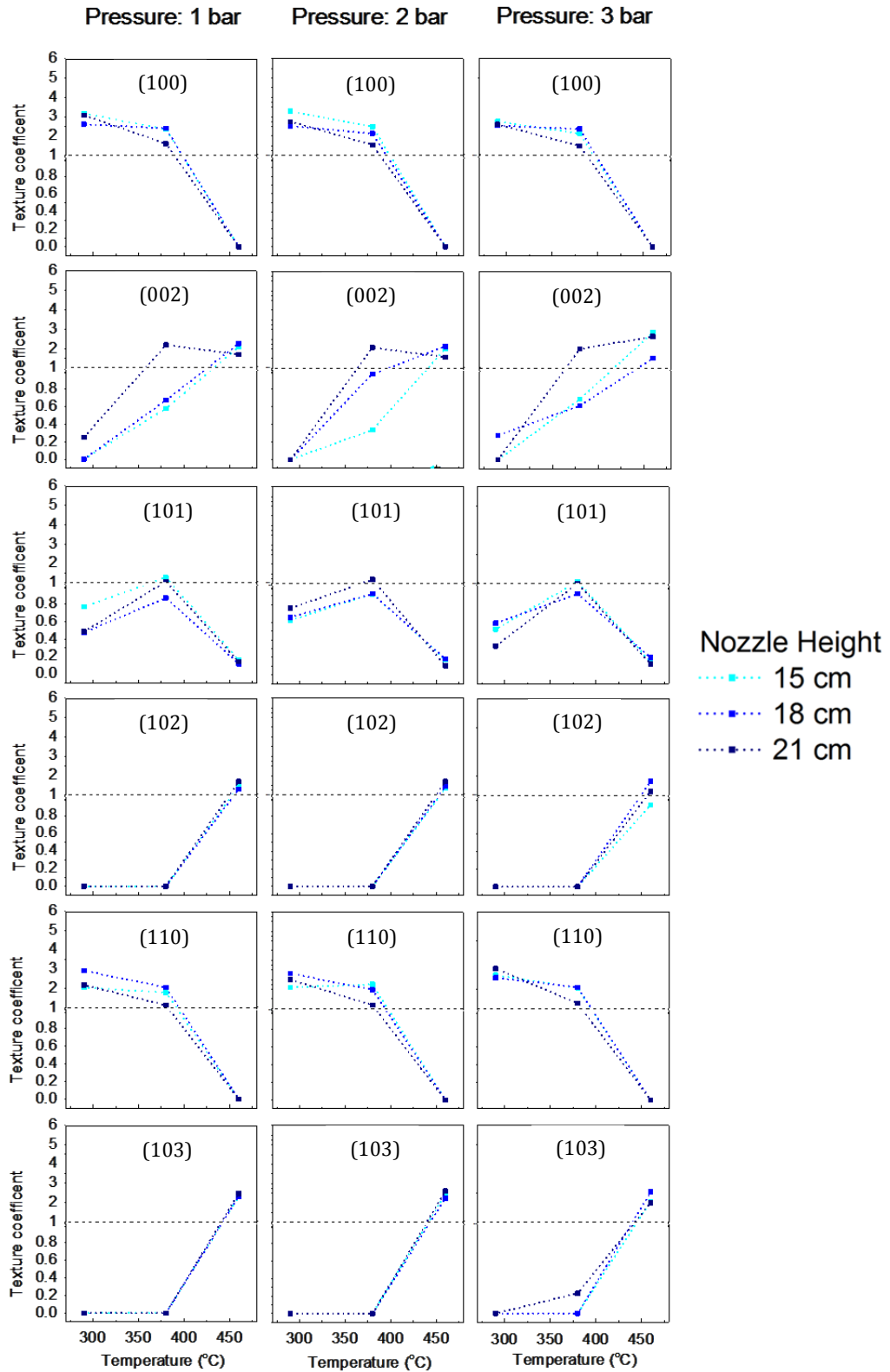


Figure 4. 10 – Texture coefficients of different crystal orientations (top to bottom - (100), (002), (101), (102), (110) and (103)) for ZnO films from temperature, nozzle size and height optimisation experiments. In this case pressures of 1,2 and 3 bars are displayed from left to right. A texture of 1 indicates zero texturing highlighted by dashed line.

In films grown at 'St: 460 °C' the (100), (101) and (110) orientations disappear. This suggests that the majority of droplets fully evaporate before the surface. The emergence of the (102) and (103) peaks suggest these growth directions are linked with droplets following pathway four. It is also possible that these orientations are enabled purely by the higher temperature. The lack of difference in height and pressure variation suggests that the later may be more likely. The (002) still shows equal preferential growth suggesting a proportion of droplets are still undergoing pathway three.

Increased gas pressure acts in two ways upon the droplets, both reducing the size pushing towards pathway four, and increasing velocity pushing towards pathway one. These factors may often be of equal importance, thus, cancelling each other. This would explain how trends are similar at most pressures variations.

Films with the greatest texturing towards the (002) orientation were found using the following parameters:

- St: 380 °C | D: 21 cm | CGP: 1 bar
- St: 380 °C | D: 21 cm | CGP: 2 bar
- St: 460 °C | D: 15 cm | CGP: 2 bar
- St: 460 °C | D: 18 cm | CGP: 2 bar
- St: 460 °C | D: 21 cm | CGP: 3 bar

From analysis of the texturing of the film it is believed that these conditions are optimum for deposition via pathway three.

The crystallite size of all films were calculated using the Scherrer equation using the (101) orientation, the only peak present in all films. Results are shown in Figure 4. 11. The average crystallite size ranges from ~ 3 – 60 nm. There is a clear trend of increased crystallite size with temperature. This is likely driven by the increased crystallinity of films caused by the higher temperatures.

In general the distance from nozzle to substrate only has a small influence. Pressure plays a role in at 'St: 460 °C', where the crystallite size is reduced in the 'CGP: 3 bar' films. The greatest crystallite size is seen in 'St: 460 °C | D: 18 cm | CGP: 1 bar' sample.

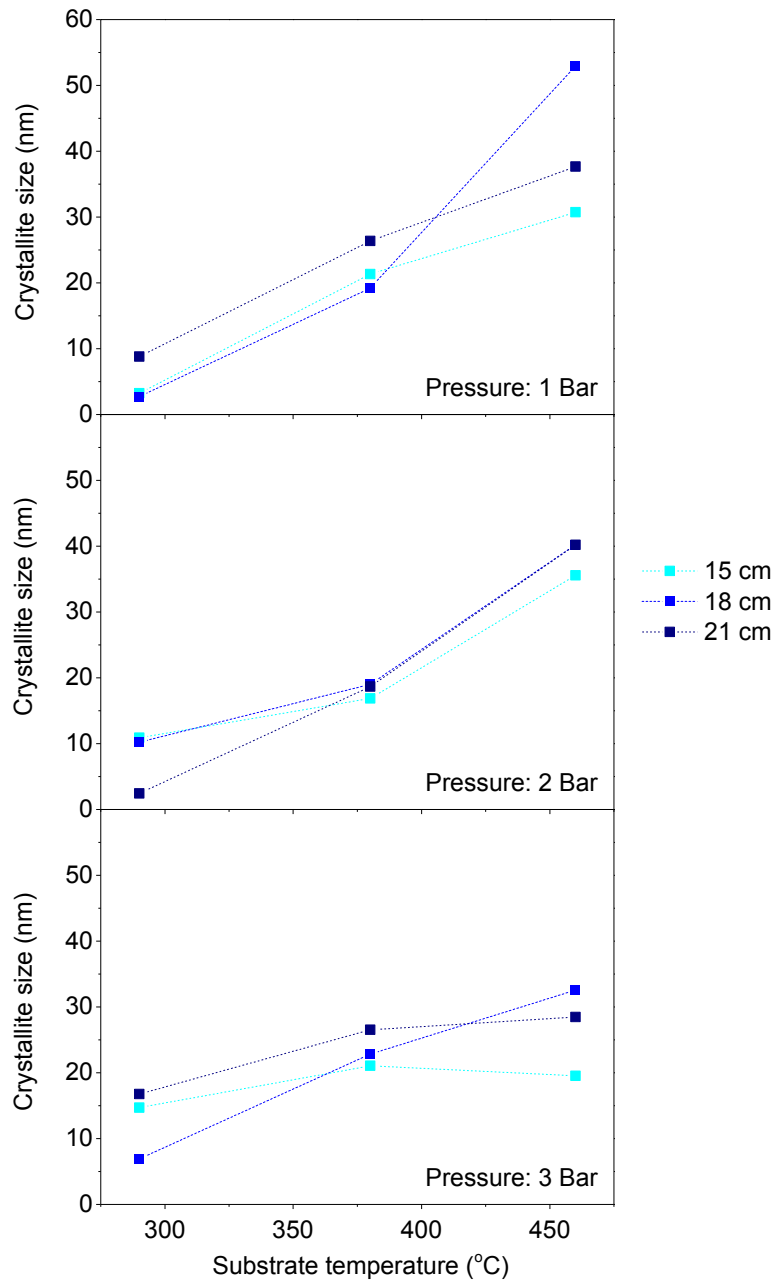


Figure 4. 11 - The crystallite sizes derived from $d_{(101)}$ from temperature, gas pressure and nozzle height optimisation.

4.2.7.3 Optical analysis

The transparency of the films was also measured using UV-Vis spectroscopy. The average transmittance of the films was calculated between 400-900 nm (excluding the fundamental absorption of ZnO at ~ 360 nm). These are shown for all conditions in Figure 4. 12.

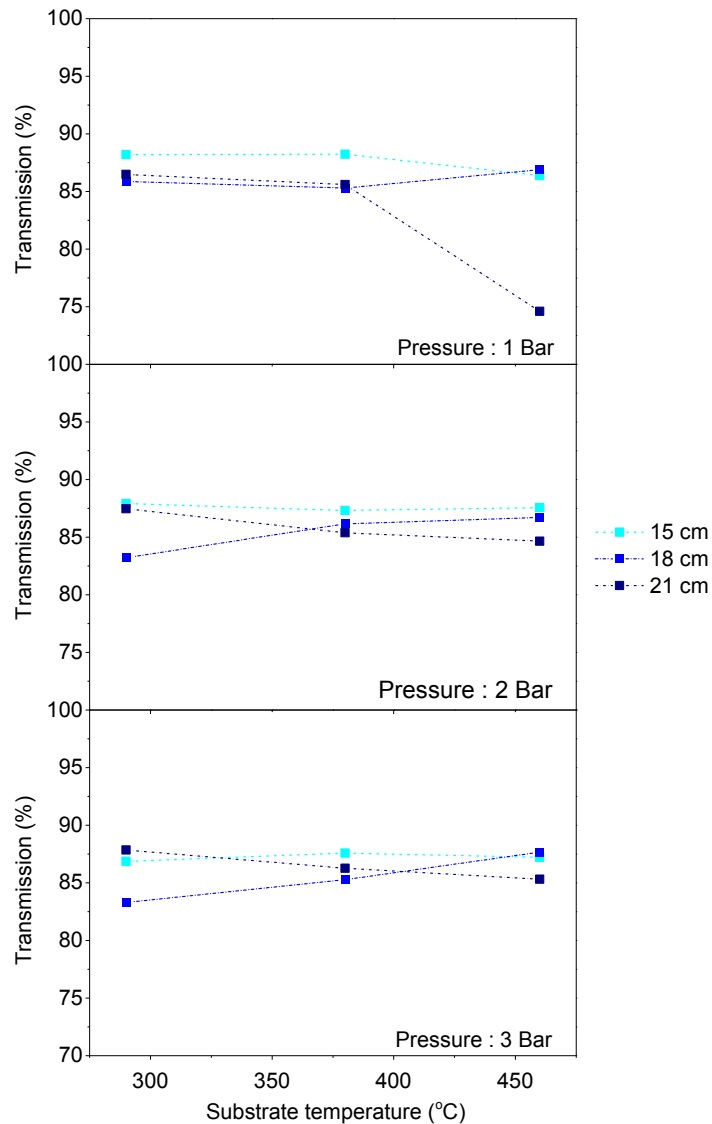


Figure 4. 12 - The average transmission from temperature, gas pressure and nozzle height optimisation experiments. The average transmission was taken to negate the influence of interference fringes and between 400 – 900 nm to avoid the fundamental absorption of ZnO found at ~360 nm.

There are no global trends seen in the transmittance data, the films show excellent transparency to visible light excluding the sample deposited at ‘St: 500 °C | D: 21 cm | CGP: 1 bar’. These conditions were mostly likely to promote droplets to undergo pathway four, causing non-transparent particulates to impact on the surface. In low concentrations, these particles are likely to be carried from the substrate by the carrier gas, however, at high concentrations some particles are likely to adhere to the surface. These would act to lower the transmittance of the film.

The anomalously thick films at 'St: 300 °C | D: 18 cm | CGP: 3 bar' shows slightly decreased transmittance. This is to be expected due to the unexpectedly high thickness in this sample.

4.2.7.4 Analysis of electronic properties

The electronic properties of the films were studied using AC Hall effect measurements (Figure 4. 13). This technique allows the splitting of the resistivity into the charge carrier concentration and charge mobility components as discussed in section 2.4.3. Detailed work on the electronic properties of native ZnO deposited in atmospheric conditions are mostly unreported in literature owing to its high resistivity. These measurements are made possible by using an AC field Hall measurements (described in 2.4.3.2), however, this means that there are few literature results for comparison.

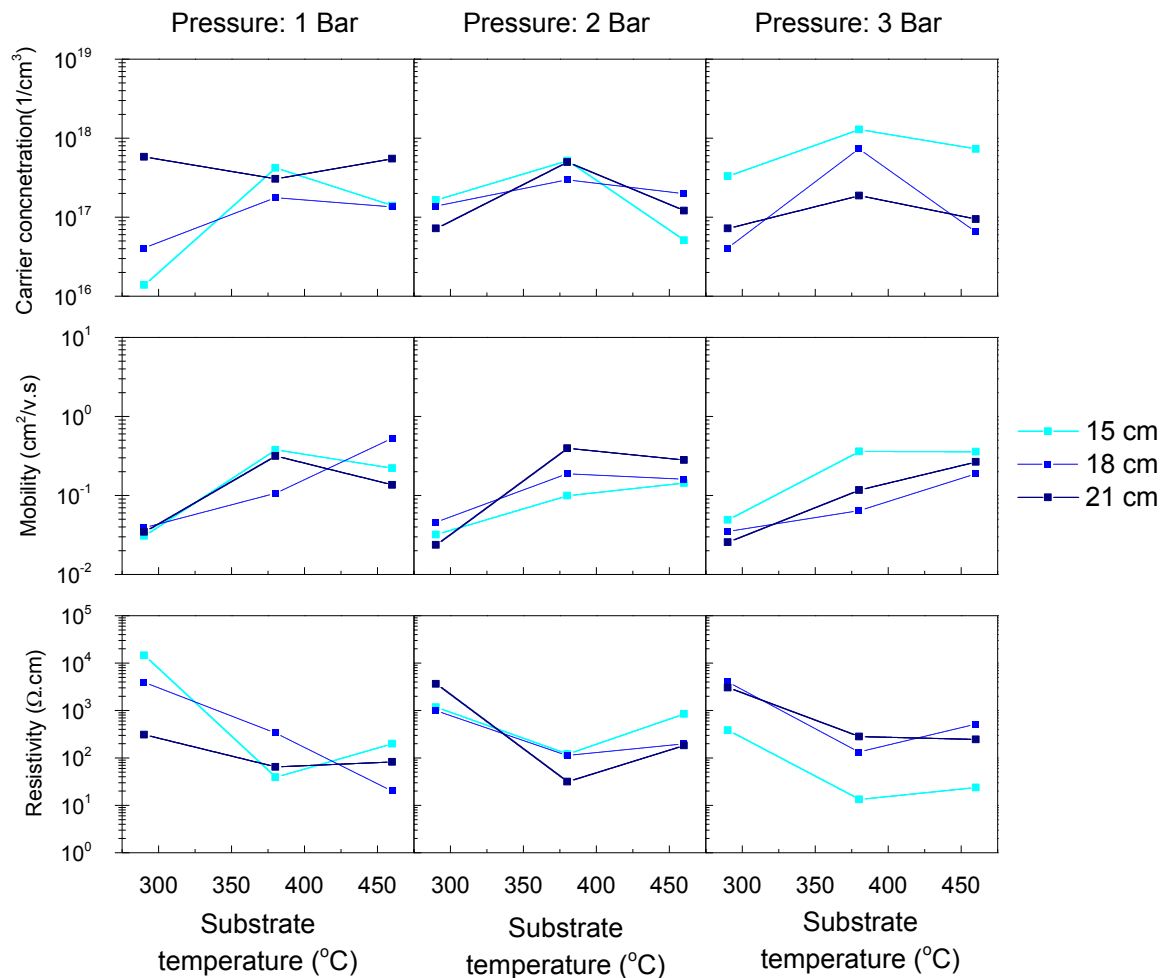


Figure 4. 13 - AC Hall effect measurements temperature, gas pressure and nozzle height optimisation experiments. Charge carrier concentration, charge mobility and resistivity as shown (top to bottom), pressure of 1, 2 and 3 bar are displayed (left to right)

The substrate temperature has the greatest effect on resistivity. Films deposited at ‘St: 290 °C’ generally display significantly higher resistivities than those grown at higher temperatures; this is driven by increased charge mobility across all samples. This is believed to be linked to the increase in crystallite size, as seen in Figure 4. 11. Smaller grains suggest an increase in grain boundaries, thus, an increase in grain boundary scattering. This scattering mechanism would be expected to be prominent in the small grain sizes, such as those seen in ‘St: 290 °C’ samples. The low charge carrier concentrations suggest that ionised impurity scattering would not be influential. When the crystallite size is plotted against the charge mobility, a possible relationship can be discerned ($R^2:0.54$ shown in Figure 4. 14.), supporting this theory.

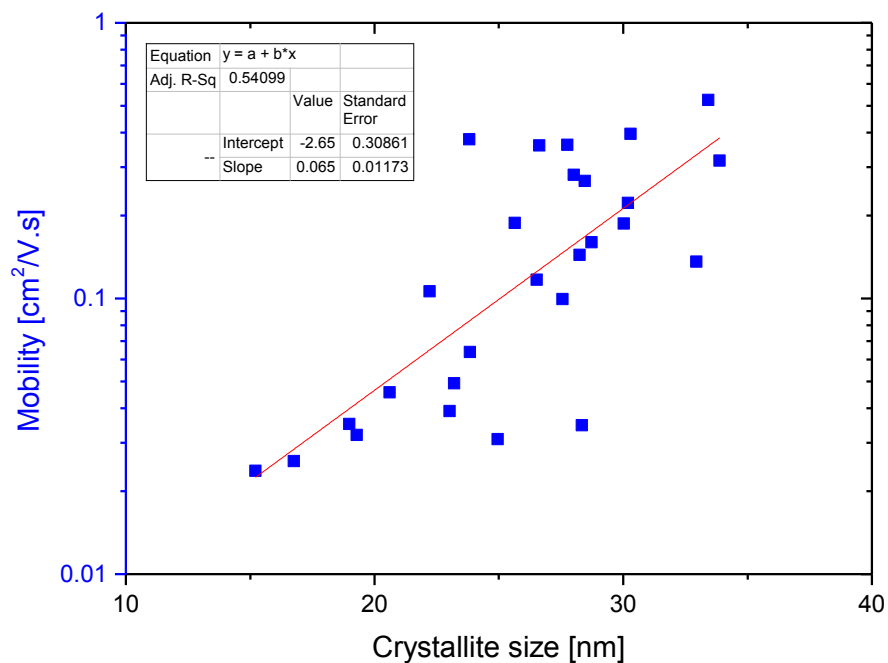


Figure 4. 14 – The crystallite size plotted against the charge mobility from temperature, gas pressure and nozzle height optimisation.

Films deposited at 'St: 380 °C' show the lowest resistivity values with the exception of the 'D: 18 cm | CGP: 1 bar sample'. When the temperature was increased to 'St: 460 °C' the resistivity is seen to increase. This is driven by a decrease in charge carrier concentration which occurs in all samples, with the exception of the 'D: 21 cm | CGP: 1 bar' sample. Studying structural properties of the films grown at 'St: 380 and 460 °C' there were no trends to explain the decrease in charge carrier concentration. Therefore, it follows that this decrease not due to structural changes and, instead, the result of variations in the intrinsic defect chemistry.

It reasonable to deduce that the films deposited at 380 °C have an increased level of n-type intrinsic defects compared with those grown at 460 °C. This may be caused by reduced surface free energy during deposition. This would result in atoms directed to the local energy minima associated with defect states in the ZnO lattice. An increased level of defect states such as Zn_i or V_o would lead to these observations. Another possibility is that the increased temperature allows the migration of atoms within the lattice; this would lead to the compensation or elimination of defects.

4.2.7.4.1 Figure of merit (FOM)

A figure of merit was used to find the most desirable film for use as a TCO in terms of transparency and conductivity. Calculated by ' T^{10}/Rs ', it balances the importance of transmittance and resistivity equally. It impacts heavily on films which fall outside of the values of each require for use in application. This method was originally proposed by Haacke *et al.* [143] The figure of merit for the samples are shown in Figure 4. 15.

The observed FOM values are low, this is because native ZnO films are typically well below the required conductivity for TCO applications. Using this method, however, it becomes possible to compare samples taking both transparency and resistivity into account.

The most promising conditions are seen at:

- St: 380 °C | D: 15 cm | CGP: 1 bar (~175 nm)
- St: 380 °C | D: 21 cm | CGP: 2 bar (~145 nm)
- St: 380 °C | D: 15 cm | CGP: 3 bar (~120 nm)
- St: 460 °C | D: 15 cm | CGP: 3 bar (~140 nm)

Lower temperature conditions are desirable in terms of industrial processing thus the 460 °C was excluded. The higher deposition rate and reduced carrier gas consumption led to the parameters: 380 °C – 15 cm – 1 bar to be carried forward in further study of ZnO films.

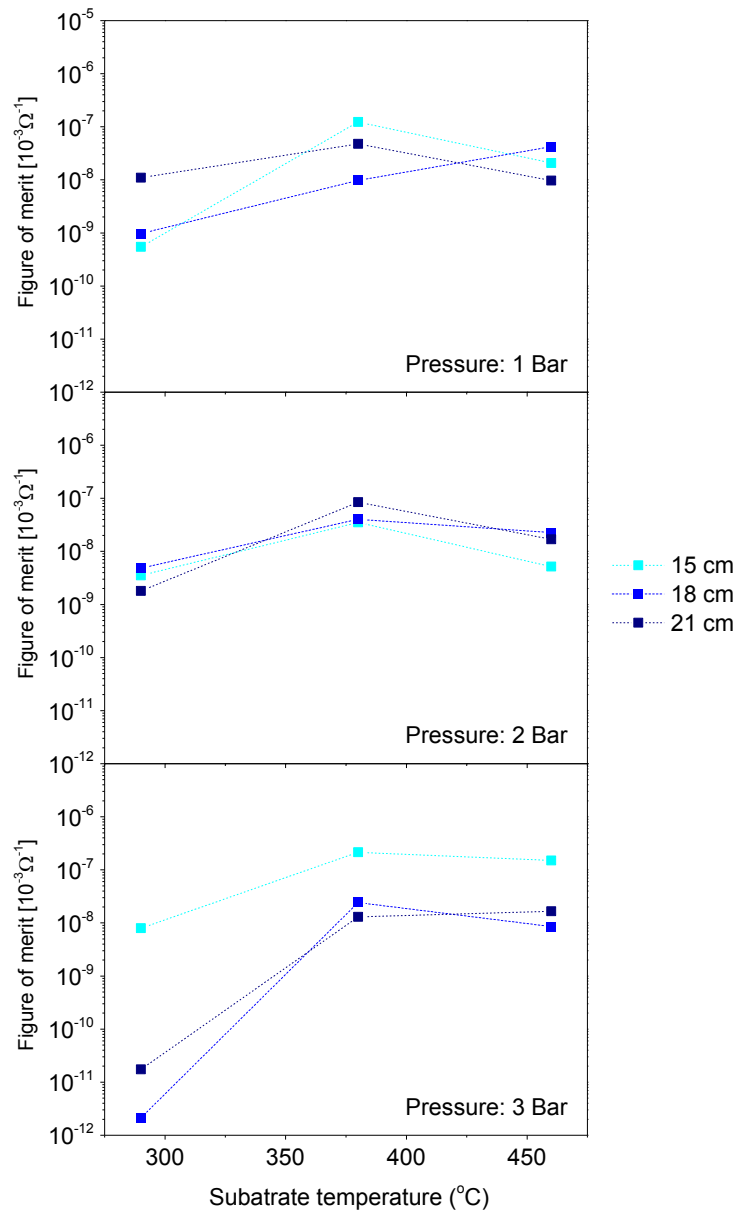


Figure 4. 15 – Figure of merit for TCO applications from temperature, gas pressure and nozzle height optimisation experiments.

4.2.8 Precursor concentration

The concentration of precursor solution affects the deposition rate. The part it may play (if any) in which pathway the droplet undergoes is not obvious. However, each droplet is likely produce a larger amount of precipitate and the deposition rate will be heavily influenced.

van Heerden *et al* studied the structural properties of films deposited from zinc acetate precursor concentrations of 0.05, 0.2 and 0.4 M at a substrate temperature of 420 °C. [131] Films were all shown to have a (002) texturing; this was more intense in the lowest concentration sample. This report, like others studying the concentration, saw large changes in film thickness when the concentration was varied. This made it difficult to make decisive conclusions on the effect of purely the concentration. (see section 4.2.7.1)

Tarwal *et al* suffered similar problems showing the structural, morphological and optical effects of precursors concentrations of 0.1, 0.2, 0.3 and 0.4 M. [138] In this report the thickness increased from 300 – 900 nm over the concentration range. Contrary to van Heerden's findings greater (002) texturing was seen in the higher molarity samples. Roughness was seen to increase in the higher concentration films although this would be expected with increasing thickness. The optical transmittance was also seen to be lower in the thicker, higher concentration films.

Other reports show similar (002) texturing increases and optical transmittance decreases with increasing concentration. However, in all these reports, thickness remains an issue. One such report studies precursor concentration between 0.05-0.15 M in 0.025 M steps (thickness 100-400 nm). [144] Hall effect measurements (experimental parameters not specified) were conducted; the lowest resistivities were seen in the 0.1 M samples. This decrease was driven by variations in charge mobility; the charge carrier concentration, however, was seen to be stable. Variable thickness was found to cause uncertainty in their low concentration samples. The report also suggests that high resistivity in their high precursor concentrations is linked with failure of the precursor salt to fully decompose during deposition. This claim, however, is unsubstantiated in the report. In a later report, films were deposited from 0.05, 0.1 and 0.15 M solutions. [145] Films were claimed to have equal thickness of ~230 nm, although, perhaps this is questionable as all other parameters are said to be equal. From XRD, crystallite sizes are found to be ~78 nm in at all concentrations with the films switching from a (101) to a (002) texture from 0.05 – 0.1 M.

4.2.9 Precursor concentration experiments

In this experiment, the precursor concentration was set to: 0.05, 0.1, 0.2 and 0.4 M. Other parameters were set as described in Table 4. 4.

CG	HT (°C)	D	CGP (bar)	St	PL (s)	SoP (s/p)	Cy	NS (mm)
N ₂	380	15	1	Soda lime	25	5	1-7	0.2

Table 4. 4 – Experimental parameters for precursor concentration investigation

The thickness, structural, optical and electronic properties of each film was studied. How conditions affect each parameter, and how they may be linked, is covered in the sections below.

4.2.9.1 Thickness tests

A thickness trend was carried out so that structural and electrical properties of comparable films could be investigated (Figure 4. 16). Linear cycles to thickness trends are seen at all concentrations.

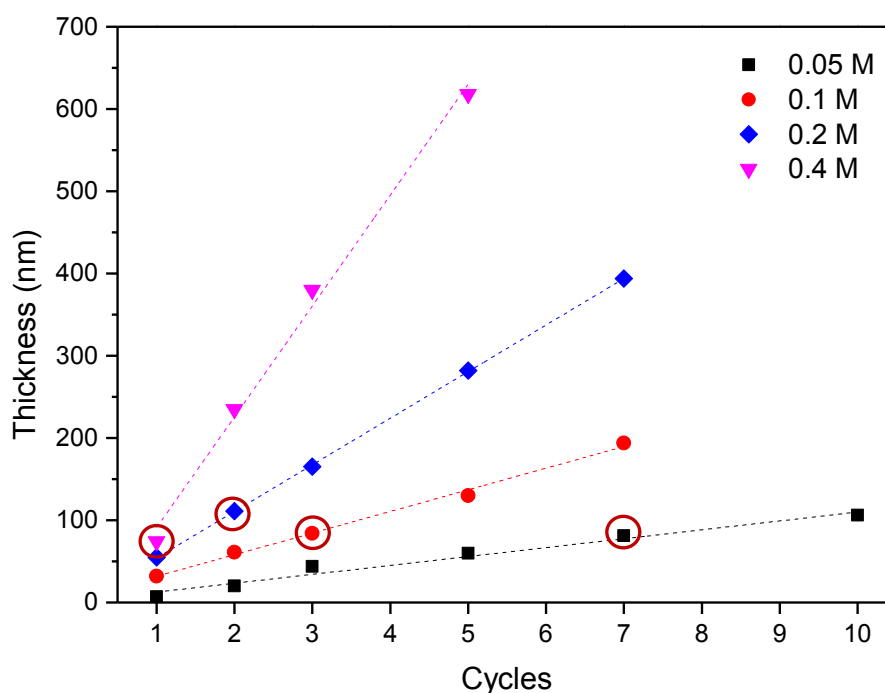


Figure 4. 16 – Thickness trends in precursor concentration experiment. Zinc acetate concentration was set to 0.05, 0.1, 0.2 and 0.4 M and films were deposited for 1-10 spray cycles. Circled points indicate samples of comparable thickness used for further study.

Films circled in Figure 4. 16 were seen to have comparable thickness. Films grown from 0.1, 0.2 and 0.4 M solutions were maintained at the set temperature on the hotplate post deposition so that all films received the same level of annealing. The aim of this was to mitigate potential differences arising from the different deposition times.

4.2.9.2 Structural Analysis

XRD analysis was performed on all films; a full XRD dataset is shown in Appendix (section A.3). XRD data of films with comparable thickness are shown in Figure 4. 17.

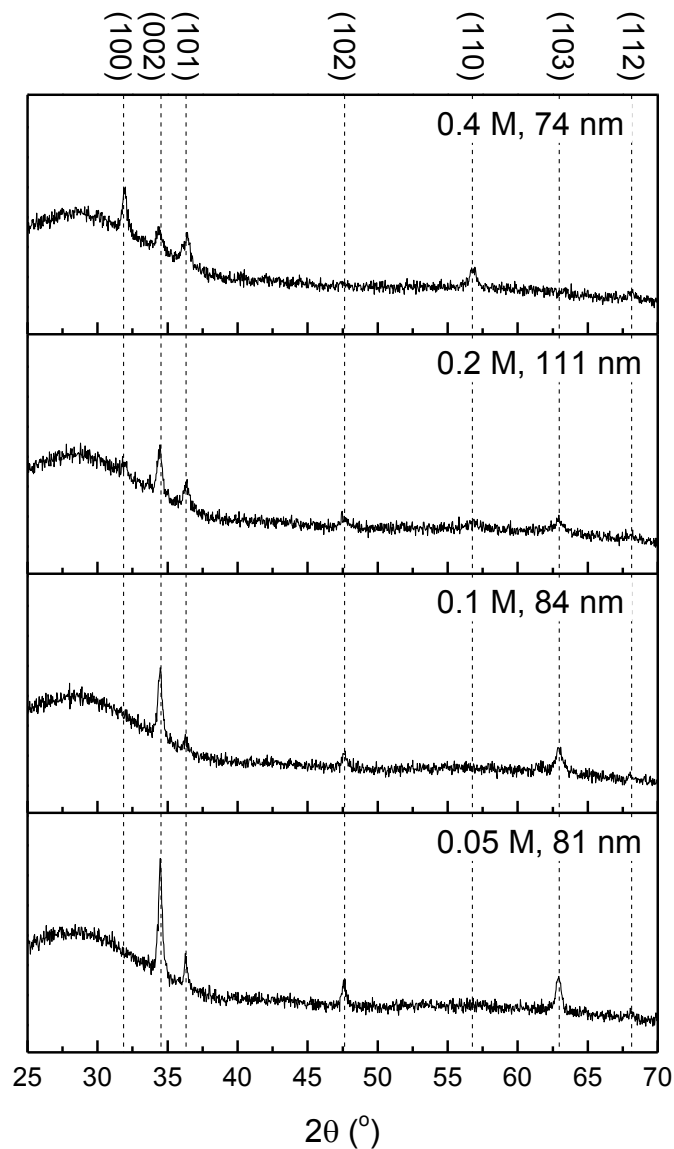


Figure 4. 17 – XRD patterns of comparable thickness ZnO films from precursor concentration experiments.

Texture coefficients of the different orientations were extracted from the XRD patterns shown in Figure 4. 18. A decrease in (002) texturing is seen as the precursor concentration is increased. This is coupled with an increase in the (100) and (101) orientation. Increased (002) texturing in lower concentration samples agrees with the findings of van Heerden *et al* [131] and disagrees with those by Shinde *et al* [144] and Tarwal *et al*. [138] The results presented from this work, however, are not comparable as the (100) is not seen in previous studies. These samples show a texturing shift from the (101) to (002) orientation as concentration is decreased.

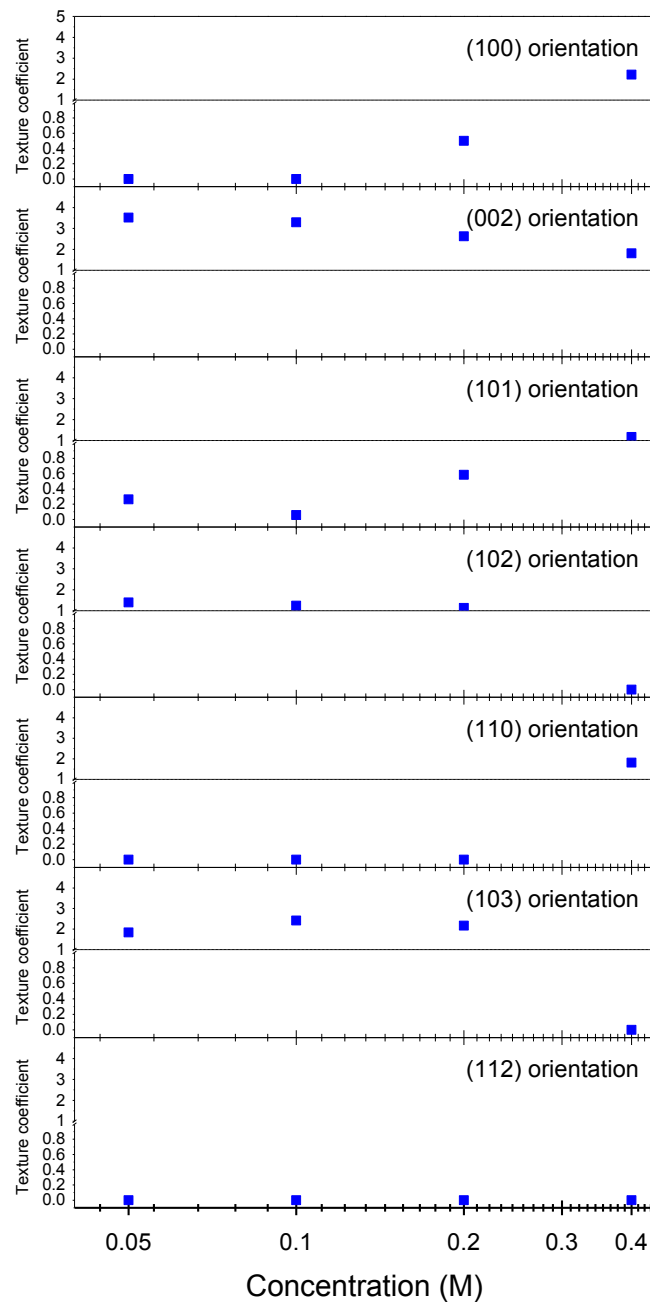


Figure 4. 18 – Texture coefficient from precursor concentration experiment

The droplet pathways are likely to be similar; this is because the parameters which are believed to affect the pathway are fixed. The difference is the amount of the precipitate left when the solvent has been removed. This could mean that the rate of vapourisation of the precipitate is reduced leading to the droplets being driven towards pathway one. There is some evidence for this in the XRD patterns, where films deposited at higher concentrations display similar attributes to those deposited at lower temperatures (in which pathway one/two is believed to be occurring).

Another potential explanation for the observed texturing is the differing deposition rate. Films deposited from higher concentration solutions have much higher deposition rates; the cumulative energy loss as a result of decomposition and crystallisation may result in a lower surface energy. This would also display similar attributes to films deposited at a lower temperature. It is likely that both factors play a role.

In previous studies, the deposition conditions are believed to be drive droplets further towards pathway four. At this extreme, the texturing is believed to randomise away from the (002) orientation. The increased texturing seen at high concentration can also be seen to fit the theory. A shift from pathway four to pathway three with increased concentration would result in this observation.

The crystallite size was extracted from the XRD data (Figure 4. 19). A decrease in crystallite size can be seen from 26.0 nm in the 0.05 M sample to 14.2 nm in the 0.4 M sample. This decrease is not seen in other literature examining, however, previous studies have examined a structurally different set of films. This decrease is likely due to a decrease in crystallinity from the increased deposition rate.

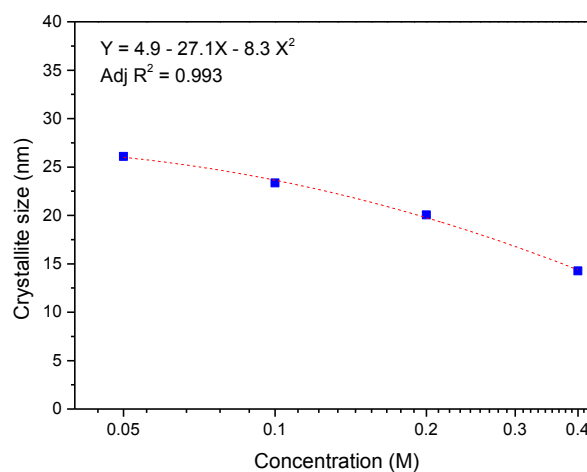


Figure 4. 19 – The crystallite size from precursor concentration experiment calculated using the Scherrer equation from the (002) peak

4.2.9.3 Optical analysis

The optical properties of deposited films were investigated by UV-Vis spectroscopy shown in Figure 4. 20.

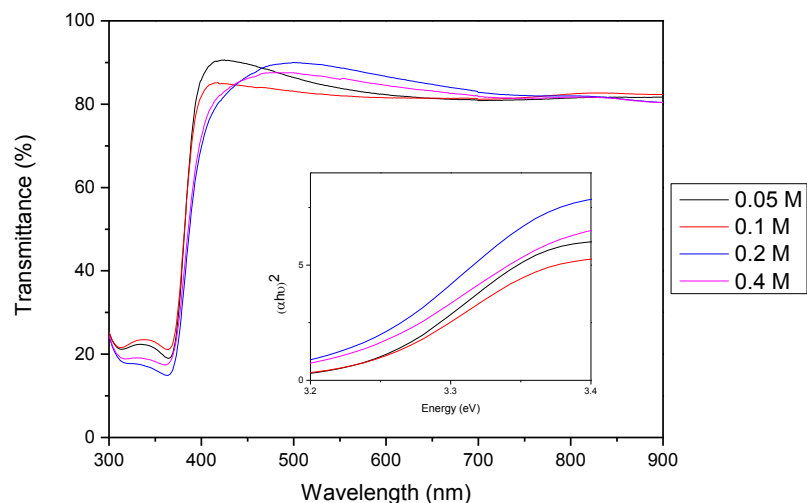


Figure 4. 20 - Optical transmittance of samples with varying precursor concentration. Insert shows Tauc analysis of optical data.

Tauc analysis (Figure 4. 20 – insert) was used to investigate whether thickness had a significant effect on the band gap of the films. Results are displayed in Figure 4. 21.

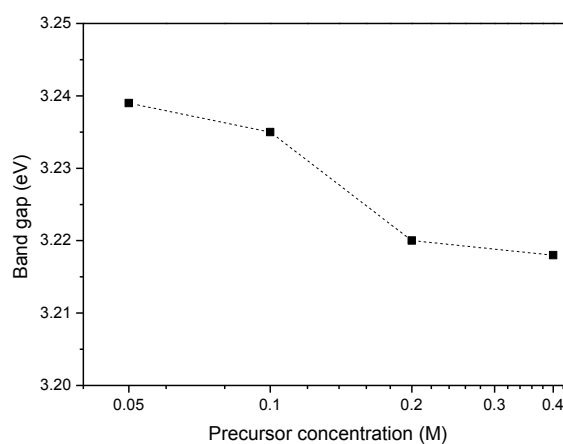


Figure 4. 21 - Varying electronic band gap of ZnO with increasing precursor concentration

The data shows a decrease in the electronic band gap of the ZnO of 0.02 eV between 0.05 and 0.2 M which may be linked to variation in intrinsic defect chemistry within the films.

4.2.9.4 Analysis of electronic properties

The electronic properties of the films were studied using AC Hall effect measurements shown in Figure 4. 22.

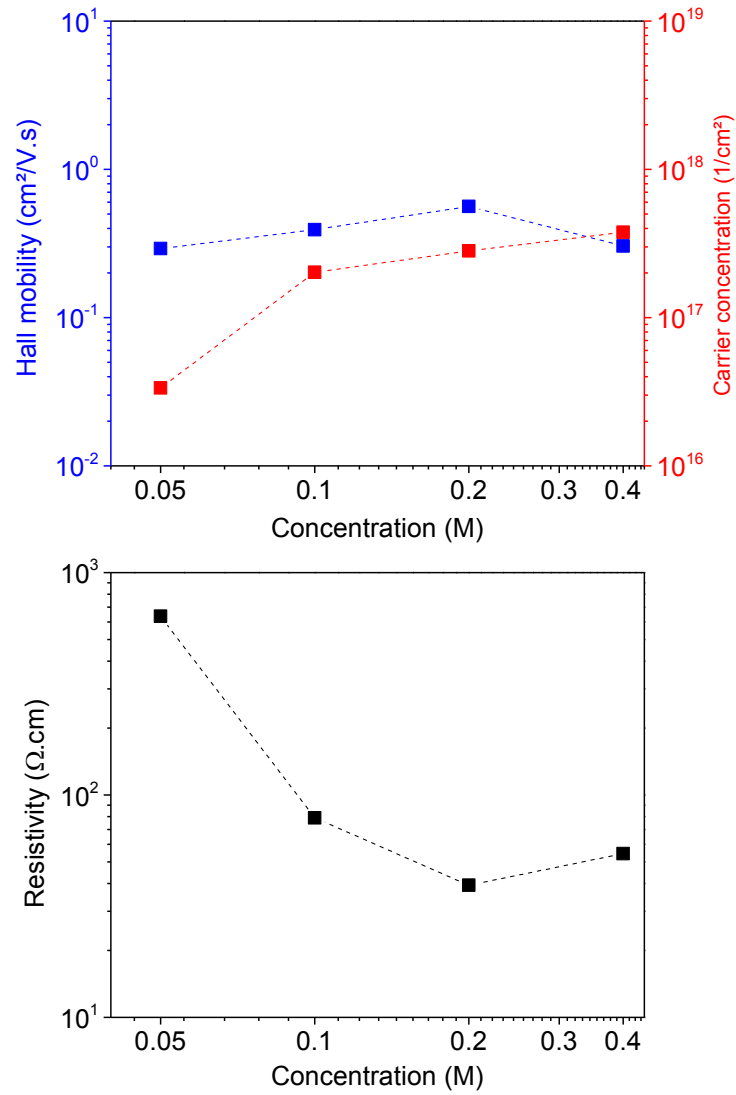


Figure 4. 22 – AC Hall effect measures from precursor concentration experiment

The resistivity is seen to decrease as the precursor concentration increases until 0.2 M whereupon a slight increase is seen. This decrease is driven by an increase in charge carrier concentration of nearly an order of magnitude between 0.05 and 0.1 M, and continuing to increase up until 0.4 M. The charge carrier concentration is linked to the defect chemistry of the material. Films grown more slowly are likely to be more stoichiometric due to the film growth dynamics and plentiful supply of oxygen. As ZnO typically forms n-type defects (V_o and Zn_i), it follows that a more stoichiometric film would be expected to have fewer free carriers. An oxygen rich environment would also reduce the number of charge trapping V_{zn} states again increasing the charge carrier concentration.

Charge mobility is also seen to increase from 0.05 – 0.2 M, despite a decrease in crystallite size (Figure 4. 19). This is consistent with the theory that charge trapping states are reduced as concentration increases. The reduction in charge mobility for the 0.4 M sample may be linked to the changes in structure seen between 0.2 – 0.4 M. A similar structural change however, is seen in nozzle size experiments (section 4.2.11) without an observed decrease in charge mobility. This decrease could instead be linked with the decreased thickness. Indeed a sharp decrease in crystallite size is also observed from ~20 – 15 nm, potentially increasing grain boundary scattering. This results in an increase in resistivity despite the increase in the charge carrier concentration. The sample grown at 0.2 M displays the minimum resistivity.

The decrease in band gap does not coincide with decrease in the charge carrier concentration as would be expected with Burstein-Moss shift. The increase in charge carrier concentration is, conversely, coupled with a decrease in the band gap. Again it may be that band gap narrowing dominates, however, it is also possible that the differences in the scattering from the change in orientation may affect band gap measurement. As ZnO forms a hexagonal, uniaxial crystal, it has different optical vibrational modes on the c-axis than the other two. This means that the refractive index may be slightly altered when the crystallites are preferentially aligned to the (002) orientation. This may result in the observed decrease in the measured band gap. [146] These measurements could be improved by considering the reflectivity when measuring the optical band gap.

4.2.10 Nozzle size

The size of a nozzle is known to affect the droplet size and deposition rate which in turn may influence the film properties. Nozzle diameters of 0.2 mm [147], [148], 0.3 mm, [149] 0.5 mm [150], 1 mm [151], 1.5 mm [152] have been reported in pneumatic SP. However a direct comparison of different nozzle diameters in the same system is yet unreported.

4.2.11 Nozzle size experiments

The nozzle size was investigated at 0.2, 0.35 and 0.5 mm. The nozzle size dictates the flow rate and the size of the droplets produced. Larger nozzle sizes will produce bigger droplets which, in theory, will shift the system towards pathway one.

Other parameters were fixed as described in Table 4. 5, pause length was adjusted for the three different nozzle sizes: 25 s was used for the 0.2 mm diameter nozzle; 30 s was used for the 0.35 mm and 45 s was used for the 0.5 mm nozzle.

CG	HT (°C)	D	CGP (bar)	St	PC (M)	SoP (s/p)	Cy
N ₂	380	15	1	Soda lime	0.1	5	1-4

Table 4. 5 – Fixed parameters in nozzle size experiments

The thickness, structural, optical, topographic and electronic properties of each film was studied. How conditions affect each parameter and how they may be linked is covered in the following sections.

4.2.11.1 Thickness calibration

A thickness trend was measured so that structural and electrical properties of comparable films could be investigated (Figure 4. 23). Linear cycles to thickness trends are seen at all concentrations.

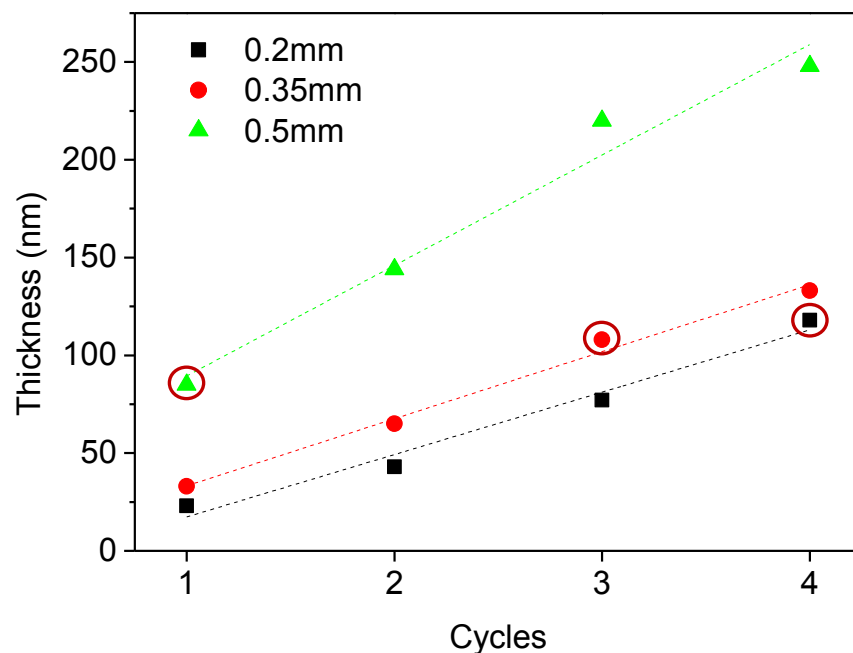


Figure 4. 23 – Thickness trends nozzle size experiment. Nozzle diameters of 0.2, 0.35 and 0.5 mm were used (black squares, red circles, green triangles respectively) and films were deposited for 1-4 spray cycles. Circles indicate films of comparable thickness used in further study.

Samples circled in Figure 4. 23 were seen to have comparable thickness. Films grown from 0.2 mm and 0.35 mm were maintained at the set temperature on the hotplate post deposition so that all films received the same level of annealing, this aim of this was to mitigate potential differences arising from the different deposition times.

4.2.11.2 Structural analysis

XRD analysis was performed on all films; a full XRD dataset is shown in Appendix (section A.4). XRD data of films with comparable thickness are shown in Figure 4. 24.

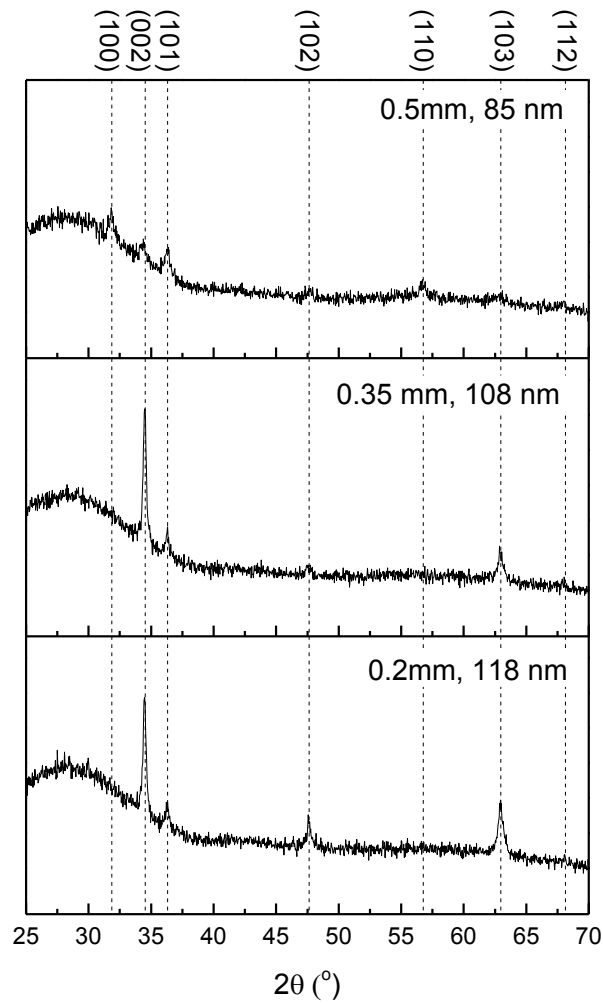


Figure 4. 24 – XRD patterns of comparable thickness ZnO films from nozzle size experiment

Texture coefficients of the different orientations were extracted from the XRD patterns and shown in Figure 4. 25. Films grown using a 0.5 mm nozzle are seen to be randomly orientated, however, when using a 0.35 mm and 0.2 mm nozzles a (002) and (103) texturing is observed. The films grown using the 0.35 mm nozzle in particular shows a high texturing towards the (002) with a texture coefficient of 4.3. The crystallinity is much improved with smaller nozzle size.

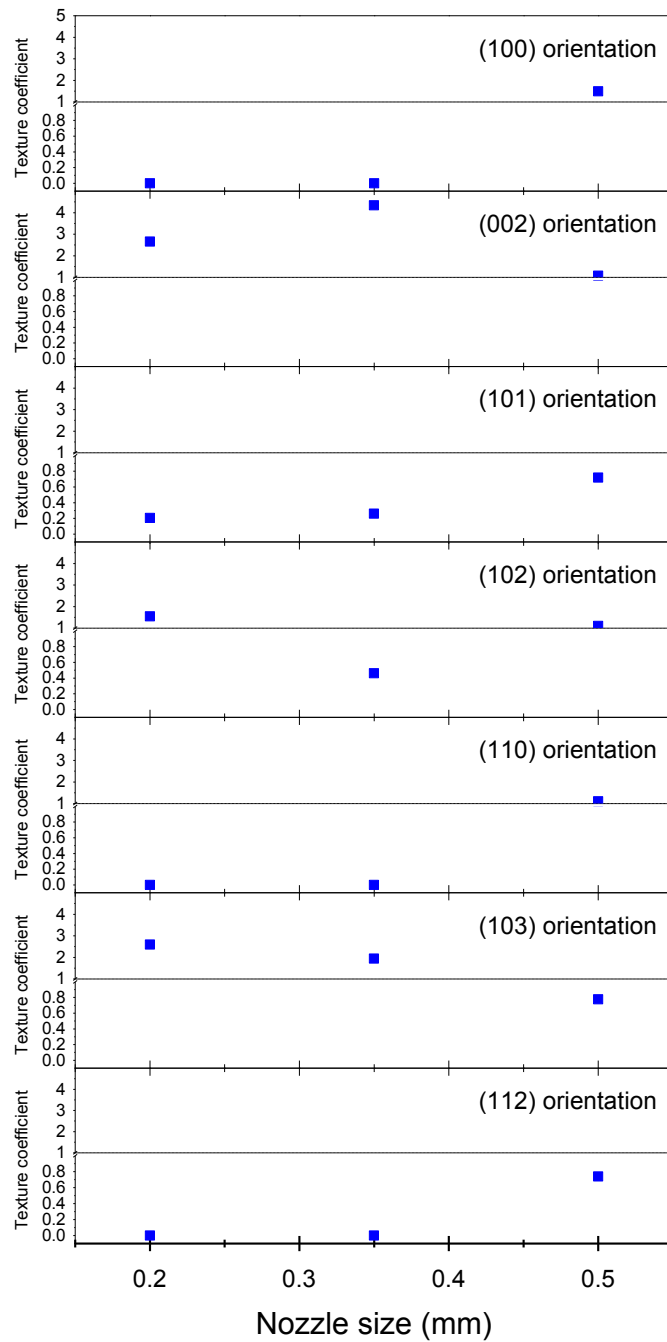


Figure 4. 25 - Texture coefficients from nozzle size experiment

A reliable crystallite size could not be extracted from the 0.5 mm sample, however, crystallite sizes of 30 and 31 nm could be extracted for the 0.2 and 0.35 mm samples respectively. SEM micrographs were collected to compare the grain size of all three sample as well as to study other topographic features.

4.2.11.3 Topographic Analysis

SEM micrographs were collected of film shown in Figure 4. 26. The surface of 0.2 and 0.5 mm films are significantly different. The 0.2 mm sample contains large (~100nm) plate-like grains. They are of roughly similar size and shape bearing some resemblance to the hexagonal/tilted-hexagonal shape expected from a (002) and (103) texture respectively. In contrast the 0.5 mm sample contains significantly smaller grains of varying size and shape (maximum ~50 nm minimum ~3 nm). The random shape may reflect the random orientation seen in the film.

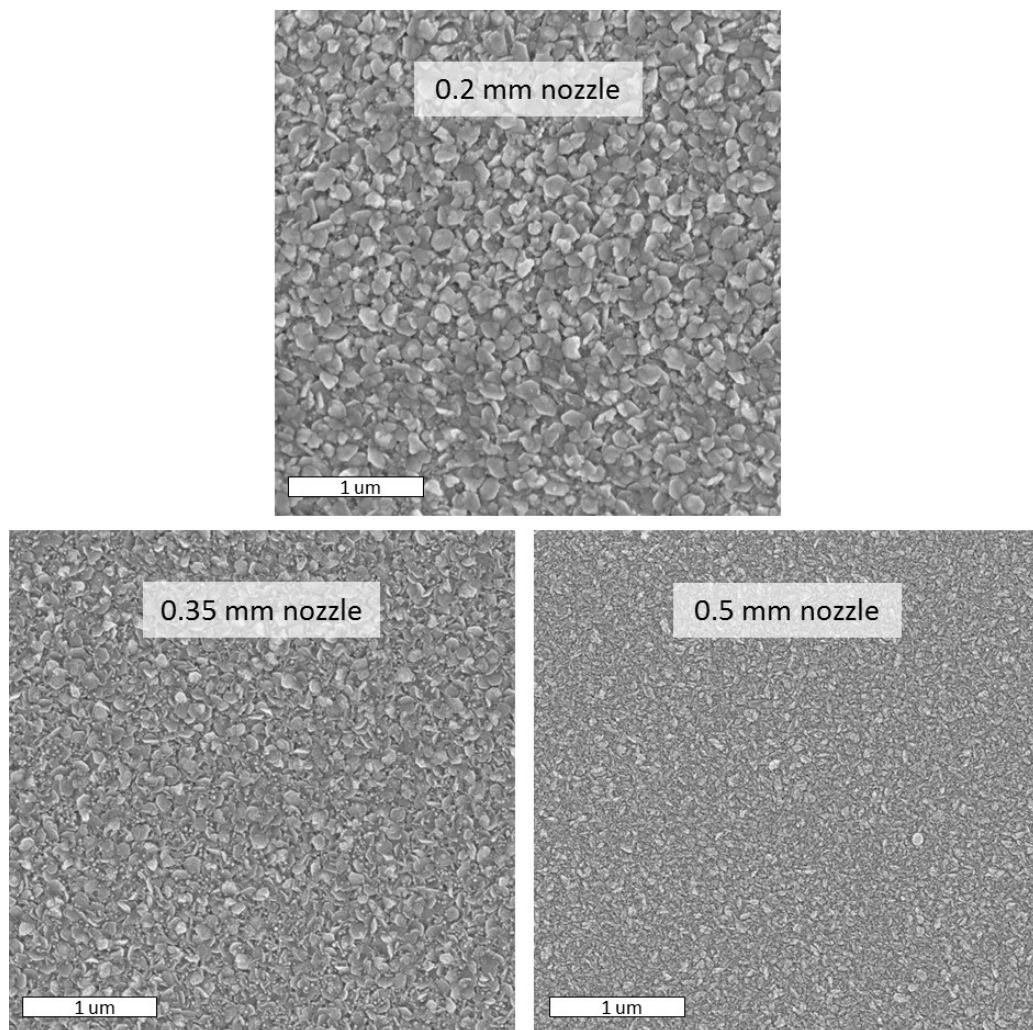


Figure 4. 26 – SEM micrographs of films from nozzle size experiment.

The 0.35 mm sample bears a resemblance to the 0.2 mm sample in that many large hexagon plate-like grains can be seen. It differs in that a number of very small particulate like grains can also be seen which bear more resemblance to the 0.5 mm sample. This was perhaps to be expected, as the deposition pathway for the 0.35 mm nozzle lie between the two extremes.

The grain size from SEM and crystallite size from XRD are significantly different. This is not necessarily a problem as the two measurements are of slightly different properties. The Scherrer equation for example is a whole sample measurement, whilst, SEM is a view of the surface. When using the Scherrer equation, this work assumes crystallites to be spherical. Non-spherical crystallites would therefore cause inaccuracy in the experiment, particularly when a material shows preferential growth direction. SEM also suffers inaccuracy in grain size calculation due to this factor; the surface largely shows the preferential growth direction and may not reflect the overall actually grain size. Lastly, there is the inherent difference between crystallites (measured in XRD) and grains (measured in SEM). Crystallites are areas of the same crystalline growth whereas the grains seen in micrographs may contain more than one crystallite.

4.2.11.4 Optical analysis

The optical properties of deposited films were investigated by UV-Vis spectroscopy shown in Figure 4. 27.

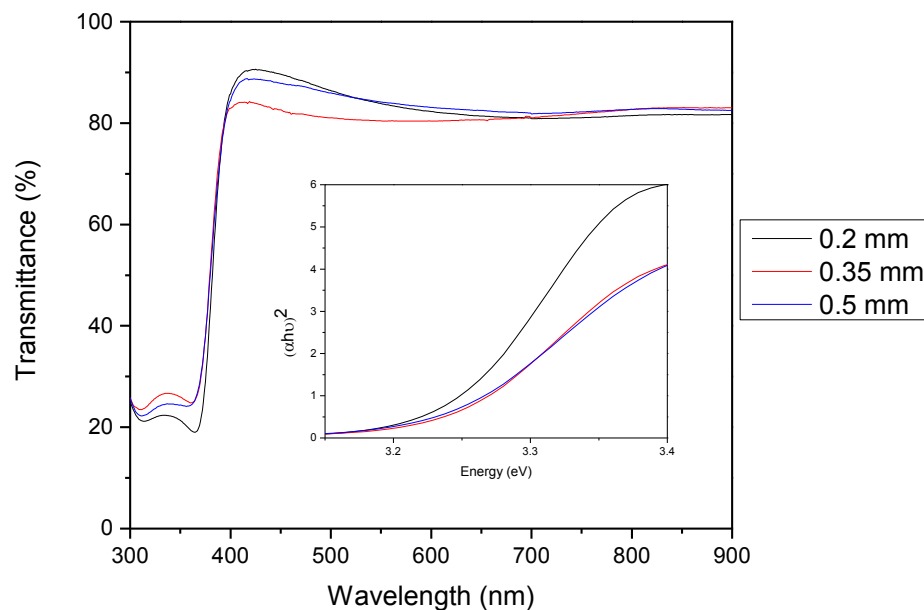


Figure 4. 27 - Optical transmittance of samples of different nozzle sizes. Insert shows Tauc analysis of optical data.

Tauc analysis (Figure 4. 27– insert) was used to investigate whether nozzle size had a significant effect on the band gap of the films. Results are displayed in Figure 4. 28.

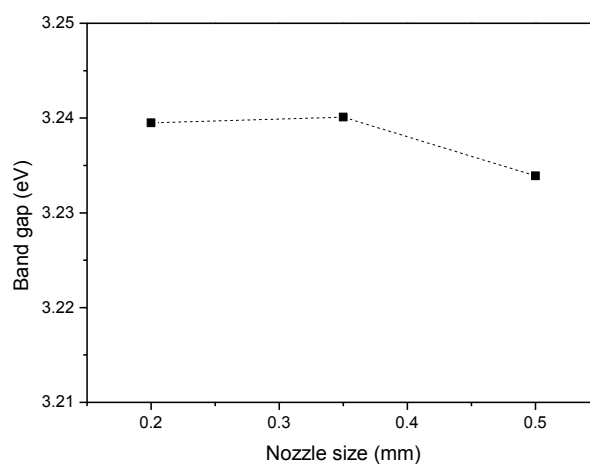


Figure 4. 28 - Varying electronic band gap of ZnO with increasing thickness. Trend line is purely to guide the eye.

The data shows little change to the band gap although the slight decrease in the 0.5 mm sample is consistent with the decrease in (002) orientation discussed earlier.

4.2.11.5 Electronic analysis

The electronic properties of the films were studied using AC Hall effect measurements shown in Figure 4. 29.

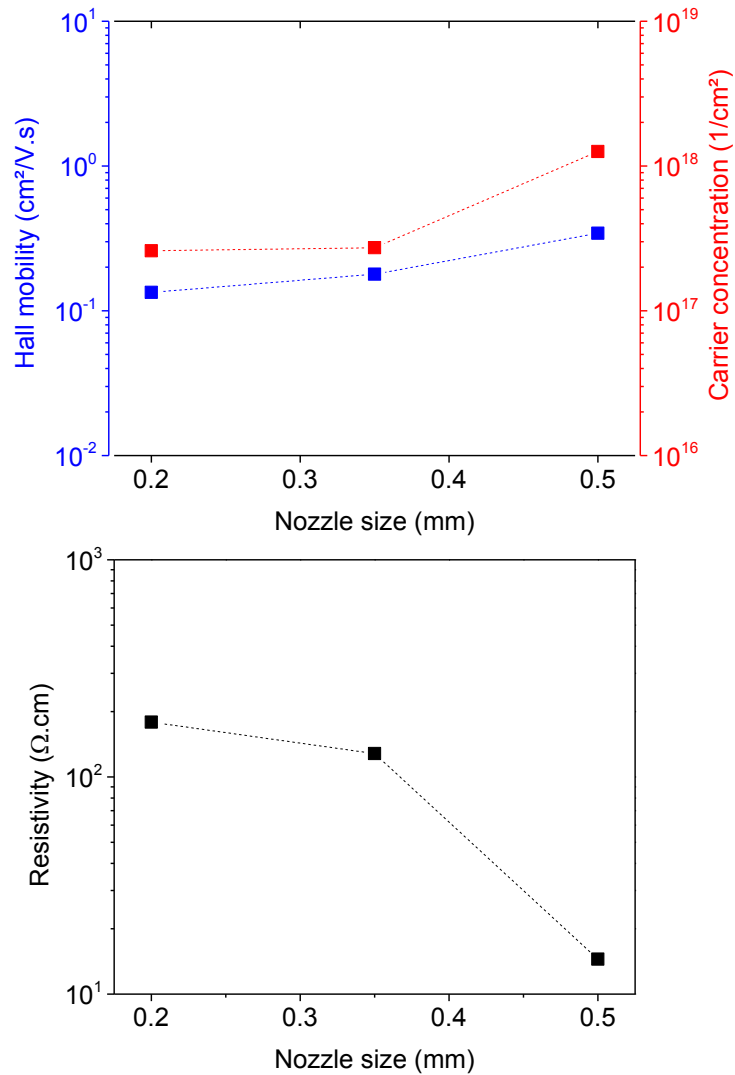


Figure 4. 29 – AC Hall effect measures from nozzle size experiment

The 0.5 mm nozzle size exhibits a significantly lower resistivity than the other two, dropping by nearly an order of magnitude. This is largely driven by a sharp increase in charge carrier concentration. A similar effect was seen in the precursor concentration experiments, where faster deposition rates resulted in less textured films with greater charge carrier concentration. These results back up the hypothesis that the fast growth rate is resulting in desirable defect chemistry. This in turn leads to a slightly improved charge mobility and significantly improved charge carrier concentration.

The increased charge mobility is surprising as there is a visible reduction in grain size from SEM measurements. This is expected to lead to increased grain boundary scattering.

In temperature, gas pressure and nozzle height experiments films with greater (002) texturing showed the most desirable electronic properties. This difference may be linked to the temperature required to activate defects. This is because films grown at 'St: 290 °C' show significantly lower charge carrier concentrations, despite exhibiting similar structural properties to films grown from a precursor concentration of 0.2 M or nozzle size of 0.5 mm.

4.2.12 Carrier Gas

The carrier gas used may potentially play a role in the defect chemistry of the ZnO films. Notionally, it is intended to play no role in the reaction, however, the external environment plays a key role in the properties of ZnO prepared by SP thus the effect of the carrier gas must be considered. Commonly used carrier gases are: compressed air [111], [130] and nitrogen, [131], [153] although, oxygen has also been used [141].

Jongthammanurak *et al* studied the difference between using nitrogen and air as carrier gases using ultrasonic SP at temperatures ranging from 350 – 430 °C. [154] Structurally the carrier gases appear to have little effect, however within the range of 375-415 °C resistivities are seen to be three orders of magnitude lower when grown using nitrogen compared to using air (1 and 3000 Ω.cm respectively). The setup of the chamber used meant that the films were effectively growing in nitrogen/air environments. This work suggests that the film growth is heavily reliant on the carrier gas used due to the varying oxygen partial pressure.

As well as differences in the oxygen:zinc ratio in a film, a factor which should be considered is the possibility for nitrogen to act as a dopant. This is most likely by a substitution into an oxygen site and is typically used to achieve p-type conductivity. N doped ZnO has been shown using ammonium acetate as a precursor by SP [155] and it is also claimed that this can be achieved by annealing in N₂. [156]

There has been no dedicated study comparing the effect of the carrier gases using pneumatic spray pyrolysis in ambient conditions.

4.2.13 Carrier gas experiments

In this work, ZnO was deposited using compressed air, nitrogen, argon and oxygen to investigate the effect of the carrier gas. The effect of N₂ doping was compared to the inert gas Ar. The O content of the carrier gas was investigated by increasing in O ratio from 0 % in Ar, ~20 % in air and 100 % in O₂. Other parameters were fixed as described in Table 4. 6. A higher hotplate temperature (500 °C) was used because N dopants are suggested to activate into p-type donors at this temperature. [155] The other parameters were fixed to take this into account.

HT (°C)	D	CGP (bar)	St	PC (M)	PL (s)	SoP (s/p)	Cy	NS (mm)
500	18	1	Soda lime	0.1	25	5	3	0.2

Table 4. 6 – Experimental parameters for carrier gas investigation

Thickness was found not to be effected by the differing gases and so was fixed to 150 nm. The structural, optical and electronic properties of each film were studied. How conditions affect each parameter and how they may be linked is covered in the sections below.

Structural analysis

XRD analysis was performed on all films; the results are displayed in Figure 4. 30.

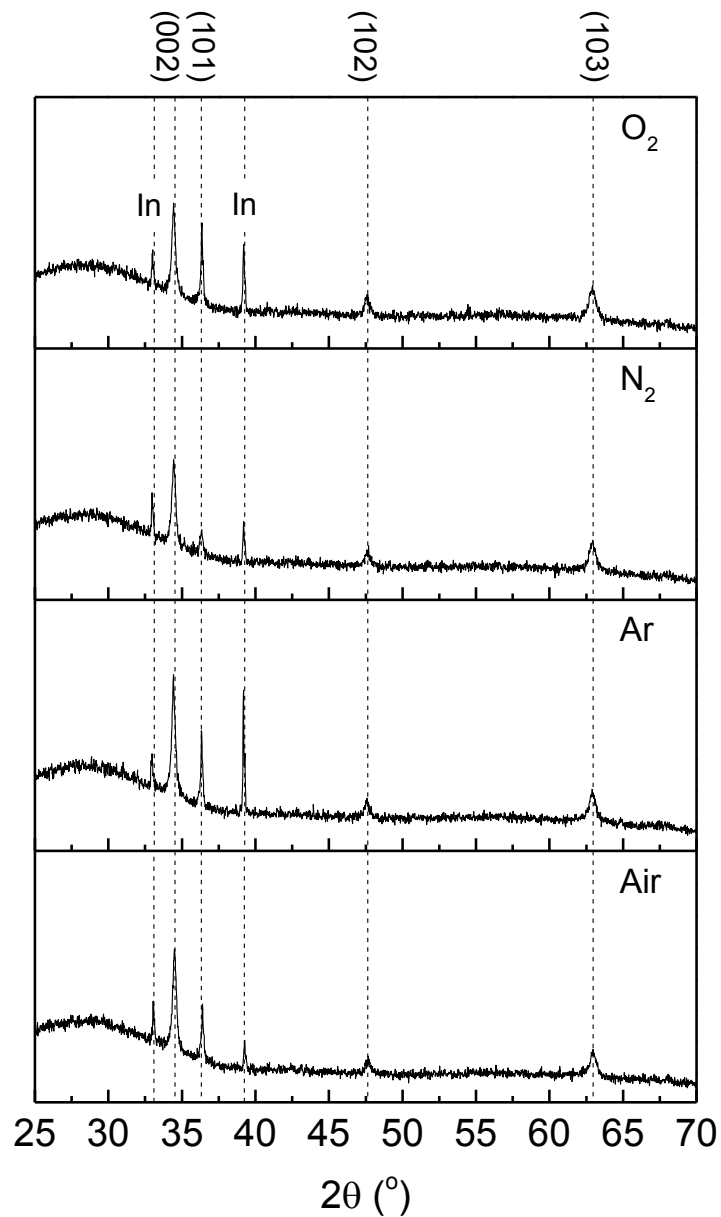


Figure 4. 30 – XRD patterns of comparable thickness ZnO films from carrier gas experiment. XRD was performed upon films after Hall effect measurements, thus there are peaks present from the indium contacts labelled 'In' which should not be considered in analysis (the In peaks at $\sim 33^\circ$ are close to the ZnO (100) but on close inspection are slightly shifted).

On first glance the films show little variation in crystallinity or texturing. The texture is quantified in Figure 4. 31, the only variation seen is a shift from the (101) to the (103) orientation for the N₂ sample. The (002) orientation remains the dominant texture for all carrier gases.

If any differences were to be seen in the films due to varying oxygen content, it follows that the films deposited using oxygen and air carrier gases would differ from those using Ar. This is not the case. Whilst the pathway is not clear there is a possibility that the structural properties may be influenced by the likely presence of small amounts of H₂O in the nitrogen gas. This could explain the subtle difference in the XRD pattern.

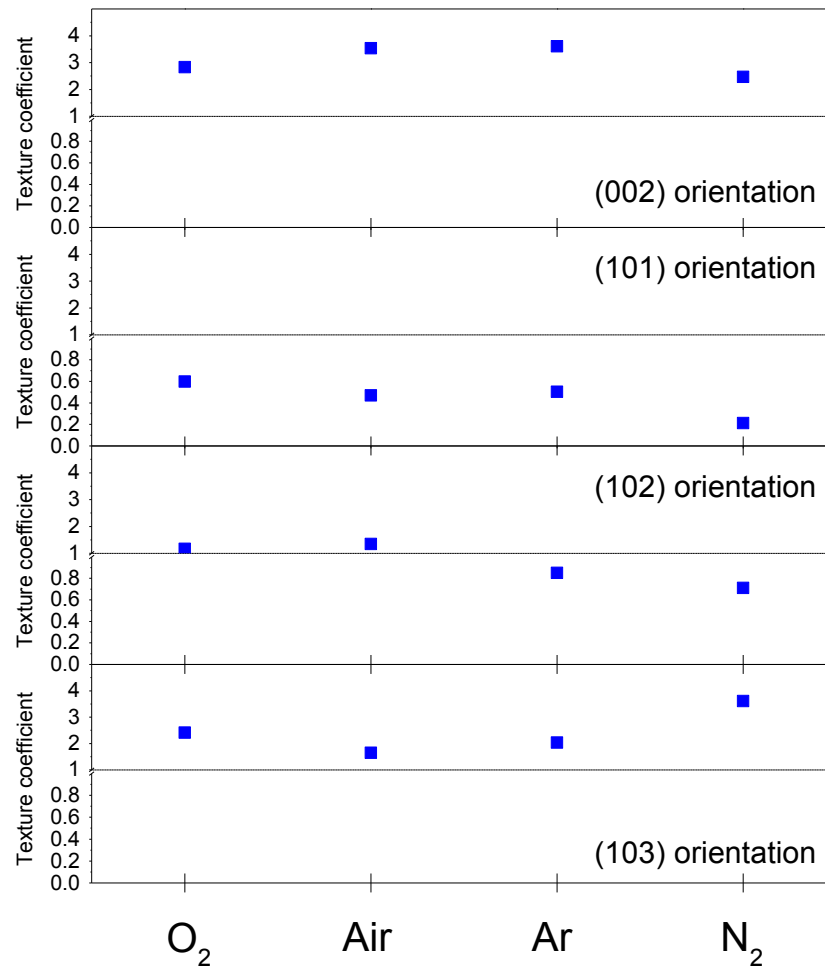


Figure 4. 31 – Texture coefficients from carrier gas experiment.

4.2.13.1 Optical analysis

The optical properties of deposited films were investigated by UV-Vis spectroscopy shown in Figure 4. 32.

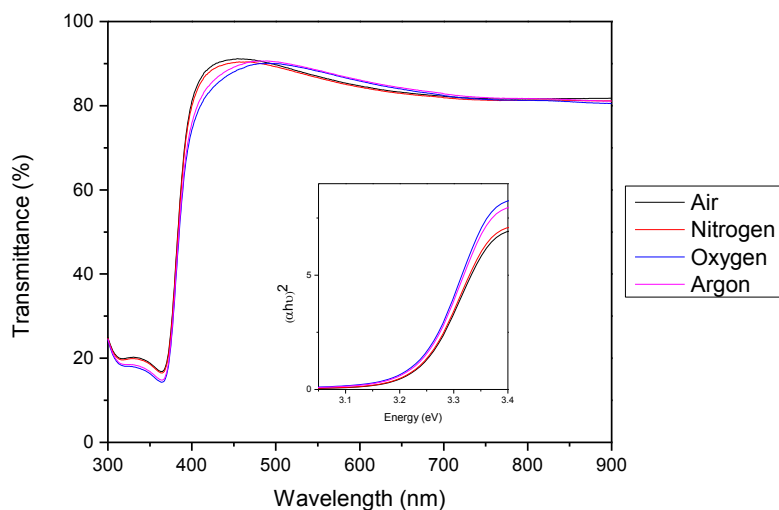


Figure 4. 32 - Optical transmittance of samples with varying carrier gas. Insert shows Tauc analysis of optical data.

Tauc analysis (Figure 4. 33- insert) was used to investigate whether thickness had a significant effect on the band gap of the films. There was no change in band gap observed. All films measured a band gap of 3.237 eV.

4.2.13.2 Electronic analysis

The electronic properties of the films were studied using AC Hall effect measurements shown in Figure 4. 33.

It is clear from the Hall results that the different carrier gases have negligible influence on the electronic properties. The charge carrier concentration and the charge mobility are comparable for all gases and this is reflected in the stable resistivity.

The fact that carrier gas type does not affect the charge carrier concentration suggests that, under the present conditions, there is ample oxygen from the solvent, organic component of the precursor salt, and the surrounding environment to produce a stoichiometric film. Films grown in vacuum using physical deposition methods (see 1.6.1) or in nitrogen environments, such as those by Jongthammanurak *et al*, show significantly higher charge carrier concentrations. This suggests the oxygen partial pressure in surrounding environment has a great impact on the defect chemistry.

One explanation for the lack of improvement in properties is that the films receive annealing in air between spray cycles. This would allow oxygen to enter a deficient system and give the results seen in Figure 4. 33. An interesting follow up experiment would be to maintain a flow of an oxygen free gas during the deposition process to see if this would affect results.

The small decrease in charge carrier concentration between Ar and N₂ deposited films may be evidence for a small amount of nitrogen doping – the acceptor defect formed would compensate some n-type carriers. However, the difference is too small for any confidence in this theory. Further experiments would be needed to better study this hypothesis.

The charge carrier concentration and resulting resistivity seen in these films is low in comparison to films seen in similar conditions. The hotplate temperature was raised to a higher temperature than previously used; this may explain the disparity. Droplets may have been pushed further towards pathway four, or, a more stoichiometric film may have been produced.

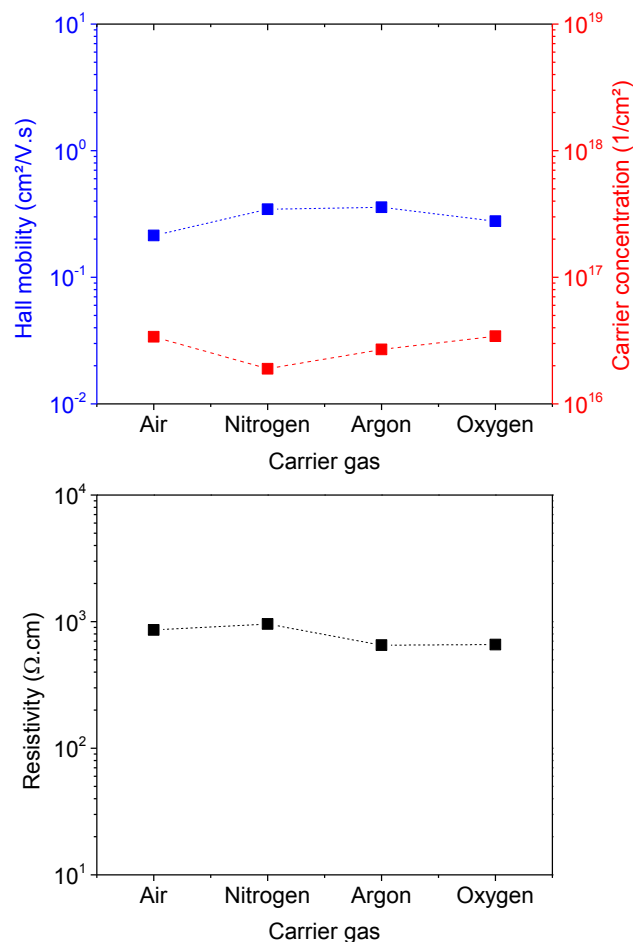


Figure 4. 33 – AC Hall effect measures from carrier gas experiment

4.2.14 Growth on different surfaces

The substrates were chosen for their low cost and transparency. As the droplets should be evaporated before they reach the substrate the wettability should not play a large role is deposition dynamics. The surface of the substrate may however have an influence on the adsorption properties of the vapour and the growth of the first layer of the film. This section describes how different surfaces can be used to template growth.

There have been relatively few reports investigating the effect of different surfaces in thin film growth in SP, although, much coverage is seen studying the growth of nanostructures. A report by Boyle *et al* describes a two stage hydrothermal growth of ZnO micro-columns, where a thin first layer acts as template for the second producing much improved nano-structuring. [157] This work has been followed up extensively in the growth of nano-structures [158]–[160] and has been extended to film growth using hydrothermal techniques. [161] There is little literature discussing substrate templating ZnO films using a roll to roll compatible technique such as spray pyrolysis. Here the effect of using Zn O seed layers to increase the orientation of spray deposited ZnO is investigated.

4.2.15 Different surface experiments

ZnO films were grown on bare soda lime glass, 10 nm of highly (002) orientated ZnO grown by pulsed laser deposition (PLD), and 10 nm ZnO was grown by atomic layer deposition (ALD). For comparison films were grown on soda lime glass and on a transistor base to show growth on a polycrystalline silicon/gold surface.

CG	HT (°C)	D	CGP (bar)	St	PC (M)	PL (s)	SoP (s/p)	Cy	NS (mm)
Air	425	15	1	-	0.1	25	5	3	0.2

Table 4. 7 – Fixed parameters in surface experiments

100 nm films of ZnO were deposited upon the different layers using SP with the other parameters fixed as described in Table 4. 7.

4.2.15.1 Structural analysis

XRD analysis was performed on all films with the results are displayed in Figure 4. 34. The films show a stark difference in crystallinity. Films grown by SP on bare glass and on 20 nm of ALD ZnO display similar structures. They are comparable with films seen earlier in the chapter. The 10 nm of PLD is entirely textured towards the (002) orientation and is highly crystalline showing similar intensity to SP films of ten times the thickness. The peak is much broader; this is likely due to a much diminished grain size and can be linked to the thickness. When SP films are deposited upon a surface composed of 10 nm PLD deposited ZnO a clear templating effect is seen. The resulting film's XRD pattern is many orders more intense than a film of similar thickness grown purely using SP. The film is also entirely textured towards the (002) orientation, matching that of the surface below.

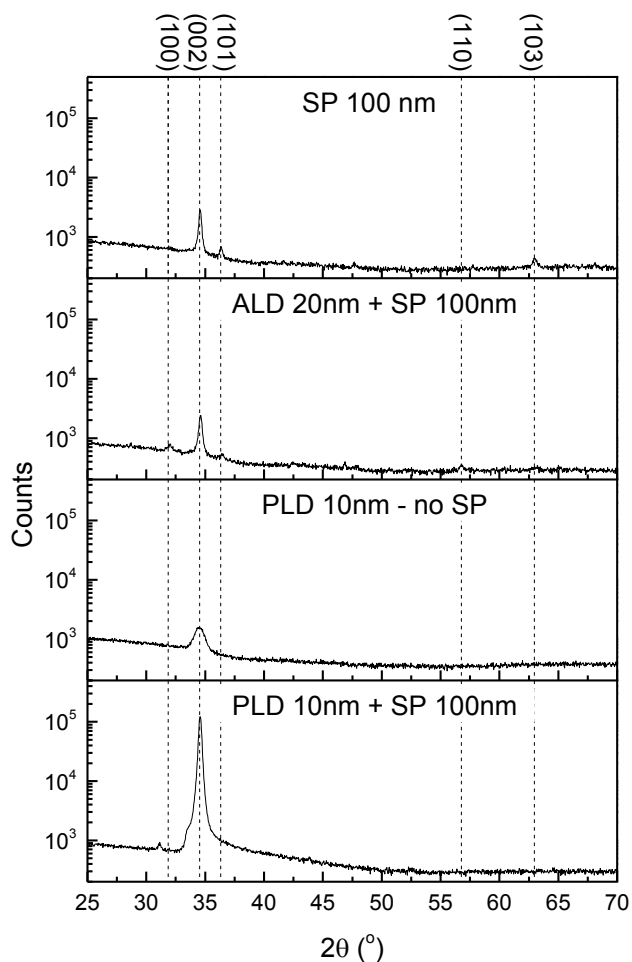


Figure 4. 34 – XRD patterns of ZnO films grown upon different surfaces. The x-axis' displaying the intensity are set to a logarithmic scale so that films can be compared.

4.2.15.2 Topographic and cross sectional analysis

SEM micrographs were taken of the different films; the results are shown in Figure 4. 35.

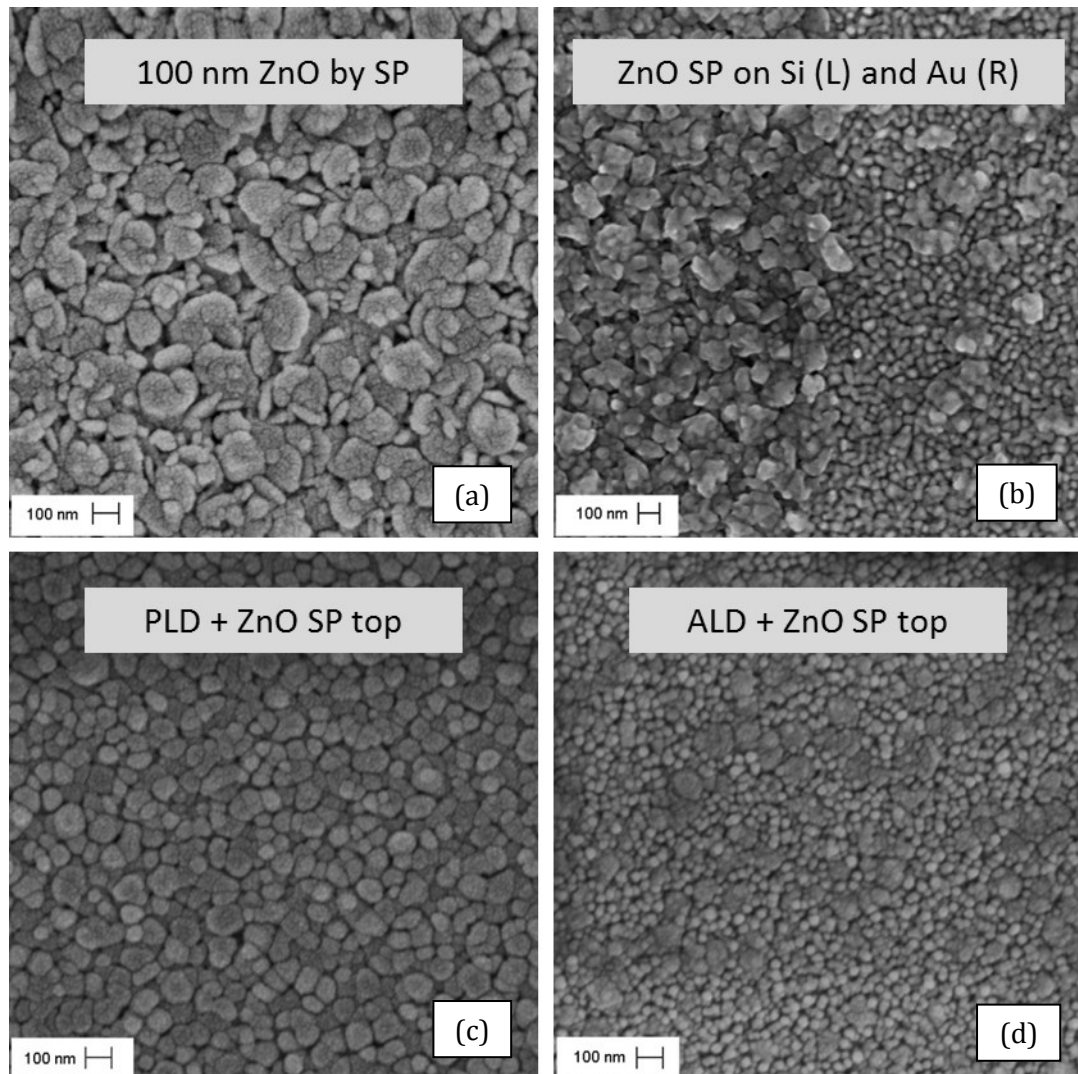


Figure 4. 35 – SEM micrographs of ZnO growth on various substrates. (a) shows 100 nm of ZnO grown on a soda-lime base. (b) shows 100 nm of ZnO grown on 10 nm of PLD deposited ZnO (glass substrate). (c) shows 100 nm of ZnO grown on 10 nm of ALD deposited ZnO (glass substrate). (d) shows 100 nm of ZnO grown on a transistor base with polycrystalline silicon on the left and gold on the right

The results show very different properties depending on the surface. The ZnO film grown on base glass (shown in Figure 4. 35 - (a)) as with previous samples, displays a 'flake like' surface made up of a large distribution of grain sizes. The ZnO grown on PLD deposited ZnO (shown in Figure 4. 35 - (c)) displays much clearer hexagon like shapes and a more consistent grain size. The film also appears to be smoother, however, the presence of much more defined grains leaves some gaps between columns.

The ZnO grown on ALD deposited ZnO (shown in Figure 4. 35 - (d)) display much smaller grain sizes, however, there are patches of larger grains seen throughout the micrograph. The ZnO film grown on the transistor base (shown in Figure 4. 35 - (b)) shows a clear division between the two regions (polycrystalline silicon and gold) and is an excellent example of how the different surfaces direct the growth in identical conditions. The ZnO grown on silicon closely resembles that grown on soda-lime glass whereas the ZnO grown on gold resembles that grown on ALD deposited ZnO. It is likely that these two sections may have different electrical properties; this is worth considering when measuring transistors using ZnO deposited by spray pyrolysis.

TEM cross sectional images were taken of ZnO grown on glass and on the PLD deposited base, these are shown in Figure 4. 36. The cross sections show large differences: the film grown on bare glass (Figure 4. 36 - right) shows many small grains of no distinct shape; the film grown on the PLD base (Figure 4. 36 - left) however shows very large grains, they are columnar and grow vertically from the base to the surface.

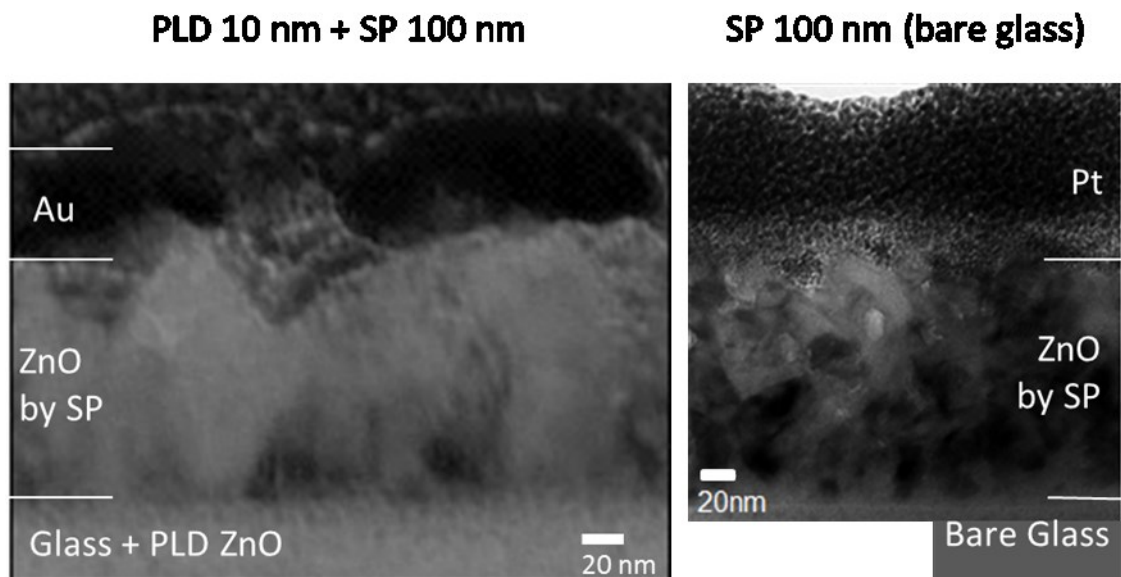


Figure 4. 36 – Left shows TEM cross section of a ZnO film sprayed on to 10 nm of PLD grown ZnO. Right shows TEM cross section of a ZnO film sprayed on bare glass. The individual layers are labelled with the glass substrate at the bottom, above this the PLD grown ZnO then the sprayed ZnO, gold was sputtered on top to prevent charging from the electron microscope, platinum is deposited on the surface to protect the lamella from damage from the FIB.

4.2.15.3 Electronic Analysis

The electronic properties of films grown on bare glass and on 10 nm of PLD ZnO were studied using AC Hall effect measurements shown in Figure 4. 37.

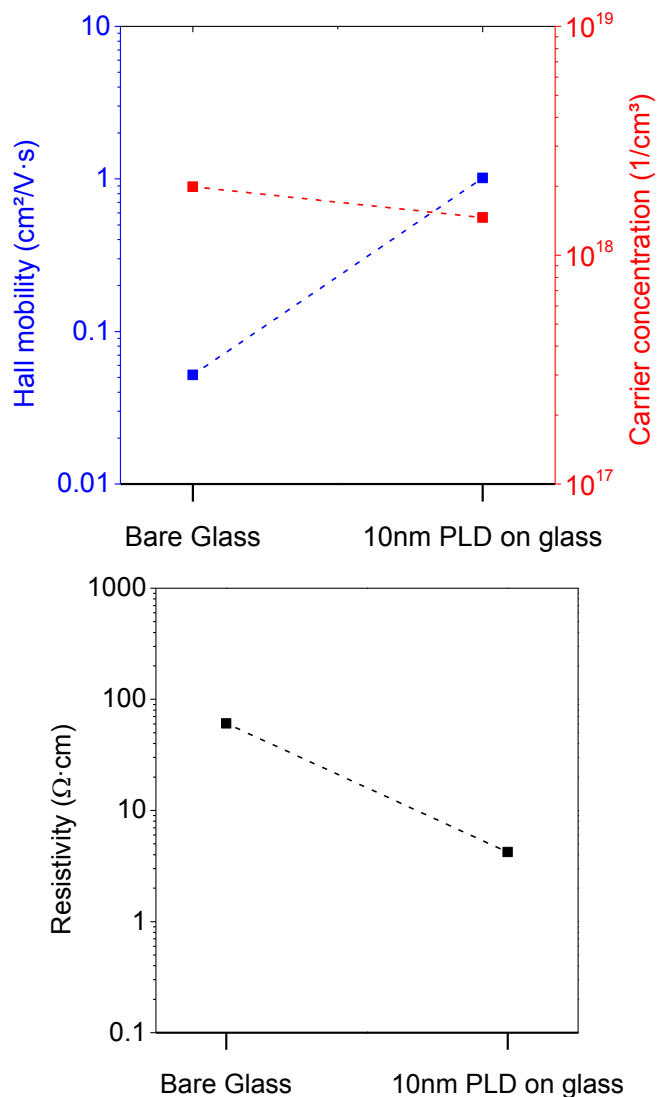


Figure 4. 37 – Hall charge mobility and charge carrier concentration (left) and resistivity (right) of ZnO films grown on a bare glass surface and PLD grown ZnO surface. Trend lines are purely to guide the eye.

There is over an order of magnitude decrease in the resistivity of the film grown on the PLD base compared with on bare glass. This is driven by an equal increase in the charge mobility. The charge carrier concentration is largely unaffected.

This is expected from the structural and electron microscopic analysis, the large increase in grain size is likely to severely reduce grain boundary scattering accounting for the increase in charge mobility and reduction in resistivity.

It is clear that using a highly textured seed layer can template growth in a quasi-epitaxial manner. The greatest templating was seen in a PLD derived seed layer, whereas, the less (002) orientated ALD derived seed layer was ineffective. This may have interesting implications for TCO applications. PLD is not a cost efficient method of templating growth however; if this type of templating was possible in a less costly manner, it could provide a method of reducing resistivity of solution processed ZnO to the levels of vacuum deposition methods.

4.3 Conclusions

This chapter aimed to give a systematic review of deposition parameters finding optimum conditions to deposit optically transparent and low resistivity ZnO. It also aimed to fill a gap in the literature in terms of the linking the deposition parameters, the structural properties and the electronic properties. This was made possible by novel AC field Hall effect measurements, where low charge mobility samples could be accurately measured.

The chapter started with a review of the state of the art in terms of the spray deposition of ZnO, identifying the deposition parameters most conducive to the deposition of crystalline and optically transparent films. A number of potential parameters were highlighted from the literature. Two parameters were initially deemed superior based on this investigation and some preliminary studies:

- Precursor salt - zinc acetate dihydrate,
- Precursor solvent - methanol + 2.5 vol% acetic acid.

4.3.1.1 Thickness studies

A limitation in many literature sources was the limited reporting and variation in sample thickness. The importance of consistent sample thickness was highlighted:

- Variation in preferential orientation is seen,
- Variation in the electronic band gap is seen,
- Variation in the charge carrier concentration and charge mobility are seen.

4.3.1.2 Substrate temperature, Gas Pressure and Stage Height studies

The remaining parameters were systemically investigated, maintaining a consistent thickness and the structural and optoelectronic properties studied. Firstly the three linked parameters of substrate temperature, stage height and carrier gas pressure were studied

- Substrate temperature has the greatest influence on the structural properties,
 - The greatest texturing towards (002) orientation is seen between 380-460 °C,
 - Stage height and carrier gas pressure dictate the optimum conditions for (002) growth between this temperature range.
- The lowest resistivity and greatest transparency was seen between

380 – 460 °C. No clear link between the texturing and optoelectronic properties could be deciphered however, a loose trend between the charge mobility and crystallite size emerged.

- The most conducive conditions for spraying ZnO for TCO applications was found at 380 °C – 15 cm – 1 bar.

4.3.1.3 Precursor concentration studies

Using these conditions, variations in the precursor concentration were investigated.

- A thickness calibration study was implemented to achieve consistent thickness for the experiment.
- The precursor concentration was linked to degree of preferential orientation by:
 - Variations in growth rate or
 - Variations in the droplet pathway
- Electronic properties largely dictated by charge carrier concentration
 - Increased deposition rate is believed to lead to more intrinsic defects
 - 0.2 M sample showed lowest resistivity

4.3.1.4 Nozzle size studies

Variations in film properties were investigated when altering the nozzle size.

- A thickness trend was implemented to achieve consistent thickness for study
- The largest nozzle size (0.5 mm) display reduced crystallinity and less texturing
 - Proposed to be due to growth rate or droplet pathway
- SEM showed the 0.5 mm film to have a much smaller grain size
- Electronic properties largely dictated by charge carrier concentration
 - Increased deposition rate is believed to lead to more intrinsic defects
 - 0.5 mm sample showed lowest resistivity, 0.35 and 0.2 mm roughly equal

4.3.1.5 Carrier gas studies

Variations in film properties were investigated when altering the carrier gas.

- Films deposited from different carrier gases display similar structural, optical and electrical properties
- The type of carrier gas is believed not to affect film properties

- The deposition environment is not believed to be dominated by the carrier gas instead the atmospheric conditions take precedence.

4.3.1.6 Different surfaces study

The ability to template ZnO films was investigated using ZnO seed layers created from PLD and ALD. These were compared with bare glass, silicon and gold surfaces.

- The PLD seed layer show greatly improved crystallinity and texturing to ALD seed layer and to the control
- SEM showed the PLD seed layer gave larger and more defined grains compared to the control, the ALD seed layers gave a decrease in grain size
- The PLD showed greatly reduced resistivity compared to the control driven by an increase in charge mobility.

CHAPTER V – DOPING AND ANNEALING STUDIES ON ZnO PREPARED BY SPRAY PYROLYSIS

5.1 Introduction

Chapter IV was focused on optimising the spray conditions to deposit thin films of ZnO. The aim of this was to produce a native film most compatible for application in transparent conducting oxide applications. In Chapter V, work is directed towards investigating how native and external defects can be introduced to influence the structural and optoelectronic properties.

This chapter first investigates using external dopants as a source of improved conductivity. Having optimised the doping of ZnO, it moves on to investigate methods to the control of the native defects in the doped films using annealing techniques.

5.2 Doping Studies

The most common additives to ZnO films are the group 3 dopants: Al, Ga and In. The 3+ ions can substitute for Zn²⁺ in the lattice adding an electron to the conduction band for every substituent. This is well documented to increase the charge carrier concentration and lowers the resistivity.

Merchant *et al* used spray pyrolysis to dope ZnO with 3+ ions: B, Al, Ga, In, As, Mo, La, Fe and Gd and studied the interplay between dopant level and resistivity in undoped and annealed films. [109] A table of their results is shown in Table 5. 1.

Dopant	Film thickness (nm)	Resistivity - as-deposited ($\Omega\cdot\text{cm}$)
none	1000	3830
Al 2 at%	500	0.250
In 1 at%	1000	98.7
Ga 4 at%	300	1.15
Mo 4at%	200	2110
B 0.5at%	300	770
La 1 at%	500	31200
Gd 2 at%	500	51000

Table 5. 1- The minimum resistivity of ZnO doped with a series of dopants. Dopant % was optimised for each dopant. Reproduced from Table 1 of Reference [109].

Annealing in hydrogen at 300 °C was seen to reduce the conductivity of all films by a number of orders of magnitude.

Following on from initial studies (Table 5. 1), Merchant *et al* investigated the case of Al doped ZnO in detail. A dramatic drop in resistivity between 0-1 at% was seen reaching a minimum at 2 at%. The resistivity then increases dramatically past 3 at%. The full trend is displayed in Figure 5. 1.

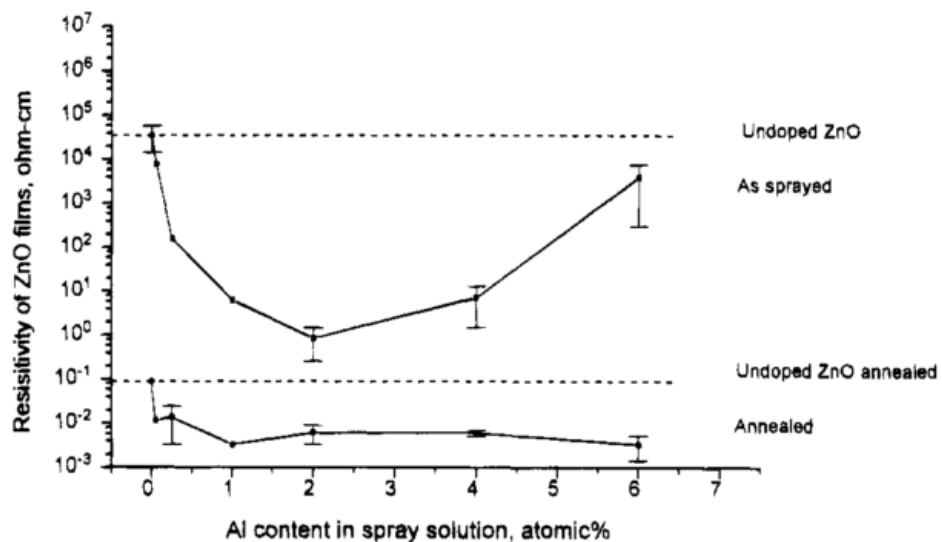


Figure 5. 1 - Effects of Al doping on resistivity of ZnO, films range from 300-600 nm in thickness. Reproduced from figure 3 of reference 103.

Since these early efforts, spray pyrolysis has become a more common technique. Advances have been made to improve results by modifying the processing conditions, this has been achieved by: optimising precursors; [110] using ultrasonic nozzles; [105], [162] and depositing in oxygen and water poor environments. [163]

AZO has featured in a many of the literature studies investigating SP. Minimum resistivities of AZO films typically are in the ranges of 10^{-3} Ω .cm for as-deposited films and 10^{-4} Ω .cm for annealed films. Comparing literature values for an outright 'best' method remains difficult due to the large number of different set-ups and conditions used. As discussed in section 4.2.3, the thickness of the films can have a great effect on electronic properties. This effect is highlighted in a report by Arnou *et al*, [164] where films of 250 – 300 nm show minimum resistivities of ~ 1 Ω .cm, however, films of 1800 nm display resistivities in the range of 1×10^{-2} Ω .cm. For many TCO applications, particularly in solar cells, films are ideally in the range of 100 – 150 nm, [165] this is to maximise transmittance and increase cell efficiency. This brings in to question the relevance of low resistivities seen in thicker films when discussing their potential in solar cell applications. It is worth highlighting that the competition, industrial ITO, is typically 150 nm thick.

It is also important, when comparing literature values, to determine whether a film have received a post deposition anneal, and, if that anneal was performed in an oxygen deficient environment. The importance of this factor is highlighted by Merchant *et al* in Figure 5. 2, where the relationship between thickness and electronic properties is shown, before and after a vacuum anneal (10^{-3} bar and 400 °C). This study includes Al, Ga and In doping. [11]

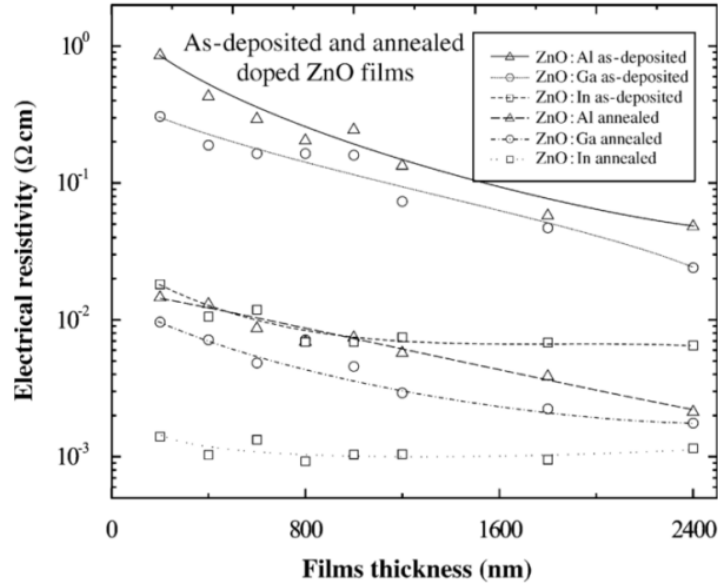


Figure 5. 2 – Effects of thickness and vacuum anneal on Al, Ga and In doped ZnO films. Reproduced from Figure 7 of reference [11].

Following vacuum annealing, the resistivity of AZO, GZO and IZO films all decrease by roughly two orders of magnitude. The reason for this decrease is cited to be due to the creation of an oxygen deficient film; with the increased conductivity suggested to be caused by oxygen vacancies. Whilst the current thinking is that oxygen vacancies do not actively increase conductivity (see section 1.4.1.1.1) the benefit of vacuum annealing is clear.

5.2.1 Preliminary results on trivalent dopants

Preliminary work for this report, studying the doping of ZnO, focused on the incorporation of a number of trivalent ions. Group 3 salts: Al, Ga and In as well as Y, Bi and Ce (which preferentially form 3+ ions) were added to the precursor solution at 2 at%. Optimised spray parameters calculated in Chapter IV were used as shown in Table 5. 2.

CG	HT (°C)	D	CGP (bar)	St	PC (M)	PL (s)	SoP (s/p)	Cy	NS (mm)
N ₂	400	18	1	Soda lime	0.1	25	5	3	0.2

Table 5. 2 – Spray parameters of initial trivalent doping experiment

The sheet resistance of the six films were recorded, as shown in Figure 5. 3. The results are displayed in terms of sheet resistance rather than as resistivity as reliable thickness measurements could not be achieved for all films.

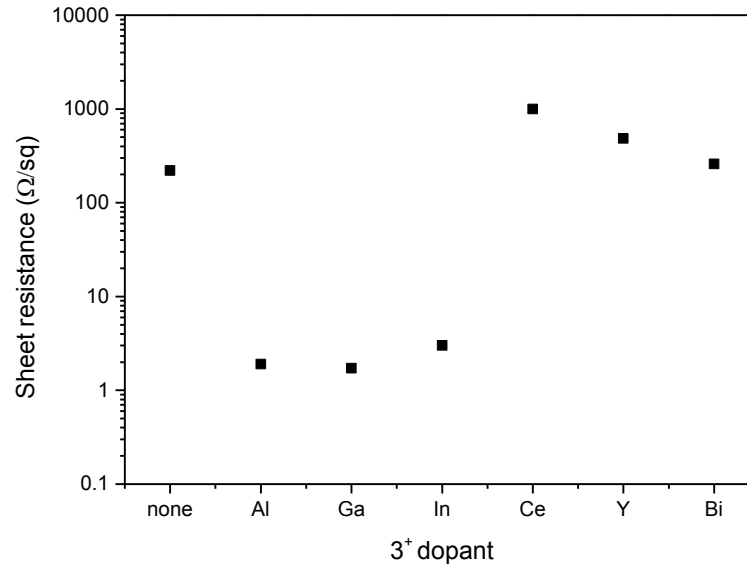


Figure 5. 3 – Sheet resistances of ZnO films doped with 2 atomic percent of Al, Bi, Ce, Ga, In and Y.

ZnO films doped with Bi, Ce and Y show sheet resistances similar to those recorded in undoped ZnO films. This suggests that these dopants have not substitutionally doped into the ZnO lattice or, if substitutional doping has occurred, the ions have not been suitable to donate a free carrier to the conduction band of the ZnO system.

If the Bi, Ce and Y ions have not substituted into the lattice it is possible they have segregated to grain boundaries or as large networks of complex defects (including anti-sites). The size of these ions means that EDX would provide an excellent method to study the location of these ions in more detail.

On the contrary the Al, Ga and In doped films show a two order of magnitude decrease in the sheet resistance. This suggests that the dopants have successfully substituted for zinc ions in the lattice and donated free charge carriers to the lattice. The success of Al, Ga and In doping compared with Ce, Y, and Bi is attributed to the different ionic radii of the species. Substituent impurities must replace the Zn^{2+} ion which has an ionic radius of 0.60 Å. The ionic radii of dopants studied is as follows: $Al^{3+} = 0.39$ Å, $Ga^{3+} = 0.47$ Å, $In^{3+} = 0.62$ Å, $Ce = 1.01$ Å, $Y = 0.90$ Å $Bi = 0.96$ Å. [35] The group three elements are close enough to zinc in size to fit into the wurtzite lattice whilst Bi, Ce and Y are not (their covalent radii show similar results). Furthermore, Bi, Ce and Y do not easily take four coordinate positions. XRD analysis did not highlight any secondary phases and there is little shift in the peak position of the (002) reflection to suggest strain to the lattice (see Appendix A.5). However, it is likely that these phases are outside the detection limit of the machine.

5.2.2 Al doped ZnO

Following this preliminary work, a study was performed using AZO to determine the mechanisms behind the increase in conductivity caused by doping ZnO with group 3 elements.

A literature search was performed to investigate the optimum doping level and the resistivities achieved to date. Table 5. 3 shows a selection of Al doped ZnO from literature with thicknesses more than 300 nm.

Al at%	Thickness (nm)	Resistivity ($\Omega\cdot\text{cm}$)	Hall Charge mobility ($\text{cm}^2/\text{V}\cdot\text{s}$)	Charge carrier concentration (cm^{-3})	Year of study
3	~1000	3×10^{-3}	-	-	2007 [166]
3	2400	8×10^{-2}	-	-	2007 [11]
2	~450	9×10^{-1}	-	-	1995 [109]
2	1000	4×10^{-3}	12	9×10^{19}	2000 [167]
2	1800	2.1×10^{-2}	3	9×10^{19}	2014 [164]
2.5	600	3×10^{-2}	-	-	2007 [153]
3	600	2×10^{-2}	1	3×10^{20}	2010 [168]
3	600	1×10^{-2}	~5	$\sim 7 \times 10^{19}$	2010 [169]
3	603	2×10^{-3}	8	8×10^{20}	2013 [101]
~1.75	~500	5×10^{-2}	-	-	2014 [170]
1	400	3.3	20	1×10^{17}	2015 [171]
1	1260	2×10^{-2}	0.6	9×10^{20}	2015 [171]

Table 5. 3 – Electronic properties of AZO films more than 300 nm cited in literature

It is clear that the electronic properties of AZO films are excellent in thick films, however, their thickness would make them inappropriate for many optoelectronic devices. As such, a literature study of spray deposited AZO films was undertaken for films under 300 nm thick. The results of which are shown in Table 5. 4.

Al at%	Thickness (nm)	Resistivity ($\Omega\cdot\text{cm}$)	Year of study
1	270	1.3	2012 [172]
1	200	0.8	2006 [141]
2	275	1.75	2014 [164]
3	~200	0.6	2004 [173]
0.3	200	3	2006 [174]
3	200	0.9	2007 [11]
1.5	~285	0.1	2011 [175]
3	45	3	2014 [116]

Table 5. 4 – Electronic properties of films less than 300 nm cited in literature

In films less than 300 nm thick, much diminished resistivities are seen. The optimum resistivity is also less clear with reports showing it to be in the range of 0.1 – 3 Ω .cm at a doping level of between 1 and 3 at%.

The Hall effect has been used regularly to extract the charge mobility and charge carrier concentration from the resistivity. Films measured in Table 5. 3 typically used Hall effect measurements in DC mode. Due to the poor charge mobility of as-deposited ZnO produced by spray pyrolysis at low thicknesses, large errors are seen in the measured Hall voltage. These errors are the result of a high noise level arising from the thermoelectric voltage and misalignment voltage (see section 2.4.3). These errors are also present in measured ZnO films with a low dopant concentration.

In the present work, recent advances in measuring the Hall effect has allowed the accurate measurement of low thickness and low dopant level AZO, GZO and IZO films. Using AC Hall measurements, a clear picture of the nature in which dopant impurities impact on the electronic properties is provided for 150 nm films at a range of doping levels. This measurement technique also allows for a more accurate study of the optimum doping level for this system. This was necessary due to the range of optimum doping levels cited in the literature (see Table 5. 4)

5.2.2.1 Experiments upon AZO

This section investigates as-deposited, trivalently doped ZnO films of 150 nm thickness to optimise the electronic properties and propose mechanisms for the observations.

Films were deposited with doping levels of 0, 0.5, 1, 1.5 and 2 at%. The sheet resistance of the deposited films was measured using the 4PP technique and the thickness was measured by using profilometry. The resistivity was extracted from the sheet resistance and plotted in Figure 5. 4.

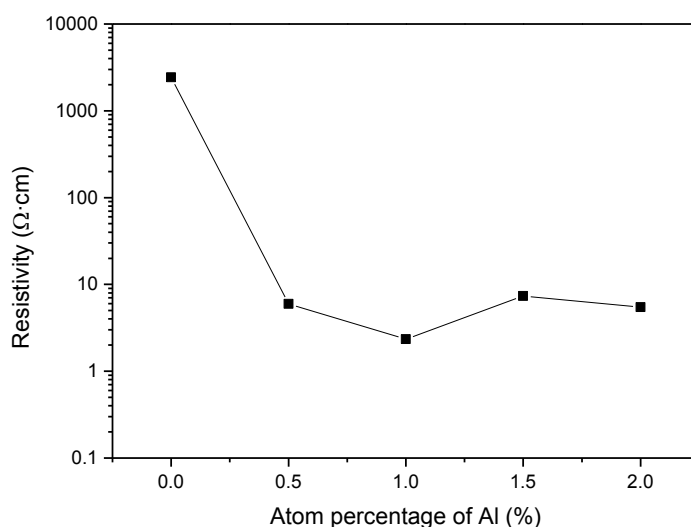


Figure 5. 4 – The resistivities of aluminium doped ZnO films as measured by four point probe. Dopant concentration was varied from 0-2 at% in 0. 5 at% intervals.

The addition of dopant gives the expected decrease in resistivity with the addition of Al. A decrease of over three orders of magnitude is observed when the amount of Al is increased from 0 – 0.5 at%. This occurs as the aluminium atoms substitutionally dope for zinc atoms in the lattice and supply free charge carriers to the system. A minimum is seen at 1 at%, after this there is a slight increase in resistivity. It is proposed that charge carriers reach a saturation point as dopants can no longer fill substitutional positions. This hypothesis was investigated using Hall effect measurements to dissect the resistivity into the charge carrier and charge mobility components, shown in Figure 5. 5

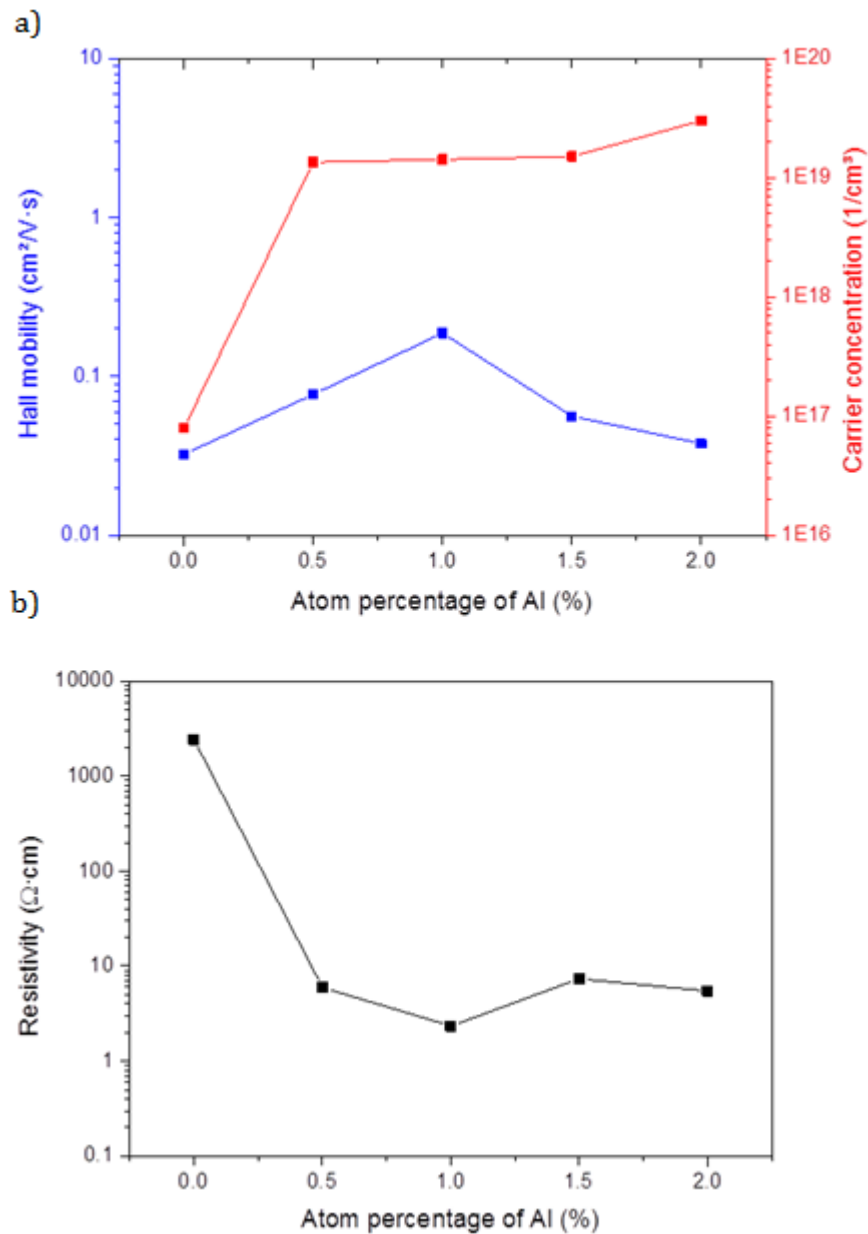


Figure 5. 5 – a) displays the Hall charge mobility and charge carrier concentrations of aluminium doped ZnO. b) displays the resistivity of the same films as measured from the Hall effect. The samples used are the same as those measured by four point probe in Figure 5. 4.

The resistivities of the films measured using the Hall effect, shown in Figure 5. 5, match almost perfectly with those measured by four point probe, shown in Figure 5. 4. This adds confidence to the accuracy of both techniques.

The Hall charge mobility of the ZnO film appears to increase with doping, reaching a maximum at 1.0 at% Al doping. After this point it decreases to the original level; as reflected in subtle changes to the resistivity. The resistivity of the films however, appears to be dominated by the charge carrier concentration with a fall of three orders of magnitude observed following the onset of doping.

Figure 5. 5 clearly shows that the decrease in resistivity is driven by a two order of magnitude increase in charge carrier concentration between 0 and 0.5 at%. After 0.5 at% increasing levels of dopant have little effect on the charge carrier concentration; the samples doped with 0.5, 1 and 1.5 at% Al ions all display values within a range of $1 \times 10^{19} \text{ cm}^{-3}$. It is proposed that between 0 and 0.5 at% the aluminium reaches its solubility limit in the ZnO lattice. This would mean that, above 0.5 at%, the aluminium no longer dopes substitutionally, and instead, will fill other defect positions; form a secondary phase of a zinc/aluminium mixed oxide; or precipitate out into a secondary phase of entirely aluminium oxide.

XRD patterns were taken of the samples, shown in Figure 5. 6, and the differences in crystal structure was analysed to assess these conclusions.

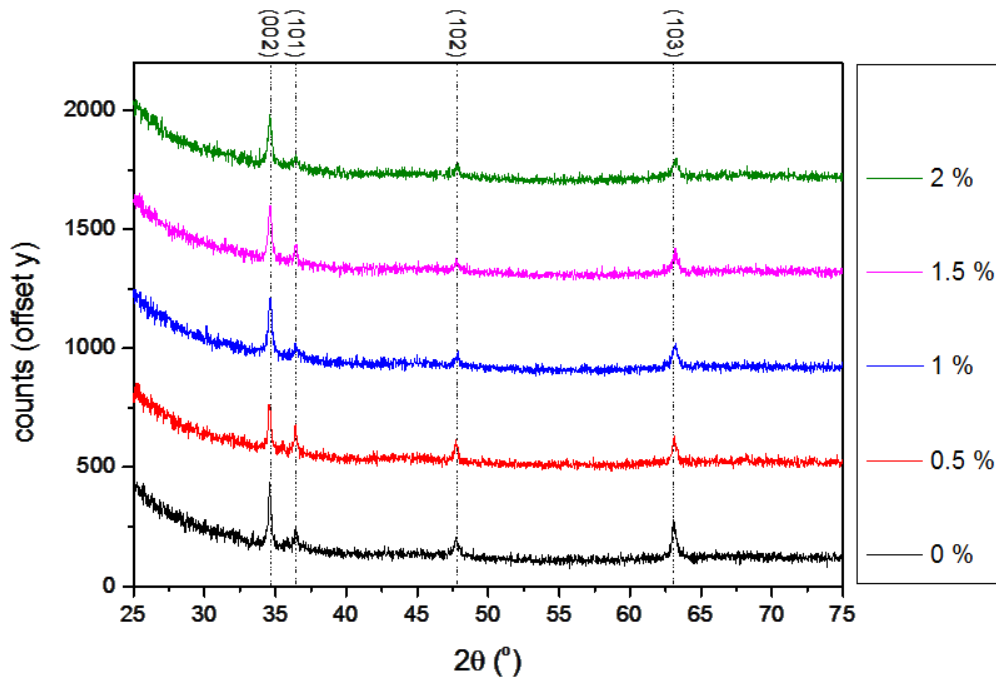


Figure 5. 6 – XRD patterns of ZnO films doped with 0-2 at% Al on glass substrates. The different orientations of the wurtzite structure are labelled.

The Al doping does not have a significant effect on the appearance of the XRD pattern. The relative intensities of the orientations remain relatively consistent throughout. The XRD patterns do not shed any light on the varying charge mobility seen in the doped samples. The charge mobility maxima at 1 at% Al displays a similar XRD pattern to the minima at 0 and 2 at% Al.

XRD patterns shown in Figure 5. 6, do not display the presence of secondary phases developing after 0.5 at%, however, this does not confirm that they are not present. It is unlikely the secondary phases would be seen at such a low concentration using this technique. Furthermore, the most probable secondary phase (Al_2O_3) crystallises at a much higher temperature than those used for deposition and would likely to be amorphous, and not detectable by XRD, if it were present. As such, a more powerful technique was required to probe the samples to gain an improved understanding of position the aluminium within the lattice.

Cross sectional TEM was performed, and EDX was used to analyse the elemental composition of the film. A lamella was cut from films doped at 0.5 and 2 at% aluminium using a FIB and the cross sections were imaged using TEM. Point scans were carried out upon samples using EDX to confirm that the dopant in the precursor solution had transferred into the film at the correct atomic percentages. The results of this analysis are shown in Figure 5. 7 and Figure 5. 8

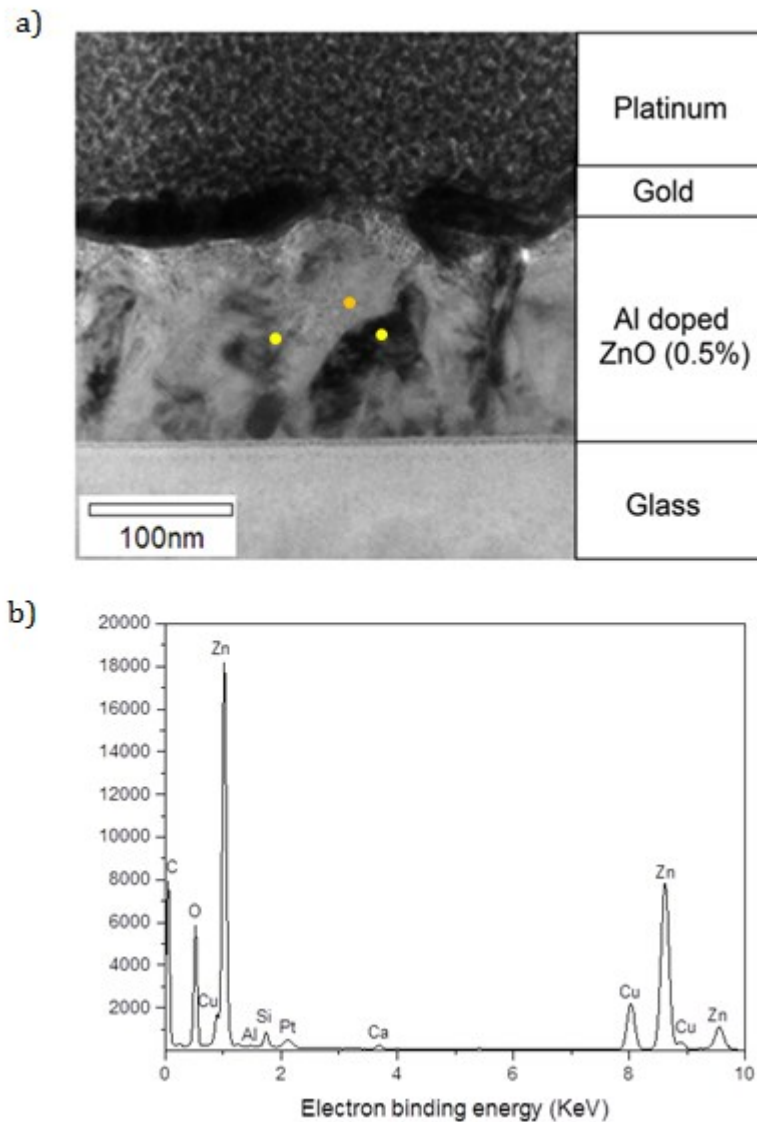


Figure 5. 7 - a) shows a TEM image of a ZnO film doped with 0.5 at% aluminium, the glass substrate and protective layers are also labelled. b) shows an EDX elemental spectra (orange dot area on a)), zinc, oxygen and aluminium are labelled. Peaks from silicon and platinum can also be seen along with copper which originates from the sample holder. Two other point scans (yellow dots on a)) were also taken showing similar spectra.

The three point scans were taken within grains, giving an average Al composition of 0.55 at% within the film. This suggests that the ratio of oxide to dopant from the precursors is transferred into the film. The 0.05 at% difference in the calculated at% and intended doping level is within error of the equipment.

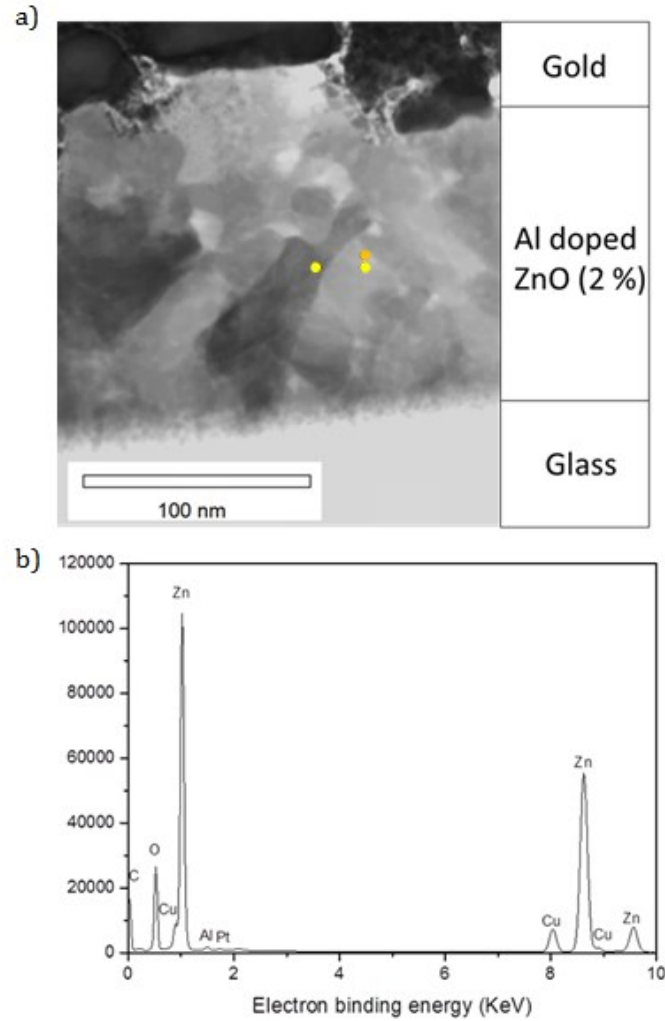


Figure 5. 8 -a) shows a TEM image of a ZnO film doped with 2 at% aluminium, the glass substrate and protective layers are also labelled. b) shows an EDX elemental spectra - zinc, oxygen and aluminium are labelled. Peaks from platinum can also be seen along with copper which originates from the sample holder. The position of the three point scans are marked, with the sample shown in b) in orange and the position of two repeated measurements in yellow.

The spectra suggest that the aluminium is well distributed throughout the film and shows that the dopant level in the deposited films can be accurately controlled by addition of dopant salt into the precursor. There were not obvious secondary phases seen in the films, however, it has been suggested that phases of aluminium can precipitate and migrate to grain boundaries. [153], [176], [177] To investigate whether this was the case for films doped past 0.5 at% an EDX line scan was performed across a grain boundary on the 2 at% aluminium doped sample.

The first study determined whether the areas of different shades on the TEM micrographs actually represented different grains. By taking a highly resolution image of the films the different crystallite regions can be identified. A typical TEM micrograph is shown in Figure 5. 9.

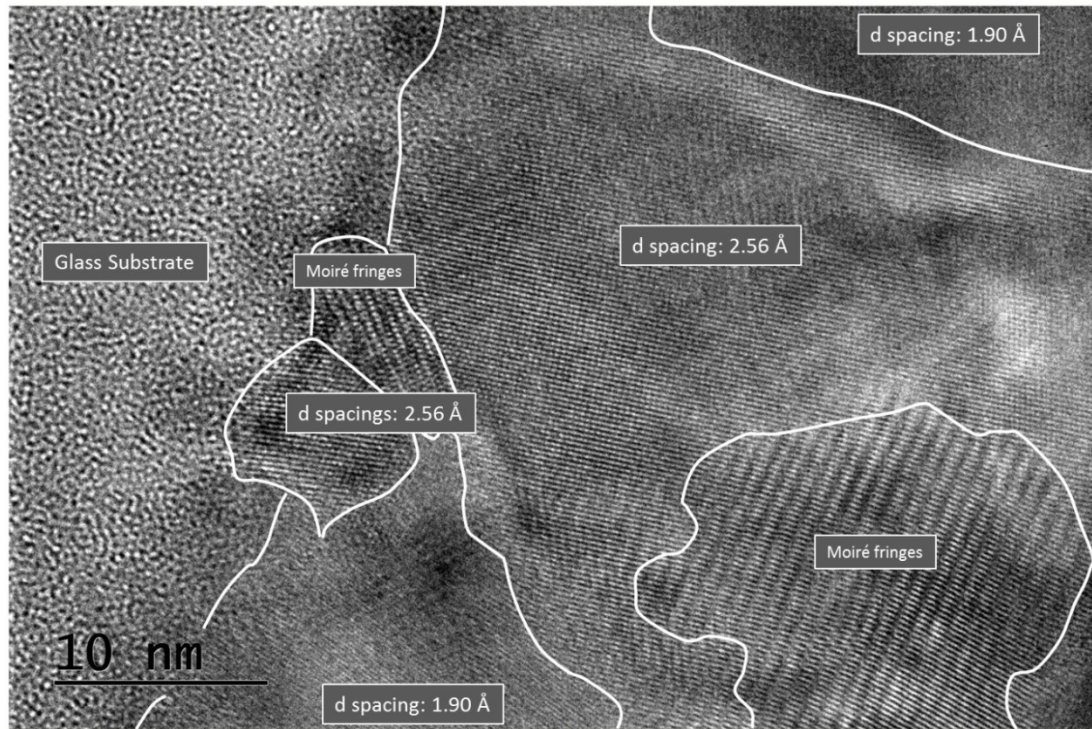


Figure 5. 9 – A TEM image of ZnO doped with 2 at% Al. Individual crystallite regions are highlighted in white.

Figure 5. 9 shows the positions of the different crystallites based upon the interference lines. These lines are caused by the lattice and the gap between the lines represents the lattice spacing. The d spacing of the different orientations, extracted from the XRD patterns shown in Figure 5. 6, are specified in Table 5. 5.

Crystallite orientation	d spacing (Å)
(002)	2.59
(101)	2.47
(102)	1.91
(103)	1.47

Table 5. 5 – d spacings of different orientations taken from the 2 at% AZO XRD data.

The distances between the interference lines were measured using the imaging software 'ImageJ'. An average was taken of 20 measurements. The areas with a d spacing of 1.90 Å are crystallites in the (102) orientation whilst the areas of with a d spacing of 2.56 Å are likely crystallites in the (002) orientation, although due to a very similar d spacing, it is not possible to discount the possibility that some, or all, of these sections are in fact crystallites in the (101) orientation.

The image in Figure 5.9 shows that the film is polycrystalline with grains consisting of individual crystallites. The size and shape of the crystallites are consistent with the areas of different shades seen in the SEM and TEM images of the ZnO film. Therefore an EDX line scan across these areas will give an elemental profile between two crystalline grains and any build-up of aluminium in these areas would be detected. An EDX line scan across a grain boundary is shown in Figure 5.10.

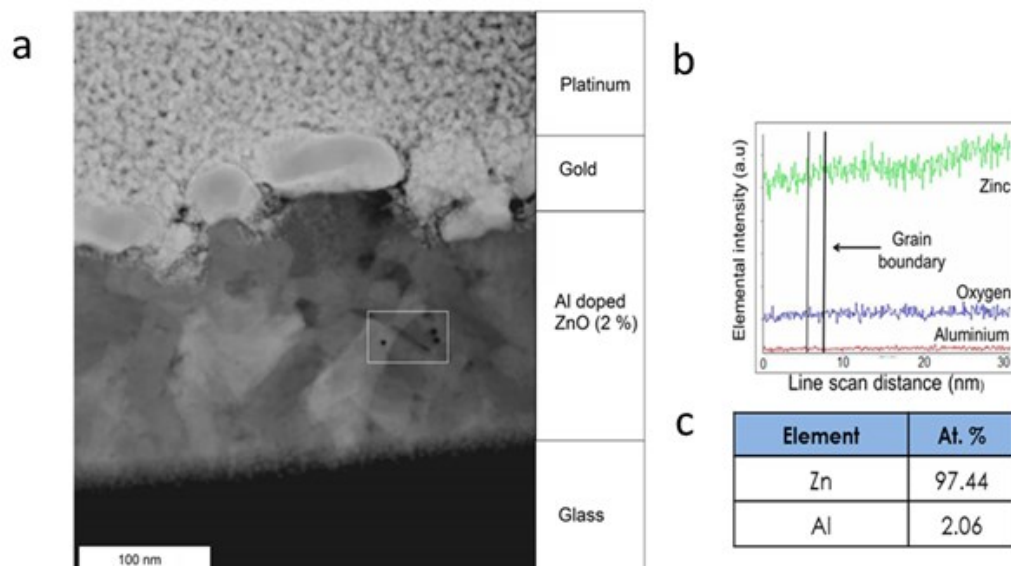


Figure 5.10 – EDX line scan of 2 at% Al doped ZnO. a) shows a dark field image of a cross section of the ZnO film. The different layers in the cross section are labelled and the damaged area where the line scan was performed (as well as three point scans) is highlighted in the white square. b) shows the elemental intensity of zinc, oxygen and aluminium across the line scan. c) shows the average elemental percent of Zn and Al across the scan.

The line scan confirms the point scans; there is 2 at% Al present in the film. Across the grain boundary there is no noticeable variation in the levels of Al, and the Al appears to be spread homogeneously throughout the film. There are no Al rich areas observed, this implies that the aluminium is being taken up evenly by the ZnO lattice.

It was impossible to measure the oxygen content accurately using this technique so Zn:O ratios were not investigated

The film with the highest doping level was chosen to provide the most sensitive signal. If there is no variation in aluminium content across the grain boundary of the 2 at% sample, it can be safely assumed that this is also the case for the films with less aluminium present. This suggests that the aluminium is not migrating to the grain boundaries, eliminating grain boundaries as a significant site for the aluminium build up post 0.5 at% (when the charge carrier concentration saturates).

If secondary phases are eliminated, two possibilities remain for the position of the Al in the lattice once all donor substitutional sites are filled. One possible destination for the Al is that, after the saturation point, the ions could fill interstitial sites. It has been suggested that the lattice strain can become too great when there are many smaller ions present. This could force the ions to fill neutral, interstitial sites and no longer add charge carriers to the system. If this were the case, the lattice strain should be visible in the XRD spectra, with either peak broadening or shifts in the position of the reflections. This was not seen in the XRD pattern shown in Figure 5. 6. The lack of visible lattice strain in the XRD spectra suggests this process was also not dominant.

The other possibility is that the dopants could remain in the substitutional positions, but become forced into neutral donors. It has been suggested that when too many 3+ dopant ions are present the repulsive effect of the extra positive charges will force further dopant ions into the standard 2+ state. [178]. Al would then become a neutral donor not adding free carriers to the conduction band but remaining in a substitutional position within the lattice.

To gain further insight into the mechanisms driving the saturation, the points between 0 – 0.5 at% were studied in detail. It is between these dopant percentages that the charge carrier concentration increases by two orders of magnitude and there are few studies to date examining this doping region in the spray pyrolysis system. Examining the structural and optoelectronic properties over this region may help elucidate the nature of Al doping in the ZnO system.

5.2.3 Aluminium at Low Doping Levels

The increase in the charge carrier concentration occurs between 0 and 0.5 at% Al content. The results measured do not however, give any insight as to a specific percentage the charge carrier concentration saturates. This work is not seen in the literature as the Hall effect measurements are difficult to obtain at high resistivity. Advances in measurement techniques using AC Hall effect in 'high resistivity' mode allowed the probing of aluminium down to low dopant levels.

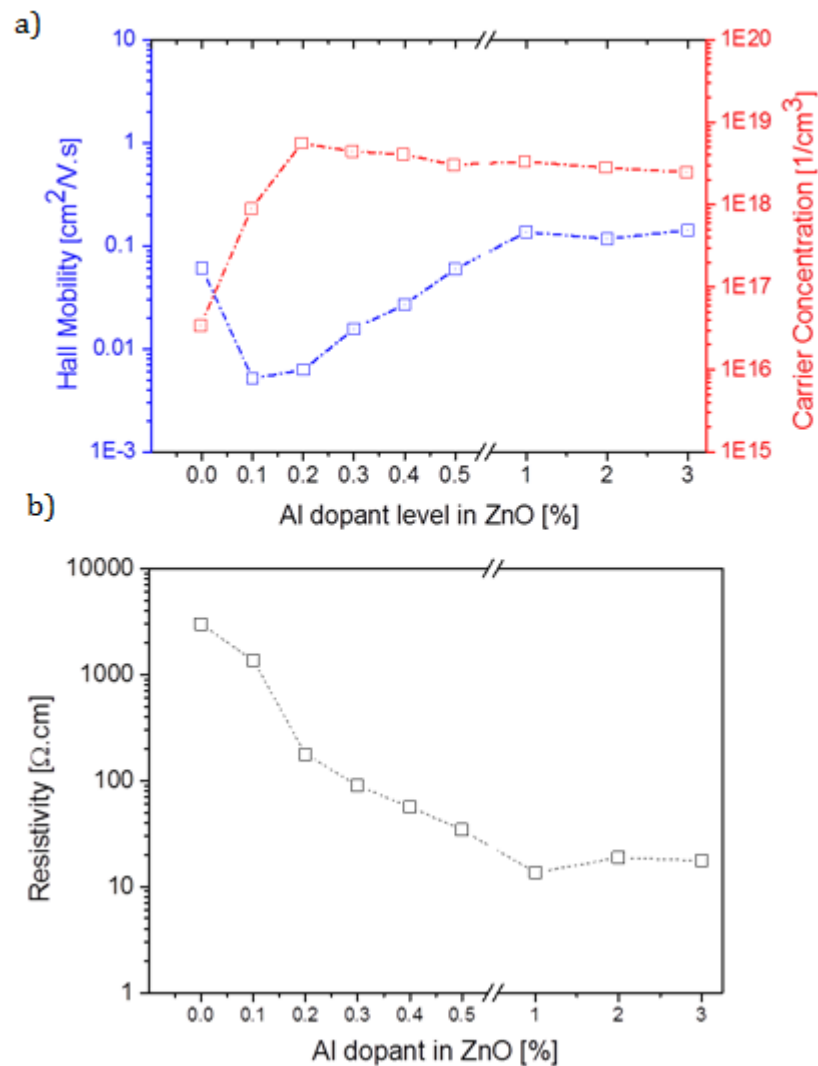


Figure 5. 11 - a) shows the Hall charge mobility and charge carrier concentration of aluminium doped into ZnO at 0-3 at% highlighting low level doping from 0-0.5 at%. Charge carrier concentration is displayed in red and hall charge mobility in blue. b) shows the resistivity of those same films.

Figure 5. 11 shows the measured charge carrier concentration, AC Hall charge mobility and resistivity values for the AZO. This data matches well with that displayed in Figure 5. 5 and fills in the gap between 0 and 0.5 at%. The addition of 0.1 at% Al results in a sharp rise in free carriers: from $3.65 \times 10^{16} \text{ cm}^{-3}$ in ZnO to $8.84 \times 10^{17} \text{ cm}^{-3}$. The increase in charge carrier concentration saturates at 0.2 at% and $5.61 \times 10^{18} \text{ cm}^{-3}$. After saturation little variation in charge carrier concentration is observed.

The charge mobility falls sharply on the addition of Al from $0.07 \text{ cm}^2/\text{V.s}$ to $0.005 \text{ cm}^2/\text{V.s}$. The carrier charge mobility begins to increase above 0.1 at% doping with the carrier charge mobility of undoped ZnO eventually being recovered. When comparing charge carrier concentration and charge mobility, it appears that the carrier charge mobility initially mirrors the charge carrier concentration data suggesting a correlation between the two.

As a result of the variation in the charge carrier concentration and charge mobility, significant changes in film resistivity are seen where doping to 1 at% results in a 2 orders of magnitude reduction in resistivity from the undoped ZnO ($3000 \text{ }\Omega\cdot\text{cm}$) reaching a minimum value of $13.6 \text{ }\Omega\cdot\text{cm}$. At a film thickness of around 150 nm, the film properties measured are consistent with films of comparable thickness reported in the literature and new trends at low doping levels highlighted in this work.

5.2.3.1 Analysis by UV-Vis for Low Dopant Studies

By studying the optical properties of the ZnO system information can be gained regarding the size of the band gap. As this can be altered by the addition dopants to the system it gives up another method of investigating dopant behaviour in the films. UV-Vis spectroscopy was used to analyse if there were any changes to the optical properties upon the addition of aluminium to the system (Figure 5. 12).

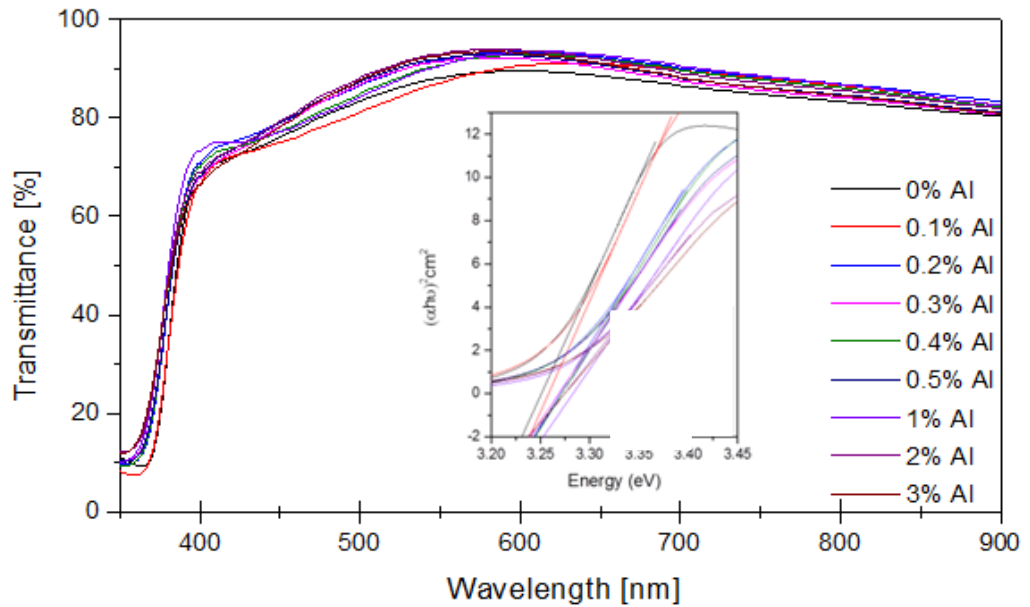


Figure 5. 12 – UV-Vis spectra of ZnO films doped 0 - 3 at% Al. Insert shows Tauc plots of films

The spectra of the doped films match well. All display excellent transmittance of over 85 % at 530 nm. This data suggests that doping has little effect on the optical properties of the films. From the UV-Vis spectra the band gap was extracted using Tauc plots (Figure 5. 12 – insert). The band gap of the oxide films remains similar in all films. A slight increase of 0.01 eV is seen between 0 and 1 at% which may be attributed to a Burstein-Moss shift.

5.2.3.2 Analysis by XRD for Low Dopant Studies

The films were analysed by XRD to study the effects of Al addition on the structural properties at low doping levels shown in Figure 5. 13.

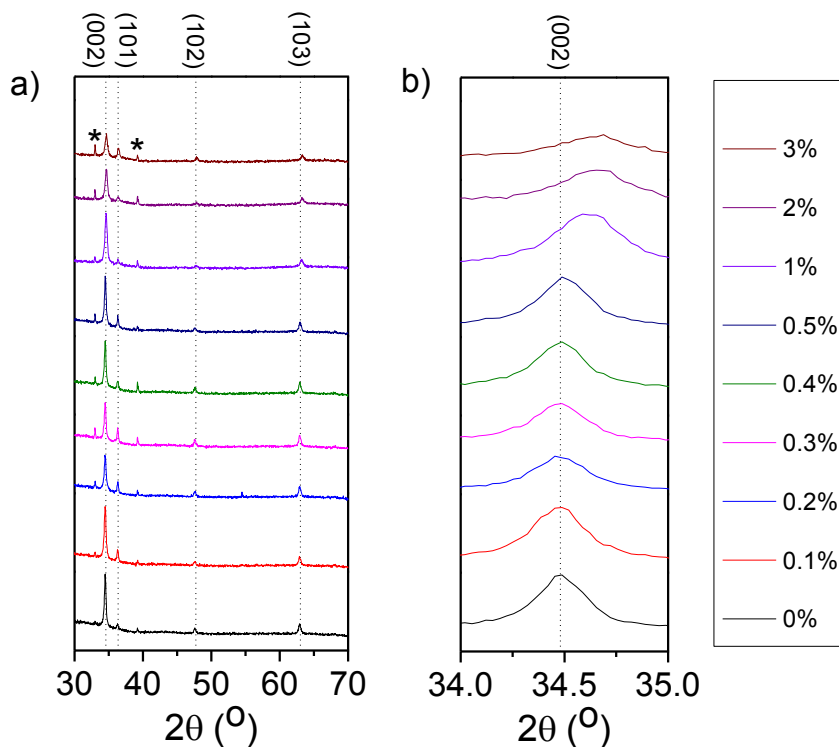


Figure 5. 13 – XRD patterns of Al doped films. a) shows the full spectrum of each dopant level on an offset axis. b) shows a zoomed in view of the dominant (002) orientation.

The XRD patterns display a preferential orientation towards the (002) reflection in all films. Looking at the pattern between 34-35 $^{\circ}$ 2θ , the intensity and position can be seen to vary at higher dopant levels, with a shift to higher angles seen in the 1, 2 and 3 at% samples and a decrease in intensity seen in the 2 and 3 at% samples. The UV-Vis data (Figure 5. 12) confirms profilometry measurements giving confidence that the decrease in crystallinity is not due to any thickness related effect. Therefore, this change must be due to structural changes within the film.

Aluminium incorporated into interstitial sites can add strain to the system and this in turn could decrease the crystallinity. This could help identify the position of the aluminium in the lattice post 0.2 at%. However, strain in the system should also cause a peak broadening effect; this cannot be seen in the diffraction patterns and therefore this explanation is unlikely. Furthermore, a shift to higher angles would suggest a decrease in the lattice size; this wouldn't be expected from the addition of interstitial atoms.

Analysis of the texture coefficients, extracted from XRD patterns of the films, confirms a strong preference towards the (002) orientation for all dopant concentrations (Figure 5. 14). There is a drop in the degree of preferred (002) orientation from 0-0.5 at% which is coupled with an increase in the (103) orientation.

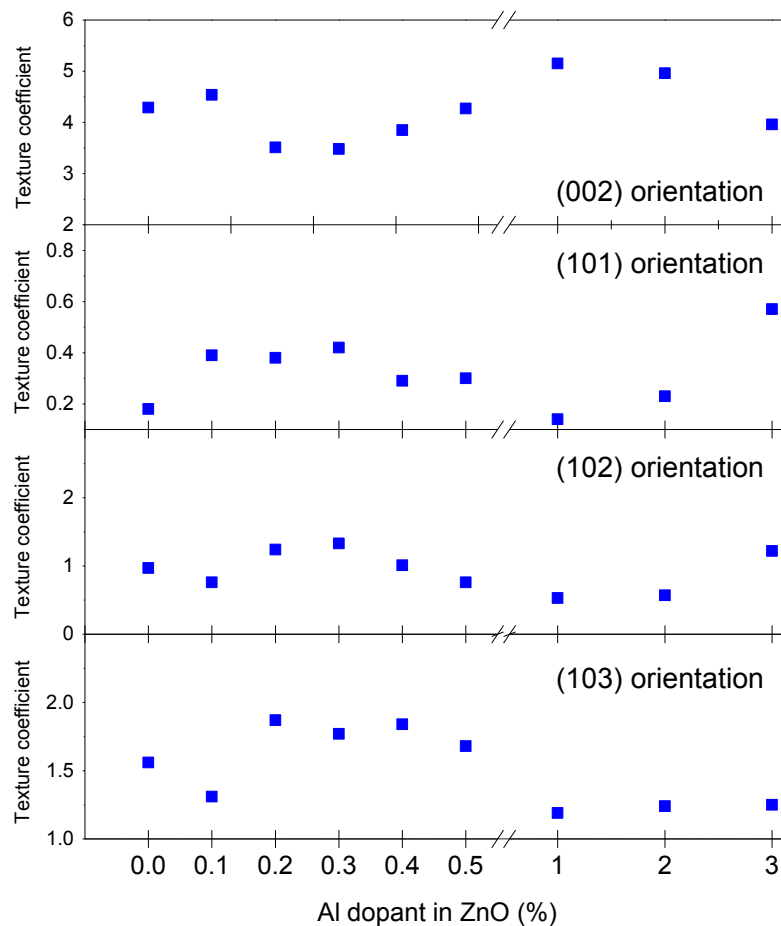


Figure 5. 14 – Texture coefficients of ZnO doped with varying levels of aluminium extracted from Figure 5. 13.

The trend in the (002) texturing, shown in Figure 5. 13, may give some insight into the variation in charge mobility. The decrease in (002) texture from 0-0.2 at%, then subsequent increase to a maximum at 1 at%, matches the trend seen in the charge mobility. The crystallite size was extracted from the XRD patterns shown in Figure 5. 13 using the Scherrer equation. In a system where grain boundaries dominate the charge mobility, the crystallite size can have a profound effect on the electronic properties. The crystallite sizes of the aluminium doped samples are shown in Figure 5. 15.

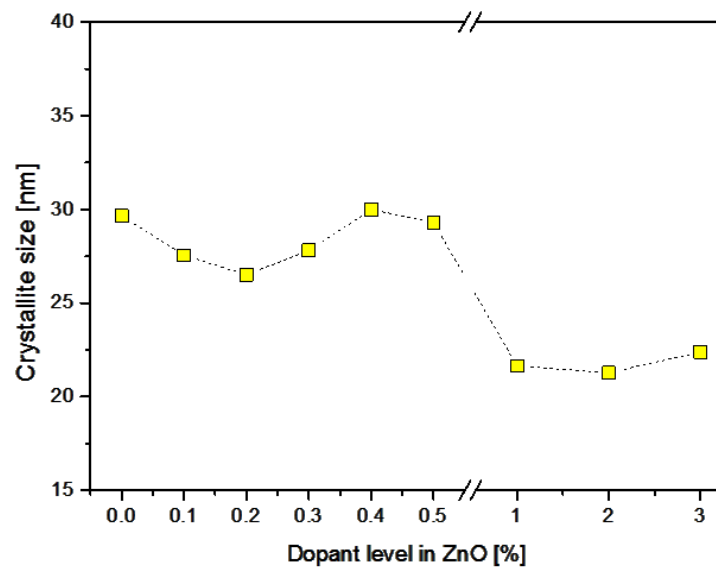


Figure 5. 15 – Crystallite size of ZnO samples doped with varying levels of aluminium.

The crystallite sizes are similar until 0.5 at% where a decrease of 6 nm is seen in the average size. This drop in crystallite size is not reflected in the electrical properties, suggesting that the electronic properties are not dominated by grain boundaries but, instead, by another parameter. As the crystallite size is calculated from the XRD peak width, there is another possible explanation; the observed broadening may be caused by lattice strain and not the crystallite size. Considering the addition of Al to the lattice, such strain is possible and indeed probable. Whether this would be the dominant process however, is not clear. As such, SEM was used to directly probe the grain size of the film.

5.2.3.3 Analysis by SEM for Low Dopant Studies

To gain a more in depth idea of how doping affects the grain size and topography of the ZnO films three SEM micrographs were recorded and are shown in Figure 5. 16.

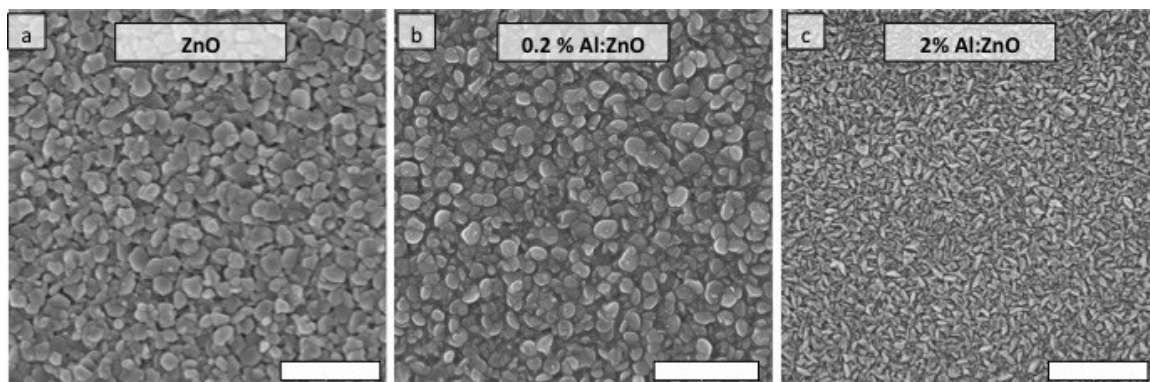


Figure 5. 16 – SEM micrographs of films doped with a) 0 at%, b) 0.2 at% and c) 2 at%. Scale markers indicate 1 μm .

The micrographs displayed in Figure 5. 16 were taken at 0 at% (a); at the point of carrier saturation 0.2 at% (b); and after the charge mobility has plateaued at 2 at% (c). At 0.2 at% doping the grains show no appreciable change in size or shape compared with undoped ZnO. However, when doping is increased to 2 at% the film appears to be comprised of much smaller grains than the undoped ZnO. The shape of the grains also appears to be affected by the increasing dopant level. Changes in the surface morphology may be consistent with the subtly reduced (002) peak intensity observed in the XRD data. The change in size displayed in the SEM micrographs is much more dramatic than was suggested by XRD analysis. In both methods however, grain size decreases with increased doping.

A decrease in grain size would increase the grain boundary concentration in the system. If grain boundary scattering dominated, a decrease in the charge mobility would be expected. The measured electrical properties however, show an increase in charge mobility. As such, grain boundary scattering can be excluded as a dominant factor in determining electronic properties.

5.2.3.4 Analysis of doping mechanisms in AZO

Analysing the data described above, and in partnership with theory described in Chapter I, a mechanism for the electronic behaviour is proposed:

1. Electronic properties: 0-0.2 at% aluminium doping
 - The observed electronic properties are explained by Al^{3+} impurities filling Zn^{2+} positions in the wurtzite lattice.
 - The increase in charge carrier concentration is caused by free electrons added to the conduction band by Al_{Zn} defects.
 - The reduction in charge mobility is believed to be caused by the combined effect of an increase in ionised impurity scattering, as suggested by theory on scattering mechanisms (see 1.4.3.3); an increased charge-charge and charge-phonon interactions; [179] and changes in the orientation of the films as suggested by texture analysis.
 - The increase in charge carriers far outweighs the reduction in charge mobility and results in a sharp decrease in resistivity

2. Electronic properties: 0.2-1 at% aluminium doping
 - The electronic activity in this previously unstudied region was not easily explained.
 - The continued decrease in lattice spacing beyond the saturation point, measured from XRD analysis, suggests that Al^{3+} ions are not filling interstitial sites.
 - TEM analysis, coupled with the sustained drop in resistivity, implies that the formations of insulating secondary phases e.g. Al_2O_3 or ZnAl_2O_4 are unlikely.
 - Considering the low at% at which the saturation occurs; the hypothesis that charged species force subsequent ions into neutral, non-donating states appears unlikely.
 - The decrease increase crystallite size confirms that the process is not driven by grain boundary scattering.
 - Finally the variations in (002) orientation could potentially explain the increase in charge mobility but does not explain the saturation in charge carrier concentration.

The hypothesis proposed to explain these observations, is that Al^{3+} impurities combine with V_{Zn} to form hybrid $\text{Al}_{\text{Zn}}V_{\text{Zn}}$ acceptor defects. This theory is explain in detail below:

- At 0.2 at% the measured charge carrier concentration saturates.
- As Al_{Zn} defects are added to the system, the Fermi energy is increased and the energy of V_{Zn} doubly accepting defect is lowered.
- Singly accepting hybrid $\text{Al}_{\text{Zn}}V_{\text{Zn}}$ defects become thermodynamically preferable.
- Further free electrons from the Al^{3+} are trapped in this defect and do not add to the conduction band.
- V_{Zn} doubly trapping defects are replaced by singly trapping $\text{Al}_{\text{Zn}}V_{\text{Zn}}$ defects, as proposed by Johansen *et al* [29]. This allow easier movement of charge across the thin film increasing charge mobility.
- The decrease in resistivity from 0.2-1 at% is driven by the increase in charge mobility caused by the filling of charge trapping states
- This theory requires the assumption that the ambient deposition conditions result in an oxygen rich growth environment. This reduces the formation energy of V_{Zn} acceptor defects and also increases the formation energy of Zn_i and V_o donor defects.
- This theory is also consistent with the lower charge carrier concentrations measured in SP deposited films compared with zinc rich environments of well-studied vacuum techniques such as PLD and magnetron sputtering - where charge carrier concentrations in the order of 10^{21} cm^{-3} are reported. [46]

Testing for these hybrid defects would provide for interesting future work in this field however in this thesis the theory remains as speculation.

3. Electronic properties: 1-3 at% aluminium doping

- Al no longer forms Al_{Zn} defects, instead migrating to grain boundaries at concentrations lower than our EDX detection limit.
- Charge carrier concentration remains saturated as no further electrons are added to the conduction band
- Charge mobility stabilises as $\text{Al}_{\text{Zn}}V_{\text{Zn}}$ defects are no longer formed meaning that electrons do not passivate trapping states.
- Resistivity begins to increase (albeit slowly) as insulating secondary phases begin to form

5.3 Doping with Gallium and Indium

Other group 3 dopants also show promise at improving the conductivity of ZnO both in the literature and from initial experiments. This section investigates the properties of Ga and In doped films and compares them with those doped with Al.

The mechanism for improved conductivity is the same as for aluminium; the 3⁺ ions substitute into the ZnO lattice replacing the zinc ions and adding free charge carriers to the conduction band.

ZnO films doped with 0 – 3 at% Ga and In were deposited under the same conditions and dopant range as for the aluminium doped samples.

The electrical properties of the samples were measured using the Hall effect, shown in Figure 5. 17 and Figure 5. 18.

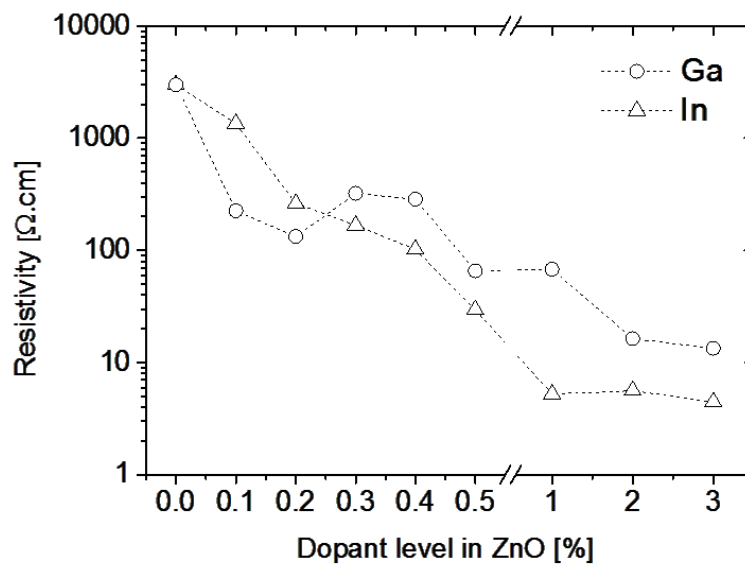


Figure 5. 17 – Resistivity of ZnO films doped with 0-3 at% of gallium and indium.

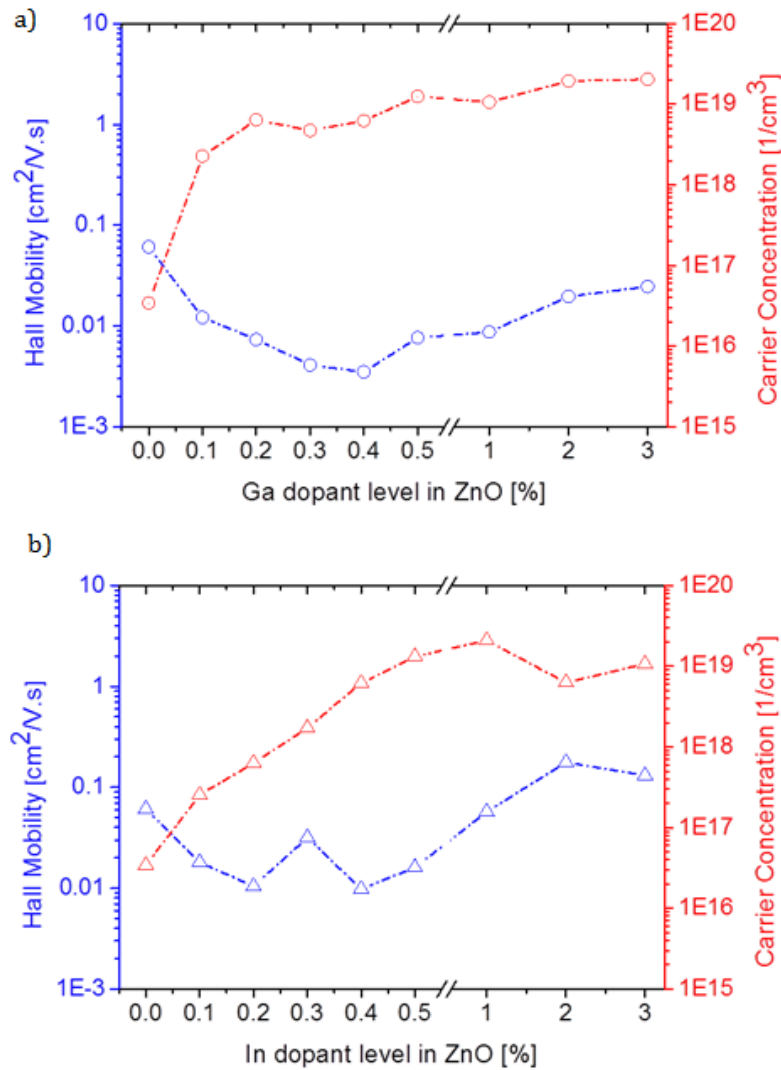


Figure 5. 18 - Hall charge mobility and hall charge carrier concentration of ZnO samples doped with 0-3 at% gallium (a) and indium (b).

In Figure 5. 17 the resistivity is shown to decrease by two orders of magnitude between 0 and 0.5 at% in both Ga and In doped samples. In the GZO samples the resistivity then slowly decreases until 3 at%. In the IZO samples the resistivity continues to decrease sharply until 1 at%, whereupon, it levels off and remains stable until 3 at%. Figure 5. 18 suggests that the three orders of magnitude decrease in resistivity is driven by a three order of magnitude increase in the charge carrier concentration. The saturation points of the dopants differ from the AZO trend, however, the drop and subsequent recovery of charge mobility, replicates that trend observed for the AZO samples.

The saturation level of carriers in the samples varies according to the dopant. AZO reaches a maximum charge carrier concentration of $5.36 \times 10^{18} \text{ cm}^{-3}$ at 0.3 at% (at this point GZO measures $4.74 \times 10^{18} \text{ cm}^{-3}$ and IZO measures $1.71 \times 10^{18} \text{ cm}^{-3}$); GZO saturates at 0.5 at% with a charge carrier concentration of $1.24 \times 10^{19} \text{ cm}^{-3}$ (here IZO measures $1.32 \times 10^{19} \text{ cm}^{-3}$); and IZO saturates at 1 at% with a charge carrier concentration of $2.01 \times 10^{19} \text{ cm}^{-3}$.

The maximum amount of dopant which can be incorporated into the lattice may be linked to the ionic radii of the different dopants. The 3+ dopants are substituting for zinc in a 4 coordinate lattice position, usually filled by a zinc ion (0.6 Å). The Al^{3+} ion (0.39 Å) has the largest difference with the Zn, followed by Ga^{3+} (0.47 Å), and then In^{3+} (0.62 Å) which has the most similar ionic radius. The size difference is believed to increase lattice strain and thus lower the solubility of the dopant in the lattice. The indium with the closest match in ionic radius has the highest solubility and aluminium with the poorest match has the lowest solubility.

This hypothesis must be taken loosely, however, as the covalent nature of the ZnO bonding must also be considered. Zn = 1.20 Å; Al = 1.24 Å; Ga = 1.23 Å; In = 1.42 Å. The covalent radii show that Ga has the closest match with Zn, whilst In displays the poorest. If the hypothesis is to be believed it is on the assumption that the bonding in IZO has a largely ionic nature.

5.3.1 UV-Vis analysis of GZO and IZO

UV-Vis spectra of the samples were recorded to study whether the different dopants affected the optical properties of the ZnO films. The results are displayed in Figure 5.19, the UV-Vis spectra for AZO is included for reference.

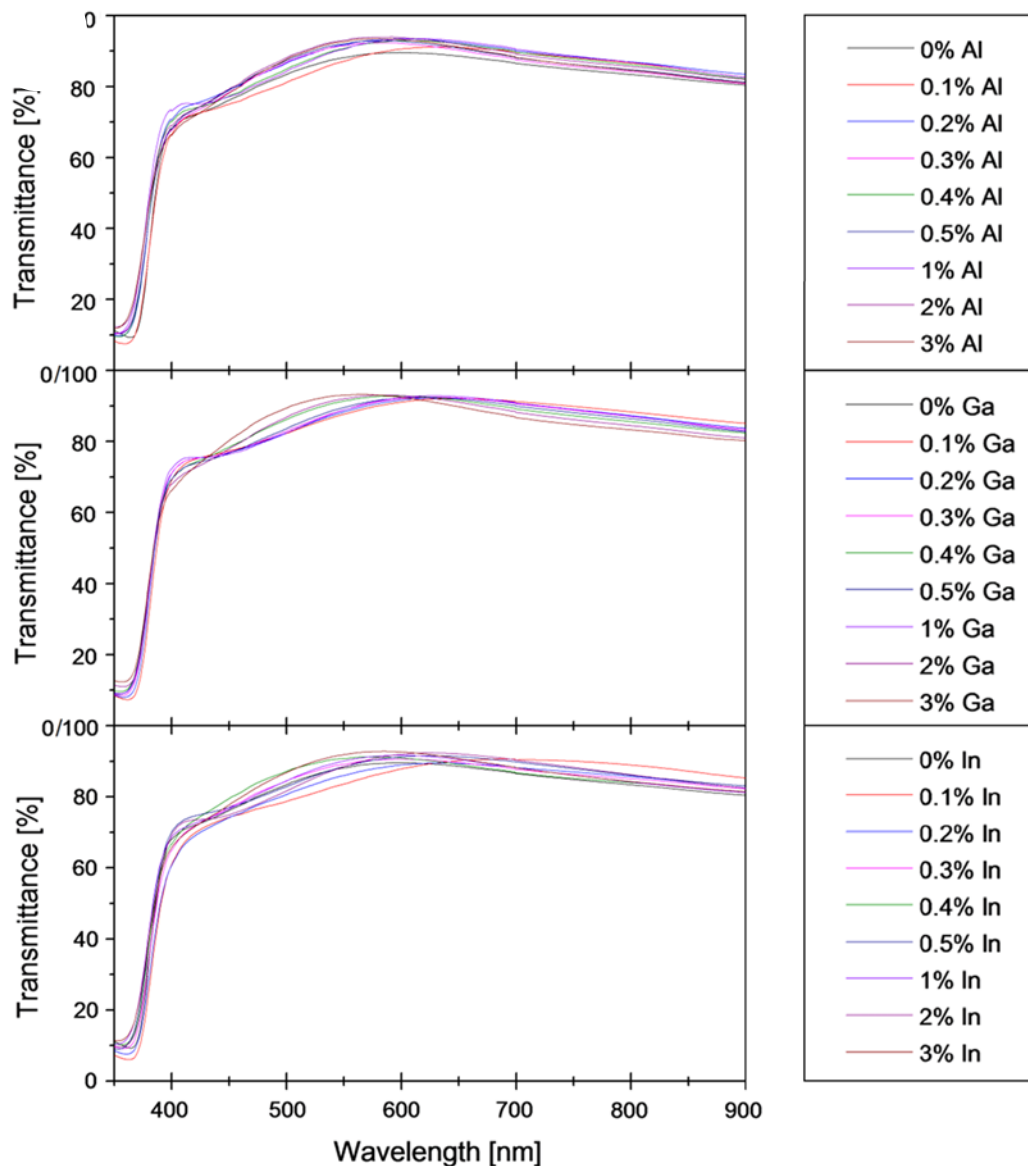


Figure 5. 19 - UV-Vis spectra of ZnO films doped with Al, Ga and In from 0-3 at%

The shape and transmittance of all spectra are similar, showing little variation both with increasing dopant level, and between samples of different dopants. The data suggests that varying dopant types and dopant level (at least up to 3 at%) has no discernible effect on the optical transmission. The films all show an excellent transmittance upwards of 80 % at 530 nm, once again showing the suitability of doped ZnO films for using as transparent coatings. The interference patterns are not strong enough to measure the thickness of the films, however, the similar shape and intensity of the spectra is enough to suggest that the films are of very similar thickness. This is confirmed by profilometry measurements. Considering the large influence film thickness can have on the electronic properties, shown in section 4.2.2, the similar measured thickness of the films gives confidence in the validity of these results.

Tauc analysis was also performed upon the Ga and In doped films shown in Figure 5. 20, the Al doped samples are included for comparison.

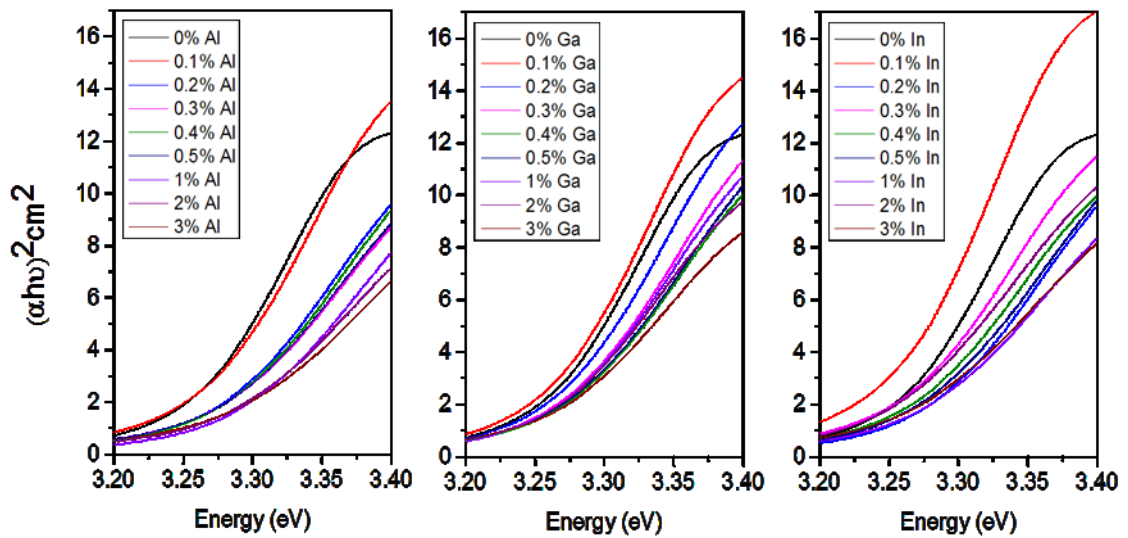


Figure 5. 20 – Tauc analysis of ZnO films doped with Al, Ga and In from 0-3 at%.

The linear part of each line was fitted using Origin software. The band gap was calculated from the gradient and y intercept of the linear fit. All films were all found to be 3.24 ± 0.003 eV and there are no global trends to be seen in the bands gaps of the sample.

The IZO doped samples generally exhibit a slightly lower bandgap; this is observed across all samples, including that at 0 at%. The difference is believed to be a results of minor measurement errors, in particular, from the reference used in the UV-Vis analysis.

5.3.2 XRD analysis of GZO and IZO

XRD patterns were taken of the Ga and In doped films and the results compared with those doped with Al shown in Figure 5. 21.

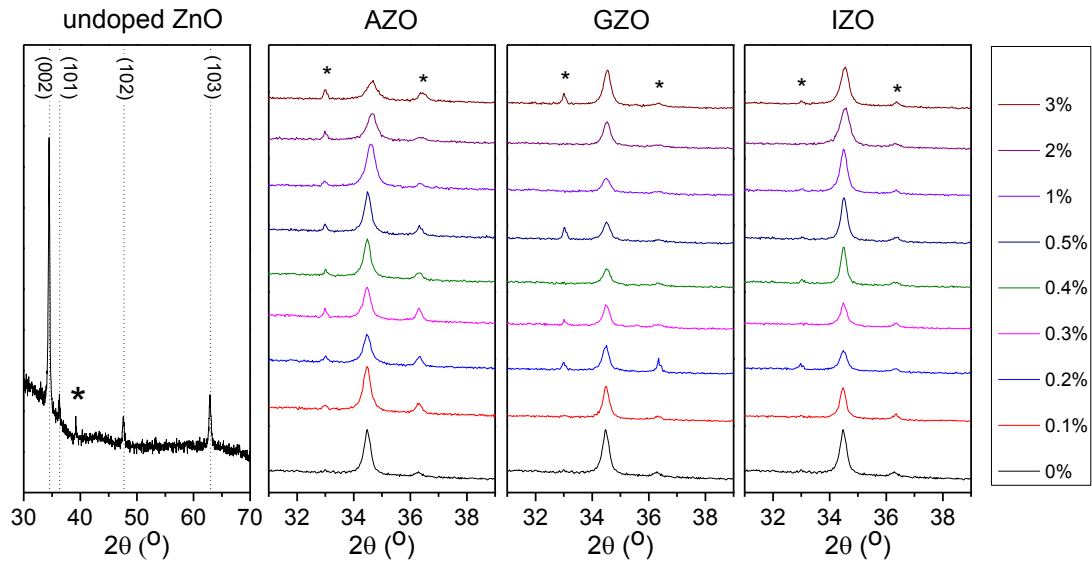


Figure 5. 21 – XRD patterns of ZnO films doped with Al, Ga and In from 0-3 at%. Films were measured post analysis by Hall effect and *s represent metallic indium. a) shows the full pattern of undoped ZnO, b)-d) highlight the dominant (002) peak for AZO, GZO and IZO respectively.

The XRD patterns display a similar preferential orientation towards the (002) reflection at all dopant percentages and across all dopants. Studying the (002) peak in more details, uncovers subtle changes to the crystallinity. Overall there appears to be a general decrease in crystallinity as dopant level increases. This affect is more pronounced as the ion size is reduced (AZO>GZO>IZO) suggesting this may be a result of lattice strain.

Differences in the lattice size caused by doping with Ga and In was measured from the $d_{(002)}$ spacing calculated from the positions in Figure 5. 21. No discernable change in lattice size is seen upon addition of Ga and In with all films displaying a $d_{(002)}$ of 2.58 Å.

The degree of texturing towards (002), (101), (102) and (103) was calculated from the XRD patterns shown in Figure 5. 21, the results of which are shown in Figure 5. 22.

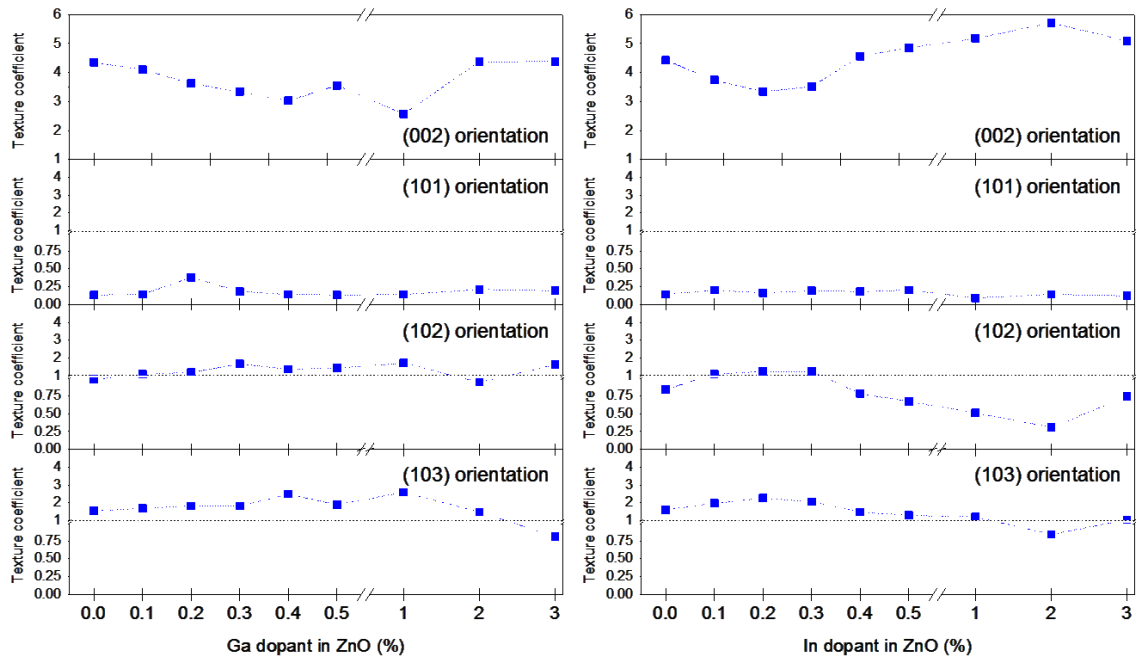


Figure 5. 22 – Texture coefficients of (002), (101), (102) and (103) orientations for GZO and IZO films doped from 0-3 at%.

The degree of preferential orientation towards the (002) once again matches well with the trends in charge mobility; in fact the correlation is stronger with GZO and IZO than it is with AZO. These correlations are highlighted in Figure 5. 23.

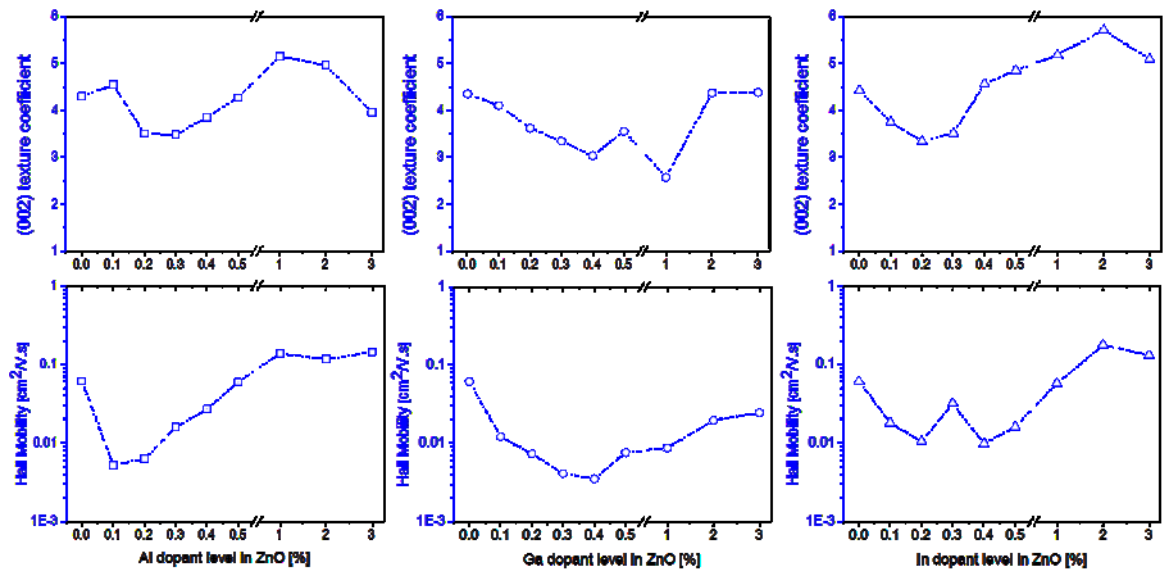


Figure 5. 23 – (002) Texture coefficients of 0-3 at% AZO, GZO and IZO (top) compared with carrier charge mobility (bottom)

Whether the variation in charge mobility is driven by the degree of (002) texturing, or that both the charge mobility and texture are controlled by an exterior factor is not clear.

In favour of texturing directing charge mobility; greatly improved charge mobility was observed when undoped ZnO was templated towards the (002) as seen section 4.2.15 (albeit with large increases to crystallinity and grain size).

However, the changes in texturing can be also associated with changes to the defect chemistry. This is seen as addition of dopant impurities causes variations in the texturing of films. The fact that impurities defects formed are electronically active, suggests that the trends seen in texture and charge mobility are both linked to the variations in defect states present in the films.

The crystallite size was extracted from the XRD patterns shown in Figure 5. 21 using the Scherrer equation. The crystallite sizes of the GZO and IZO samples are shown in Figure 5. 24.

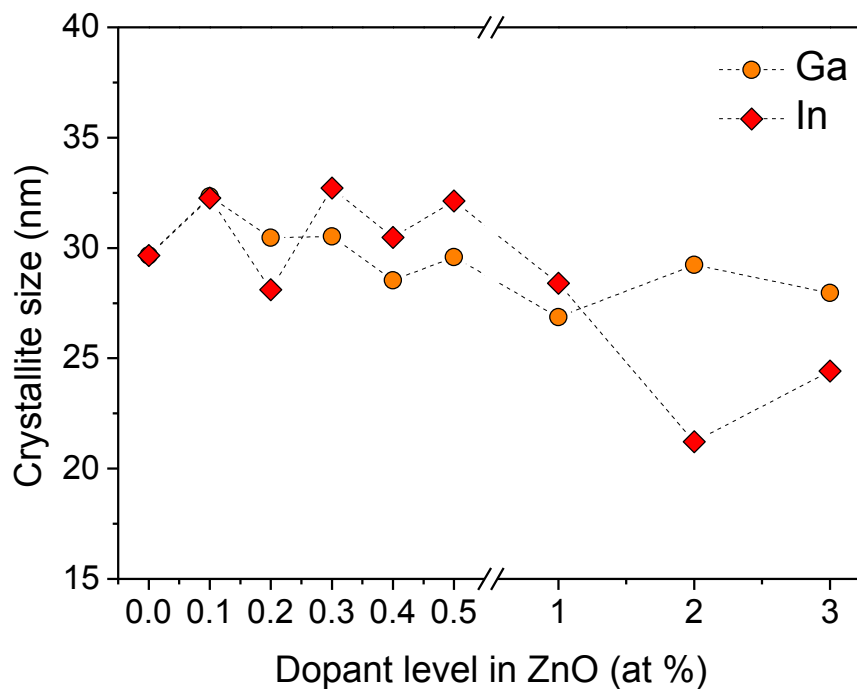


Figure 5. 24 – Crystallite size of ZnO samples doped with varying levels of Ga (orange) and In (red).

The crystallite sizes of GZO and IZO are similar until 0.5 at%. After this point a decrease of 10 nm is seen in the average size of IZO crystallites to a minimum of 21 nm. GZO does not decrease in the same way as IZO (or AZO). Again the drop in crystallite size is not reflected in the electrical properties of IZO backing up the theory the electronic properties are not dominated by grain boundaries in trivalently doped ZnO.

5.3.3 SEM analysis of GZO and IZO

To gain a more in depth idea of how doping affects the grain size and topography of the ZnO films, three SEM micrographs were recorded for GZO and IZO at doping of 0, 0.2 and 2 at%. These are shown in Figure 5. 25, the micrographs for AZO are shown for comparison.

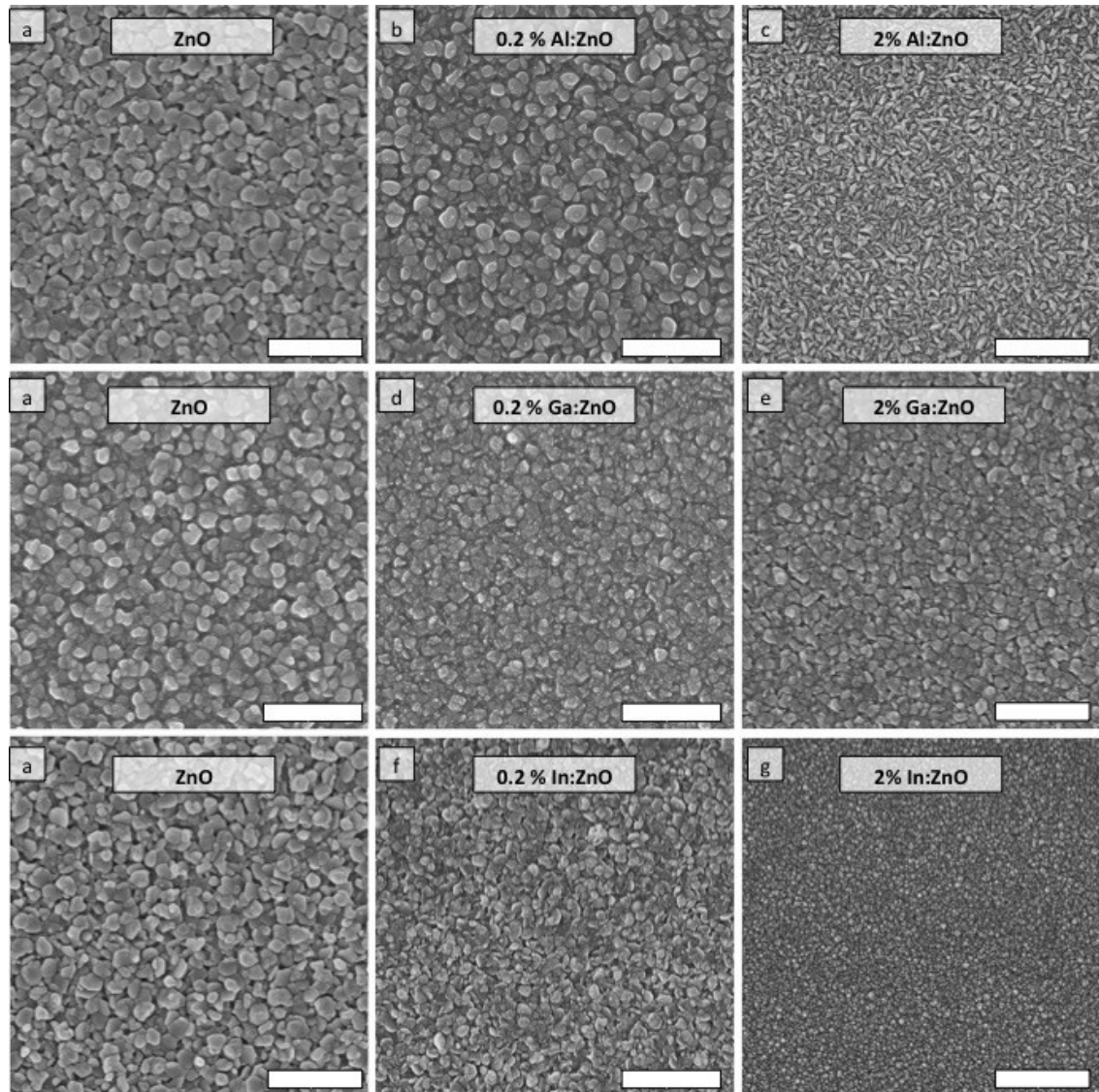


Figure 5. 25 – SEM micrographs of films doped with a) 0 at%, b) 0.2 at% AZO, c) 2 at% AZO, d) 0.2 at% GZO, e) 2 at% GZO, f) 0.2 at% IZO and g) 2 at% IZO. Scale markers indicate 1 μm.

The micrographs displayed in Figure 5. 25 were taken at 0, 0.2 and 2 at% for comparison with AZO. At 0.2 at% doping the GZO shows little change in size or shape compared with ZnO, whereas, a slight decrease is seen in IZO. When doping is increased to 2 at% GZO once again seems to show little change, however, the IZO film shows a large decrease in grain size.

The changes in the surface morphology are consistent with crystallite size measurements taken by XRD (Figure 5. 24) and back up the conclusions that the electronic properties are not dominated by grain size but instead by ionised impurity scattering.

5.3.4 Doping mechanisms in GZO and IZO and a comparison with AZO

Analysing the data described in section 5.3 and in partnership with theory, mechanisms for discrete sections of GZO and IZO doping are proposed.

5.3.4.1 Doping with Gallium

1. Electronic properties: 0-0.2 at% gallium doping

- The observed electronic properties are explained by Ga^{3+} impurities filling Zn^{2+} positions in the wurtzite lattice. The doping of Ga is very similar to that of Al.
- The increase in charge carrier concentration is caused by free electrons added to the conduction band by Ga_{Zn} defects.
- Reduction in charge mobility is believed to be caused by the combined effect of an increase in ionised impurity scattering; and an increased charge-charge/ charge-phonon interactions.
- The reduction in charge mobility happens more gradually for Ga^{3+} ions compared with Al^{3+} ions. This is reflected in, or driven by, changes in the orientation of the films observed in texture analysis.
- The increase in charge carriers drives a sharp decrease in resistivity very similar to that seen in AZO

2. Electronic properties: 0.2-3 at% gallium doping

- Once again the theory proposed involves hybrid defects, this time Ga^{3+} impurities combine with V_{Zn} to form hybrid $\text{Ga}_{\text{Zn}}V_{\text{Zn}}$ acceptor defects:

- Measured charge carrier concentration slows greatly at 0.2 at%. As Ga_{Zn} are added, the Fermi energy is increased allowing the creation singly accepting hybrid $\text{Ga}_{\text{Zn}}\text{V}_{\text{Zn}}$ defects. Further free electrons from the Ga^{3+} are trapped in this defect and do not add to the conduction band.
- In GZO, the charge carrier concentration increases gradually until 3 at%; this suggests that some Ga_{Zn} are still formed and are not trapped.
- The increase thereafter, until 3 at%, is again explained by the replacement of V_{Zn} doubly trapping defects by $\text{Ga}_{\text{Zn}}\text{V}_{\text{Zn}}$ singly trapping defects allowing easier movement of charge across the thin film.
- The decrease in resistivity from 0.2-3 at% is driven by the increase in charge mobility, caused by the filling of charge trapping states.

3. Electronic properties: after 3 at% gallium doping

- The saturation point of Ga_{Zn} defects and migrating to grain boundaries occurs after 3 at% and is not seen in this data set. The increased solubility of Ga in the ZnO lattice is likely caused by the close match of ionic (and covalent) radii. Further experiments would be needed to study the effects of doping past 3 at%.

5.3.4.2 Doping with Indium

1. Electronic properties: 0-0.4 at% indium doping

- The observed electronic properties are explained by In^{3+} impurities filling Zn^{2+} positions in the wurtzite lattice, the doping of In is similar to that of Al and Ga.
- The increase in charge carrier concentration is caused by free electrons added to the conduction band by In_{Zn} defects. The charge carrier concentration does not saturate in this region
- Again the reduction in charge mobility is caused by the combined effect of an increase in ionised impurity scattering; an increased charge-charge and charge-phonon interactions.
- The reduction in charge mobility occurs at a similar rate to Ga^{3+} and this is reflected in, or driven by, changes in the orientation of the films observed in texture analysis.
- This increase in charge carriers drives a sharp decrease in resistivity similar to that seen in AZO and GZO

2. Electronic properties: 0.4-1 at% indium doping

- The theory again uses hybrid defects, this time In^{3+} impurities combine with V_{Zn} to form hybrid $\text{In}_{\text{Zn}}V_{\text{Zn}}$ acceptor defects:
- Measured charge carrier concentration increases steadily until 1 at%. As In_{Zn} are added the Fermi energy is increased. However, the close match in ionic radii of Zn^{2+} and In^{3+} mean that the In_{Zn} remains preferable at higher doping levels. $\text{In}_{\text{Zn}}V_{\text{Zn}}$ begin to form past 0.5 at% as the rise in charge carrier concentration slows. At this at%, some free electrons from the In^{3+} are trapped in this defect and do not add to the conduction band.
- The charge mobility continues to decrease until 0.4 at%, as ionised impurity scattering, charge-charge and charge-phonon interactions, and/or orientation changes continue to act. The increase from 0.4 at% to 3 at% is explained by the replacement of V_{Zn} doubly trapping defects by $\text{In}_{\text{Zn}}V_{\text{Zn}}$ singly trapping defects allowing easier movement of charge across the thin film.
- The decrease in resistivity from 0.2-1 at% is driven by both an increase to the charge carrier concentration and an increase in charge mobility caused by the filling of charge trapping states.

3. Electronic properties: 1-3 at% indium doping

- The saturation point of In_{Zn} defects appears to lie at 1 at%. At this point, In^{3+} ions begin to migrate grain boundaries. This is reflected in a plateauing in the resistivity and a drop in charge mobility.

5.4 Annealing studies on Al, Ga and In doped ZnO

It is well documented that post deposition annealing treatment can improve the electronic properties of spray deposited ZnO, this is highlighted in Figure 5. 1. A literature review was undertaken to study the state of the art in terms of minimum resistivities achieved in AZO films deposited by spray pyrolysis, the results of which are shown in Table 5. 6.

Al at%	Thickness (nm)	Resistivity ($\Omega\text{.cm}$)	Hall Charge mobility ($\text{cm}^2/\text{V.s}$)	Charge carrier concentration (cm^{-3})	Anneal temp ($^{\circ}\text{C}$)	Anneal environment	Year and reference
3	200	3.6×10^{-3}	7	2.5×10^{20}	600	$\text{N}_2 + 5\% \text{H}_2$	2012 [105]
3	2400	2×10^{-3}	-	-	400	Vacuum	2007 [11]
0.3	1000	0.9	-	-	700	O_2	2004 [180]
3	~200	1×10^{-1}	-	-	500	N_2	2004 [173]
3	~200	1×10^{-2}	-	-	500	$\text{N}_2 + 5\% \text{H}_2$	2004 [173]
1	~450	1.4×10^{-3}	-	-	350	H_2	1995 [109]
2	2200	9.1×10^{-3}	4.4	1.6×10^{20}	400	$\text{Ar} + \text{H}_2$	2014 [164]
1.2	6600	2×10^{-3}	-	-	400	H_2	1991 [181]
1.75	~500	7×10^{-3}	-	-	350	N_2	2014 [170]
3	600	4×10^{-3}	~1	~ 10^{20}	400	Vacuum	2007[153]

Table 5. 6 – Electronic properties of AZO films cited in literature allowing post deposition annealing

Data in Table 5. 6 shows how AZO films show excellent electronic properties after annealing, even at lower thicknesses. Indeed some are close to the state of the art for any TCO using this technique. An inherent problem, however, with this lies in the extra processing step required to achieve these properties. This partly negates the advantages of the technique in that it would no longer be as rapid or low cost. Nevertheless such treatments still offer economic advantages to vacuum techniques and are worthy of further study.

The mechanism behind the increased conductivity from post depositional annealing treatments is not well understood despite many investigations. Further study in the this area, using theories developed in the previous section, may help elucidate the mechanics behind the improved electronic properties.

Looking back over theory discussed in section 1.4.1, the native point defects of ZnO are highlighted and the potential roles of V_O and Zn_i and hydrogen impurities in adding charge carriers to the conduction band are studied. Annealing in oxygen deficient environments can, unsurprisingly, create oxygen vacancies in the lattice. [172]

If these defects were to act as donors, two electrons would be added to conduction band resulting in an increase in charge carrier concentration. This theory is considered unlikely however, due to the fact that oxygen vacancies are deep donors, [23] therefore, such donations would require too great an energy to occur at high levels. Another theory is that the annealing process could cause desorption of oxygen acceptor states at the surface or at grain boundaries. These states act as electron traps to remove free carriers and lower charge mobility. [182] The removal of desorbed oxygen trapping states by annealing, would act to increase the charge carrier concentration and improve charge mobility. The final commonly held theory is that annealing may facilitate unintentional hydrogen doping in the films. This mechanism is possible because, unlike some other semiconductors, in ZnO hydrogen acts exclusively as a donor adding an electron to the conduction band. [27] The hydrogen impurity like group three dopants acts as a donor at low Fermi energy. When the formation energy increases at high Fermi energy, it can form a hybrid defect with V_{Zn} defects release free carriers as described in section 5.3.4.

n-type conductivity is most prevalent in zinc-rich films. One possibility is that this is solely due to the lower formation energies of V_O and Zn_i defects. It is proposed however, that the increase in the formation energy of V_{Zn} defect is also likely to be an important factor. The oxygen deficient deposition environment found in vacuum deposition techniques favours the growth of zinc-rich 'as deposited' films. When using solution techniques however, a post deposition treatment is required to achieve these enhanced electronic properties.

5.4.1 Annealing studies on AZO

Six ZnO films, doped at 2 at% Al, were deposited to study the effects of annealing. Three films were annealed at 500 °C for 2 hours in an ambient environment. The other three films were annealed at 500 °C for 2 hours in vacuum. Spray parameters are set as previously described in Table 5. 2.

5.4.1.1 Analysis by Hall Effect

The pressure was reduced to 1×10^{-6} Torr during anneals. Following this annealing treatment, the electronic properties were investigated using Hall effect measurements (at room temperature). The results of this study are shown in Figure 5. 26.

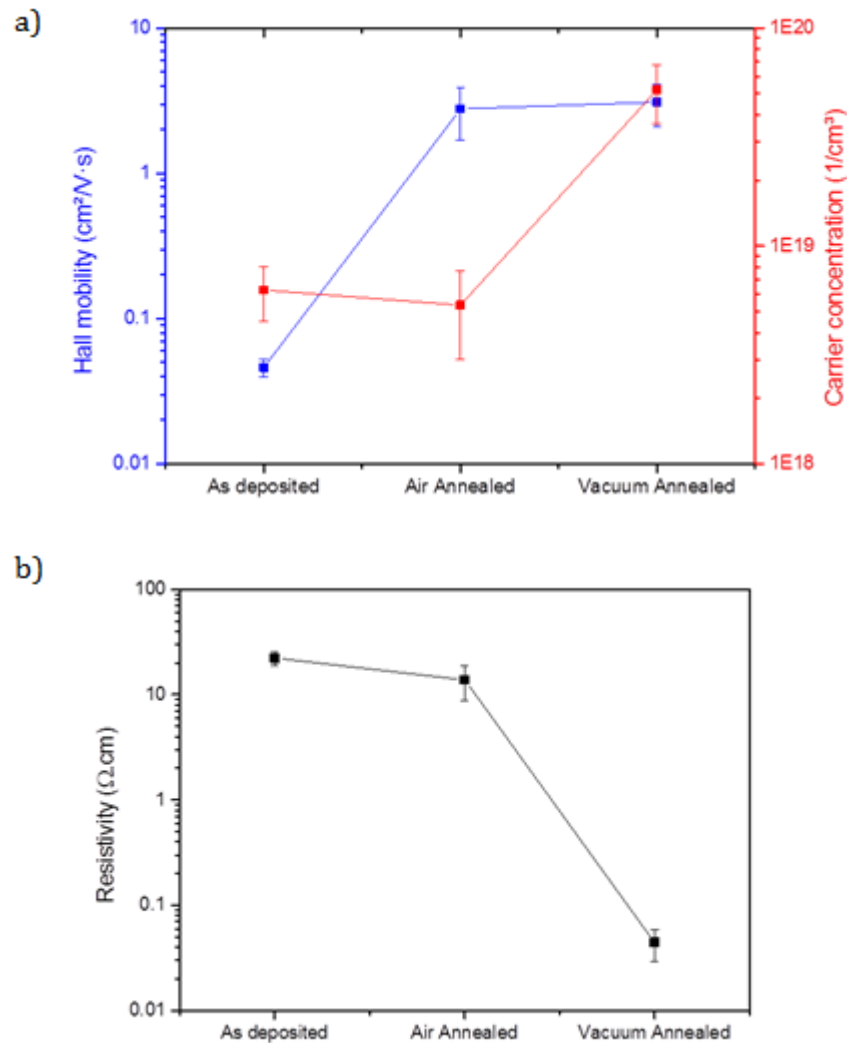


Figure 5. 26 – Electronic properties of AZO films as-deposited and following annealing in ambient and vacuum environments. a) shows the charge carrier concentration and carrier charge mobility), b) shows the resistivity.

Annealing in ambient air and in vacuum both increase the charge mobility from roughly 0.04 - 3 cm²/V.s. This increase alone, however, does not appear to have a major impact on the resistivity. The air annealed sample is only slightly lower in resistivity than the as-deposited sample.

This is explained partly by the variations in charge carrier concentration. From the as-deposited sample to the air annealed, there is a subtle decrease seen in the charge carrier concentration. In the vacuum annealed sample, however, the increase in charge mobility is coupled with an order of magnitude increase in free carriers. This drives a two order of magnitude decrease in the resistivity.

The structural properties of the films were studied by XRD to gain a clearer idea of the mechanisms most likely to be driving the decrease in resistivity. Following this a detailed mechanism is proposed

5.4.1.2 XRD analysis of Annealed AZO

The films were analysed by XRD to study how annealing affects the structure of the AZO films. Typical XRD patterns are shown in Figure 5. 27.

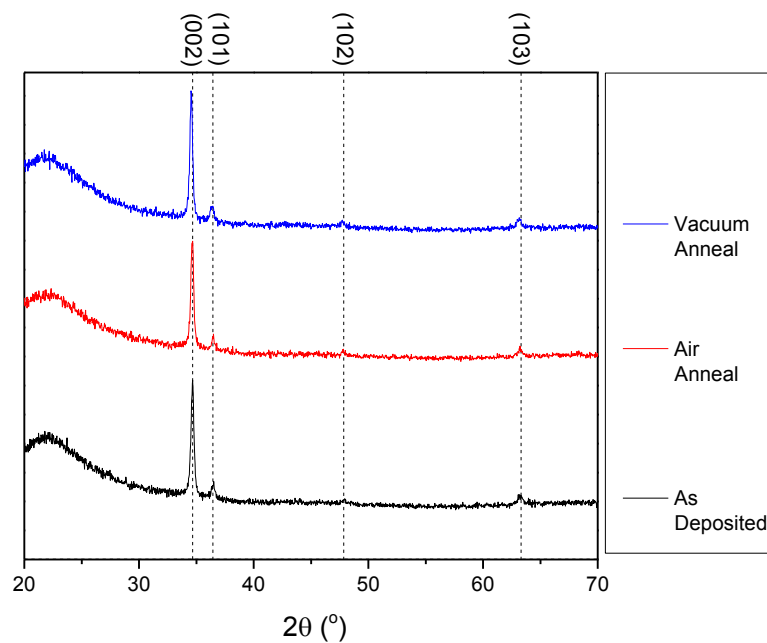


Figure 5. 27 – Typical XRD patterns of as-deposited AZO and following anneal in air and in vacuum.

A shift is seen in the position of the (002) peak position highlighted in Figure 5. 28 and seen in all measured XRD patterns.

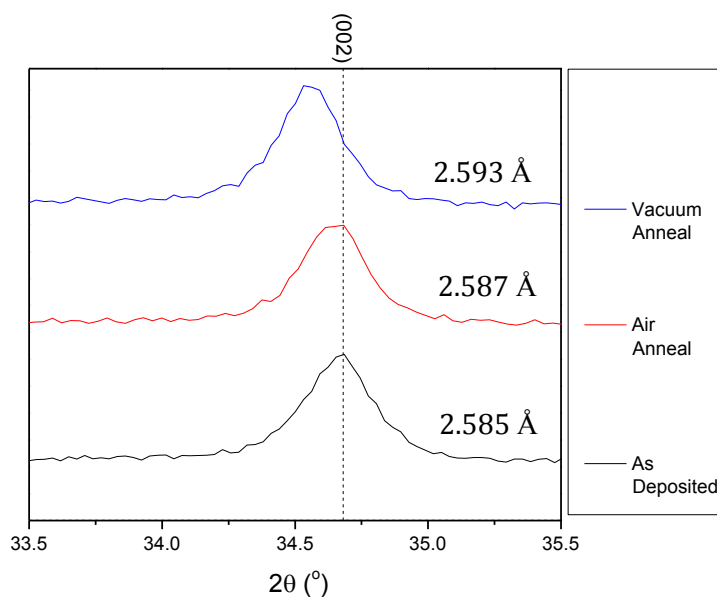


Figure 5. 28 – The peak position of the (002) reflection of ‘as deposited’ AZO, following annealing in air, and in vacuum $d_{(002)}$ spacing for each film is also displayed.

This shift suggests an increase in lattice spacing. A small increase is seen after annealing in air whereas a pronounced increase is seen after vacuum annealing. This is indicative of thermally or vacuum induced changes in the defect chemistry as macroscopically, the film remains unchanged. Mechanisms to explain this are discussed in detail below.

5.4.1.3 Defect Mechanisms in Annealed AZO

- The large increase in charge mobility upon annealing AZO films in air, coupled with the lack of change to the structure, suggests that a speciation change is occurring at the grain boundaries or the surface rather than reorganisation within the grains themselves.
- The removal of impurities at the grain boundaries provides an explanation for the increase in charge mobility without any significant variation being observed in charge carrier concentration.
- Upon annealing AZO films in vacuum, there are significant changes to the electronically active defects. This is observed in the large increase to the charge carrier concentration.
 - As conditions are moved towards a zinc-rich regime, the removal of V_{Zn} defects would result in a decrease in lattice size, therefore, this mechanism seems unlikely.

- Desorption of oxygen to remove trapping states from grain boundaries seems possible. This mechanism, however, does not account for the increase observed in the lattice spacing.
 - Donor defects which do give an increase in lattice spacing are Zn_i and H_i . Zn_i defects in particular, become more favourable in zinc-rich conditions. However, even in zinc-rich conditions, the high formation energies at high Fermi energies makes both defects unlikely contributors.
 - V_o^{**} lead to an increase in the lattice size (section 1.4.1.1.1) and become more favourable in zinc rich conditions. The fact that they are deep donors however, suggests that they too cannot provide the answer to the increase in n-type conductivity.
- As there is no obvious solution considering just one defect, it is concluded that there must be two or more mechanisms working to give the observed trends in the data. The formation energy of many of the defects is too high to provide these observations. This must take precedence in the chosen hypothesis. The most thermodynamically appealing solution involves the creation of V_o and removal of V_{Zn} .

It is proposed that an increase in the V_o^{**} defect causes the observed increase in lattice size. These are considered electronically inactive and cannot cause the observed increase in free carriers. In parallel, however, removal of V_{Zn} compensating defects provides the observed increase in free carriers. The lattice decrease expected is compensated for by the creation of V_o defects. It has been suggested that H_i can act to pacify the V_{Zn} defect [183] and this would help to further reduce the presence of the acceptor defect.

This proposal fits with the theoretically predicted lattice modifications from the two defects. Oxygen vacancies give a 23 % increase in lattice size whereas a zinc vacancies lead to just a 10 % reduction. Assuming roughly as many V_o are created as V_{Zn} are removed a small increase in lattice size would be observed. This theory is therefore consistent with the data.

In addition to this hypothesis, it is also possible that meta-stable defect clusters could be induced by the kinetics of the deposition technique. Much more difficult to interpret, these may have a contribution to the observed properties of the material.

The hypothesis attributes the rise in charge carrier concentration, following annealing, to removal of charge trapping states and not to the creation any new carrier species. This implies that there are existing, albeit trapped, n-type carriers in the as-deposited film. The cause of this inherent n-type conductivity in ZnO films, the topic of much debate, is not given further clarity in this work.

5.4.2 Further Annealing studies on AZO

To test this hypothesis, and further study the mechanisms involved, AZO samples used in Figure 5. 18 were subjected to subsequent anneals in Ar and O₂.

Annealing was carried out in argon rather than in vacuum due to technical problems with the vacuum furnace after initial experiments. Annealing in argon is believed to release oxygen from ZnO samples in the form of O₂ or H₂O, therefore, is suitable to provide the required zinc rich conditions. [28]

The aim of the experiment was to shift the system from the oxygen rich regime in as-deposited films, to a zinc-rich regime. This was achieved by annealing in argon. The electronic properties were measured using the Hall effect and changes to the lattice spacing were extracted from XRD measurements. The samples were then annealed in oxygen to revert the films back to an oxygen rich regime. The electronic and structural properties were then re-measured. Finally, the films were annealed once more in argon to bring the system to the zinc-rich regime and further electronic and structural measurements were made.

5.4.2.1 Analysis by Hall effect measurements

Hall effect measurements, shown in Figure 5. 29, generally show the expected trends. Annealing in argon gives an increase in charge carrier concentration and charge mobility and decrease in resistivity in films of all doping levels.

These results are in agreement with the electronic properties of AZO following vacuum annealing, seen previously in Figure 5. 26. The effects are less pronounced following an Ar anneal than that seen following vacuum annealing. It is proposed that vacuum annealing allows for greater removal of oxygen from the system than argon annealing.

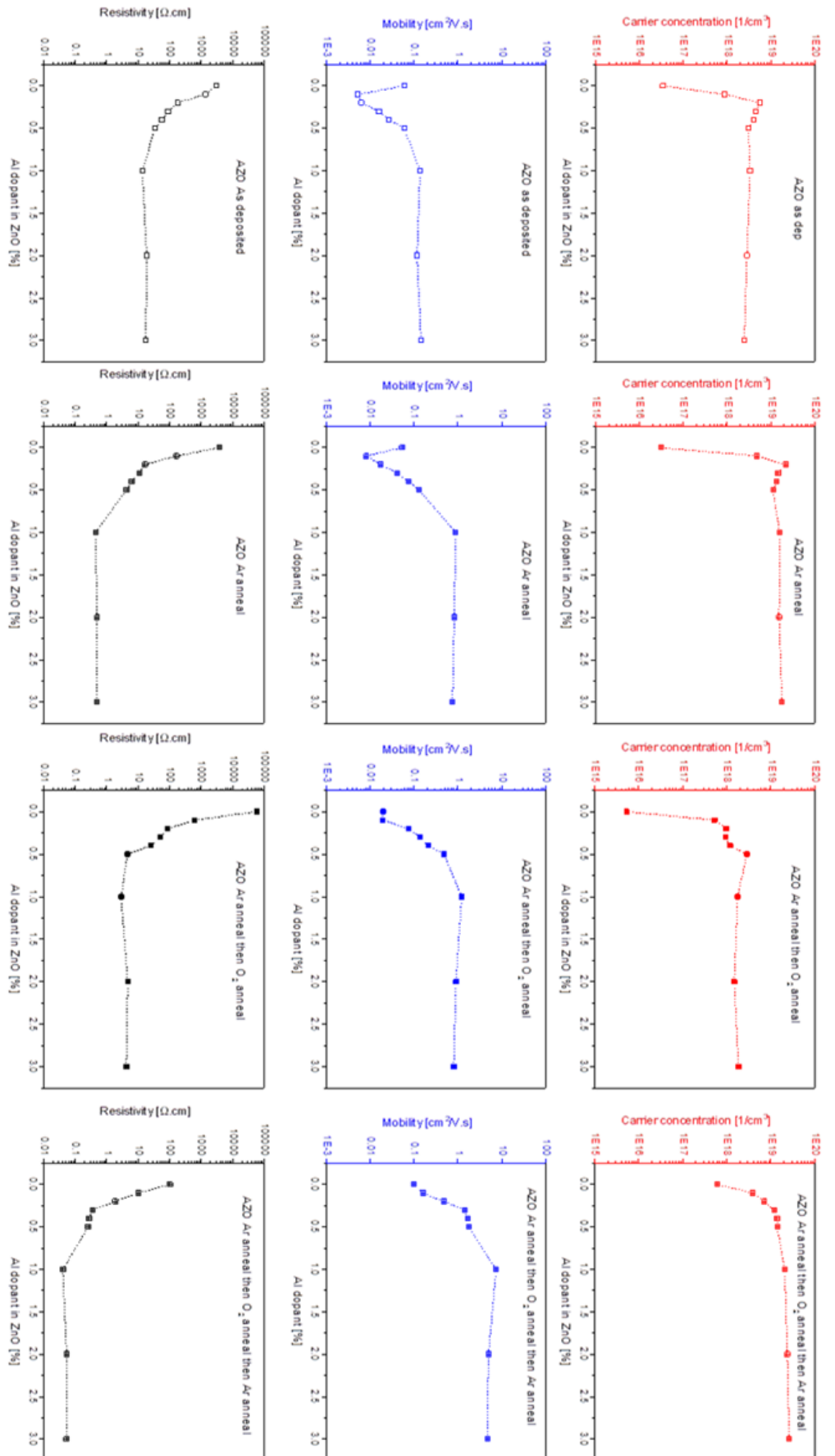


Figure 5. 29 – Charge carrier concentration, charge mobility and resistivity of 0-3 at% AZO as-deposited films and following subsequent two hours annealing treatments at 500 °C in Ar, O₂ then a second anneal in Ar.

Three typical points, at doping levels of 0.2, 1 and 2 at%, have been extracted from results shown in Figure 5. 29 to provide a clearer idea of the trends seen. These are displayed in Figure 5. 30.

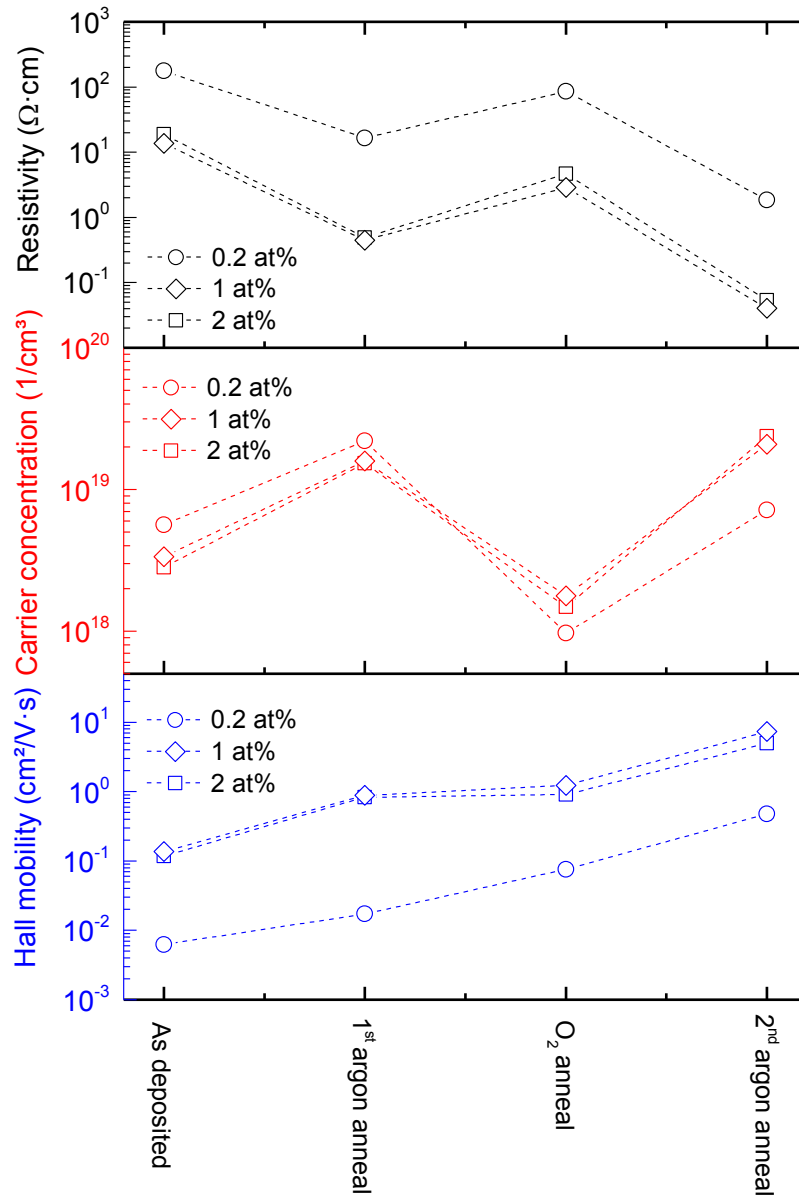


Figure 5. 30 – Trends in Hall effect measurements following annealing treatment experiment for of 0.5, 1 and 3 at% AZO

Following XRD measurements, mechanisms for the observed behaviour are proposed.

5.4.2.2 Analysis by XRD

The structure of the films were analysed by XRD to detect any variation in the position of the (002). Such changes can be attributed to changes in the lattice spacing as observed in vacuum annealed samples. Typical XRD patterns of the as-deposited samples and following all three anneals are shown in Figure 5. 31.

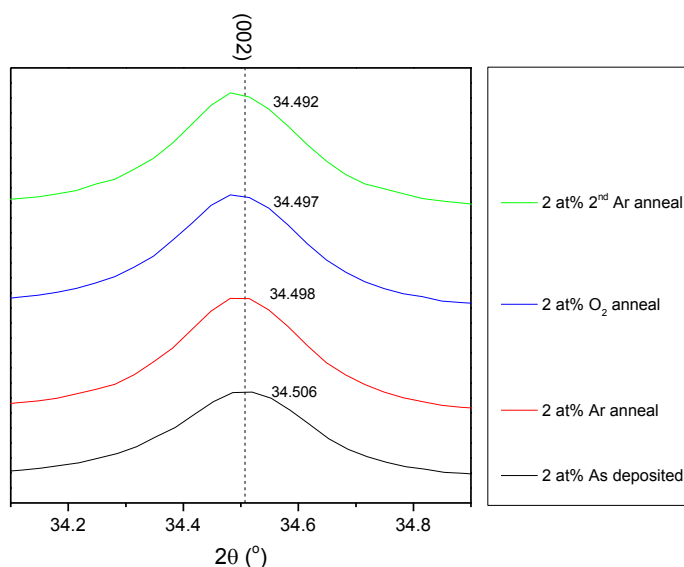


Figure 5. 31 – XRD measurements of the (002) position of as-deposited 2 at% AZO and following subsequent anneals in argon, oxygen then a second anneal in argon.

It is clear from the patterns that there is little change in the position of the (002) peak position. The increase in lattice spacing observed following vacuum anneal is not seen to nearly the same extent in the argon anneal. This may be expected as the increase in charge carrier concentration and charge mobility are less. This suggests that the effect switch from oxygen-zinc regimes is less pronounced following argon anneal than following vacuum anneals

5.4.2.3 Mechanisms for observations

- The ingress of charge carriers from the system following annealing in argon and egress following annealing in oxygen is clear to see.
 - o This gives support to the notion that the charge carrier concentration is directly linked to the zinc/oxygen ratio in the system and the ingress and egress of V_{Zn} donor compensating defects.

- To gain further proof of the film composition x-ray photoemission spectroscopy (XPS) analysis could be used. EDX analysis was obtained, however, it was not possible to distinguish oxygen in the film from that in the substrate.
 - Photoluminescence spectroscopy could be used to confirm the migration of V_{Zn} in and out of the system. [184] This was technique was attempted however no results could be obtained on the oxide system.
- The charge mobility of the system is seen to increase upon all annealing treatments.
 - The increase is partly attributed to speciation changes at grain boundaries.
 - This is backed up by the observation that charge mobility is increased more dramatically in the 2 at% which has smaller grains (more grain boundaries) than on the 0.2 at% sample which has larger grains (Figure 5. 25).
 - The charge mobility, however, increases by much less in the 1 and 2 at% following annealing in oxygen.
 - It is proposed that the stagnation in charge mobility on oxygen annealing is caused by the recreation of V_{Zn} acceptor defects
 - V_{Zn} act as charge trapping states and would compensate for the increase in charge mobility expected from the speciation changes.
 - Additionally, annealing in O_2 is likely to mean that some oxygen adsorbs to the surface and grain boundaries producing trapping states. This provides another mechanism for the lack of increase.

5.4.3 Stability of defects

The usefulness of improvements to the electronic properties brought about by annealing is dependent upon their. If the defects are not stable in ambient conditions, it would restrict their application to encapsulated devices.

To investigate the long term stability of induced defects, an undoped ZnO sample and an AZO sample (doped at 2 at%) were annealed in vacuum using the conditions described in section 5.4.1. The films were stored in ambient conditions and the electronic properties measured over the course of 180 days. Improvements to the electronic properties are observed to be stable for the length of the study, shown in Figure 5. 32. There are no significant decreases in charge carrier concentration or in charge mobility over this time in either the ZnO sample or the AZO sample.

The data suggests that the created defects are inherently stable in ambient conditions and resistant to photo-degradation. This is promising for the practical use of this technology.

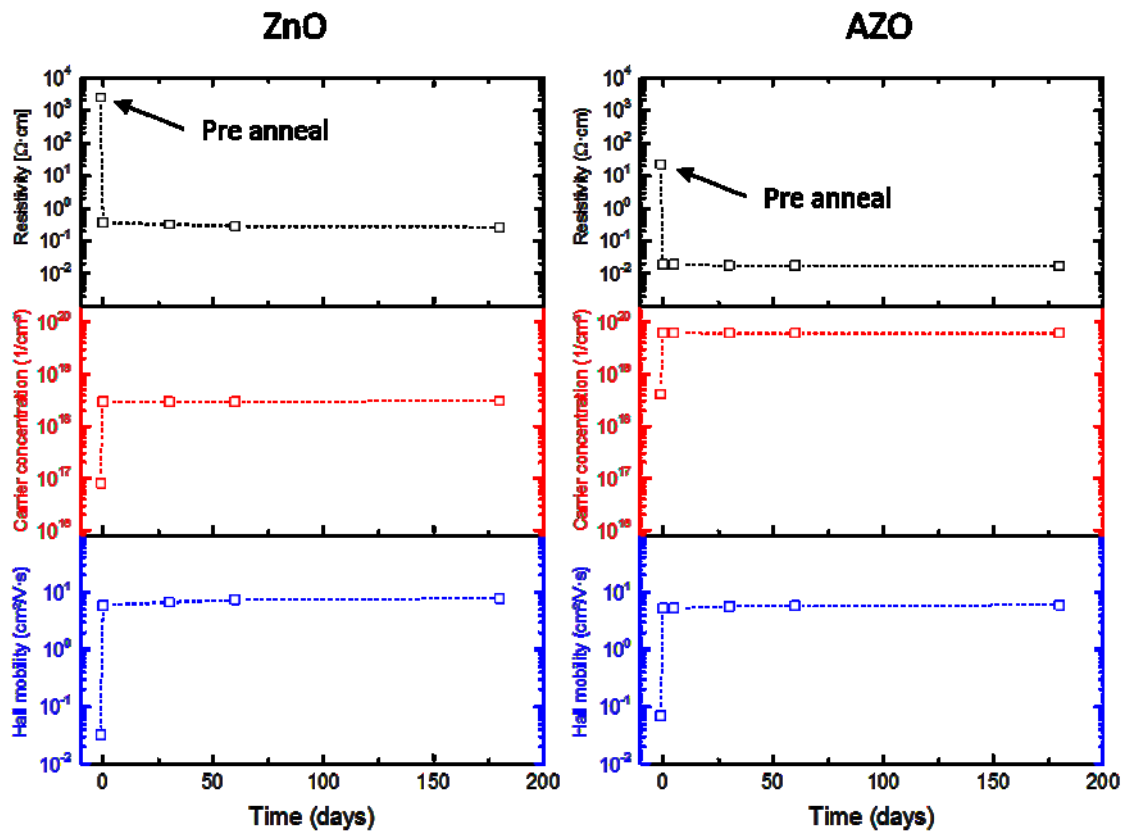


Figure 5. 32 – Stability of vacuum induced defects in ZnO and 2 at% AZO over 180 days

5.4.4 Conclusions on group three doping studies

Whatever the cause of inherent n-type conductivity, it is clear that the electronic properties of ZnO, AZO, GZO and IZO can be controlled using post deposition annealing to great effect. Improvements to charge mobility are possible without changes to the charge carrier concentration. It is also possible to produce a large decrease in the resistivity of samples by increasing the charge carrier concentration. These improvements are inherently stable and the technology has potential for real world application.

The films shown this section are not at the state of the art for the field, where resistivities of down to $3 \times 10^{-3} \Omega \cdot \text{cm}$ have been shown to be possible at this thickness using spray pyrolysis. The annealing process has not been optimised fully and it is believed that further work on this system could lower the resistivity of the films to be consistent with literature.

CHAPTER VI – CONCLUSIONS AND FURTHER WORK

The work presented has focused on spray pyrolysis of doped ZnO as a transparent conducting oxide. An extensive study of spray pyrolysis processing conditions is provided. Using the AC field Hall effect technique the electronic properties of high resistivity native and lightly doped ZnO have been probed. This has given novel insight into the effect of processing conditions on the charge mobility and charge carrier concentration and helped link the electronic properties to observed structural properties. It has also facilitated a comprehensive investigation into the introduction of dopants into the ZnO system studying the doping mechanisms and the nature of the intrinsic defects upon doping.

A thorough review of the background theory and experimental methods is given in Chapters I and II. Equipped with an understanding of the underlying principles, initial experimental results in Chapter III quickly exposed the need for an improved deposition method. The remainder of the chapter details the design and fabrication of a custom, automated spray rig and presents data displaying the enhanced film quality and repeatability of the system.

Chapter IV describes the utilisation of the automated rig to carry out an in depth study of deposition parameters. A critique is given of the literature concerning precursor solvent; precursor salt; precursor concentration; substrate temperature; nozzle height; nozzle size; carrier gas pressure; and carrier gas parameters. The importance of maintaining film thickness when comparing samples is highlighted and brings into question some of the conclusions made in previous studies. Owing to the lack of complete study of all parameters performed on one deposition system in the literature, an examination of the structural and electronic properties of each parameter is provided in this work.

Of all the parameters studied the substrate temperature is shown to have the largest impact on the structural properties of ZnO, this is consistent with literature results. However, these properties were also affected by a number of other parameters, the variations in structural and optical properties when altering nozzle height and carrier gas pressure and substrate temperature is displayed. This examination brings the literature forward a further stage by analysis these films by AC Hall effect measures, the first study of its kind, showing the optimal conditions for the greatest charge carrier concentration and charge mobility.

The structural, optical and electronic properties are studied for a number of other parameters including varying the precursor concentration; the nozzle size; the speed of the stage and the carrier gas. These parameters in particular are not well studied in the literature and more complete investigations are made in this report.

The major outcome of this research shows that the structural properties can be tuned to control the charge carrier concentration. Examining this with respect to the structural properties suggests that the faster deposition rates are a good way of implanting defects into the system and thus increasing the charge carrier concentration. Charge mobility appears to be grain boundary dominated, with increases to crystallite size (fewer grain boundaries) showing significant increases in charge mobility.

Future work lies in the fine control of film properties to optimise ZnO layers in devices such as for the semiconducting component of thin film transistors (TFTs) and as electron transport layers in solar cells. Some initial work was undertaken in these fields. Preliminary TFT devices showed that the non-optimised films acted as degenerate semiconductors leading to poor device performance. Preliminary solar cells displayed a maximum power conversion of 1.03 %. Surprisingly the lower conductivity, slower deposition rate films gave better efficiencies than a faster deposition rate, despite the better measured conductivity the faster deposition rate samples. Further studies examining this phenomenon further and better optimising films sprayed using this system for PV applications would be interesting.

The final work of Chapter IV highlights effects of depositing on different surfaces. The enhanced charge mobility when depositing upon a textured surface created by PLD shows the possibility of pseudo epitaxial growth by spray pyrolysis and opens the door to further studies of this kind. PLD is an expensive route to create a textured surface, investigating low cost transparent substrates which provide similar epitaxy offers an interesting route to improved conductivity in spray deposited ZnO for TCO applications.

The work also paves the way for comparative studies on different oxide systems. Initial studies were performed depositing SnO₂ using the automated rig. The different precursor salt (SnCl₂) required re-optimisation with early results suggesting that SnO₂ offers greatly enhanced electronic properties when deposited in ambient conditions. As-deposited, undoped SnO₂ produced films of comparable optoelectronic properties to those deposited by PLD. This is attributed to a more naturally oxygen deficient system owing to the Sn:O ratio in this system. In terms of a rapid, low cost, ambient deposition the SnO₂ looks more promising.

The first challenge to overcome in possible future work in this field may involve maintaining spray equipment in increased acidity brought about by the SnCl₂ precursor salt. Following this, doping with F or Sb offers a route to greater conductivity which could be explored.

Chapter V utilises the optimal conditions for depositing low resistivity ZnO from Chapter IV, and investigates the trivalent dopants as a means to the further reduce conductivity.

Preliminary investigations studied a range of trivalent dopants. It was determined that group three elements formed the best dopant species due to their ionic/covalent radii and their preferred coordination number. There is potential for further work here carrying out a study of all potential dopants and recording the doping ability of each. An investigation into the optimum Al doping level was implemented owing to the lack of a definitive answer in the literature. The structural and optoelectronic properties of films doped between 0 and 3 at% were studied with the aim of elucidating doping mechanisms and identifying the associated changes in the physical properties.

Studies revealed that the uncertainty as to the optimum doping level in literature was caused by an interplay between the charge carrier concentration and charge mobility; this meant that the lowest resistivity could be found between 1 and 3 at%. The increase in charge carrier concentration was seen to saturate between 0 and 0.5 at%, continued reduction in resistivity was the result of a recovery in charge mobility. The region between 0 and 0.5 at% had not yet been investigated in the literature. This report studied this low doping regime and determined the point of charge carrier saturation addition to be 0.2 at% in AZO. Experiments were replicated in GZO and IZO yielding similar results albeit with different saturation points (GZO ~ 0.5 at%, IZO 1 at%).

This was found to be significantly lower than implied by literature the location of the Al dopant past this saturation point was investigated. In parallel, the cause for the increase in charge mobility following this saturation was studied. Using cross sectional TEM, SEM, XRD and UV-Vis the physical properties of films were studied to identify characteristic properties of different dopant locations. Dopant was not seen to be migrating to grain boundaries, a mechanism often cited as the potential route to carrier saturation. A number of other possibilities were considered and a mechanism proposed in line with experimental observations.

An interesting future study would be to verify this mechanism, ideally by observation of the identified $\text{Al}_{\text{Zn}}\text{V}_{\text{Zn}}$ hybrid defect and an investigation of its varying concentration in the system. Detection and identification of defects in AZO is considered difficult, photo-luminescence spectroscopy is one possibility however, there are many interpretations of the signals received and the sensitivity of the technique was seen to be a problem in a preliminary study made for this work. Furthermore, similar studies could be made on the GZO and IZO systems.

To further reduce the resistivity of doped ZnO to a level in which it may find potential application as TCO annealing in an oxygen poor environment was essential. The AZO, system was investigated annealing both in vacuum and Ar environments showing a decrease in resistivity. High vacuum annealing was seen to give greater reductions in resistivity than Ar annealing. Samples were systematically annealed in oxygen poor then oxygen rich environments, highlighting the importance of intrinsic defects to the use of ZnO as a TCO. Mechanisms for the observations were proposed involving the creation and destruction of V_{Zn} defects. At this level of annealing these defects are seen to be stable in ambient conditions for >180 days.

This work could be followed by a full study of the annealing conditions, varying oxygen partial pressure, and also, in increasingly high vacuum and studying the conductivity of the system. It would also be useful to investigate the hydrogen partial pressure of the system. Following this it would be of interest to study the stability of samples annealed in each environment as TCOs which do not require encapsulation have a significant advantage.

REFERENCES

- [1] T. Minami, "Transparent conducting oxide semiconductors for transparent electrodes," *Semicond. Sci. Technol.*, vol. 20, no. 4, pp. S35–S44, 2005.
- [2] D. Alemu, H.-Y. Wei, K.-C. Ho, and C.-W. Chu, "Highly conductive PEDOT:PSS electrode by simple film treatment with methanol for ITO-free polymer solar cells," *Energy Environ. Sci.*, vol. 5, no. 11, p. 9662, 2012.
- [3] T. O. Mason, S. P. Harvey, K. R. Poeppelmeier, K. Ellmer, R. Kykyneshi, J. Zeng, D. P. Cann, M. Mizuhashi, H. Hosono, C. G. Granqvist, Y. Shigesato, H. Ohta, T. J. Coutts, D. L. Young, T. a Gessert, A. Sleight, D. S. Ginley, J. D. Perkins, D. C. Paine, B. Yaglioglu, J. Berry, J. Robertson, B. Falabretti, N. T. Zno, and D. C. Olson, *Handbook of Transparent Conductors*. 2011.
- [4] H. Bisht, H.-T. Eun, A. Mehrkens, and M. . Aegerter, "Comparison of spray pyrolyzed FTO, ATO and ITO coatings for flat and bent glass substrates," *Thin Solid Films*, vol. 351, no. 1–2, pp. 109–114, Aug. 1999.
- [5] H. Ohta, M. Orita, M. Hirano, H. Tanji, H. Kawazoe, and H. Hosono, "Highly electrically conductive indium–tin–oxide thin films epitaxially grown on yttria-stabilized zirconia (100) by pulsed-laser deposition," *Appl. Phys. Lett.*, vol. 76, no. 19, p. 2740, 2000.
- [6] H. Agura, A. Suzuki, T. Matsushita, T. Aoki, and M. Okuda, "Low resistivity transparent conducting Al-doped ZnO films prepared by pulsed laser deposition," *Thin Solid Films*, vol. 445, no. 2, pp. 263–267, 2003.
- [7] Z. Zhao, D. . Morel, and C. . Ferekides, "Electrical and optical properties of tin-doped CdO films deposited by atmospheric metalorganic chemical vapor deposition," *Thin Solid Films*, vol. 413, no. 1–2, pp. 203–211, Jun. 2002.
- [8] N. Nishimoto, Y. Yamada, Y. Ohnishi, N. Imawaka, and K. Yoshino, "Effect of temperature on the electrical properties of ITO in a TiO₂ /ITO film," *Phys. Status Solidi*, vol. 210, no. 3, pp. 589–593, 2013.
- [9] F. N. Kotsonis and C. D. Klaassen, "Toxicity and distribution of cadmium administered to rats at sublethal doses.," *Toxicol. Appl. Pharmacol.*, vol. 41, no. 3, pp. 667–80, Sep. 1977.
- [10] H. Tong, Z. Deng, Z. Liu, C. Huang, J. Huang, H. Lan, C. Wang, and Y. Cao, "Effects of post-annealing on structural, optical and electrical properties of Al-doped ZnO thin films," *Appl. Surf. Sci.*, vol. 257, no. 11, pp. 4906–4911, Mar. 2011.

- [11] M. de la L. Olvera, H. Gomez, A. Maldonado, H. Gómez, and A. Maldonado, "Doping, vacuum annealing, and thickness effect on the physical properties of zinc oxide films deposited by spray pyrolysis," *Sol. Energy Mater. Sol. Cells*, vol. 91, no. 15–16, pp. 1449–1453, Sep. 2007.
- [12] Z. C. Feng, *Handbook of Zinc Oxide and Related Materials: Volume One, Materials*. 2012.
- [13] K. Ellmer, A. Klein, and B. Rech, "Transparent Conductive Zinc Oxide: Basics and Applications in Thin Film Solar Cells," p. 460, 2007.
- [14] H. Morkoç and Ü. Özgür, *Zinc Oxide: Fundamentals, Materials and Device Technology*. 2009.
- [15] G. Parravicini, *Solid state physics*. .
- [16] J. Singleton, "Band theory and electronic properties of solids," 2004.
- [17] G. Grosso and G. P. Parravicini, *Solid state physics*. Academic Press, 2003.
- [18] P. Atkins and J. de Paula, *Atkins Physical Chemistry*, Seventh. 2002.
- [19] A. Kobayashi, O. F. Sankey, S. M. Volz, and J. D. Dow, "Semiempirical tight-binding band structures of wurtzite semiconductors: AlN, CdS, CdSe, ZnS, and ZnO," *Phys. Rev. B*, vol. 28, no. 2, pp. 935–945, 1983.
- [20] J. S. Blackemore, *Solid State Physics*, 2nd ed. 1985.
- [21] F. a. Kröger and H. J. Vink, "Relations between the Concentrations of Imperfections in Crystalline Solids," *Solid State Phys. - Adv. Res. Appl.*, vol. 3, no. C, pp. 307–435, 1956.
- [22] M. Grundmann, *The Physics of Semiconductors*. 2006.
- [23] A. Janotti and C. G. Van De Walle, "Native point defects in ZnO," *Phys. Rev. B - Condens. Matter Mater. Phys.*, vol. 76, no. April, pp. 1–22, 2007.
- [24] S. Lany and A. Zunger, "Dopability, intrinsic conductivity, and nonstoichiometry of transparent conducting oxides," *Phys. Rev. Lett.*, vol. 98, no. 4, pp. 2–5, 2007.

- [25] S. Lany and A. Zunger, "Assessment of correction methods for the band-gap problem and for finite-size effects in supercell defect calculations: Case studies for ZnO and GaAs," *Phys. Rev. B - Condens. Matter Mater. Phys.*, vol. 78, no. 23, pp. 17–20, 2008.
- [26] K. Lorenz, E. Alves, E. Wendler, O. Bilani, W. Wesch, and M. Hayes, "Damage formation and annealing at low temperatures in ion implanted ZnO," *Appl. Phys. Lett.*, vol. 87, no. 19, p. 191904, 2005.
- [27] C. G. Van De Walle, "Hydrogen as a cause of doping in zinc oxide," *Phys. Rev. Lett.*, vol. 85, no. 1, pp. 1012–1015, 2000.
- [28] W.-W. Feng, S. Cho, M.-S. Wang, and D. D. Dung, "Co-contribution of hydrogen impurities and native defects might be the answer for the n-type conductivity in ZnO," *Phys. Lett. A*, vol. 380, no. 3, pp. 480–484, 2016.
- [29] K. M. Johansen, L. Vines, T. S. Bjørheim, R. Schifano, and B. G. Svensson, "Aluminum Migration and Intrinsic Defect Interaction in Single-Crystal Zinc Oxide," *Phys. Rev. Appl.*, vol. 3, no. 2, p. 024003, 2015.
- [30] K. H. Kim, K. C. Park, and D. Y. Ma, "Structural, electrical and optical properties of aluminum doped zinc oxide films prepared by radio frequency magnetron sputtering," *J. Appl. Phys.*, vol. 81, no. 1997, p. 7764, 1997.
- [31] J. H. Lee and B. O. Park, "Transparent conducting ZnO:Al, In and Sn thin films deposited by the sol-gel method," *Thin Solid Films*, vol. 426, no. 1–2, pp. 94–99, 2003.
- [32] S. Chen, M. E. A. Warwick, and R. Binions, "Effects of film thickness and thermal treatment on the structural and opto-electronic properties of Ga-doped ZnO films deposited by sol-gel method," *Sol. Energy Mater. Sol. Cells*, vol. 137, pp. 202–209, 2015.
- [33] K. U. Sim, S. W. Shin, a. V. Moholkar, J. H. Yun, J. H. Moon, and J. H. Kim, "Effects of dopant (Al, Ga, and In) on the characteristics of ZnO thin films prepared by RF magnetron sputtering system," *Curr. Appl. Phys.*, vol. 10, no. SUPPL. 3, pp. S463–S467, 2010.
- [34] M. D. McCluskey and S. J. Jokela, "Defects in ZnO," *J. Appl. Phys.*, vol. 106, no. 7, pp. 0–13, 2009.
- [35] W. M. Haynes, T. J. Bruno, and D. R. Lide, *CRC Handbook of Chemistry and Physics*, 88th ed. 2013.

- [36] M. Gabás, A. Landa-Cánovas, J. Luis Costa-Krämer, F. Agulló-Rueda, A. R. González-Elipe, P. Díaz-Carrasco, J. Hernández-Moro, I. Lorite, P. Herrero, P. Castellero, A. Barranco, and J. Ramón Ramos-Barrado, "Differences in n-type doping efficiency between Al- and Ga-ZnO films," *J. Appl. Phys.*, vol. 113, no. 16, p. 163709, 2013.
- [37] T. Minami, H. Sato, H. Nanto, and S. Takata, "Highly Conductive and Transparent Silicon Doped Zinc Oxide Thin Films Prepared by RF Magnetron Sputtering," *Jpn. J. Appl. Phys.*, vol. 25, no. Part 2, No. 9, pp. L776–L779, 1986.
- [38] Q. Yu, H. Yang, W. Fu, L. Chang, J. Xu, C. Yu, R. Wei, K. Du, H. Zhu, M. Li, and G. Zou, "Transparent conducting yttrium-doped ZnO thin films deposited by sol-gel method," *Thin Solid Films*, vol. 515, no. 7–8, pp. 3840–3843, Feb. 2007.
- [39] T. Minami, T. Yamamoto, and T. Miyata, "Highly transparent and conductive rare earth-doped ZnO thin films prepared by magnetron sputtering," *Thin Solid Films*, vol. 366, no. 1–2, pp. 63–68, May 2000.
- [40] a Sanchez-Juarez, a Tiburcio-Silver, a Ortiz, E. P. Zironi, and J. Rickards, "Electrical and optical properties of fluorine-doped ZnO thin films prepared by spray pyrolysis," *Thin Solid Films*, vol. 333, no. 1–2, pp. 196–202, 1998.
- [41] H. Saeki, H. Tabata, and T. Kawai, "Magnetic and electric properties of vanadium doped ZnO films," *Solid State Commun.*, vol. 120, no. 11, pp. 439–443, Nov. 2001.
- [42] P. R. Chalker, P. A. Marshall, P. J. King, K. Dawson, S. Romani, P. A. Williams, J. Ridealgh, and M. J. Rosseinsky, "Atomic layer deposition of germanium-doped zinc oxide films with tuneable ultraviolet emission," *J. Mater. Chem.*, vol. 22, no. 25, p. 12824, 2012.
- [43] Z. Y. Zhong and T. Zhang, "Microstructure and optoelectronic properties of titanium-doped ZnO thin films prepared by magnetron sputtering," *Mater. Lett.*, vol. 96, pp. 237–239, Apr. 2013.
- [44] G. . Paul, S. Bandyopadhyay, S. . Sen, and S. Sen, "Structural, optical and electrical studies on sol-gel deposited Zr doped ZnO films," *Mater. Chem. Phys.*, vol. 79, no. 1, pp. 71–75, Mar. 2003.
- [45] S. Hirotooshi, T. Minami, and S. Takata, "Highly transparent and conductive group IV impurity-doped ZnO thin films prepared by radio frequency magnetron sputtering," *J. Vac. Sci. Technol. A Vacuum, Surfaces, Film.*, vol. 11, no. May 2015, p. 2975, 1993.

- [46] H. Agura, H. Okinaka, S. Hoki, T. Aoki, A. Suzuki, T. Matsushita, and M. Okuda, "Low-resistive and transparent AZO films prepared by PLD in magnetic field," *Electr. Eng. Japan (English Transl. Denki Gakkai Ronbunshi)*, vol. 151, no. 2, pp. 40–45, 2005.
- [47] D. H. Zhang and H. L. Ma, "Scattering mechanisms of charge carriers in transparent conducting oxide films," *Appl. Phys. A Mater. Sci. Process.*, vol. 62, no. 5, pp. 487–492, 1996.
- [48] P. Wagner and R. Helbig, "P. WAGNER und R. HELBIG Institut für Angewandte Physik der Universität Erlangen-Nürnberg, 852 Erlangen, Glückstr. 9, W. Germany," *J. Phys. Chem. Solids*, vol. 35, no. 3, p. 327, 1974.
- [49] J. Zook, "Piezoelectric Scattering in Semiconductors," *Phys. Rev.*, vol. 136, no. 3A, pp. A869–A878, 1964.
- [50] P. Erhart, K. Albe, and A. Klein, "First-principles study of intrinsic point defects in ZnO: Role of band structure, volume relaxation, and finite-size effects," *Phys. Rev. B - Condens. Matter Mater. Phys.*, vol. 73, no. 20, pp. 1–9, 2006.
- [51] Y. Imanaka, M. Oshikiri, K. Takehana, T. Takamasu, and G. Kido, "Cyclotron resonance in n-type ZnO," *Phys. B Condens. Matter*, vol. 298, no. 1–4, pp. 211–215, 2001.
- [52] K. Ellmer, "Resistivity of polycrystalline zinc oxide films: current status and physical limit," *J. Phys. D. Appl. Phys.*, vol. 34, no. 21, pp. 3097–3108, 2001.
- [53] D. H. Zhang, "Adsorption and photodesorption of oxygen on the surface and crystallite interfaces of sputtered ZnO films," *Mater. Chem. Phys.*, vol. 45, no. 3, pp. 248–252, 1996.
- [54] E. Burstein, "Anomalous optical absorption limit in InSb [4]," *Phys. Rev.*, vol. 93, pp. 632–633, 1954.
- [55] T. S. Moss, "The Interpretation of the Properties of Indium Antimonide," *Proc. Phys. Soc. Sect. B*, vol. 67, pp. 775–782, 1954.
- [56] I. Hamberg, C. G. Granqvist, K. F. Berggren, B. E. Sernelius, and L. Engström, "Band-gap widening in heavily Sn-doped In₂O₃," *Phys. Rev. B*, vol. 30, no. 6, pp. 3240–3249, 1984.
- [57] P. Rodnyi and I. Khodyuk, "Optical and luminescence properties of zinc oxide (Review)," *Opt. Spectrosc.*, vol. 111, no. 5, pp. 776–785, 2011.

- [58] B. Guo, Z. R. Qiu, and K. S. Wong, "Intensity dependence and transient dynamics of donor-acceptor pair recombination in ZnO thin films grown on (001) silicon," *Appl. Phys. Lett.*, vol. 82, no. 14, p. 2290, 2003.
- [59] W. Shan, W. Walukiewicz, J. W. Ager, K. M. Yu, Y. Zhang, S. S. Mao, R. Kling, C. Kirchner, and a. Waag, "Pressure-dependent photoluminescence study of ZnO nanowires," *Appl. Phys. Lett.*, vol. 86, no. 15, p. 153117, 2005.
- [60] M. Liu, a. H. Kitai, and P. Mascher, "Point defects and luminescence centres in zinc oxide and zinc oxide doped with manganese," *J. Lumin.*, vol. 54, pp. 35-42, 1992.
- [61] D. C. Reynolds, D. C. Look, B. Jogai, C. W. Litton, G. Cantwell, and W. C. Harsch, "Determination of defect pair orientation in ZnO," *Solid State Commun.*, vol. 109, pp. 419-422, 1999.
- [62] R. R. Thankalekshmi, S. Dixit, and a C. Rastogi, "Doping sensitive optical scattering in zinc oxide nanostructured films for solar cells," vol. 4, no. 1, pp. 9-14, 2013.
- [63] X. L. Chen, X. H. Geng, J. M. Xue, D. K. Zhang, G. F. Hou, and Y. Zhao, "Temperature-dependent growth of zinc oxide thin films grown by metal organic chemical vapor deposition," *J. Cryst. Growth*, vol. 296, no. 1, pp. 43-50, 2006.
- [64] A. Janotti, C. G. Van de Walle, and C. G. Van De Walle, "Fundamentals of zinc oxide as a semiconductor," *Reports Prog. Phys.*, vol. 72, no. 12, p. 126501, 2009.
- [65] D. Kim and H. Kim, "Self-textured transparent conductive oxide film improves efficiency of solar cells," *SPIE Newsroom*, pp. 5-7, 2010.
- [66] J. Müller, B. Rech, J. Springer, and M. Vanecek, "TCO and light trapping in silicon thin film solar cells," *Sol. Energy*, vol. 77, no. 6, pp. 917-930, 2004.
- [67] X. Hou and K. L. Choy, "Processing and Applications of Aerosol-Assisted Chemical Vapor Deposition," *Chem. Vap. Depos.*, vol. 12, no. 10, pp. 583-596, 2006.
- [68] T. Tynell and M. Karppinen, "Atomic layer deposition of ZnO: a review," *Semicond. Sci. Technol.*, vol. 29, p. 043001, 2014.
- [69] A. Yamada, B. Sang, and M. Konagai, "Atomic layer deposition of ZnO transparent conducting oxides," *Appl. Surf. Sci.*, vol. 112, pp. 216-222, 1997.

- [70] J. Malm, E. Sahramo, J. Perälä, T. Sajavaara, and M. Karppinen, "Low-temperature atomic layer deposition of ZnO thin films: Control of crystallinity and orientation," *Thin Solid Films*, vol. 519, no. 16, pp. 5319–5322, 2011.
- [71] T. Minami, H. Sato, H. Nanto, and S. Takata, "Group III impurity doped zinc oxide thin films prepared by RF magnetron sputtering," *Jpn. J. Appl. Phys.*, vol. 24, no. 10, pp. L781–L784, 1985.
- [72] J. B. Franklin, J. B. Gilchrist, J. M. Downing, K. a. Roy, and M. a. McLachlan, "Transparent conducting oxide top contacts for organic electronics," *J. Mater. Chem. C*, vol. 2, no. 1, p. 84, 2014.
- [73] K. Ramamoorthy, C. Sanjeeviraja, M. Jayachandran, K. Sankaranarayanan, P. Misra, and L. M. Kukreja, "Development of a novel high optical quality ZnO thin films by PLD for III-V opto-electronic devices," *Curr. Appl. Phys.*, vol. 6, no. 1, pp. 103–108, 2006.
- [74] E. J. Luna-Arredondo, a. Maldonado, R. Asomoza, D. R. Acosta, M. a. Meléndez-Lira, and M. de la L. Olvera, "Indium-doped ZnO thin films deposited by the sol-gel technique," *Thin Solid Films*, vol. 490, no. 2, pp. 132–136, 2005.
- [75] M. Jun and J. Koh, "Effects of Annealing Temperature on Properties of Al-Doped ZnO Thin Films prepared by Sol-Gel Dip-Coating," vol. 8, no. 1, pp. 163–167, 2013.
- [76] S. Peulon and D. Lincot, "Cathodic electrodeposition from aqueous solution of dense or open-structured zinc oxide films," *Adv. Mater.*, vol. 8, no. 2, p. 166, 1996.
- [77] T. Pauporté, G. Bataille, L. Joulaud, and F. J. Vermersch, "Well-aligned ZnO nanowire arrays prepared by seed-layer-free electrodeposition and their cassie-wenzel transition after hydrophobization," *J. Phys. Chem. C*, vol. 114, no. 1, pp. 194–202, 2010.
- [78] R. R. Chamberlin and J. S. Skarman, "Chemical Spray Deposition Process for Inorganic Films," *J. Electrochem. Soc.*, vol. 113, no. 1, pp. 86–89, Jan. 1966.
- [79] F. Paraguay D., W. Estrada L., D. R. Acosta N., E. Andrade, and M. Miki-Yoshida, "Growth, structure and optical characterization of high quality ZnO thin films obtained by spray pyrolysis," *Thin Solid Films*, vol. 350, no. 1–2, pp. 192–202, Aug. 1999.
- [80] G. Korotcenkov, V. Brinzari, J. Schwank, M. DiBattista, and A. Vasiliev, "Peculiarities of SnO₂ thin film deposition by spray pyrolysis for gas sensor application," *Sensors Actuators B Chem.*, vol. 77, no. 1–2, pp. 244–252, Jun. 2001.

- [81] J. C. Manificier, J. P. Fillard, and J. M. Bind, "Deposition of In₂O₃/SnO₂ layers on glass substrates using a spraying method," *Thin Solid Films*, vol. 77, no. 1–3, pp. 67–80, Mar. 1981.
- [82] S. M. Rozati and T. Ganj, "Transparent conductive Sn-doped indium oxide thin films deposited by spray pyrolysis technique," *Renew. Energy*, vol. 29, no. 10, pp. 1671–1676, Aug. 2004.
- [83] L. Dghoughi, F. Ouachtari, M. Addou, B. Elidrissi, H. Erguig, a. Rmili, and a. Bouaoud, "The effect of Al-doping on the structural, optical, electrical and cathodoluminescence properties of ZnO thin films prepared by spray pyrolysis," *Phys. B Condens. Matter*, vol. 405, no. 9, pp. 2277–2282, 2010.
- [84] W. Siefert, "Properties of thin In₂O₃ and SnO₂ films prepared by corona spray pyrolysis, and a discussion of the spray pyrolysis process," *Thin Solid Films*, vol. 120, no. 4, pp. 275–282, Oct. 1984.
- [85] L. Filipovic, S. Selberherr, G. C. Mutinati, E. Brunet, S. Steinhauer, A. Köck, J. Teva, J. Kraft, J. Siegert, and F. Schrank, "Methods of simulating thin film deposition using spray pyrolysis techniques," *Microelectron. Eng.*, vol. 117, pp. 57–66, Apr. 2014.
- [86] P. Scherrer, "Bestimmung der Grösse und der inneren Struktur von Kolloidteilchen mittels Röntgenstrahlen," *Nachrichten von der Gesellschaft der Wissenschaften zu Göttingen, Math. Klasse*, vol. 1918, pp. 98–100, 1918.
- [87] B. D. Cullity and S. R. Stock, *Elements of X Ray Diffraction*, 3rd ed. Prentice Hall, 2001.
- [88] U. Holzwarth and N. Gibson, "The Scherrer equation versus the 'Debye-Scherrer equation,'" *Nat Nano*, vol. 6, no. 9, p. 534, Sep. 2011.
- [89] M. . Tokumoto, a Smith, C. . Santilli, S. . Pulcinelli, a. . Craievich, E. Elkaim, a Traverse, and V. Briois, "Structural electrical and optical properties of undoped and indium doped ZnO thin films prepared by the pyrosol process at different temperatures," *Thin Solid Films*, vol. 416, no. 1–2, pp. 284–293, 2002.
- [90] B. L. Gabriel, *SEM: A User's Manual for Materials Science*. 1985.
- [91] B. Voutou, E. Stefanaki, and K. Giannakopoulos, *Electron Microscopy : The Basics*. 2008.
- [92] H.-Y. Joo, H. J. Kim, S. J. Kim, and S. Y. Kim, "Spectrophotometric analysis of aluminum nitride thin films," *J. Vac. Sci. Technol. A Vacuum, Surfaces, Film.*, vol. 17, no. 3, p. 862, 1999.

- [93] J. B. Franklin, "Pulsed Laser Deposition of Zinc Oxide Thin Films for Optoelectronic Applications," 2012.
- [94] M. Deen and F. Pascal, "Electrical Characterization of Semiconductor Materials and Devices," *Handb. Electron. Photonic Mater.*, pp. 409–438, 2007.
- [95] L. J. van der Pauw, "A method of measuring specific resistivity and Hall effect of discs of arbitrary shape," *Philips Res. Reports*, vol. 13, no. 1, pp. 1–11, 1958.
- [96] K. Ellmer, *Characterization of Materials*. John Wiley & Sons, 2012.
- [97] J. Lindemuth and S.-I. Mizuta, "Hall measurements on low mobility materials and high resistivity materials," vol. 8110, no. 5, p. 81100I–81100I–7, 2011.
- [98] A. Bashir, P. H. Wöbkenberg, J. Smith, J. M. Ball, G. Adamopoulos, D. D. C. Bradley, and T. D. Anthopoulos, "High-Performance Zinc Oxide Transistors and Circuits Fabricated by Spray Pyrolysis in Ambient Atmosphere," *Adv. Mater.*, vol. 21, no. 21, pp. 2226–2231, 2009.
- [99] S. Karakaya and O. Ozbas, "Boron doped nanostructure ZnO films deposited by ultrasonic spray pyrolysis," *Appl. Surf. Sci.*, vol. 328, pp. 177–182, Feb. 2015.
- [100] D. P. Pham, H. T. Nguyen, B. T. Phan, T. M. D. Cao, V. D. Hoang, V. A. Dao, J. Yi, and C. V. Tran, "In and Ga Codoped ZnO Film as a Front Electrode for Thin Film Silicon Solar Cells," *Adv. Condens. Matter Phys.*, vol. 2014, pp. 1–7, 2014.
- [101] N. Jabena Begum and K. Ravichandran, "Effect of source material on the transparent conducting properties of sprayed ZnO:Al thin films for solar cell applications," *J. Phys. Chem. Solids*, vol. 74, no. 6, pp. 841–848, 2013.
- [102] N. Rashidi, V. L. Kuznetsov, J. R. Dilworth, M. Pepper, P. J. Dobson, and P. P. Edwards, "Highly conducting and optically transparent Si-doped ZnO thin films prepared by spray pyrolysis," *J. Mater. Chem. C*, vol. 1, no. 42, p. 6960, 2013.
- [103] V. Gokulakrishnan, V. Purushothaman, E. Arthi, K. Jeganathan, and K. Ramamurthi, "Effect of vacuum annealing on the structural, optical, and electrical properties of spray-deposited Ga-doped ZnO thin films," *Phys. Status Solidi*, vol. 209, no. 8, pp. 1481–1486, 2012.
- [104] R. Anandhi, R. Mohan, K. Swaminathan, and K. Ravichandran, "Influence of aging time of the starting solution on the physical properties of fluorine doped zinc oxide films deposited by a simplified spray pyrolysis technique," *Superlattices Microstruct.*, vol. 51, no. 5, pp. 680–689, May 2012.

- [105] R. Pandey, S. Yuldashev, H. D. Nguyen, H. C. Jeon, and T. W. Kang, "Fabrication of aluminium doped zinc oxide (AZO) transparent conductive oxide by ultrasonic spray pyrolysis," *Curr. Appl. Phys.*, vol. 12, no. 4, pp. S56-S58, Dec. 2012.
- [106] F. Chouikh, Y. Beggah, and M. S. Aida, "Optical and electrical properties of Bi doped ZnO thin films deposited by ultrasonic spray pyrolysis," *J. Mater. Sci. Mater. Electron.*, vol. 22, no. 5, pp. 499-505, May 2011.
- [107] T. Aarii and A. Kishi, "The effect of humidity on thermal process of zinc acetate," *Thermochim. Acta*, vol. 400, no. 1-2, pp. 175-185, 2003.
- [108] U. Alver, T. Kiliç, E. Bacaksiz, T. Küçükömeroğlu, S. Nezir, I. H. Mutlu, and F. Aslan, "Synthesis and characterization of spray pyrolysis Zinc Oxide microrods," *Thin Solid Films*, vol. 515, no. 7-8, pp. 3448-3451, 2007.
- [109] J. De Merchant and M. Cocivera, "Preparation and doping of zinc oxide using spray pyrolysis," *Chem. Mater.*, no. 16, pp. 1742-1749, 1995.
- [110] M. de la L. Olvera, a. Maldonado, J. Vega-Pérez, and O. Solorza-Feria, "Aluminum-doped zinc oxide (ZnO:Al) thin films deposited on glass substrates by chemical spray starting from zinc pentanedionate and aluminum chloride," *Mater. Sci. Eng. B*, vol. 174, no. 1-3, pp. 42-45, Oct. 2010.
- [111] R. Romero, D. Leinen, E. a. Dalchiele, J. R. Ramos-Barrado, and F. Martín, "The effects of zinc acetate and zinc chloride precursors on the preferred crystalline orientation of ZnO and Al-doped ZnO thin films obtained by spray pyrolysis," *Thin Solid Films*, vol. 515, no. 4, pp. 1942-1949, 2006.
- [112] E. Bacaksiz, M. Parlak, M. Tomakin, a. Özçelik, M. Karakız, and M. Altunbaş, "The effects of zinc nitrate, zinc acetate and zinc chloride precursors on investigation of structural and optical properties of ZnO thin films," *J. Alloys Compd.*, vol. 466, no. 1-2, pp. 447-450, 2008.
- [113] M. Krunks and E. Mellikov, "Zinc oxide thin films by the spray pyrolysis method," *Thin Solid Films*, vol. 270, no. 1-2, pp. 33-36, 1995.
- [114] A. Maldonado, M. de la L. Olvera, R. Asomoza, E. P. Zironi, J. Canetas-Ortega, and J. Palacios-Gómez, "Characteristics of spray pyrolytic ZnO:In thin films grown from zinc acetate and indium nitrate," *J. Vac. Sci. Technol. A*, vol. 15, no. 1997, pp. 2905-2907, 1997.
- [115] E. Arca, K. Fleischer, and I. V. Shvets, "Influence of the precursors and chemical composition of the solution on the properties of ZnO thin films grown by spray pyrolysis," *J. Phys. Chem. C*, vol. 113, no. 50, pp. 21074-21081, 2009.

- [116] G. Kenanakis, N. Katsarakis, and E. Koudoumas, "Influence of precursor type, deposition time and doping concentration on the morphological, electrical and optical properties of ZnO and ZnO:Al thin films grown by ultrasonic spray pyrolysis," *Thin Solid Films*, vol. 555, pp. 62–67, 2014.
- [117] J.-F. Guillemoles, D. Lincot, P. Cowache, and J. Vedel, "Solvent Effect on ZnO Thin Films Prepared by Spray Pyrolysis," *Tenth E.C. Photovolt. Sol. Energy Conf. SE - 156*, pp. 609–612, 1991.
- [118] a. Guillén-Santiago, M. D. L. L. Olvera, a. Maldonado, R. Asomoza, and D. R. Acosta, "Electrical, structural and morphological properties of chemically sprayed F-doped ZnO films: Effect of the ageing-time of the starting solution, solvent and substrate temperature," *Phys. Status Solidi Appl. Res.*, vol. 201, no. 5, pp. 952–959, 2004.
- [119] B. P. Whim and P. G. Johnson, Eds., *Directory of Solvents*. Dordrecht: Springer Netherlands, 1996.
- [120] F. Caillaud, A. Smith, and J.-F. Baumard, "Effect of pH of the Solution on the Deposition of Zinc Oxide Films by Spray Pyrolysis," *J. Am. Ceram. Soc.*, vol. 76, no. 4, pp. 998–1002, 1993.
- [121] S. Chen, R. M. Wilson, and R. Binions, "Synthesis of highly surface-textured ZnO thin films by aerosol assisted chemical vapour deposition," *J. Mater. Chem. A*, vol. 3, no. 11, pp. 5794–5797, 2015.
- [122] a Maldonado, R. Asomoza, J. Cañetas-Ortega, E. . Zironi, R. Hernández, R. Patiño, and O. Solorza-Feria, "Effect of the pH on the physical properties of ZnO:In thin films deposited by spray pyrolysis," *Sol. Energy Mater. Sol. Cells*, vol. 57, no. 4, pp. 331–344, 1999.
- [123] E. Zaleta-Alejandre, J. Camargo-Martinez, a. Ramirez-Garibo, M. L. Pérez-Arrieta, R. Balderas-Xicohténcatl, Z. Rivera-Alvarez, M. Aguilar-Frutis, and C. Falcony, "Structural, electrical and optical properties of indium chloride doped ZnO films synthesized by Ultrasonic Spray Pyrolysis technique," *Thin Solid Films*, vol. 524, pp. 44–49, 2012.
- [124] S. Major, a. Banerjee, K. L. Chopra, and K. C. Nagpal, "Thickness-dependent properties of indium-doped ZnO films," *Thin Solid Films*, vol. 143, no. 1, pp. 19–30, 1986.
- [125] C. Messaoudi, D. Sayah, and M. Abd-lefdil, "Transparent conducting undoped and indium-doped zinc oxide films prepared by spray pyrolysis," *Phys. Status Solidi*, vol. 151, no. 1, pp. 93–97, 1995.

- [126] M. a. Lucio-López, A. Maldonado, R. Castanedo-Pérez, G. Torres-Delgado, and M. de la L. Olvera, "Thickness dependence of ZnO:In thin films doped with different indium compounds and deposited by chemical spray," *Sol. Energy Mater. Sol. Cells*, vol. 90, p. 2362, 2006.
- [127] N. Fujimura, T. Nishihara, S. Goto, J. Xu, and T. Ito, "Control of preferred orientation for ZnOx films: control of self-texture," *J. Cryst. Growth*, vol. 130, no. 1-2, pp. 269-279, 1993.
- [128] A. K. Gyani, O. F. Z. Khan, P. O. O'Brien, and D. S. Urch, "On the use of basic zinc acetate $Zn_4O(CH_3CO_2)_6$ as a novel precursor for the deposition of ZnO by low-pressure metallo organic chemical vapour deposition: their characterization by low energy electron induced X-ray emission spectroscopy," *Thin Solid Films*, vol. 182, pp. 3-6, 1989.
- [129] T. Y. Ma, S. H. Kim, H. Y. Moon, G. C. Park, Y. J. Kim, and K. W. Kim, "Substrate temperature dependence of ZnO films prepared by ultrasonic spray pyrolysis," *Japanese J. Appl. Physics, Part 1 Regul. Pap. Short Notes Rev. Pap.*, vol. 35, no. 12 A, pp. 6208-6211, 1996.
- [130] F. Zahedi, R. S. Dariani, and S. M. Rozati, "Effect of substrate temperature on the properties of ZnO thin films prepared by spray pyrolysis," *Mater. Sci. Semicond. Process.*, vol. 16, no. 2, pp. 245-249, 2013.
- [131] J. . van Heerden and R. Swanepoel, "XRD analysis of ZnO thin films prepared by spray pyrolysis," *Thin Solid Films*, vol. 299, no. 1-2, pp. 72-77, 1997.
- [132] O. Dobrozhan, D. Kurbatov, A. Opanasyuk, H. Cheong, and A. Cabot, "Influence of substrate temperature on the structural and optical properties of crystalline ZnO films obtained by pulsed spray pyrolysis," *Surf. Interface Anal.*, vol. 47, no. 5, pp. 601-606, 2015.
- [133] T. Prasada Rao, M. C. Santhosh Kumar, a. Safarulla, V. Ganesan, S. R. Barman, and C. Sanjeeviraja, "Physical properties of ZnO thin films deposited at various substrate temperatures using spray pyrolysis," *Phys. B Condens. Matter*, vol. 405, no. 9, pp. 2226-2231, 2010.
- [134] S. D. Lee, S.-H. Nam, M.-H. Kim, and J.-H. Boo, "Synthesis and Photocatalytic Property of ZnO nanoparticles Prepared by Spray-Pyrolysis Method," *Phys. Procedia*, vol. 32, pp. 320-326, 2012.
- [135] R. Ayouchi, D. Leinen, F. Martín, M. Gabas, E. Dalchiele, and J. R. Ramos-Barrado, "Preparation and characterization of transparent ZnO thin films obtained by spray pyrolysis," *Thin Solid Films*, vol. 426, no. 1-2, pp. 68-77, 2003.

- [136] M. Vent, E. Kärber, T. Unt, A. Mere, and M. Krunk, "The effect of growth temperature and spraying rate on the properties of ZnO:In films," *Phys. Status Solidi*, vol. 9, no. 7, pp. 1604–1606, 2012.
- [137] M. G. Ambia, M. N. Islam, and M. O. Hakim, "The effects of deposition variables on the spray-pyrolysis of ZnO thin-film," *J. Mater. Sci.*, vol. 29, no. 24, pp. 6575–6580, 1994.
- [138] N. L. Tarwal and P. S. Patil, "Superhydrophobic and transparent ZnO thin films synthesized by spray pyrolysis technique," *Appl. Surf. Sci.*, vol. 256, no. 24, pp. 7451–7456, 2010.
- [139] G. L. Messing, S.-C. Zhang, and G. V. Jayanthi, "Ceramic Powder Synthesis," *J. Am. Ceram. Soc.*, vol. 76, no. 11, pp. 2707–2726, 1993.
- [140] a R. Babar, P. R. Deshamukh, R. J. Deokate, D. Haranath, C. H. Bhosale, and K. Y. Rajpure, "Gallium doping in transparent conductive ZnO thin films prepared by chemical spray pyrolysis," *J. Phys. D. Appl. Phys.*, vol. 41, p. 135404, 2008.
- [141] a. El Manouni, F. J. Manjón, M. Mollar, B. Marí, R. Gómez, M. C. López, and J. R. Ramos-Barrado, "Effect of aluminium doping on zinc oxide thin films grown by spray pyrolysis," *Superlattices Microstruct.*, vol. 39, no. 1–4, pp. 185–192, Jan. 2006.
- [142] W. L. Estrada, D. R. N. Acosta, E. Andrade, and M. Miki-yoshida, "Growth , structure and optical characterization of high quality ZnO thin films obtained by spray pyrolysis," *Thin Solid Films*, vol. 350, pp. 192–202, 1999.
- [143] G. Haacke, "New figure of merit for transparent conductors," *J. Appl. Phys.*, vol. 47, no. 9, pp. 4086–4089, 1976.
- [144] S. S. Shinde, C. H. Bhosale, and K. Y. Rajpure, "Structural, optical, electrical and thermal properties of zinc oxide thin films by chemical spray pyrolysis," *J. Mol. Struct.*, vol. 1021, pp. 123–129, 2012.
- [145] R. Mariappan, V. Ponnuswamy, and M. Ragavendar, "Influence of molar concentration on the physical properties of nebulizer-sprayed ZnO thin films for ammonia gas sensor," *Mater. Sci. Semicond. Process.*, vol. 16, no. 5, pp. 1328–1335, 2013.
- [146] N. Mehan, M. Tomar, V. Gupta, and A. Mansingh, "Optical waveguiding and birefringence properties of sputtered zinc oxide (ZnO) thin films on glass," *Opt. Mater. (Amst.)*, vol. 27, no. 2, pp. 241–248, Nov. 2004.

- [147] S. M. Rozati and S. Akesteh, "Characterization of ZnO:Al thin films obtained by spray pyrolysis technique," *Mater. Charact.*, vol. 58, pp. 319–322, 2007.
- [148] G. K. Mani and J. B. B. Rayappan, "Impact of annealing duration on spray pyrolysis deposited nanostructured zinc oxide thin films," *Superlattices Microstruct.*, vol. 67, pp. 82–87, 2014.
- [149] M. Abdullah, K. Khairurrijal, B. W. Nuryadin, and E. Sustini, "Synthesis of Oxide Particles Using a Polymer-Assisted Spray Pyrolysis Reactor, and a Percolation Explanation of Particle Separation," *Int. J. Chem. React. Eng.*, vol. 8, 2010.
- [150] M. Sathiya, K. Ramesha, G. Rousse, S. S. Shinde, a. P. Korade, C. H. Bhosale, and K. Y. Rajpure, "Influence of tin doping onto structural, morphological, optoelectronic and impedance properties of sprayed ZnO thin films," *J. Alloys Compd.*, vol. 551, pp. 688–693, 2013.
- [151] a. Khoury, R. al Asmar, M. Abdallah, G. E. H. Moussa, and a. Foucaran, "Comparative study between zinc oxide elaborated by spray pyrolysis, electron beam evaporation and rf magnetron techniques," *Phys. Status Solidi*, vol. 207, no. 8, pp. 1900–1904, 2010.
- [152] C. M. Muiva, T. S. Sathiaraj, and K. Maabong, "Effect of doping concentration on the properties of aluminium doped zinc oxide thin films prepared by spray pyrolysis for transparent electrode applications," *Ceram. Int.*, vol. 37, no. 2, pp. 555–560, Mar. 2011.
- [153] H. Gómez-Pozos, a. Maldonado, and M. D. L. L. Olvera, "Effect of the [Al/Zn] ratio in the starting solution and deposition temperature on the physical properties of sprayed ZnO:Al thin films," *Mater. Lett.*, vol. 61, no. 7, pp. 1460–1464, Mar. 2007.
- [154] S. Jongthammanurak, M. Witana, T. Cheawkul, and C. Thanachayanont, "The effects of carrier gas and substrate temperature on ZnO films prepared by ultrasonic spray pyrolysis," *Mater. Sci. Semicond. Process.*, vol. 16, no. 3, pp. 625–632, 2013.
- [155] J.-L. Zhao, X.-M. Li, J.-M. Bian, W.-D. Yu, and C.-Y. Zhang, "Growth of nitrogen-doped p-type ZnO films by spray pyrolysis and their electrical and optical properties," *J. Cryst. Growth*, vol. 280, no. 3–4, pp. 495–501, 2005.
- [156] S. Dhara and P. K. Giri, "Stable p-type conductivity and enhanced photoconductivity from nitrogen-doped annealed ZnO thin film," *Thin Solid Films*, vol. 520, no. 15, pp. 5000–5006, 2012.
- [157] D. S. Boyle, K. Govender, and P. O'Brien, "Novel wet-chemical routes to nano- and microstructured semiconductor layers for improved efficiency photovoltaic devices," *Thin Solid Films*, vol. 431–432, no. 9, pp. 483–487, May 2003.

- [158] F. Solís-Pomar, E. Martínez, M. F. Meléndrez, and E. Pérez-Tijerina, "Growth of vertically aligned ZnO nanorods using textured ZnO films," *Nanoscale Res. Lett.*, vol. 6, no. 1, p. 524, 2011.
- [159] R. B. Peterson, C. L. Fields, and B. A. Gregg, "Epitaxial chemical deposition of ZnO nanocolumns from NaOH solutions," *Langmuir*, vol. 20, no. 12, pp. 5114–5118, 2004.
- [160] D. Wang and C. Song, "Controllable Synthesis of ZnO Nanorod and Prism Arrays in a Large Area," pp. 12697–12700, 2005.
- [161] S. Hirano, K. Masuya, and M. Kuwabara, "Multi-Nucleation-Based Formation of Oriented Zinc Oxide Microcrystals and Films in Aqueous Solutions," *J. Phys. Chem. B*, vol. 108, no. 15, pp. 4576–4578, Apr. 2004.
- [162] S. W. Seo, S. H. Won, H. Chae, and S. M. Cho, "Low-temperature growth of highly conductive and transparent aluminum-doped ZnO film by ultrasonic-mist deposition," *Korean J. Chem. Eng.*, vol. 29, no. 4, pp. 525–528, 2012.
- [163] S. Gledhill, A. Grimm, D. Greiner, W. Bohne, M. Lux-Steiner, and C. H. Fischer, "Doping induced structural and compositional changes in ZnO spray pyrolysed films and the effects on optical and electrical properties," *Thin Solid Films*, vol. 519, no. 13, pp. 4293–4298, 2011.
- [164] P. Arnou, J. W. Bowers, and J. M. Walls, "Aluminium-doped zinc oxide deposited by ultrasonic spray pyrolysis for thin film solar cell applications," pp. 308–313, 2014.
- [165] K. Schulze, B. Maennig, K. Leo, Y. Tomita, C. May, J. Hüpkes, E. Brier, E. Reinold, and P. Bäuerle, "Organic solar cells on indium tin oxide and aluminum doped zinc oxide anodes," *Appl. Phys. Lett.*, vol. 91, no. 7, pp. 1–4, 2007.
- [166] Z. Ben Achour, T. Ktari, B. Ouertani, O. Touayar, B. Bessais, and J. Ben Brahim, "Effect of doping level and spray time on zinc oxide thin films produced by spray pyrolysis for transparent electrodes applications," *Sensors Actuators A Phys.*, vol. 134, no. 2, pp. 447–451, Mar. 2007.
- [167] T. Y. Ma and S. C. Lee, "Effects of aluminum content and substrate temperature on the structural and electrical properties of aluminum-doped ZnO films prepared by ultrasonic spray pyrolysis," *J. Mater. Sci. Mater. Electron.*, vol. 1, pp. 305–309, 2000.
- [168] B. J. Babu, A. Maldonado, S. Velumani, and D. D. I. Eléctrica-sees, "Deposition and Characterization of ZnO : Al Thin Films by Ultrasonic Spray Pyrolysis," no. i.

- [169] B. J. Babu, a. Maldonado, S. Velumani, and R. Asomoza, "Electrical and optical properties of ultrasonically sprayed Al-doped zinc oxide thin films," *Mater. Sci. Eng. B*, vol. 174, no. 1-3, pp. 31-37, Oct. 2010.
- [170] E. Arca, K. Fleischer, and I. Shvets, "Tuning the crystallographic, morphological, optical and electrical properties of ZnO:Al grown by spray pyrolysis," *Thin Solid Films*, vol. 555, pp. 9-12, 2014.
- [171] F. A. Garcés, N. Budini, R. D. Arce, and J. A. Schmidt, "Effect of thickness on structural and electrical properties of Al-doped ZnO films," *Thin Solid Films*, vol. 574, pp. 162-168, Jan. 2015.
- [172] H. Hung-Chun Lai, T. Basheer, V. L. Kuznetsov, R. G. Egdell, R. M. J. Jacobs, M. Pepper, and P. P. Edwards, "Dopant-induced bandgap shift in Al-doped ZnO thin films prepared by spray pyrolysis," *J. Appl. Phys.*, vol. 112, no. 2012, 2012.
- [173] J.-H. Lee and B.-O. Park, "Characteristics of Al-doped ZnO thin films obtained by ultrasonic spray pyrolysis: effects of Al doping and an annealing treatment," *Mater. Sci. Eng. B*, vol. 106, no. 3, pp. 242-245, Feb. 2004.
- [174] M. T. Mohammad, a. a. Hashim, and M. H. Al-Maamory, "Highly conductive and transparent ZnO thin films prepared by spray pyrolysis technique," *Mater. Chem. Phys.*, vol. 99, no. 2-3, pp. 382-387, Oct. 2006.
- [175] S. Tewari and A. Bhattacharjee, "Structural , electrical and optical studies on spray-deposited aluminium-doped ZnO thin films," vol. 76, no. 1, pp. 153-163, 2011.
- [176] R. Pandey, S. Yuldashev, H. D. Nguyen, H. C. Jeon, and T. W. Kang, "Fabrication of aluminium doped zinc oxide (AZO) transparent conductive oxide by ultrasonic spray pyrolysis," *Curr. Appl. Phys.*, vol. 12, pp. S56-S58, Dec. 2012.
- [177] S.-Y. Kuo, W.-C. Chen, F.-I. Lai, C.-P. Cheng, H.-C. Kuo, S.-C. Wang, and W.-F. Hsieh, "Effects of doping concentration and annealing temperature on properties of highly-oriented Al-doped ZnO films," *J. Cryst. Growth*, vol. 287, no. 1, pp. 78-84, Jan. 2006.
- [178] Y. Wu, P. M. Hermkens, B. W. H. Van De Loo, H. C. M. Knoop, S. E. Potts, M. a. Verheijen, F. Roozeboom, and W. M. M. Kessels, "Electrical transport and Al doping efficiency in nanoscale ZnO films prepared by atomic layer deposition," *J. Appl. Phys.*, vol. 114, 2013.
- [179] R. P. Wang, G. Xu, and P. Jin, "Size dependence of electron-phonon coupling in ZnO nanowires," *Phys. Rev. B*, vol. 69, no. 11, p. 113303, 2004.

- [180] M. Soliman Selim, M. Chandra Sekhar, and a. R. Raju, "Preparation and characterization of thin films of ZnO:Al by nebulized spray pyrolysis," *Appl. Phys. A Mater. Sci. Process.*, vol. 78, no. 8, pp. 1215–1218, May 2004.
- [181] A. F. Aktaruzzaman, G. L. Sharma, and L. K. Malhotra, "Electrical, optical and annealing characteristics of ZnO:Al films prepared by spray pyrolysis," *Thin Solid Films*, vol. 198, no. 1–2, pp. 67–74, Mar. 1991.
- [182] P. Nunes, a Malik, B. Fernandes, E. Fortunato, P. Vilarinho, and R. Martins, "Influence of the doping and annealing atmosphere on zinc oxide thin films deposited by spray pyrolysis," *Vacuum*, vol. 52, pp. 45–49, 1999.
- [183] E. V. Lavrov, J. Weber, F. Börrnert, C. G. Van de Walle, and R. Helbig, "Hydrogen-related defects in ZnO studied by infrared absorption spectroscopy," *Phys. Rev. B*, vol. 66, no. 16, p. 165205, 2002.
- [184] T. Sekiguchi, N. Ohashi, and Y. Terada, "Effect of hydrogenation on ZnO luminescence," *Japanese J. Appl. Physics, Part 2 Lett.*, vol. 36, no. 3 A, pp. 3711–3716, 1997.

APPENDIX

Data from Chapter III

A. 1 Coding for Spray Rig (see section 3.3)

The automated spray rig was programmed on an Arduino Uno microcontroller in C++. Two stepper motors were used to move the gun trigger and the stage; to make this possible an 'Adafruit MotorShield' was attached. Two buttons and an LED from TinkerKit were included to control the program. The appropriate libraries were included to facilitate this.

The coding for all components is given below:

```
// include the appropriate libraries

#include <TinkerKit.h>
#include <Wire.h>
#include <Adafruit_MotorShield.h>
#include "utility/Adafruit_PWMServoDriver.h"

//define inputs and outputs on arduino

TKButton startbutton (I3);
TKButton stopbutton (I2);
int TKButton (LOW);
TKLed led(O4);
Adafruit_MotorShield AFMS = Adafruit_MotorShield();
Adafruit_StepperMotor *myMotor = AFMS.getStepper(200, 2);
Adafruit_StepperMotor *myActuator = AFMS.getStepper(200, 1);

//Set spray conditions

// a = number of iterations, b = position of stage and trigger, c = seconds delayed between sprays 1s
= 1000

int a = 5;
int b = 0;
int c = 25000;

//run program

void setup(){

    //welcome message

    Serial.println("Hi my name is Errol my belly is full of flammables and I'm liable explode at any
moment. In the meantime let's deposit some films :)");

    //initiate motors and set speeds

    Serial.begin(9600);
    AFMS.begin();
    myMotor->setSpeed(100);
    myActuator->setSpeed(9000);}
```

```

void loop(){

    //wait for start button to be pressed

    if(startbutton.read() == LOW){
        led.on();
    }
    if(stopbutton.read() == HIGH){
        led.off();
        myActuator->step(600, FORWARD, DOUBLE);
        myActuator->release();
        delay (30000);
        myActuator->step(600, BACKWARD, DOUBLE);
        myActuator->release();
    }

    // when start button pressed

    if (startbutton.read() == HIGH){

        while (stopbutton.read() == LOW){

            //runs the spray cycle "a" times

            for(int spraycycle = 1; spraycycle <= a; spraycycle++){

                // press trigger

                Serial.println("start spraying");
                myActuator->step(600, FORWARD, DOUBLE);
                myActuator->release();
                b = 1;

                // run belt motor

                Serial.println("run belt motor");
                myMotor->step(1000, FORWARD, DOUBLE);
                myMotor->release();
                myActuator->step(600, BACKWARD, DOUBLE);
                myActuator->release();
                b = 2;

                // stop at one end and wait for 'c' seconds

                delay (c);

                //return to start position

                myActuator->step(600, FORWARD, DOUBLE);
                myActuator->release();
                b = 1;
                myMotor->step(1000, BACKWARD, DOUBLE);
                myMotor->release();
                myActuator->step(600, BACKWARD, DOUBLE);
                myActuator->release();
                b = 0;

                // stop again and wait for 'c' seconds

                delay (c);
            }
        }

        //if stop button is pressed – to allow program to be manually terminated, b gives
        position of stage and directs action
    }
}

```

```
    if (stopbutton.read() == HIGH && b == 1){
        myActuator->step(600, BACKWARD, DOUBLE);
        myActuator->release();
        myMotor->step(500, BACKWARD, DOUBLE);
        myMotor->release();
    }
    if (stopbutton.read() == HIGH && b == 2){
        myMotor->step(1000, BACKWARD, DOUBLE);
        myMotor->release();
    }

    if (stopbutton.read() == HIGH && b == 0){
    }
}
}
```

Data from Chapter IV

A.2 XRD patterns from section 4.2.7.2

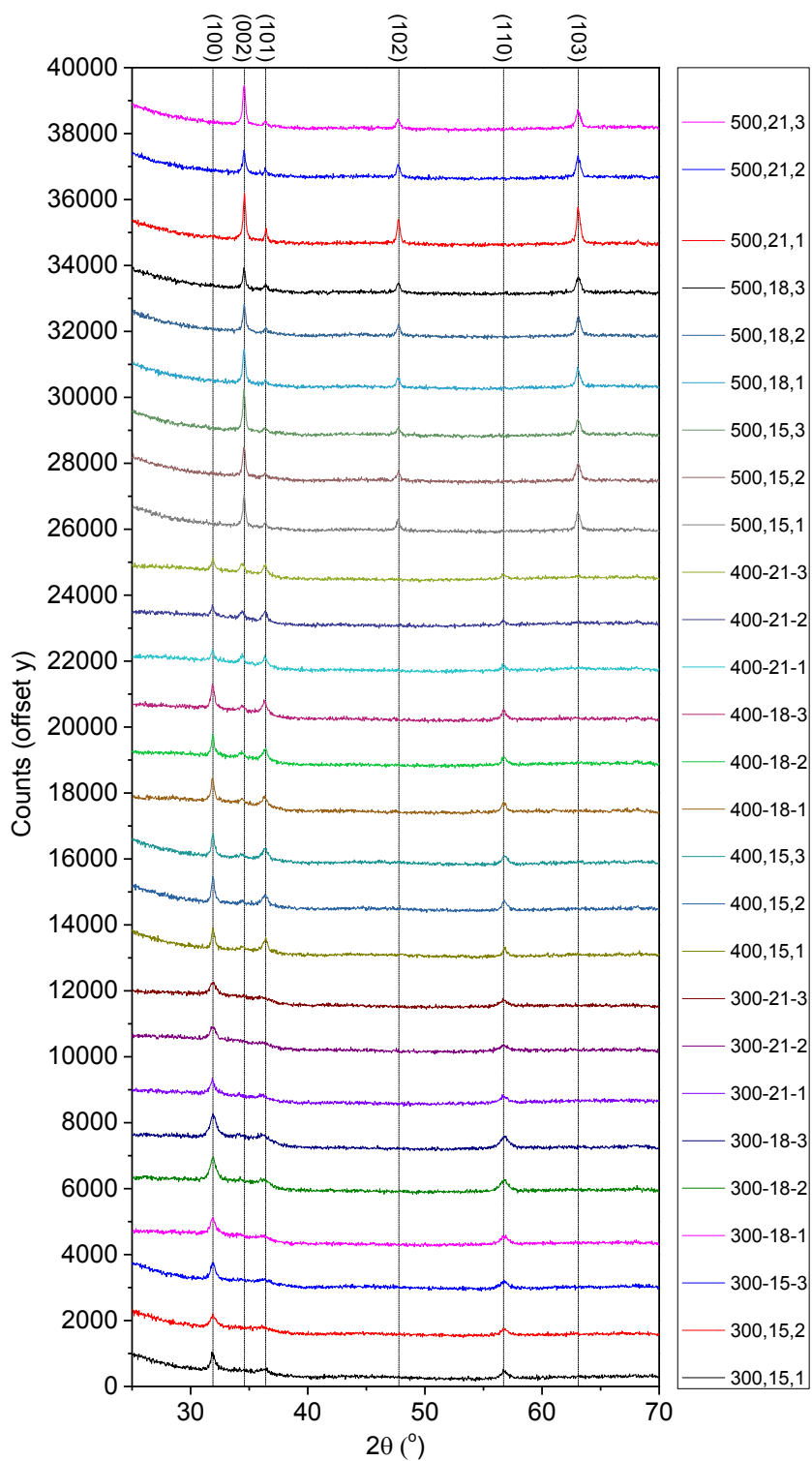


Figure A. 1 - Full XRD patterns from substrate temperature, stage height, gas pressure experiments

A.3 XRD patterns from section 4.2.9.2

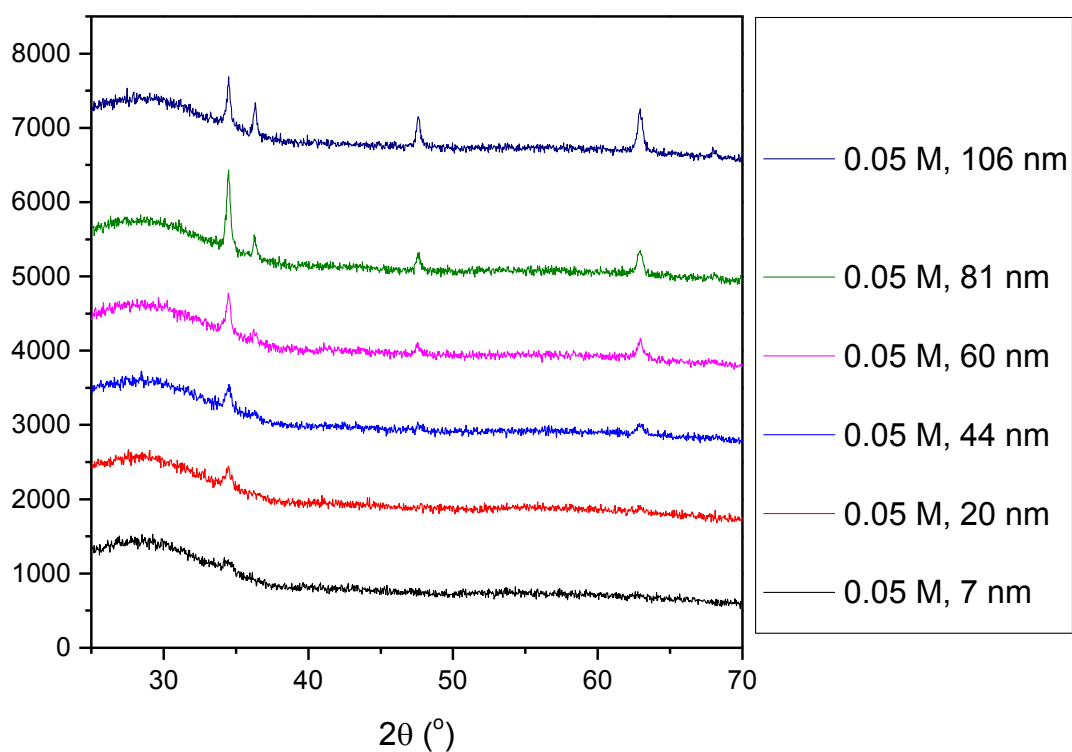


Figure A. 2 – Precursor concentration experiments: 0.05M

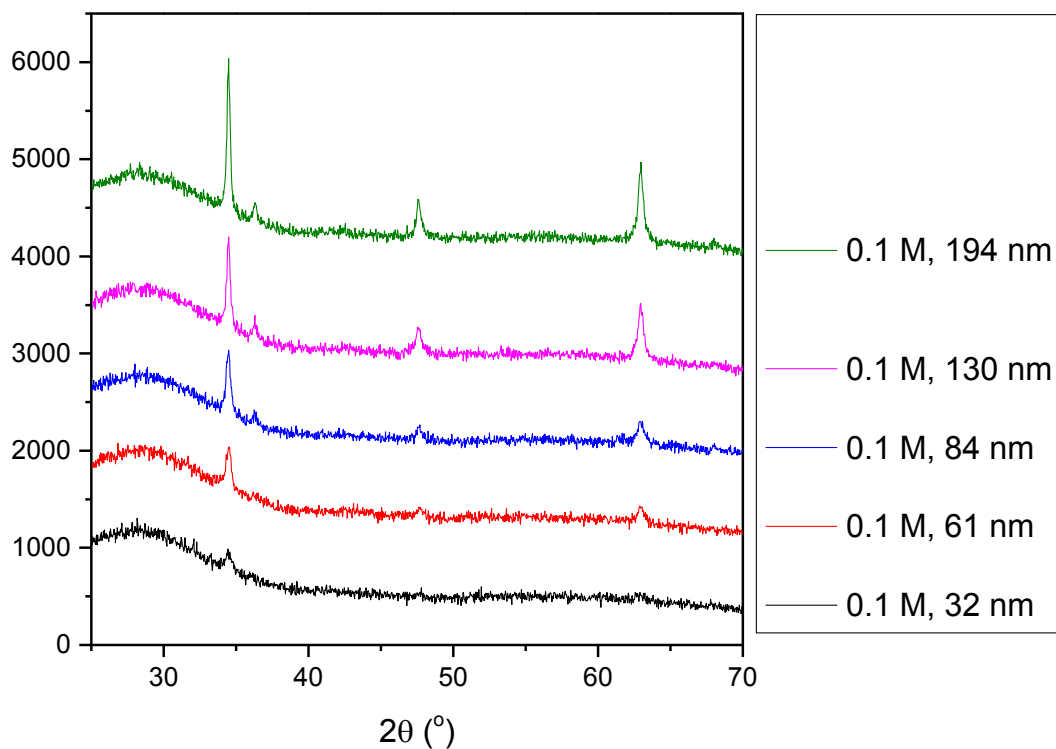


Figure A. 3 – Precursor concentration experiments: 0.1M

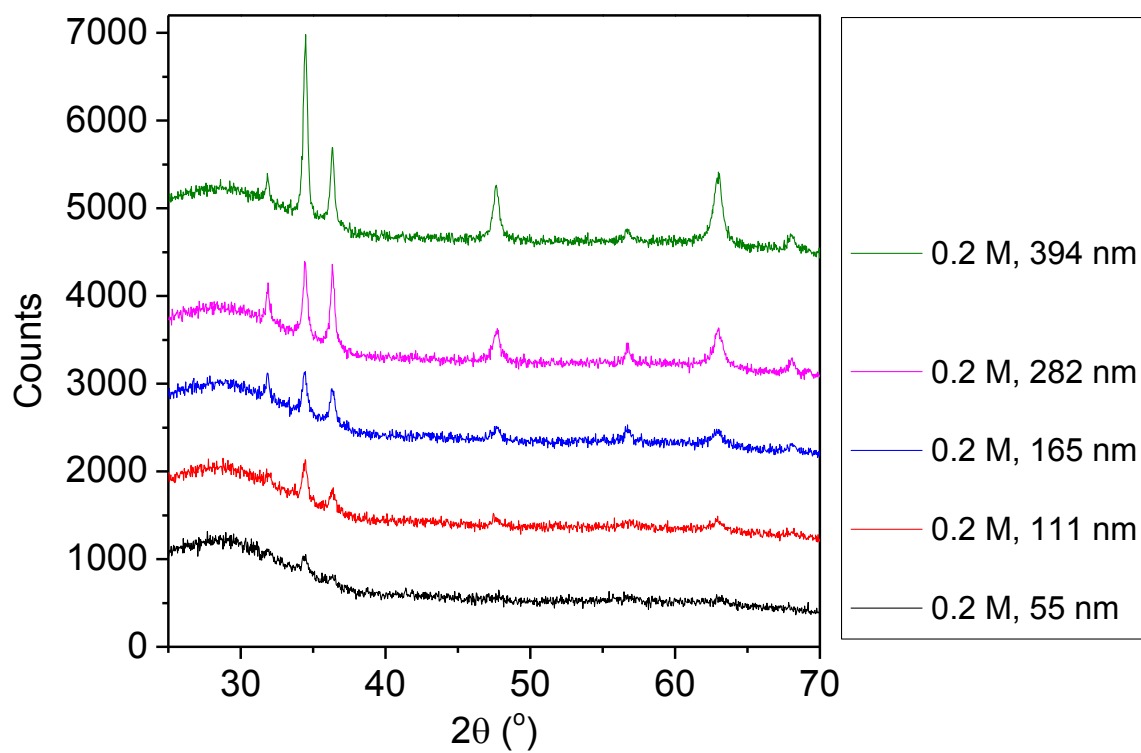


Figure A. 4 – Precursor concentration experiments: 0.2M

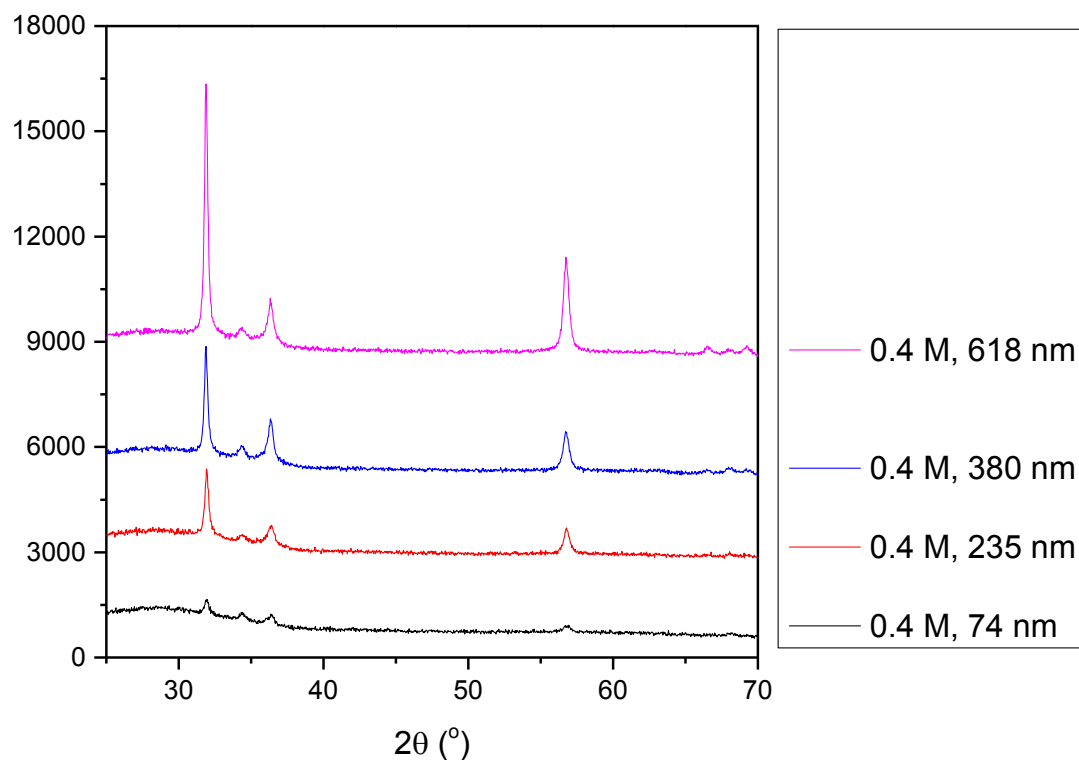


Figure A. 5– Precursor concentration experiments: 0.4M

A.4 XRD patterns from section 4.2.11.2

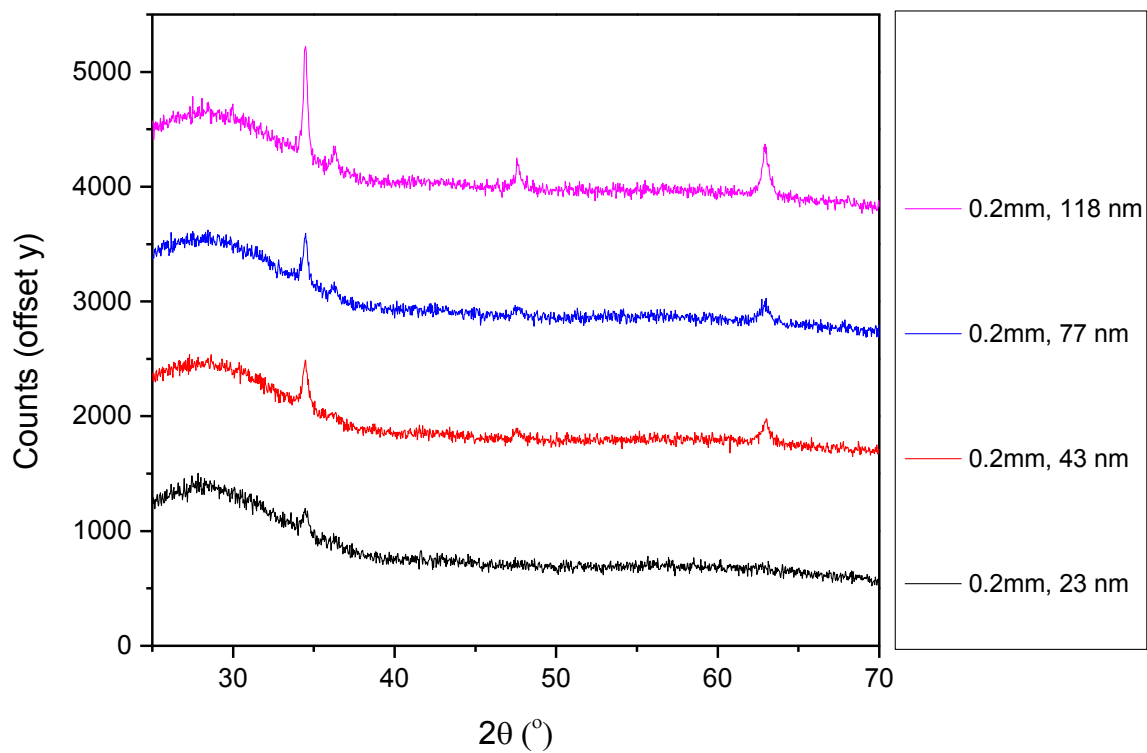


Figure A. 6 – Nozzle size experiments: 0.2mm

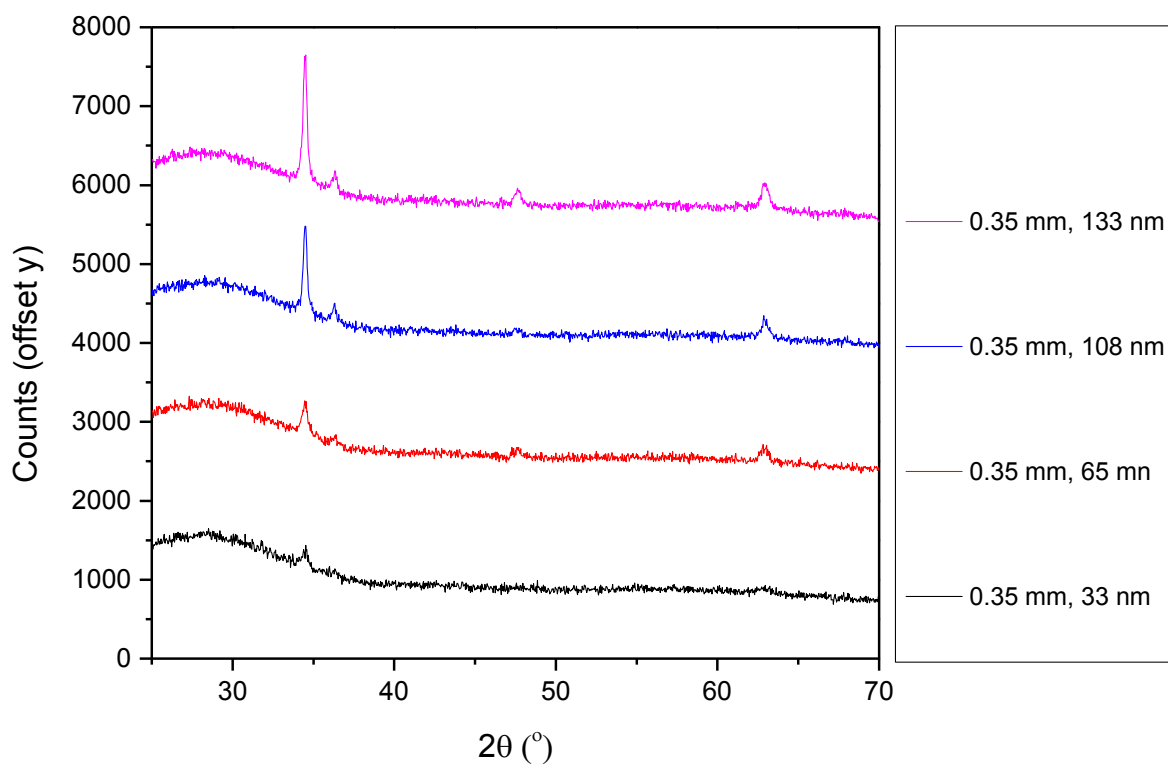


Figure A. 7 – Nozzle size experiments: 0.35mm

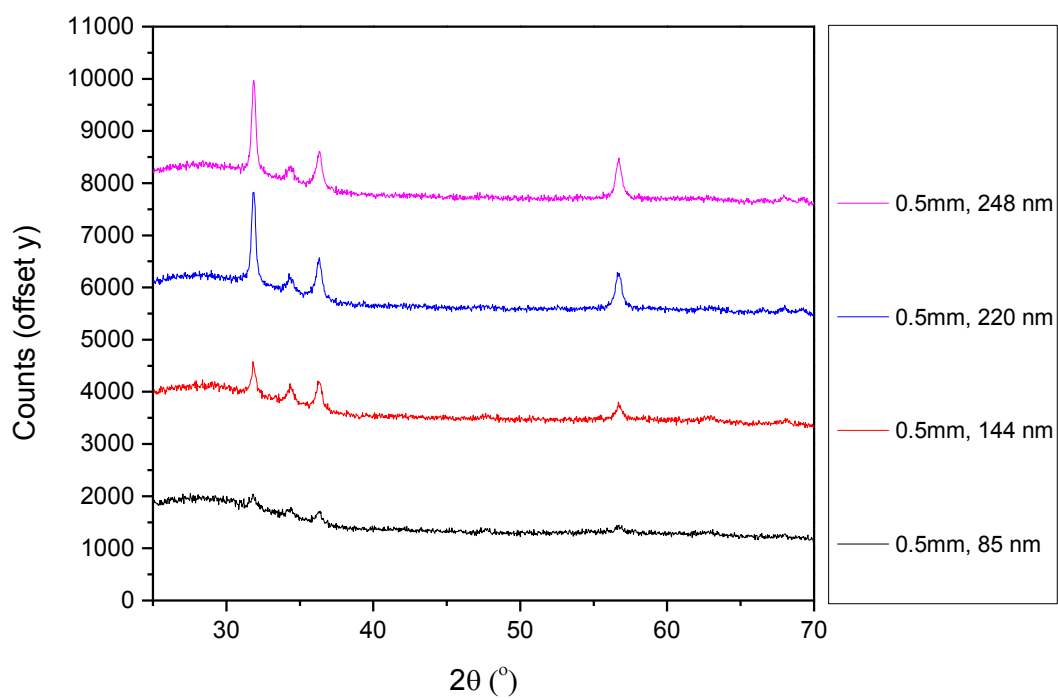


Figure A. 8 – Nozzle size experiments: 0.5mm

Data from Chapter V

A.5 XRD data from section 5.2.1

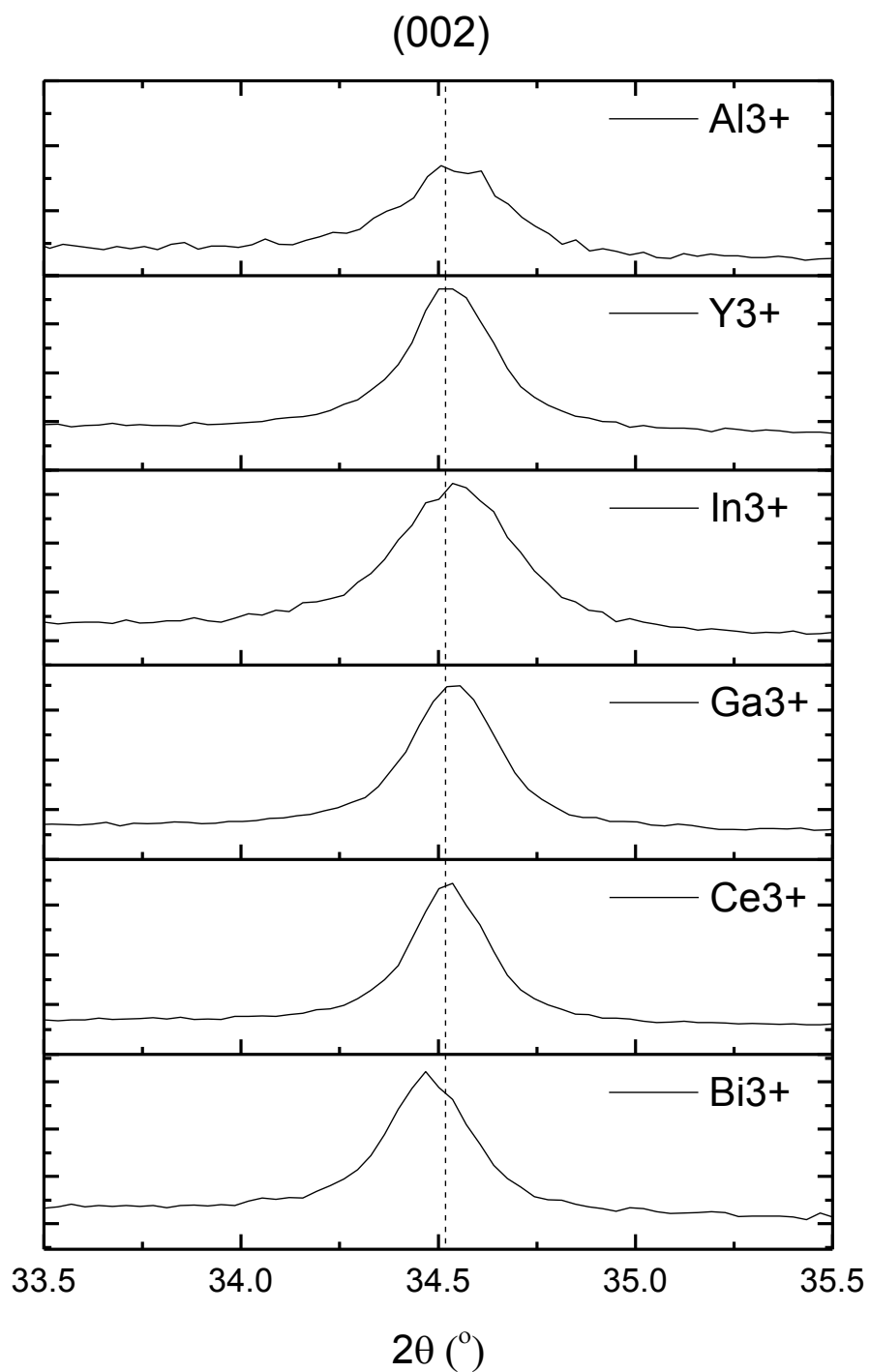


Figure A. 9 – XRD patterns of ZnO doped with Al, Y, In, Ga, Ce and Bi. The (002) reflection is highlighted to show minimal peak shift.